

Quantum Vacuum Nonlinearities in the All-Optical Regime

Dissertation

zur Erlangung des akademischen Grades
doctor rerum naturalium (Dr. rer. nat.)



**FRIEDRICH-SCHILLER-
UNIVERSITÄT
JENA**

vorgelegt dem Rat der Physikalisch-Astronomischen Fakultät der
Friedrich-Schiller-Universität Jena

von M.Sc. Leonhard Klar
geboren am 06.03.1995 in Oberhausen

Gutachter

1. Prof. Dr. Holger Gies,
Theoretisch-Physikalisches Institut,
Friedrich-Schiller-Universität Jena, Deutschland
2. Prof. Dr. Dr. Carsten Müller,
Institut für Theoretische Physik I,
Heinrich Heine Universität Düsseldorf, Deutschland
3. Dr. Anton Ilderton,
Institute for Particle and Nuclear Physics,
University of Edinburgh, Vereinigtes Königreich

Datum der Disputation: 11.10.2022

Für Hans und Ursula Rohde

Zusammenfassung

Die fundamentale Theorie zur Beschreibung der Wechselwirkung von Licht und Materie in der modernen Physik ist die Quantenelektrodynamik. Sie charakterisiert das Quantenvakuum als Fluktuationen von Elektron-Positron-Paaren auf extrem kurzen Zeit- und Längenskalen, wodurch das Vakuum polarisiert ist. Im Jahr 1936 zeigte die theoretische Behandlung von Werner Heisenberg und Hans Euler, dass die Polarisierung des Quantenvakuums nichtlineare Wechselwirkungen zwischen starken elektromagnetischen Feldern vermittelt und damit Maxwells lineare Theorie der Elektrodynamik im Vakuum erweitert.

Die Quantenelektrodynamik ist die best getestete Quantenfeldtheorie, dennoch steht der experimentelle Nachweis von Prozessen der Nichtlinearität des Quantenvakuums noch aus. Die Fortschritte in der modernen Hochintensitätslaserforschung geben Anlass zur Annahme, dass Experimente Phänomene wie Vakuum Doppelbrechung oder Photon-Photon-Streuung, induziert durch die Vakuumsfluktuationen, in absehbarer Zeit bestätigen. Neben dem technischen Anspruch an Erzeugung und Kontrolle starker elektromagnetischer Felder ist der enorme Hintergrund an Photonen der treibenden Laserstrahlen eine Herausforderung. In dieser Arbeit zeigen wir auf, wie neue theoretische Konzepte Messungen der Signatur der Nichtlinearität des QED Vakuums jenseits des Hintergrundes in Kollisionsexperimenten rein optischer Hochintensitätslaserpulse ermöglichen.

Mithilfe des Vacuum Emission Pictures entwerfen wir zunächst eine formale Behandlung der Signalphotonen, die der Nichtlinearität entspringen. Dabei entwickeln wir die Methode der Kanalanalyse des Signals; sie ermöglicht das Zerlegen des Signal in Beiträge verschiedener Laserpulse und liefert eine Interpretation mikroskopischer Prozesse.

Auf Basis dieser Erkenntnisse untersuchen wir zwei verschiedene experimentelle Szenarien und identifizieren erkennbare Signale. Im ersten Fall betrachten wir die Kollision zweier Hochintensitätslaserpulse, die sich nur in ihren Fokusbreiten unterscheiden. Wir stellen eine numerische Methode zur Identifizierung der Regionen, in denen das Signal den Hintergrund dominiert, vor. Damit untersuchen wir das Verhalten des erkennbaren Signals insbesondere in Hinblick auf die Auswirkungen der Fokusbreite des Sondenstrahls. Besonders erwähnenswert ist, dass eine Maximierung der messbaren Signalphotonen nicht durch minimale Fokussierung erreicht wird. Dies ist mit dem Zusammenspiel aus Intensität im Wechselwirkungsvolumen und Abfallverhalten des Hintergrundes im Fernfeld erklärbar. Mithilfe eines elliptischen Querschnitts des Sondenpulses lässt sich das Signal zusätzlich verstärken. Ferner zeigen wir, dass eine erkennbare Signatur der Vakuum Doppelbrechung im optischen Bereich erreichbar ist.

In einem zweiten Aufbau wird die elastische und inelastische Photon-Photon-Streuung, vermittelt durch die Nichtlinearität des Quantenvakuums, untersucht. Basierend auf einer Kollision von vier Laserpulsen verschiedener Oszillationsfrequenzen beobachten wir Signale in Bereichen außerhalb der Vorwärtsrichtung der treibenden Laser sowie mit Frequenzen jenseits der Laserfrequenzen. Diese Eigenschaften erlauben eine Messung des Signals jenseits des Hintergrundes. Die vorhergegangene Kanalanalyse hilft nicht nur bei der Interpretation der Ergebnisse, sondern sie ermöglicht auch eine effektive Verstärkung des Signals bei gleichbleibenden experimentellen Einschränkungen.

Abstract

The fundamental theory describing the interaction of light and matter in modern physics is quantum electrodynamics. It characterizes the quantum vacuum via fluctuations of electron-positron pairs on extremely short time and length scales, whereby the vacuum is polarized. In 1936, theoretical investigations by Werner Heisenberg and Hans Euler showed that the polarization of the quantum vacuum mediates nonlinear interactions between strong electromagnetic fields, extending Maxwell's linear theory of electrodynamics in vacuum.

Quantum electrodynamics is the best tested quantum field theory, yet experimental evidence of quantum vacuum nonlinearity processes is still pending. Progress in modern high-intensity laser research gives reason to believe that experiments will confirm phenomena such as vacuum birefringence or photon-photon scattering induced by vacuum fluctuations in the foreseeable future. In addition to the technical requirement of generating and controlling strong electromagnetic fields, the enormous background of photons of the driving laser beams is a challenge. In this work, we demonstrate how new theoretical concepts enable measurements of the signature of the QED vacuum nonlinearity beyond the background in collision experiments of all-optical high-intensity laser pulses.

Using the vacuum emission picture, we first design a formal treatment of the signal photons encoded by the nonlinearities. To this end, we develop the method of channel analysis of the signal; it allows the signal to be decomposed into contributions from different laser pulses and provides an interpretation of microscopic processes.

Based on these findings, we study two different experimental scenarios and identify discernible signals. In the first case, we consider the collision of two high-intensity laser pulses that differ only in their focus waist sizes. We present a numerical method to identify the regions where the signal dominates the background. Furthermore, we use this to investigate the behavior of the discernible signal, particularly with respect to the effects of the waist size of the probe beam. Of particular note, maximization of the measurable signal photons is not achieved by minimal focusing. This can be explained by the interplay of intensity in the interaction volume and decay behavior of the background in the far field. With the help of an elliptical cross section of the probe pulse, the signal can be further enhanced. Moreover, we show that a discernible signature of vacuum birefringence is achievable in the all-optical regime.

In a second setup, elastic and inelastic photon-photon scattering mediated by the nonlinearity of the quantum vacuum is investigated. Based on a collision of four laser pulses of different oscillation frequencies, we observe signals in regions beyond the forward direction of the driving lasers as well as with frequencies beyond the laser frequencies. These features allow us to measure the signal beyond the background. The preceding channel analysis not only helps in the interpretation of the results, but it also allows effective amplification of the signal while maintaining experimental constraints.

Contents

1. Introduction	3
2. Foundations	11
2.1. Heisenberg-Euler Lagrangian in One-Loop Quantum Electrodynamics	11
2.2. Modern Optics	18
2.2.1. Gaussian Beams and Pulses	18
2.2.2. Modern Laser Facilities	26
3. Probing the QED Vacuum Nonlinearities with Strong Electromagnetic Fields	31
3.1. Vacuum Emission Picture	32
3.2. Channel Analysis: Key to Optimization	37
3.2.1. Collision of Several Arbitrary Pulses	37
3.2.2. Signal Photon Amplitude and Channels	39
3.2.3. Performing the Fourier Integral	42
3.2.4. From the Channel Signal Photon Amplitude to the Density	45
3.2.5. Physical Interpretation of the Channels	48
4. Discernible Signal of QED Vacuum in Exemplary Scenarios	55
4.1. Signature of QED Vacuum Nonlinearities in a Two-Beam Collision	58
4.1.1. Collision Geometry and Pulse Properties	59
4.1.2. Region of Discernible Signal	62
4.1.3. Discernible Polarization Insensitive Signal	65
4.1.4. Discernible Vacuum Birefringence	80
4.2. Elastic and Inelastic Photon-Photon Scattering	82
4.2.1. Collision Geometry and Pulse Modeling	83
4.2.2. Analysis of the Signature of Quantum Vacuum Nonlinearities	85
4.2.3. Applying of the Channel Analysis	92
5. Conclusion	97
A. Notations and Conventions	101
B. Appendix	103
B.1. Vacuum Polarization in QED	103
B.2. Approaches Beyond the Standard Model	105
B.2.1. Born-Infeld Model	105
B.2.2. Axion-like Particles	107

Contents

B.2.3. Millicharged Particles	108
Bibliography	110
List of Figures	135
List of Tables	137
Abbreviations	139
Danksagungen	141
Ehrenwörtliche Erklärung	143

1.

Introduction

“Natura abhorret vacuum.”

— François Rabelais, *Gargantua and Pantagruel* [1]

Nothingness, the void, the absence of something, matter, perhaps light, temperature – the vocabulary of scientists, philosophers, and artists throughout world history seems to be full of paraphrases for a space devoid of matter. Perhaps the most widely used term is, however, *vacuum*, originating from the Latin word *vacuus* meaning *empty* [2]. As manifold as the choice of words is, so manifold is the understanding of what exactly the vacuum is supposed to be and whether it exists at all.

The vacuum has always attracted the interests of philosophers; this is already evident in the discussions in ancient Greece in the 5th and 4th century BC. Especially Aristotle was considered as a convinced representative of the perception that there is no vacuum in Nature. In his work *physics book IV* he argues in particular against the doctrine of Democritus and Leucippus, who are known as the founders of atomism [3]. In their eyes the natural world consists of two fundamental principles: atoms and void [4, 5]. For these philosophers, atoms were small indivisible bodies, varying in shape and size, containing no holes and able to move through the void. And Aristotle was skeptical about the concept of void. Whereas his opponents saw an existence of the void in the fact that bodies can move, contract or increase by filling the void, Aristotle criticized that in such processes only a displacement of one body from another takes place. He concluded that it “is evident, then, that it is easy to refute the arguments by which they prove the existence of the void.” [3, Chapter 7].

In the Middle Ages the essential discussions about the existence of the vacuum took place in the Arab and Persian world. The foundation of these discourses was established in the 9th century by Abu Ya’qūb Ibn Ishāq al-Kindī (Latinized as Alkindus). Al-Kindī translated many ancient writings into Arabic and thus enabled the Muslim educated class to access the knowledge of Hellenistic philosophers [6, 7]. Abu Nasr al-Fārābī (Latinized as Alfarabius) was one of the scholars of the first half of the 10th century who adopted the doctrine of Aristotle and rejected the existence of the void [8, 9]. In contrast to al-Fārābī, Hasan Ibn al-Haytham (Latinized as Alhazen), who lived in the second half of the 10th century, developed a profound understanding of optics, even though he was in conflict with Aristotle’s doctrine. Thus he spoke out against an instantaneous transmission of light, as it was usual among the students of Aristotle, but advocated the idea of a finite speed of light. Likewise he supported the idea of the existence of the void, just like his Persian contemporary Ibn Sina (Latinized

as Avicenna) [9–12].

Knowledge of the natural sciences in the thirteenth-century European High Middle Ages was dominated by the understandings of Christian friars such as Albertus Magnus and Roger Bacon, who were strongly influenced by the rediscovered writings of Aristotle and by Muslim sources such as al-Fārābī and Ibn Sina. Unlike Ibn Sina, Bacon declared that Nature prevents the vacuum. This was also the view of Thomas Aquinas, a student of Albertus Magnus, who believed that an empty space was useless and God would not create anything useless. That the concept of a vacuum had passed into a theological dispute is also shown by the Condemnation of 1277, promulgated by Étienne Tempier, bishop of Paris, in which it was proclaimed that God, as an almighty creator, could create the vacuum even if it did not exist [12–15]. This condemnation was the beginning of the abandonment of the Aristotle doctrine, although it lasted for centuries.

With his rejection of the void – and thus of the vacuum – Aristotle formed an all-embracing doctrine that far transcends scientific discourse and has penetrated into religion and art for centuries [16]. To Aristotle was assigned the citation “Nature abhors a vacuum”, although this does not occur once in his work *physics*. The vacuum was mystified; in arts the *horror vacui*, the fear of the vacuum, arose. Although this designation of art that avoids emptiness was introduced later by the art critic Mario Praz of the 20th century [17]. Another example of how much Aristotle’s thoughts influenced the Renaissance art is the novel *Gargantua and Pantagruel* by the French humanist François Rabelais in the 30s of the 16th century which introduced the phrase “Natura abhorret vacuum” into literature [1].

Starting with the Scientific Revolution around 1550, triggered by the paradigm shift of the astronomical model after Nicolaus Copernicus, European intellectuals increasingly faced their *horror vacui*. The first experiments with artificially produced vacua took place in the 17th century. Evangelista Torricelli’s barometer made it possible to measure different air pressures; however, one of the most spectacular experiments on vacua at this time was carried out by Otto von Guericke, the mayor of Magdeburg who had studied also at the university of Jena. In 1654, he presented his *Magdeburg Hemispheres* to the Reichstag in Regensburg: a vacuum was created between two hemispheres using the air pump invented by von Guericke. Even the force of sixteen horses pulling on the hemispheres could not separate them. Only by re-entering air von Guericke was able to separate the hemispheres effortlessly [15, 18–20]. This demonstrated that by removing air, the pressure could be changed. But what exactly remains in a chamber from which the air has been pumped out still had to be debated in the scientific and philosophical discussions of the Enlightenment. From today’s point of view, however, Toricelli’s and von Guericke’s experiments are explained by thermodynamics. The concept of vacuum used here is to be understood technically; with decreasing pressure the mean free path of gas particles is increased. In the present work such a technical vacuum is expressly not examined.

During the Age of Enlightenment, Gottfried Wilhelm Leibniz was one of the declared opponents of the existence of a vacuum, which is evident from his correspondence with the British philosopher Samuel Clarke [21, 22]. The latter was a friend of Isaac Newton, who in turn assumed an emptiness for the undisturbed movement of celestial bodies. At the

same time Newton asked himself the question, how gravity interacts, because it obviously affects also through the vacuum. But the absolute vacuum in space was in conflict with Newton's first law, which defines an inertial frame by the state absence of forces or absolute rest [23]. If there is an absolute rest, then there must be a relative reference point to which the body rests. A possible solution being more and more discussed in science is the existence of an omnipresent aether mediating fundamental physics, e.g. the motion of light, which was even suggested by Newton himself [24]. Christiaan Huygens, also a supporter of the aether theory, founded the wave theory of light in the 17th century with the understanding of light as a longitudinal wave propagating through the aether, also referred as luminiferous aether, though it is the Latin paraphrase for light bearing aether.

With the acceptance of the aether as a scientific standard, also legitimized by Leonhard Euler, who described the aether in the 18th century with an extremely low density and at the same time high elasticity [25], enormous progress was made in the field of optics in the age of the Industrial Revolution in Europe in the 18th and 19th centuries. Étienne Louis Malus discovered the polarization of light in 1809, which disclosed light to propagate as a transverse wave, contrary to Huygen's assumption. And James Clerk Maxwell elaborated his formalization of electromagnetism under the assumption that light is given by electromagnetic waves in the aether, just as sound waves can exist only in air. It was Heinrich Hertz who experimentally confirmed Maxwell's theory, although he was convinced that Maxwell's theory was valid even without the existence of the aether. Nevertheless, he also believed in the reality of the aether, albeit he himself had an open mind for discussions. In his lecture about the fundamental principles of physics in 1884 Hertz presented very skeptical thoughts about the theory of the aether [26–28]. Only by the experiments of Albert Abraham Michelson and Edward Williams Morley the doubt about the aether became so strong that it was no longer tenable [29,30]. The absence of a confirmation that the earth moves through the luminiferous aether, which was a repeatedly tested result by the interferometer experiments of Michelson and Morley measuring the relative velocity of light to the aether, helped the special theory of relativity of Albert Einstein to its breakthrough [31].

If even the aether was no longer tenable then the vacuum would remain empty. The *classical vacuum* is understood to be the absence of matter, i.e. something afflicted with mass. This definition allows the optional presence of force fields and radiation in the classical vacuum or, at least, they can act through it like light, which is interpreted in classical electrodynamics as field theory [19]. Due to its linearity, the superposition principle is valid for electromagnetic radiation. In the classical vacuum the Maxwell equations differ from those in matter, where effects like refraction or polarization sensitivity are observable.

One origin of radiation was considered to be the thermal emission of black-bodies, an idealized non-reflecting body. Max Karl Ernst Ludwig Planck succeeded in explaining this black-body radiation, which was first described in detail by Gustav Robert Kirchhoff in 1893. In his studies around the year 1900, Planck formulated mathematically the wavelength dependence of the intensity distribution, also called spectrum, of electromagnetic radiation at constant temperature in thermal equilibrium [32,33]. The black body radiation is a rejection of the existence of a *pure classical vacuum*, which is not only free of matter, but also of fields

like those of gravitation or electromagnetic radiation. Since according to the third law of thermodynamics the absolute zero-point cannot be reached, radiation is always present. Ten years later, Planck supplemented the concept of zero-point energy which does not vanish in the limit of zero temperature [34,35]. For the construction of his mathematical model Planck could not omit an assumption: he discretized the energy differences, which appear in Planck's formula, and introduced the constant h , which was named after him later. Thus the idea of quantum physics was born.

Alongside, with quantum mechanics, a new understanding of the vacuum as the ground state was born. This state can have a finite energy or excitation, for example for a harmonic oscillator of frequency ω the ground state energy is $E_0 = \frac{1}{2}\hbar\omega > 0$, where $\hbar = \frac{h}{2\pi}$ is the reduced Planck constant. Considering the uncertainty principle formulated by Werner Karl Heisenberg in 1927, the ground state excitation cannot have a vanishing position and at the same time possess no momentum [36]. Consequently, the *quantum vacuum* cannot be empty at all.

In 1928, Paul Adrien Maurice Dirac formulated a relativistic description of the electron, extending the Schrödinger equation which is used to describe quantum particles. As consequences of his theory, solutions of the free Dirac equation involving negative energies occurred. In order to interpret states with negative energy he established a new way of looking at the vacuum by relating it to the picture of an infinite sea of occupied states with negative energies $E_- \leq -m_e c^2$, where m_e denotes the rest mass of the electron and c the speed of light [37–39]. Free electron states have positive energy $E_+ \geq m_e c^2$ and do not collapse because the Dirac sea is already filled and due to the Pauli exclusion principle two electrons cannot have the same quantum properties [40]. The lack of occupation of a state in the Dirac sea is called a *hole*. This hole can be assigned a momentum, as well as an energy, so that Dirac recognized that it must be an antiparticle with the same mass but opposite charge to the electron: the positron. Considering a free electron and a positron recombination occurs because it is energetically more favorable for a free low-energy electron to occupy the free state in the Dirac sea. During this process of recombination, the electron radiates electromagnetic waves with the total energy $E_\gamma = E_+ - E_- \geq 2m_e c^2$ matching the energy differences of the two particles in the Dirac sea. The recombination of a low-energy electron with a positron is called *pair annihilation*. Since Einstein introduced the concept of the photon as a quantum particle of the electromagnetic field to explain the photoelectric effect in 1905, Dirac already connected the change of the energy states of an electron with the emission of photons [39,41,42].

However, Dirac's model of the quantum vacuum has some inelegance; aside from the infinite negative charge of the vacuum, it is hard to understand how another free state cannot be added to the unlimited numbers of states in the sea, apart from the fact that this behavior would entail the consequences in the form of instability of a free electron, which we do not observe in Nature. Dirac and Heisenberg were aware of the limitations of the model, as can be seen from their 1934 publications [43,44]. Here Dirac has also considered “phenomena of the nature of a polarization of a vacuum by an electromagnetic field” [43, P. 163]. Moreover, the complexity of the vacuum prompted Dirac to think about an aether in terms of quantum mechanics twenty years later [45].

In 1931, one year after the publication of Dirac's sea model, Fritz Eduard Josef Maria Sauter concluded from this model that, in the presence of a strong electric field, it must be possible to extract an occupied state from the negative energy spectrum of Dirac's sea. Because of the hole left behind in the Dirac sea and the release of a positive electron state, one speaks of electron-positron *pair production* out of the vacuum. Sauter determined the probability of such a transition and commented that it is impossible to achieve the necessary critical field strengths technically [46]. This effect of electron-positron pair generation is known as the Sauter-Schwinger effect, or often just Schwinger pair production, since Julian Seymour Schwinger formulated this effect in 1951 in a modern relativistic language of effective quantum field theory.

Back in 1934, Max Born and Leopold Infeld found a nonlinear extension of electrodynamics. Their motivation was to solve the problem of the divergent self-energy of the electron in classical electrodynamics by introducing an absolute field which acts as an upper bound of the allowed electric field strength [47]. In the limit of small field strength, their field theory provides the same behavior as Maxwell's classical electrodynamics. In addition, a nonlinear behavior as known from electrodynamics in polarized matter is shown. Erwin Rudolf Josef Alexander Schrödinger showed that Born-Infeld theory leads to phenomena known from nonlinear optics, but instead of the necessary presence of nonlinear materials, this behavior was described completely in the vacuum [48–50]. This give rise to nonlinear optics phenomena like photon-photon scattering.

Pioneering work in the field of nonlinear electrodynamics was accomplished by Heisenberg and his PhD student Hans Heinrich Euler in 1936. Independently of Born's ansatz, they deduced from Dirac's theory of the positron an alteration of Maxwell's equations in vacuum. They justified this necessity by the possibility of pair production by electromagnetic fields and the new understanding of the quantum vacuum [51–53]. It resulted in a Lagrangian for the electromagnetic fields extending Maxwell's Lagrangian by nonlinear terms. Heisenberg, Euler, and Bernhard Kockel concluded among others the effect of photon-photon scattering. In general, it predicts phenomena mediated by the nonlinear behavior of the fields, similar to the ad hoc motivated Born-Infeld model. Of particular interest are the quantitative comparisons of the predictions of these two models. James Robert McConnell quantized Born-Infeld model and compared its results with the outcome of the Heisenberg-Euler Lagrangian [54]. He did not find any difference in the lowest nontrivial order of the differential cross section for photon-photon scattering in dependence of scattering angular or photon frequency. However, the prediction of the existence of vacuum birefringence differs with the used model. Consequently, both approaches cannot be mapped to each other. Experiments so far have not provided evidence for the Born-Infeld model, whereas the theoretical framework in which the description of Heisenberg and Euler is to be classified has so far received very high experimental confirmation.

In the present thesis we will restrict ourselves to the theory of Heisenberg and Euler, since it is part of modern quantum electrodynamics (QED), a theory of the Standard Model (SM) of particle physics, which so far is in full agreement with experimental findings. Moreover, as modern relativistic field theory governing the interaction of light and matter, QED is the

best tested quantum field theory (QFT). To assess the quality of QED, it is convenient to compare the measurements of the fine-structure constant α , which quantifies the strength of the electromagnetic interaction, in experiments for different QED phenomena. The comparisons of the fine-structure constant with experimental results in the low-energy regime, such as the Lamb shift, hyperfine structure, anomalous magnetic dipole moments, atomic-recoil measurements, high-energy processes, e.g. high-energy electron-positron collisions, and in effects of condensed matter physics, such as quantum Hall effect or alternating current Josephson effect, agree extremely well [55–63].

A deep understanding of QED is mainly due to the systematic formalization of QED. The foundations of QFT, in particular of QED, were established by Julian Schwinger, Richard Phillips Feynman, Freeman John Dyson, and Shin'ichirō Tomonaga [64–68]. Using different approaches they worked out how to deal with the infinite contributions arising in calculations of QED; the methods of renormalization, like the ultraviolet cutoffs, are still used in QFT today [69–71]. Further, the work of Schwinger in 1951 led to a deeper understanding of the quantum vacuum. Using proper time methods, effective actions, Green's function approaches and the description of QED as gauge invariant theory, he determined the same Lagrangian Heisenberg and Euler established in 1936 [52, 72]. Moreover, he re-derived the probability that an electron-positron pair is created out of the vacuum by a constant electric field as Sauter did before. He confirmed that the critical electric field strength governing this effect at the Schwinger limit is $\mathcal{E}_{cr} = c^3 m_e^2 / (e \hbar) \approx 1.3 \times 10^{18} \text{ V m}^{-1}$, where e denotes the elementary charge. This high field strength has not been generated in a laboratory in a controlled fashion yet.

According to Schwinger's ideas, we understand the quantum vacuum as the presence of fluctuations of virtual particle-antiparticle pairs on extremely small time and length scales. In the case of QED, this is the electron and positron with Compton wavelength $\lambda_C = 3.86 \times 10^{-13} \text{ m}$ and Compton time $\tau_C = 1.29 \times 10^{-21} \text{ s}$ as scales. Since these particles have opposite charge, we speak of vacuum polarization. Those virtual fluctuations can be measured in QED phenomena like Delbrück scattering or the Lamb shift, since the electrostatic polarization leads to an atomic energy shift [20, 73, 74].

Delbrück Scattering is the effective scattering of gamma rays in the Coulomb field of highly charged nuclei. This scattering was verified in several experiments [75–77]. Another phenomena of strong-field QED (sfQED) in the vicinity of strongly charged ions is the effect of photon splitting; here an experimental verification was also successful [78, 79]. Apart from processes close to strongly charged nuclei operating at momentum transfers of about 100 MeV or larger, barely sfQED phenomena, which can only be explained with the help of the nonlinearity of the quantum vacuum, have been experimentally confirmed so far. These phenomena are the subject of modern research, they include nonlinear Breit-Wheeler process (creation of electron-positron pairs by a high-energy photon collision) [80–91], photon-photon scattering [92–102], vacuum birefringence and dichroism [103–121], quantum reflection [122, 123], photon merging and splitting [124, 125]; for reports and reviews, cf. [126–136]. These effects are still waiting to be experimentally demonstrated, as they require particularly high intensities of electromagnetic fields. However, these field strengths are weak compared to the critical

field strength of the Sauter-Schwinger effect.

The success in the construction of laser facilities generating ultra-intense laser pulses in the last decades gives hope that in the near future some of these phenomena may soon be experimentally verified. The state-of-the-art and in-development facilities use petawatt ($1 \text{ PW} = 10^{15} \text{ W}$) class laser pulses and create extremely strong electromagnetic fields by focusing them into a narrow volume, e.g. *OMEGA extended performance* (OMEGA EP) at *Laboratory for Laser Energetics* (LLE) of the university of Rochester in New York, USA, or the *Extreme Light Infrastructure - Nuclear Physics* (ELI-NP) in Măgurele, Romania [137, 138]. Beyond optical lasers, the *X-Ray Free Electron Laser* (XFEL) at *Deutsches Elektronen-Synchrotron* (DESY) in Hamburg, Germany, also provides high-energy ultrafast X-ray pulses that are adjustable in wavelength [139, 140]. Strongly focused laser pulses increase the local photon density extremely, enabling a very high number of photons to be considered for nonlinear effects. At the same time, such laser pulses can be used as pumps, providing an extremely strong background electromagnetic field that stimulate vacuum polarizations. These reviews give an overview about sfQED effects in strong laser fields [141–143].

For probing the quantum vacuum very strong electromagnetic fields and thus a very large number of driving laser photons are necessary. A high number of photons driving the phenomena of the quantum vacuum alone is not sufficient enough to verify those effects. The signal of the quantum vacuum – independent of which phenomenon is considered – is extraordinarily small compared to the driving laser photons (ratio $\sim 1 : 10^{20}$). Fortunately, the fact that the experimental setups for execution and measurement are becoming more and more accurate provides further prospect for early verification. Nowadays it is possible to use plasma mirrors for laser focusing [144, 145]. Another example is the progress in X-ray polarimetry, where in the meantime a polarization purity of about 10^{-10} for high-intensity X-rays is achieved [146, 147]. Further, modern optics successes in single photon detection as well as repressing and controlling the background of the driving laser beams [148, 149].

Extremely strong laser pulses and high-precision optics alone are not enough to detect the signature of the quantum vacuum. Therefore, in addition to high-resolution technology, theoretical considerations are needed as a guidance towards distinguishing the signal from the background [150–157]. Laser pulses provide spatially and temporally inhomogeneous electromagnetic fields that require a quantitatively precise theoretical analysis. In addition, various effects such as tailored laser beamss, coherent harmonic focusing or manipulation of the focal widths of the laser beams can be exploited to increase the field strengths [158–162]. Furthermore, tools for a better analysis of the signal are subject of current research, which allow a better separation of signal and background. These include channel analysis or the study of polarization behavior [102, 163–165]. However, these effects have to be analyzed on a theoretical basis before they can be implemented experimentally.

In this work we focus our attention exclusively on the signature of nonlinearities mediated by the QED vacuum polarizations in the all-optical regime. In particular, we are mainly interested in photon-photon scattering. However, we also investigate quantum vacuum birefringence. We aim to study these sfQED effects beyond their strong background so that experimental distinguishment from the background can succeed.

For this we start in Ch. 2 by recapitulating the basic theories. First, in Sec. 2.1, we turn to the Heisenberg-Euler Lagrangian: Here we limit ourselves to 1-loop QED. We derive, based on the Schwinger QFT approach, the nonlinear contributions due to our understanding of the quantum vacuum, which extend classical electrodynamics and are worth studying in the present work.

To probe these nonlinearities in an experiment, we rely on high intensity lasers in the all-optical regime. As a basis for this, Sec. 2.2 discusses the possibilities offered by modern optics for this purpose. First, in Sec. 2.2.1, Gaussian beams and pulses are formally introduced. Following this, Sec. 2.2.2 deals with the state-of-the-art in modern laser technology and shows which experimental parameters ensure realistic models for our calculations.

Ch. 3 formally deals with the treatment of photons mediated by the nonlinearity of the quantum vacuum in the background of strong electromagnetic fields. For this purpose, the vacuum emission picture is first introduced in Sec. 3.1. In this, the concept of signal photon is defined, which provides information about nonlinearities of the QED vacuum in an experiment. Using the vacuum emission picture, we then analyze the signal in Sec. 3.2. To this end, we introduce the channel analysis, a modern method that leads to a deeper theoretical understanding of the process for emitting signal photons – and in particular their properties. As a foundation, we first describe the collision of any number of laser pulses, Sec. 3.2.1, from which we determine the signal photon amplitude in Sec. 3.2.2. The formal treatment from amplitude to angle-resolved density in Sec. 3.2.3 and Sec. 3.2.4 is followed by a comprehensive interpretation of the results in Sec. 3.2.5. In doing so, we provide a microscopic understanding and also point out limitations.

In Ch. 4, we consider two different exemplary experimental scenarios leading to a measurable signature of the quantum vacuum. The focus of these analyses is on identifying the signal beyond the enormous number of background photons. For this purpose, the collision of two laser pulses differing only in their focal properties is considered in Sec. 4.1. The geometry is presented in Sec. 4.1.1, followed by a detailed introduction of the criterion for the discernibility of the signal in Sec. 4.1.2. Then, the theoretical results from Ch. 3 are applied in Sec. 4.1.3 to discuss the signal for scenarios using a probe beam with circular or elliptical cross section. Furthermore, Sec. 4.1.4 discusses vacuum birefringence. The second experimental setup addresses the collision of four laser pulses of different frequencies, Sec. 4.2, where we introduce the geometry in Sec. 4.2.1. Therefore, Sec. 4.2.2 contains a comprehensive analysis of the signature, and in Sec. 4.2.3 we relate it to the results of the channel analysis.

We end the thesis with the conclusion in Ch. 5. For remarks on the photon propagator in QED and models beyond the standard model, we refer to the appendix B.

The compilation of this thesis is solely due to the author. However, a large part of the work presented here has been published in a number of articles and in collaboration with other authors. Sec. 3.2 and Sec. 4.1 contain ideas first published in the authors single-author publication [160] and further developed in reference [164], which was written with Holger Gies and Felix Karbstein. Ch. 4 relies on two references with Holger Gies and Felix Karbstein which has been or will be published [162, 164].

2.

Foundations

“Zweitens ist es gerade eine der typischen Strukturen der theoretischen Physik, daß es die richtige Theorie nicht gibt, sondern daß jede Theorie durch sich selbst Kritik hervorruft, die darauf drängt, eine noch bessere Theorie zu suchen.”

— Günther Ludwig, *Einführung in die Grundlagen der Theoretischen Physik* [166]

First, the fundamentals on which the methodologies, analyses and discussions of this work are based are briefly presented. We distinguish here between the foundations from QED, Sec. 2.1, and modern optics, Sec. 2.2. We start in Sec. 2.1 with a detailed presentation of the Heisenberg-Euler Lagrangian, which has already been introduced in the introduction, Sec. 1. We then proceed in Sec. 2.2 with the experimental possibilities provided by modern optics to study the QED vacuum. Here, we use Gaussian beams from high-intensity lasers as starting point of calculations; Gaussian beams are the content of Sec. 2.2.1, which deals with their formal description and properties. Furthermore, in Sec. 2.2.2 we discuss the state-of-the art facilities of high-intensity laser pulses and the properties they ensure.

For further theoretical insights, we refer here to the appendix, Sec. B. In Sec. B.1, the effects of the quantum vacuum on the photon propagator in QED are presented. Furthermore, Sec. B.2 contains a deep motivation for experimental investigation of the effects of nonlinearity mediated by the quantum vacuum: there, different approaches beyond the Standard Model (BSM) are presented and how the nonlinearity of the quantum vacuum is affected by them.

For notes on the notations, conventions, and units used here, see the Sec. A.

2.1. Heisenberg-Euler Lagrangian in One-Loop Quantum Electrodynamics

In the Standard Model (SM) of particle physics, the interaction of light and matter is described by quantum electrodynamics (QED). It is a relativistic quantum field theory and an abelian gauge theory with the symmetry group $U(1)$.

The electromagnetic field is modeled by the bosonic gauge field A^μ , which is the covariant form of the electromagnetic four-potential. It defines an electromagnetic field strength tensor $F_{\mu\nu} = \partial_\mu A_\nu - \partial_\nu A_\mu$. To describe the matter, the quantized Dirac bispinor field ψ is used as an anti-commutating Grassmann-valued field. Spin-1/2 fermionic particles are involved.

The fundamental Lagrangian of QED is

$$\mathcal{L}_{\text{QED}} = \bar{\psi} i \gamma_\mu (\partial^\mu - i e_0 A^\mu) \psi - m_0 \bar{\psi} \psi - \frac{1}{4} F_{\mu\nu} F^{\mu\nu}. \quad (2.1)$$

Here we use the usual notations; the Dirac matrices γ^μ satisfy the Clifford algebra $\{\gamma^\mu, \gamma^\nu\} = -2\eta^{\mu\nu}$, where $\{A, B\} = AB + BA$ is the anticommutator. The adjoint spinor $\bar{\psi} \equiv \psi^\dagger \gamma^0$ is defined using one of the Dirac matrices γ^μ . Further, we use e_0 and m_0 for the bare, i.e. unrenormalized, elementary charge and mass of the electron. Eq. (2.1) contains the contribution $e_0 \bar{\psi} \gamma^\mu A_\mu \psi$. It gives rise to an interaction of light and matter. For more detailed information and introduction to QED as QFT, see the references [71, 167–170].

Our goal is to derive the famous Heisenberg-Euler Lagrangian and to identify the nonlinearities. There are several approaches to derive this Lagrangian; this presentation is based on the idea of Schwinger, using the proper time method [20, 72]. Further approaches can be found in the primary literature [52, 53] as well as further secondary literature [127, 128, 171–173].

We consider a vacuum state $|0\rangle$ under the influence of a strong external electromagnetic background field given by the potential A_{cl}^μ . The external field is strong enough to be treated as a classical field, therefore we can introduce an effective action Γ_{eff} and an associated Lagrangian \mathcal{L}_{eff} ,

$$\Gamma_{\text{eff}} = \int d^4x \mathcal{L}_{\text{eff}}. \quad (2.2)$$

To determine the effective action Γ_{eff} we need the full QED action

$$S = \int d^4x \mathcal{L}_{\text{QED}}, \quad (2.3)$$

which is given by the full QED Lagrangian \mathcal{L}_{QED} from Eq. (2.1). Further we define an array of all quantum fields $\Psi = (\bar{\psi}, \psi, A^\mu)^T$, where for the classical case $\Psi_{\text{cl}} = (0, 0, A_{\text{cl}}^\mu)^T$ holds. Moreover, the classical background field can be assumed to be constant over the length and time scales of the fluctuation $\lambda_C = m_e^{-1} = \tau_C$. The effective action depending on the classical fields is [174]

$$\begin{aligned} \Gamma_{\text{eff}}[\Psi] &= S[\Psi_{\text{cl}}] + \frac{i}{2} \text{STr} \left[\ln \frac{\delta^2 S[\Psi]}{\delta \Psi(x) \delta \Psi(x')} \Big|_{\Psi(x)=\Psi_{\text{cl}}=\Psi(x')} \right] + \dots \\ &= S_{\text{M}} + \Gamma_{\text{eff}}^{(1\text{-loop})} + \mathcal{O}(\alpha^2) \end{aligned} \quad (2.4)$$

where $\text{STr}[A]$ denotes the supertrace of the operator A . Besides the classical action S_{M} , we get the 1-loop effective action $\Gamma_{\text{eff}}^{(1\text{-loop})}$ to first order perturbation theory. Higher orders are suppressed by the fine-structure constant α and are therefore neglected.

The contribution of the quantum vacuum can be interpreted as quantum corrections to the classical action. If we compare two vacuum states measured at times t and $t + T$, we obtain the amplitude

$$\langle 0(t) | 0(t + T) \rangle = e^{-i E_{\text{vac}} T} = e^{i(\Gamma_{\text{eff}} - S_{\text{M}})} = e^{i(\Gamma_{\text{eff}}^{(1\text{-loop})} + \mathcal{O}(\alpha^2))} \quad (2.5)$$

given as evolution of the vacuum state governed by the quantum vacuum fluctuations with the corresponding vacuum energy E_{vac} . Here, we have assumed that the background field is time-independent, and thus the vacuum a stationary state.

The classical action S_M is reduced only to the part which is known from Maxwell's equation, because in the corresponding Lagrangian of the action only the term $\mathcal{L}_M = -\frac{1}{4}F_{\text{cl}}^{\mu\nu}F_{\mu\nu,\text{cl}}$ remains. For the 1-loop effective action $\Gamma_{\text{eff}}^{(1\text{-loop})}$, only the contribution by variation after $\delta\bar{\psi}\delta\psi$ is relevant, since all terms varied by δA^μ vanish or yield a constant due to the classical fields $\bar{\psi}_{\text{cl}}$ and ψ_{cl} being zero while only A_{cl}^μ is nonzero. It yields

$$\Gamma_{\text{eff}}^{(1\text{-loop})} = -i\text{Tr} \left[\ln \frac{\delta^2 S[A_{\text{cl}}^\mu]}{\delta\bar{\psi}\delta\psi} \right]. \quad (2.6)$$

We determine the remaining variation of the action

$$\frac{\delta^2 S[A_{\text{cl}}^\mu]}{\delta\bar{\psi}\delta\psi} = -i\not{D} + m_0, \quad (2.7)$$

where we use the gauge covariant derivative $D^\mu \equiv \partial^\mu - ie_0 A_{\text{cl}}^\mu$ and obtain

$$\Gamma_{\text{eff}}^{(1\text{-loop})} = -i \ln [\det(-i\not{D} + m_0)] = -\frac{i}{2} \ln [\det(\not{D}^2 + m_0^2)]. \quad (2.8)$$

In the last step we took advantage of the fact that the determinant was extended by the identity $\mathbb{1} = \gamma_5^2$ with $\gamma^5 = i\gamma^0\gamma^1\gamma^2\gamma^3$ and one of the Dirac matrices γ^5 was permuted to the other side of the determinant.

In the following the proper time method of Schwinger is used, according to which the trace over the natural logarithm of an arbitrary operator A/B can be represented as a proper time integral [72, 175]

$$\text{Tr} \left[\ln \frac{A}{B} \right] = - \int_0^\infty \frac{d\tau}{\tau} \text{Tr} [e^{-\tau A} - e^{-\tau B}], \quad (2.9)$$

which results in

$$\Gamma_{\text{eff}}^{(1\text{-loop})} = \frac{i}{2} \int_0^\infty \frac{d\tau}{\tau} \text{Tr} \left[e^{-\tau(\not{D}^2 + (m_0 + i\varepsilon)^2)} - e^{-\tau(\not{D}^2 + (m_0 + i\varepsilon)^2)} \Big|_{A_\mu=0} \right]. \quad (2.10)$$

Here we have introduced the addition $i\varepsilon$ to handle possible divergences that may occur. Furthermore we have to consider the contribution $\exp(-\tau\not{D}^2)|_{A_\mu=0}$ which follows from the lower limit of the variation. Using the commutator $[D_\mu, D_\nu] = ie_0 F_{\mu\nu}$ and with the definition of the spinor matrices $\sigma^{\mu\nu} \equiv \frac{i}{2}[\gamma^\mu, \gamma^\nu]$, we find

$$\not{D}^2 = -D^2 - \frac{1}{2}e_0\sigma^{\mu\nu}F_{\mu\nu}. \quad (2.11)$$

Using the Wick rotation $\tau \rightarrow i\tau$ and substituting Eq. (2.11) into Eq. (2.10), it can be rewritten as

$$\Gamma_{\text{eff}}^{(1\text{-loop})} = \frac{i}{2} \int_0^\infty \frac{d\tau}{\tau} e^{-i\tau(m_0 + i\varepsilon)^2} \text{Tr} \left[e^{i\tau(D^2 + \frac{1}{2}e_0\sigma^{\mu\nu}F_{\mu\nu})} - e^{i\tau\partial^\mu\partial_\mu} \right]. \quad (2.12)$$

Starting from the assumption $\partial_\lambda F_{\mu\nu} = 0$ of constant electromagnetic fields, i.e. the com-

mutator $[D_\lambda, F_{\mu\nu}] = 0$ vanishes, we can divide the trace into

$$\text{Tr} \left[e^{i\tau(D^2 + \frac{1}{2}e_0\sigma^{\mu\nu}F_{\mu\nu})} - e^{i\tau\partial^\mu\partial_\mu} \right] = \text{tr}_\gamma \left[e^{\tau\frac{1}{2}e_0\sigma^{\mu\nu}F_{\mu\nu}} \right] \text{tr}_x \left[e^{i\tau D^2} \right] - 4\text{tr}_x \left[e^{i\tau\partial^\mu\partial_\mu} \right], \quad (2.13)$$

where operation $\text{tr}_x[A]$ denotes the trace in coordinates space and $\text{tr}_\gamma[A]$ in spinor variables of operator A . According to this, the factor 4 in the second contribution follows from the trace over the spinor variables.

In the following, the three different traces in Eq. (2.13) are to be evaluate. First we determine $\text{tr}_x[e^{i\tau\partial^\mu\partial_\mu}]$ by interpreting the differential as four-momentum operator $P_\mu = -i\partial_\mu$ and calculate the integral in the four-momentum space

$$\text{tr}_x \left[e^{i\tau\partial^\mu\partial_\mu} \right] = \int d^4x \langle x | e^{i\tau\partial^\mu\partial_\mu} | x \rangle = \int d^4x \int \frac{d^4k}{(2\pi)^4} e^{i\tau k^2} = \frac{1}{(4\pi)^2 i\tau^2} \int d^4x. \quad (2.14)$$

The momentum space integral is not divergent because we have implicitly assumed $\text{Im}\{\tau\} > 0$ in agreement with the Wick rotation. The remaining space-time integral would be divergent if we did not consider a finite volume on which the effects of the vacuum polarization occur. This is the same assumption which allows us to assume constant external electromagnetic fields.

Next we calculate

$$\text{tr}_\gamma \left[e^{\tau\frac{1}{2}e_0\sigma^{\mu\nu}F_{\mu\nu}} \right] = \sum_i e^{i\tau e_0\lambda_i} \quad (2.15)$$

by formulating the trace as a product of the eigenvalues with the eigenvalues λ_i of $\frac{1}{2}\sigma^{\mu\nu}F_{\mu\nu}$. It is convenient to expand the expression $\frac{1}{2}\sigma^{\mu\nu}F_{\mu\nu}$ in terms of Lorentz invariant building blocks. Given an electric field \mathbf{E} and a magnetic field \mathbf{B} , the two relativistic invariants are

$$\mathcal{F} = \frac{1}{4}F^{\mu\nu}F_{\mu\nu} = \frac{1}{2}(\mathbf{B}^2 - \mathbf{E}^2), \quad \mathcal{G} = \frac{1}{4}\tilde{F}^{\mu\nu}F_{\mu\nu} = -\mathbf{B} \cdot \mathbf{E} \quad (2.16)$$

with the dual field strength tensor $\tilde{F}^{\mu\nu} = \frac{1}{2}\epsilon^{\mu\nu\alpha\beta}F_{\alpha\beta}$, where $\epsilon^{\alpha\beta\gamma\delta}$ is the Levi-Civita tensor. To distinguish the bare electromagnetic fields from the physical fields which we obtain below after renormalization, we mark the invariants with a subscript \mathcal{F}_0 and \mathcal{G}_0 . In Order to represent the 4×4 matrix $\frac{1}{2}\sigma^{\mu\nu}F_{\mu\nu}$ it is usefule to choose a concrete representation of the Dirac matrices. We choose for our purposes

$$\gamma^0 = \begin{pmatrix} \mathbb{1}_{2 \times 2} & 0 \\ 0 & -\mathbb{1}_{2 \times 2} \end{pmatrix} \quad \text{and} \quad \gamma^i = \begin{pmatrix} 0 & \sigma_i \\ -\sigma_i & 0 \end{pmatrix}, \quad (2.17)$$

where σ_i are the Pauli matrices for $i = 1, 2, 3$. By the representation of the square

$$\begin{aligned} \left(\frac{1}{2}\sigma^{\mu\nu}F_{\mu\nu} \right)^2 &= 2 \begin{pmatrix} \mathcal{F}_0 & 0 & -i\mathcal{G}_0 & 0 \\ 0 & \mathcal{F}_0 & 0 & -i\mathcal{G}_0 \\ -i\mathcal{G}_0 & 0 & \mathcal{F}_0 & 0 \\ 0 & -i\mathcal{G}_0 & 0 & \mathcal{F}_0 \end{pmatrix} \\ &= 2(\mathcal{F}_0\mathbb{1} - i\gamma^5\mathcal{G}_0) \end{aligned} \quad (2.18)$$

the eigenvalues λ_i can be identified easily. They are

$$\lambda_{1/2} = \pm \sqrt{2(\mathcal{F}_0 + i\mathcal{G}_0)}, \quad \lambda_{3/4} = \pm \sqrt{2(\mathcal{F}_0 - i\mathcal{G}_0)}. \quad (2.19)$$

If we now substitute these eigenvalues into Eq. (2.15), we obtain

$$\begin{aligned} \text{tr}_\gamma \left[e^{\tau \frac{i}{2} e_0 \sigma^{\mu\nu} F_{\mu\nu}} \right] &= 2 \cos \left(e_0 \tau \sqrt{2(\mathcal{F}_0 + i\mathcal{G}_0)} \right) + 2 \cos \left(e_0 \tau \sqrt{2(\mathcal{F}_0 - i\mathcal{G}_0)} \right) \\ &= 4 \text{Re} \left\{ \cos \left(e_0 \tau \sqrt{2(\mathcal{F}_0 + i\mathcal{G}_0)} \right) \right\}. \end{aligned} \quad (2.20)$$

For the calculation of the third trace $\text{tr}_x \left[e^{i\tau D^2} \right]$ the proper time method of Schwinger can be used again. Here the operator $e^{-i\tau D^2}$ is interpreted as proper time evolution operator. Thus an evolution equation analogous to the Schrödinger equation can be formulated, whereby D^2 acts like a Hamilton operator. With the help of this differential equation the trace can be determined to

$$\begin{aligned} \text{tr}_x \left[e^{i\tau D^2} \right] &= \frac{1}{(4\pi)^2 i\tau^2} \int d^4x \frac{e_0 \tau f_+}{\sin(e_0 \tau f_+)} \frac{e_0 \tau f_-}{\sin(e_0 \tau f_-)} \\ &= \frac{1}{(4\pi)^2 i\tau^2} \int d^4x \frac{2e_0^2 \tau^2 f_+ f_-}{\cos(e_0 \tau (f_+ - f_-)) - \cos(e_0 \tau (f_+ + f_-))} \\ &= -\frac{1}{(4\pi)^2 i\tau^2} \int d^4x \frac{(e_0 \tau)^2 \mathcal{G}_0}{\text{Im} \left\{ \cos \left(e_0 \tau \sqrt{2(\mathcal{F}_0 + i\mathcal{G}_0)} \right) \right\}} \end{aligned} \quad (2.21)$$

where $f_\pm = \frac{1}{\sqrt{2}} (\sqrt{\mathcal{F}_0 + i\mathcal{G}_0} \pm \sqrt{\mathcal{F}_0 - i\mathcal{G}_0})$. The detailed procedure can be taken from the references [20, 72, 175]. Additionally, the contribution $\left((4\pi)^2 i\tau^2 \right)^{-1} \int d^4x$ comes from the same considerations as in Eq. (2.14).

By inserting the results from Eq. (2.14), Eq. (2.15), and Eq. (2.21) into Eq. (2.12), we obtain

$$\Gamma_{\text{eff}}^{(1\text{-loop})} = \int_0^\infty \frac{d\tau}{\tau} e^{-i\tau(m_0 + i\varepsilon)^2} \frac{(-1)}{8\pi^2 \tau^2} \int d^4x \left((e_0 \tau)^2 \mathcal{G}_0 \frac{\text{Re} \left\{ \cos \left(e_0 \tau \sqrt{2(\mathcal{F}_0 + i\mathcal{G}_0)} \right) \right\}}{\text{Im} \left\{ \cos \left(e_0 \tau \sqrt{2(\mathcal{F}_0 + i\mathcal{G}_0)} \right) \right\}} + 1 \right) \quad (2.22)$$

and continue by reversing the Wick rotation $\tau \rightarrow -i\tau$ because the convergence for $\tau \rightarrow \infty$ is now assured beside poles on the τ axis which indicates Schwinger pair production, cf. [72]. Therefore, the action is

$$\Gamma_{\text{eff}}^{(1\text{-loop})} = -\frac{1}{8\pi^2} \int_0^\infty \frac{d\tau}{\tau^3} e^{-\tau m_0^2} \int d^4x \left((e_0 \tau)^2 \mathcal{G}_0 \frac{\text{Re} \left\{ \cosh \left(e_0 \tau \sqrt{2(\mathcal{F}_0 + i\mathcal{G}_0)} \right) \right\}}{\text{Im} \left\{ \cosh \left(e_0 \tau \sqrt{2(\mathcal{F}_0 + i\mathcal{G}_0)} \right) \right\}} - 1 \right). \quad (2.23)$$

The action in Eq. (2.23) is unrenormalized and diverges for $\tau \rightarrow 0$. It is therefore necessary to investigate the divergence. For this we first expand the cosh function in the numerator

and denominator by

$$\cosh(a\sqrt{2z}) = 1 + a^2 z + \frac{1}{6} a^4 z^2 + \frac{1}{90} a^6 z^3 + \mathcal{O}(z^4) \quad (2.24)$$

with $z \in \mathbb{C}$ and $a \in \mathbb{R}$. With the substitutions $a \rightarrow e_0 \tau$ and $z \rightarrow \mathcal{F}_0 + i\mathcal{G}_0$ the real part and imaginary part result in

$$\text{Re} \left\{ \cosh \left(e_0 \tau \sqrt{2(\mathcal{F}_0 + i\mathcal{G}_0)} \right) \right\} = 1 + (e_0 \tau)^2 \mathcal{F}_0 + \frac{1}{6} (e_0 \tau)^4 (\mathcal{F}_0^2 - \mathcal{G}_0^2) + \mathcal{O}(\mathcal{F}_0^3) \quad (2.25)$$

and

$$\frac{\text{Im} \left\{ \cosh \left(e_0 \tau \sqrt{2(\mathcal{F}_0 + i\mathcal{G}_0)} \right) \right\}}{(e_0 \tau)^2 \mathcal{G}_0} = 1 + \frac{1}{3} (e_0 \tau)^2 \mathcal{F}_0 + \frac{1}{90} (e_0 \tau)^4 (3\mathcal{F}_0^2 - \mathcal{G}_0^2) + \mathcal{O}(\mathcal{F}_0^3), \quad (2.26)$$

where $\mathcal{O}(\mathcal{F}_0)$ is the order in \mathcal{F}_0 and \mathcal{G}_0 , which depend on the same quantity according to Eq. (2.16). These series allow us to expand the expression in the brackets in Eq. (2.23) using power series; it yields

$$(e_0 \tau)^2 \mathcal{G}_0 \frac{\text{Re} \left\{ \cos \left(e_0 \tau \sqrt{2(\mathcal{F}_0 + i\mathcal{G}_0)} \right) \right\}}{\text{Im} \left\{ \cos \left(e_0 \tau \sqrt{2(\mathcal{F}_0 + i\mathcal{G}_0)} \right) \right\}} - 1 = \frac{2}{3} (e_0 \tau)^2 \mathcal{F}_0 - \frac{1}{45} (e_0 \tau)^4 (4\mathcal{F}_0^2 + 7\mathcal{G}_0^2) + \dots \quad (2.27)$$

and further, higher powers in \mathcal{F}_0 and \mathcal{G}_0 are not needed for the purpose of renormalization, since they are accompanied by the prefactor $(e_0 \tau)^{2n}$ with $n > 2$, which renders these terms finite.

We aim to determine the effective Lagrangian \mathcal{L}_{eff} , which extends classical physics with corrections to quantum vacuum polarization, from the corresponding effective action Γ_{eff} . With the Lagrangian of classical electrodynamics $\mathcal{L}_M = -\mathcal{F}_0$ and according to Eq. (2.2) and Eq. (2.4), the effective Lagrangian is $\mathcal{L}_{\text{eff}} = \mathcal{L}_M + \mathcal{L}_{\text{eff}}^{(1\text{-loop})} + \mathcal{O}(\alpha^2)$. Inserting the expansion Eq. (2.27) into the Lagrangian $\mathcal{L}_{\text{eff}}^{(1\text{-loop})}$ resulting from Eq. (2.23) we obtain the unrenormalized full effective 1-loop Lagrangian as power series

$$\begin{aligned} \mathcal{L}_{\text{eff}} &= -\mathcal{F}_0 - \frac{1}{8\pi^2} \int_0^\infty \frac{d\tau}{\tau^3} e^{-\tau m_0^2} \left(\frac{2}{3} (e_0 \tau)^2 \mathcal{F}_0 - \frac{1}{45} (e_0 \tau)^4 (4\mathcal{F}_0^2 + 7\mathcal{G}_0^2) + \dots \right) \\ &= - \left(1 + \frac{e_0^2}{12\pi^2} \int_0^\infty \frac{d\tau}{\tau} e^{-\tau m_0^2} \right) \mathcal{F}_0 + \frac{e_0^4}{8 \cdot 45\pi^2} \int_0^\infty d\tau \tau e^{-\tau m_0^2} \left((4\mathcal{F}_0^2 + 7\mathcal{G}_0^2) + \dots \right). \end{aligned} \quad (2.28)$$

Further we omit the reference to 1-loop order in the following notations as we stick to the 1-loop level for the remainder of this work.

In the first term of Eq. (2.28), we have summarized the contributions that are linear in \mathcal{F}_0 . There is the divergent integral, in contrast to the higher order contributions in \mathcal{F}_0 and \mathcal{G}_0 , where the proper time integral converges. The vacuum polarization can only influence the nonlinear contributions, otherwise it would have to be observable already in classical

electrodynamics. Accordingly, the prefactor of the linear contribution can be used for renormalization, where we define the wave function renormalization as

$$Z_R^{-1} = 1 + \frac{e_0^2}{12\pi^2} \int_0^\infty \frac{d\tau}{\tau} e^{-\tau m_0^2}. \quad (2.29)$$

This results in a renormalization of the electric charge $e_0 \rightarrow \sqrt{Z_R} e_0 \equiv e$ and the relativistic invariants of the electromagnetic field $\mathcal{F}_0 \rightarrow Z_R^{-1} \mathcal{F}_0 \equiv \mathcal{F}$ and $\mathcal{G}_0 \rightarrow Z_R^{-1} \mathcal{G}_0 \equiv \mathcal{G}$. We interpret the new charge e as physical charge, which we identify in the fine-structure constant $\alpha = e^2/(4\pi)$ and measure in the laboratory. Furthermore, we understand the new field strengths in \mathcal{F} and \mathcal{G} as observable field strengths. The choice of our renormalization leaves the combinations $e_0^2 \mathcal{F}_0 = e^2 \mathcal{F}$ or $e_0^2 \mathcal{G}_0 = e^2 \mathcal{G}$ invariant. We use an on-shell renormalization condition since $e = \sqrt{4\pi\alpha}$. This implies that the bare mass of the electron m_0 is set to its physical rest mass m_e , i.e. $m_0 = m_e$. An independent renormalization of the mass occurs on the 2-loop level.

With the help of this renormalization, the effective Lagrangian can now be formulated as

$$\begin{aligned} \mathcal{L}_{\text{HE}} &\equiv \mathcal{L}_{\text{eff}} \\ &= -\mathcal{F} - \frac{1}{8\pi^2} \int_0^\infty \frac{d\tau}{\tau^3} e^{-\tau m_e^2} \left((e\tau)^2 \mathcal{G} \frac{\text{Re} \left\{ \cosh \left(e\tau \sqrt{2(\mathcal{F} + i\mathcal{G})} \right) \right\}}{\text{Im} \left\{ \cosh \left(e\tau \sqrt{2(\mathcal{F} + i\mathcal{G})} \right) \right\}} - \frac{2}{3} (e\tau)^2 \mathcal{F} - 1 \right) \end{aligned} \quad (2.30)$$

without divergences. This is the famous Heisenberg-Euler Lagrangian, henceforth we denote it by \mathcal{L}_{HE} . The singular contribution of the quotient of real and imaginary part of the cosh function is canceled by the $-\frac{2}{3} (e\tau)^2 \mathcal{F}$ term. At the same time the classical contribution is ensured by $-\mathcal{F}$.

To conclude this subsection, we want to restrict the Heisenberg-Euler Lagrangian from Eq. (2.30), which includes all orders in \mathcal{F} and \mathcal{G} in the 1-loop order, to the lowest order of nonlinear contributions. There we can perform the proper time integral

$$\int_0^\infty d\tau \tau e^{-\tau m_e^2} = \frac{1}{m_e^4} \quad (2.31)$$

and the Lagrangian yields

$$\begin{aligned} \mathcal{L}_{\text{HE}} &= -\mathcal{F} + \frac{1}{45 \cdot 8\pi^2} \frac{e^4}{m_e^4} \left(4\mathcal{F}^2 + 7\mathcal{G}^2 \right) + \mathcal{O} \left((F/\mathcal{E}_{cr})^6 \right) \\ &= -\mathcal{F} + \frac{2\alpha^2}{45m_e^4} \left(4\mathcal{F}^2 + 7\mathcal{G}^2 \right) + \mathcal{O} \left((F/\mathcal{E}_{cr})^6 \right). \end{aligned} \quad (2.32)$$

Here we used the series expansion Eq. (2.27). This expansion is valid for weak fields F compared to the critical field strength $\mathcal{E}_{cr} = \frac{m_e^2}{e}$, where F denotes the modulus of the electromagnetic field strength encoded in the tensor $F_{\mu\nu}$. By expressing the Lagrangian in terms

of \mathcal{E}_{cr} , we deliver

$$\mathcal{L}_{HE} = -\mathcal{F} + \alpha \left(\frac{1}{90\pi} \frac{4\mathcal{F}^2 + 7\mathcal{G}^2}{\mathcal{E}_{cr}^2} + \mathcal{O}\left((F/\mathcal{E}_{cr})^6\right) \right), \quad (2.33)$$

This representation of \mathcal{L}_{HE} emphasizes that it is a 1-loop result since the nonlinearities are governed by an omnipresent factor of the fine-structure constant α . Considering higher loop contributions the additional terms acquire higher powers of the fine-structure constant α . A deeper analysis of the Heisenberg-Euler Lagrangian for spinor and scalar QED in various dimensions and loop orders is presented in the references [128, 176, 177].

As shown in the previous calculations, the Heisenberg-Euler Lagrangian extends the classical Maxwell equations by nonlinear terms of the external fields. These quantum corrections can be explained by the quantum vacuum, which is why we speak of quantum vacuum nonlinearities. These nonlinearities indicate phenomena like photon-photon scattering or quantum vacuum birefringence for which experimental evidence is still pending. Experiments for a potential proof of these effects are subject of the present work.

2.2. Modern Optics

Light is a key to science. We *observe* physical phenomena in experiments. Optics, as a sub-discipline of physics, is therefore indispensable to almost any kind of experiment, from astronomy to the Zeeman effect. In this sense, it is not surprising that we seek a deeper understanding of the quantum vacuum by probing it with optical methods.

Since modern optics now provide high-intensity lasers, it is obvious to use these strong field strengths for sfQED experiments. In particular, it is necessary to work out theoretically how the electromagnetic fields of these lasers interact in detail with the quantum vacuum. To work this out, an accurate formulation of these fields is needed; this is provided by optics.

Specifically, in the first part of this section, Sec. 2.2.1, we formally describe Gaussian beams and pulses. In particular, we analyze the form of the field amplitudes. Furthermore, we discuss the approximation of infinite Rayleigh ranges and extend the formulations to Gaussian beams with an elliptic cross section. In a further step, in Sec. 2.2.2, we summarize the (possible) achievements of various (future) laser facilities and compare them.

2.2.1. Gaussian Beams and Pulses

To describe optical properties of laser pulses a classical treatment without quantum corrections is justified, so that the electromagnetic fields are solutions of Maxwell's equations $\partial_\alpha F^{\alpha\mu} = 0$ and $\epsilon^{\mu\alpha\beta\gamma} \partial_\alpha F_{\beta\gamma} = 0$ in vacuum. Furthermore, we want to consider the components of the field strength separately. Linearly polarized electromagnetic waves in the vacuum are characterized by their electric and magnetic field components $\mathbf{E}(x)$ and $\mathbf{B}(x)$ pointing in the directions \mathbf{e}_E and $\mathbf{e}_B \perp \mathbf{e}_E$, and their wave vector \mathbf{k} satisfies $\mathbf{k}/|\mathbf{k}| \times \mathbf{e}_E = \mathbf{e}_B$. Those fields are called transverse electromagnetic (TEM). Due to our choice of the unit system it is possible to describe the electric and magnetic field profiles with the same profile function

$\mathcal{E}(x)$, i.e. $\mathbf{E}(x) = \mathcal{E}(x) \mathbf{e}_E$ and $\mathbf{B}(x) = \mathcal{E}(x) \mathbf{e}_B$. This allows us to focus only on this scalar field $\mathcal{E}(x)$ to characterize the profile.

We want to focus on paraxial Gaussian beams propagating in the vacuum. Starting with Maxwell's equations

$$\nabla \cdot \mathbf{E} = 0, \quad \nabla \cdot \mathbf{B} = 0, \quad \nabla \times \mathbf{E} = -\partial_t \mathbf{B}, \quad \nabla \times \mathbf{B} = \partial_t \mathbf{E}, \quad (2.34)$$

we can derive the wave equation

$$\nabla^2 \mathbf{E} - \frac{\partial^2}{\partial t^2} \mathbf{E} = 0 \quad (2.35)$$

for the electric field by applying the rotation operator on $\nabla \times \mathbf{E} = -\partial_t \mathbf{B}$ and substituting the last equation into Eq. (2.34). Since we aim to describe optical waves, we assume the time dependence can be separated as $\mathbf{E}(x) = U(\mathbf{r}) e^{-i\omega(t-t_0)} \mathbf{e}_E$, where \mathbf{r} gives the spatial coordinate, t the time, t_0 a time offset and ω the frequency of the optical wave. In vacuum the phase velocity of light is equal to the group velocity and therefore $\omega = |\mathbf{k}| = k$. This leads to the Helmholtz equation [178–181]

$$\nabla^2 U(\mathbf{r}) + k^2 U(\mathbf{r}) = 0. \quad (2.36)$$

In order to solve the Helmholtz equation in the paraxial approximation we want to introduce a coordinate transformation. The wave to be described propagates in space, which we describe with the coordinates \mathbf{r} , in the direction of the wave vector \mathbf{k} . We parameterize the optical axis with $\zeta = \mathbf{k}/|\mathbf{k}| \cdot (\mathbf{r} - \mathbf{r}_0)$, where \mathbf{r}_0 is a constant offset to the origin of the coordinate system, analogous to t_0 for the time. Obviously, it yields $k^\mu x_\mu = k\zeta - \omega t$. For distances measured orthogonally to the optical axis we use x_\perp , defined via $x_\perp^2 = |\mathbf{k}/|\mathbf{k}| \times (\mathbf{r} - \mathbf{r}_0)|^2 = |\mathbf{r} - \mathbf{r}_0|^2 - \zeta^2$. For example, if $\mathbf{k} = k\mathbf{e}_z$ holds for the wave vector, then $\zeta = z$ and $x_\perp^2 = x^2 + y^2$ follow. With these parameters, the waves can be described in a cylindrical coordinate system, where the radial distance is x_\perp and the axial coordinate is ζ . Additionally, considering several electromagnetic waves with $\mathbf{k}_1 \nparallel \mathbf{k}_2 \nparallel \mathbf{k}_3 \nparallel \dots$ we can map them onto their optical axis and formulate all interactions of those waves in the original coordinate system.

Using these cylindrical coordinates we split the Laplace operator into $\nabla^2 = \nabla_\perp^2 + \partial_\zeta^2$ and use a product ansatz $U(\mathbf{r}) = u(\mathbf{r}) e^{ik\zeta}$. Thereby, we are assuming the solution is propagating like a plane wave along the optical axis and the function $u(\mathbf{r})$ covers the residual dependences. The Helmholtz equation yields

$$\nabla_\perp^2 u(\mathbf{r}) + \frac{\partial^2}{\partial \zeta^2} u(\mathbf{r}) + 2 \left(\frac{\partial}{\partial \zeta} u(\mathbf{r}) \right) ik = 0, \quad (2.37)$$

where the terms proportional to k^2 cancel each other. Furthermore, we restrict ourselves to optical rays close to the optical axis. Therefore we assume that the change of $\partial_\zeta u(\mathbf{r})$ over a distance of the order of a wavelength $\lambda = 2\pi/k$ is small compared to $|\partial_\zeta u(\mathbf{r})|$, i.e. $|\partial_\zeta^2 u(\mathbf{r})| \ll 2k |\partial_\zeta u(\mathbf{r})|$, cf. reference [181]. This allows to neglect the second derivative in

Eq. (2.37) and we obtain the Helmholtz equation in paraxial approximation

$$\nabla_{\perp}^2 u(\mathbf{r}) + 2ik \partial_{\zeta} u(\mathbf{r}) = 0. \quad (2.38)$$

One solution of Eq. (2.38) are Gaussian beams. Those beams remain Gaussian at every point on the optical axis. In the focus, their field profile perpendicular to the optical axis follows a Gaussian decay

$$U(\mathbf{r}) \propto e^{-\frac{x_{\perp}^2}{w_0}}, \quad (2.39)$$

where w_0 is the transversed focus size. Apart from the waist, which we define at $\zeta = 0$, the radius of the beam increases with

$$w(\zeta) = w_0 \sqrt{1 + \left(\frac{\zeta}{\zeta_R}\right)^2}. \quad (2.40)$$

We call the new quantity ζ_R *Rayleigh range*. It is determined by the waist size in the focus w_0 and the wavelength λ according to $\zeta_R = \frac{\pi w_0^2}{\lambda}$; at the Rayleigh range the beam divergence $w(\zeta)$ fulfills $w(\zeta_R) = \sqrt{2}w_0$. Hence, the transversal profile away from the focus behaves as

$$U(\mathbf{r}) \propto e^{-\frac{x_{\perp}^2}{w(\zeta)}}. \quad (2.41)$$

Considering the Gaussian decay in Eq. (2.41), we are able to formulate the profile of a Gaussian beam.

We want to describe paraxial Gaussian beams with circular cross section resulting from TEM₀₀ modes. The function

$$U(\mathbf{r}) = U_0 \frac{w_0}{w(\zeta)} e^{-\frac{x_{\perp}^2}{w(\zeta)}} e^{i \left(k\zeta + k \frac{x_{\perp}^2}{2R(\zeta)} - \arctan \frac{\zeta}{\zeta_R} + \phi_0 \right)} \quad (2.42)$$

solves the paraxial Helmholtz equation, see Eq. (2.38). Here, besides the radius of curvature R , we have introduced the so-called Gouy phase $\arctan \frac{\zeta}{\zeta_R}$, an additional arbitrary phase ϕ_0 and the maximum amplitude U_0 . Fig. 2.1 illustrate the real amplitude $U(\mathbf{r})$ of the Gaussian beam with fixed choice of λ and w_0 . The factor $\exp\left(k \frac{x_{\perp}^2}{2R(\zeta)}\right)$ implies a delay of the phase away from the optical axis, thus the wavefront is curved according to the parameter $R = \zeta \left(1 + (\zeta_R/\zeta)^2\right)$. Often the inverse

$$\frac{1}{R} = \frac{\zeta}{\zeta^2 + \zeta_R^2} \quad (2.43)$$

is used. The Gouy phase – named after Louis Georges Gouy – ensures that an incoming beam from $\zeta \ll 0$ passing through the waist has a phase shift of π at $\zeta \gg 0$ with respect to the original phase. This behavior is observed in geometrical optics, cf. references [178, 179, 181–183].

To obtain the opening angle Θ of the Gaussian beam, we need to consider the slope of the beam divergence $w(\zeta)$ relative to the optical axis ζ in the limiting case far from the focus,

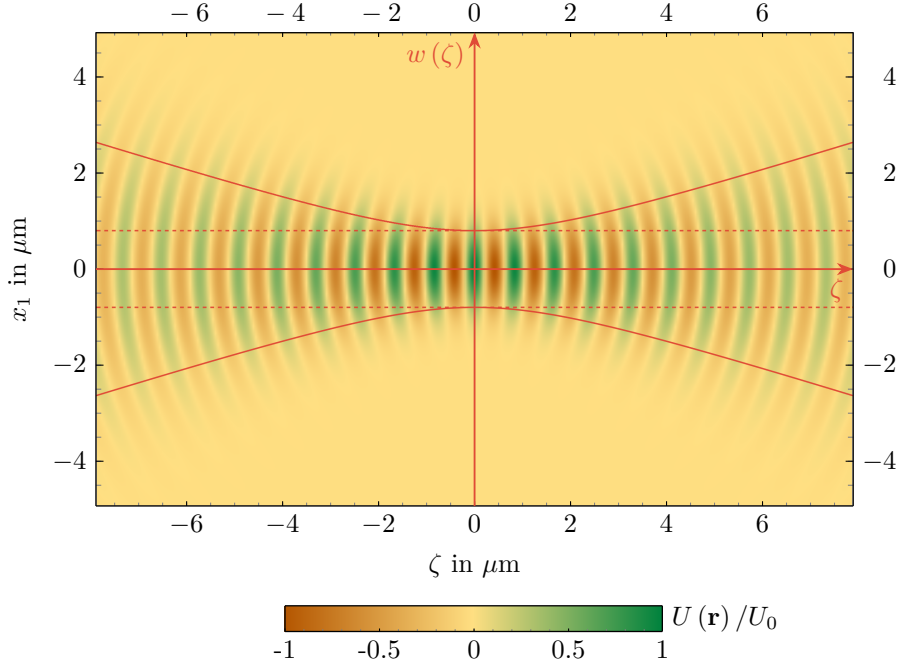


Figure 2.1.: *Paraxial Gaussian beam profile.* Illustration of a paraxial Gaussian beam propagating on the ζ axis with oscillation frequency $\omega_0 = 1.55 \text{ eV}$ and beam waist size $w_0 = \lambda$. The color code between brown and green gives the normalized amplitude $U(x_1, 0, \zeta)/U_0$ with $U_0 = U(0, 0, 0)$ corresponding to the electric field, cf. Eq. (2.42). The focus spot is at $\mathbf{r} = 0$; x_1 and x_2 refer to the axis perpendicular to the propagating direction. The function $w(\zeta)$, here in red, describes the transversal profile of the beam. The dashed lines denote the tube shape in the infinite Rayleigh range approximation.

i.e. $\zeta \gg \zeta_R$. In the limit $\zeta \rightarrow \infty$ we obtain

$$\Theta = 2 \lim_{\zeta \rightarrow \infty} \arctan \frac{w(\zeta)}{\zeta} = 2 \frac{w_0}{\zeta_R} = \frac{2\lambda}{\pi w_0} = \frac{4}{w_0 \omega}. \quad (2.44)$$

In the last step we inserted the Rayleigh range $\zeta_R = \frac{\pi w_0^2}{\lambda}$ with $\lambda = \frac{2\pi}{\omega}$. It should be noted that the divergence of the Gaussian beam becomes smaller with decreasing waist. If we assume a minimum focus width, the limit is reached at $w_0 = \lambda$. This corresponds to a maximum total aperture angle of

$$\Theta_{\max} = \frac{2}{\pi} \approx 36.476^\circ. \quad (2.45)$$

A wide beam waist therefore leads to a more narrowly bundled beam in the far field. This behavior is useful to manipulate the background of these laser beams.

So far we have studied the spatial behavior of Gaussian beams. Now we want to proceed with pulses instead of continuous beams. For this we describe again the whole field profile $\mathcal{E}(x)$. The pulse propagates along the optical axis; if we consider a constant location $\mathbf{r}' = (0, 0, \zeta')$, then we observe a field increasing and decreasing with time t . Assuming Gaussian pulses, we employ an ad hoc approximation neglecting contributions of $\mathcal{O}((\tau\omega)^{-1})$ and obtain

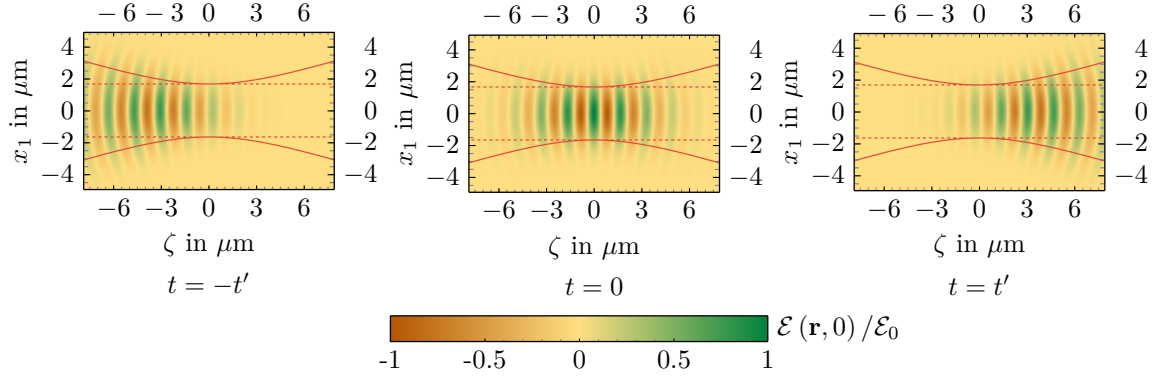


Figure 2.2.: *Propagation of a Gaussian pulse.* Illustration of a paraxial pulsed Gaussian beam propagating on the ζ axis for the times $t = -t'$, $t = 0$, and $t = t'$ with oscillation frequency $\omega_0 = 1.55$ eV, pulse duration $\tau = 15$ fs and beam waist size $w_0 = \lambda$. The color code between brown and green gives the normalized field profile $\mathcal{E}(\mathbf{r}, 0)$ at the time $t = 0$, cf. Eq. (2.47). The focus spot is at $\mathbf{r} = 0$; x_1 and x_2 refer to the axis perpendicular to the propagating direction. The function $w(\zeta)$, here in red, describes the transversal profile of the beam. The dashed lines denote the tube shape in the infinite Rayleigh range approximation.

a time envelope

$$\mathcal{E}(t, 0, 0, \zeta') \propto e^{-\frac{4(\zeta' - t + t_0)^2}{\tau^2}}. \quad (2.46)$$

Here τ indicates the pulse duration. The magnitude of the temporal envelope obviously depends on the observed location on the optical axis. Having the focus at $\zeta = 0$ it reaches its maximum there at time $t = t_0$. If we set the time offset to $t_0 = 0$, then this time is exactly when it passes the focus.

Using equation Eq. (2.42) together with the temporal envelope Eq. (2.46) are projecting onto real field components, we describe the field profile of Gaussian beams by

$$\mathcal{E}(x) = \mathcal{E}_0 \frac{w_0}{w(\zeta)} e^{-\frac{4(\zeta - t + t_0)^2}{\tau^2}} e^{-\frac{x_\perp^2}{w(\zeta)}} \cos\left(k\zeta - \omega(t - t_0) + k\frac{x_\perp^2}{2R(\zeta)} - \arctan\frac{\zeta}{\zeta_R} + \phi_0\right), \quad (2.47)$$

where \mathcal{E}_0 gives the maximum amplitude. Fig. 2.2 shows the propagation of a Gaussian pulse according to Eq. (2.47). When reaching the focal point, the magnitude of the profile is maximal. Furthermore, the effect of the temporal envelope is shown.

Here the half pulse duration $\tau/2$ and waist size w_0 indicate e^{-2} of its peak intensity. In many experimental procedures, however, the pulse duration measured at full width half maximum (FWHM) of the intensity. To convert these quantities we use the relation

$$\tau = \sqrt{\frac{2}{\ln 2}} \tau_{\text{FWHM}} \approx 1.7 \tau_{\text{FWHM}}. \quad (2.48)$$

Infinite Rayleigh range approximation

For investigating the physics encoded by the interaction of Gaussian beams it is often not necessary to consider the whole beam or pulse structure. If the relevant region can be reduced to the focus area fulfilling $\zeta \ll \zeta_R$ it is reasonable to neglect the transversal profile of the laser pulse as function of the optical axis parameter ζ and use a constant beam width w_0 , i.e. $w(\zeta) \rightarrow w_0$. The x_\perp dependence reduces to the initial assumption in Eq. (2.39).

This approximation holds in the formal limit $\zeta_R \rightarrow \infty$ and is called the *infinite Rayleigh range approximation* (IRRA). Applying this limit to the profile of Gaussian pulses, see Eq. (2.47), yields

$$\lim_{\zeta_R \rightarrow \infty} \mathcal{E}(x) = \mathcal{E}_0 e^{-\frac{4(\zeta - t + t_0)^2}{\tau^2}} e^{-\frac{x_\perp^2}{w_0^2}} \cos(k\zeta - \omega(t - t_0) + \phi_0). \quad (2.49)$$

Without an enveloping transversal profile, we estimate the Gaussian beam as an infinitely long tube with the optical axis as symmetry axis. Nevertheless, the relations for the profile in the perpendicular plane and for the pulse envelope are still Gaussian. In Fig. 2.1 and Fig. 2.2 this tube limit is illustrated by the dashed lines. Nevertheless, the relations for the profile in the perpendicular plane and for the pulse envelope are still Gaussian. The infinite Rayleigh range approximation freezes the shape of the profile in the beam waist for the whole propagation region. In the following we want to discuss which parameters control the use of the IRRA.

For continuous Gaussian beams the IRRA is only valid for the focus region with $\zeta \ll \zeta_R$. If we consider Gaussian pulses instead the temporal envelope can justify the IRRA. Using an appropriate pulse duration and assuming that the pulse passes the focal point, the pulse envelope suppresses the contributions beyond IRRA and using Eq. (2.49) instead of Eq. (2.47) is reasonable. To understand this effect, we consider Fig. 2.2 at the time $t = 0$. Here most of the beam profile is located inside the infinite tube indicated by the dashed line. To control the IRRA with the time envelope we demand

$$\tau \ll \zeta_R; \quad (2.50)$$

in fact, the weaker requirement $\tau \lesssim \zeta_R$ is usually sufficient, especially if we are interested in the intersection of several pulses with non collinear optical axes; cf. reference [102, 155].

Furthermore, we want to focus on the interaction of two beams and discuss the use of the IRRA. These two beams have a focus width $w_{0,i}$ and corresponding Rayleigh ranges $\zeta_{R,i}$, where i indicates the beam. The angle between the optical axes of these beams is θ_{ij} . To be able to apply the IRRA, the condition [102, 119, 155]

$$\frac{w_{0,i}}{\zeta_{R,j}} \ll |\sin \theta_{ij}| \quad (2.51)$$

follows from geometrical considerations for two different beams $i \neq j$. This condition can be generalized to several beams, while it must be fulfilled for all pairs. Even in this case, the

condition can be weakened somewhat. As can be seen from reference [155], for our purposes it is sufficient demand for $\frac{w_{0,i}}{\zeta_{R,j}} \lesssim |\sin \theta_{ij}|$ for all beams.

Elliptical cross section

In addition to the Gaussian beams considered so far, it is possible to deform the cross section of the beam profile at the focus spot. By passing cylindrical lenses, a Gaussian beam originating from circular TEM₀₀ modes acquires an elliptic cross section. Another method to generate elliptic Gaussian beam profiles is the use of astigmatic resonators. These resonators are constructed in such a way that they have two radii with different curvature in two perpendicular planes inside [178, 184].

First, we want to introduce a coordinate system that takes into account the elliptic properties. For this we consider the coordinates $x_1 \mathbf{e}_{x_1}$ and $x_2 \mathbf{e}_{x_2}$ orthogonal to the optical axis with $\mathbf{e}_{x_1} \perp \mathbf{e}_{x_2}$. The corresponding linearly independent unit vectors can be represented by

$$\mathbf{e}_{x_1} = \begin{pmatrix} 1 \\ 0 \end{pmatrix} \quad \text{and} \quad \mathbf{e}_{x_2} = \begin{pmatrix} 0 \\ 1 \end{pmatrix}. \quad (2.52)$$

For elliptical Gaussian beams, we identify two unequal waist sizes $w_{0,1} \neq w_{0,2}$. Further, to ensure elliptic cross sections with their semi axes not collinear with $\mathbf{e}_{x_1}, \mathbf{e}_{x_2}$, we introduce

$$\mathbf{e}_1(\epsilon) = R(\epsilon) \mathbf{e}_{x_1} \quad \text{and} \quad \mathbf{e}_2(\epsilon) = R(\epsilon) \mathbf{e}_{x_2}, \quad (2.53)$$

where $R(\epsilon)$ is the rotation by angle ϵ ; in the representation used in Eq. (2.52) it yields

$$R(\epsilon) = \begin{pmatrix} \cos \epsilon & -\sin \epsilon \\ \sin \epsilon & \cos \epsilon \end{pmatrix}. \quad (2.54)$$

From this we obtain new variables

$$x_{\perp,1} = \mathbf{e}_1(\epsilon) \cdot (\mathbf{r} - \mathbf{r}_0), \quad x_{\perp,2} = \mathbf{e}_2(\epsilon) \cdot (\mathbf{r} - \mathbf{r}_0), \quad \zeta = \frac{\mathbf{k}}{|\mathbf{k}|} \times (\mathbf{r} - \mathbf{r}_0), \quad (2.55)$$

where $\mathbf{e}_1(\epsilon)$ and $\mathbf{e}_2(\epsilon)$ describe the semi-axes pointing into the directions of the two waist sizes $w_{0,1}$ and $w_{0,2}$ and perpendicular to the optical axis. Supposing several beams for which all semi axes are collinear or perpendicular to each other, we choose \mathbf{e}_{x_1} and \mathbf{e}_{x_2} in such way that a rotation is not necessary, i.e. $R(\epsilon) = \mathbb{1}$, $x_{\perp,1} \rightarrow x_1$, $x_{\perp,2} \rightarrow x_2$.

If we consider the Gaussian decay orthogonal to the optical axis at the focus point, we require proportionality

$$\mathcal{E}(0, x_{\perp,1}, x_{\perp,2}, 0) \propto e^{-\frac{x_{\perp,1}^2}{w_{0,1}^2} - \frac{x_{\perp,2}^2}{w_{0,2}^2}}. \quad (2.56)$$

Beyond the focus, we find the corresponding beam divergences

$$w_i(\zeta) = w_{0,i} \sqrt{1 + \left(\frac{\zeta}{\zeta_{R_i}} \right)^2} \quad (2.57)$$

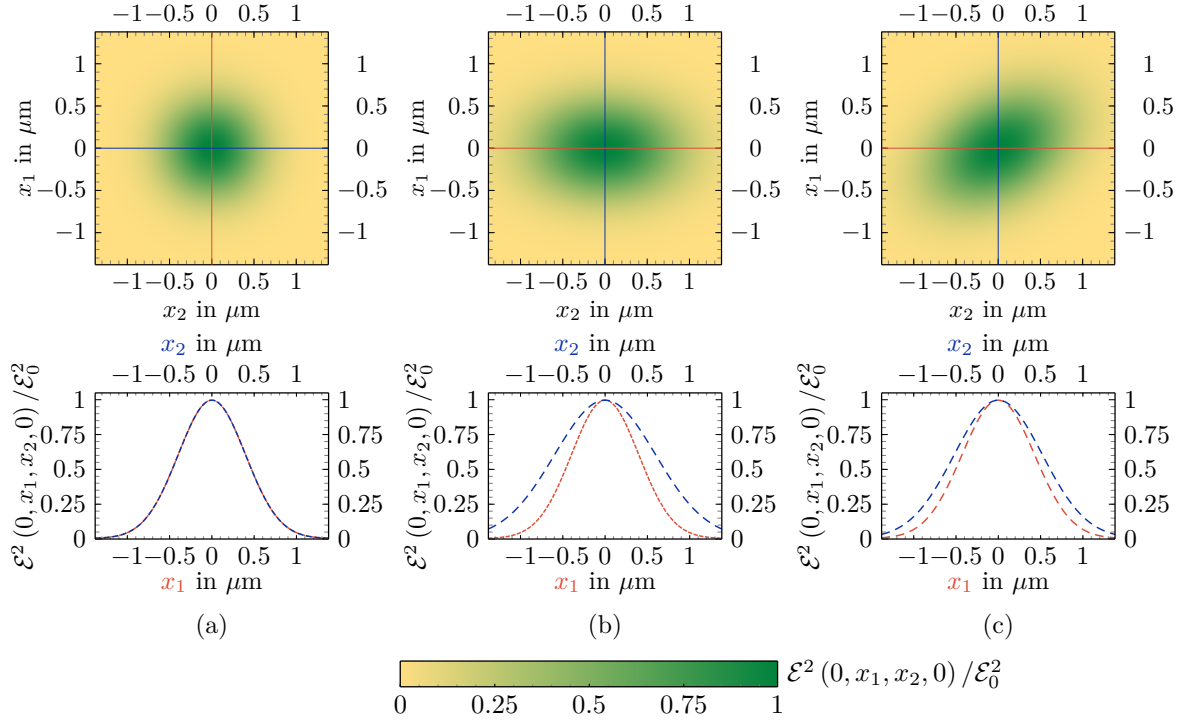


Figure 2.3.: *Profile of Gaussian beams.* Top: Illustration of the intensity profile $\mathcal{E}(0, x_1, x_2, 0)^2$ of a paraxial pulsed Gaussian beam in the plane orthogonal to the optical axis in the focus point. Bottom: Plot of the intensity profiles with dependence of only one coordinate, x_1 (tight dashed, red) or x_2 (dashed, blue), whereby all constant variables are set to their value for the focus point. The beams have an oscillation frequency $\omega_0 = 1.55$ eV, a pulse duration $\tau = 15$ fs and a beam waist size $w_0 = \lambda$. In (a) the cross section in the focus is circular, i.e. $w_{0,1} = w_{0,2} = \lambda$; (b) and (c) consider Gaussian beams with elliptic cross section with $w_{0,1} = \frac{3}{2}w_{0,2} = \frac{3}{2}\lambda$. The orientation of elliptic focus in (c) is rotated by $\epsilon = 30^\circ$ compared to (b).

with $i \in \{1, 2\}$ on the semi-axes. Here we have two Rayleigh ranges $\zeta_{R_i} = \frac{\pi w_{0,i}^2}{\lambda}$ for the Gaussian beam. Furthermore, the radius of curvature $R_i(\zeta) = \zeta \left(1 + \zeta_{R_i}^2/\zeta^2\right)$ differs on the corresponding semi-axes. With these considerations we obtain

$$\begin{aligned}
 \mathcal{E}(t, x_{\perp,1}, x_{\perp,2}, \zeta) = & \mathcal{E}_0 \sqrt{\frac{w_{0,1}w_{0,2}}{w_1(\zeta)w_2(\zeta)}} e^{-\frac{4(\zeta-t+t_0)^2}{\tau^2}} e^{-\frac{x_{\perp,1}^2}{w_{0,1}^2} - \frac{x_{\perp,2}^2}{w_{0,2}^2}} \\
 & \times \cos \left(k\zeta - \omega(t-t_0) + k\frac{x_{\perp,1}^2}{2R_1(\zeta)} + k\frac{x_{\perp,2}^2}{2R_2(\zeta)} - \frac{1}{2} \arctan \frac{\zeta}{\zeta_{R_1}} \right. \\
 & \left. - \frac{1}{2} \arctan \frac{\zeta}{\zeta_{R_2}} + \phi_0 \right)
 \end{aligned} \tag{2.58}$$

for the description of the field amplitude of Gaussian beams with elliptic cross section. The Gouy phase has also split.

In the IRRA, $\zeta \ll \zeta_{R_1}$ and $\zeta \ll \zeta_{R_2}$, it yields [163]

$$\lim_{\zeta_{R_{1/2}} \rightarrow \infty} \mathcal{E}(t, x_{\perp,1}, x_{\perp,2}, \zeta) = \mathcal{E}_0 e^{-\frac{4(\zeta-t+t_0)^2}{\tau^2}} e^{-\frac{x_{\perp,1}^2}{w_{0,1}^2} - \frac{x_{\perp,2}^2}{w_{0,2}^2}} \cos(k\zeta - \omega(t - t_0) + \phi_0). \quad (2.59)$$

The justification of this approximation is analogous to the treatment of Gaussian pulses with circular cross section.

For our choice of units the intensity results in $\mathcal{E}(x)^2$. Fig. 2.3 (a) to (c) show different intensity profiles of Gaussian beams. The top figures show the intensity distribution in the focus ($t = 0, x_1, x_2, \zeta = 0$) in the plane orthogonal to the optical axis, whereas in the bottom figure $\mathcal{E}(0, x_1, 0, 0)^2$ (tight dashed, red) and $\mathcal{E}(0, 0, x_2, 0)^2$ (dashed, blue) are plotted together for comparison. In Fig. 2.3 (a), a beam with circular cross section is plotted. Fig. 2.3 (b) and (c), on the other hand, display Gaussian beams with an elliptical cross section. As transversal coordinates x_1 and x_2 are chosen, the effect of a rotation by $\epsilon = 30^\circ$ in these coordinates is visible in Fig. 2.3 (c). The choice of the beam parameters can be taken from the figure caption.

2.2.2. Modern Laser Facilities

To correctly predict experimental scenarios for measuring the signal of quantum vacuum nonlinearities we need a solid knowledge of the capabilities of experimental physics. Therefore, in this section we discuss some examples of modern high-intensity laser facilities. Furthermore, it is necessary to know how to derive from the characteristics of high intensity laser pulses the corresponding quantities for Gaussian pulses as we describe them in section Sec. 2.2.1.

Commonly in experiments the pulse duration and the focus size are given in FWHM. For the corresponding quantities, we always use the index FWHM, i.e. τ_{FWHM} and $w_{0,\text{FWHM}}$, respectively. However, for the calculations the beam diameters, characterized by the decay to $1/e^2$, are more suitable. For the pulse duration we have already shown in Eq. (2.48) the relation between these values. The same applies to the focus size

$$w_0 = \frac{1}{\sqrt{2 \ln 2}} w_{0,\text{FWHM}} \approx 1.7 w_{0,\text{FWHM}}. \quad (2.60)$$

Experimental facilities often specify the maximum intensity \mathcal{E}_0^2 of laser pulses. Furthermore, the laser power $P \approx \frac{W}{\tau}$ serves for characterization. W is the pulse energy. Loosely speaking it can be understood as the total energy of all single photons in the pulse. A pulse with N photons of the photon energy ω has a pulse energy of $W = N\omega$. Moreover, we can estimate the pulse energy by integrating over the intensity distribution in the whole space at an arbitrary but fixed time.

For a Gaussian pulse we know that the integral over the optical axis ζ is finite. Since energy is conserved we estimate the pulse energy for the time $t = 0 = t_0$ passing the focus spot. Using Gaussian pulses with elliptical cross section in IRRA, see Eq. (2.59), the pulse

energy is given by [133, 158]

$$\begin{aligned}
W &= \int_{-\infty}^{\infty} dt \int_{-\infty}^{\infty} dx_{\perp,1} \int_{-\infty}^{\infty} dx_{\perp,2} \mathcal{E}(x)^2 \Big|_{\zeta=0} \\
&= \mathcal{E}_0^2 \int_{-\infty}^{\infty} dt e^{-\frac{8t^2}{\tau^2}} \cos^2(\omega t) \int_{-\infty}^{\infty} dx_{\perp,1} e^{-2\frac{x_{\perp,1}^2}{w_{0,1}^2}} \int_{-\infty}^{\infty} dx_{\perp,2} e^{-2\frac{x_{\perp,2}^2}{w_{0,2}^2}} \\
&= \mathcal{E}_0^2 \frac{\tau}{4} \sqrt{\frac{\pi}{2}} \left(1 + e^{-\frac{1}{8}\omega^2\tau^2}\right) \sqrt{\frac{\pi}{2}} w_{0,1} \sqrt{\frac{\pi}{2}} w_{0,2}
\end{aligned} \tag{2.61}$$

where the phase is $\phi_0 = 0$ and we used the separability of the coordinates. The pulses of the currently available high-intensity lasers consist of several cycles, so the contribution $\frac{1}{8}\omega^2\tau^2$ can be considered large for our purposes, hence the approximation

$$W \approx \sqrt{\frac{\pi}{2}} \frac{\pi}{8} \mathcal{E}_0^2 w_{0,1} w_{0,2} \tau^2 \tag{2.62}$$

is justified and we neglect subleading terms $\mathcal{O}(k^{-2}\tau^{-2})$. The maximum field amplitude

$$\mathcal{E}_0 = \sqrt{8\sqrt{\frac{2}{\pi}} \frac{W}{\pi w_{0,1} w_{0,2} \tau^2}} \tag{2.63}$$

can be estimated from the given pulse properties, namely focus sizes $w_{0,1}$, $w_{0,2}$, pulse duration τ and pulse energy W .

Here we have discussed Gaussian beams with elliptical cross section. The relations for circular Gaussian pulses follow from identifying $w_{0,1} = w_{0,2} = w$ and can also be taken from reference [133]. It yields

$$\mathcal{E}_0 = \sqrt{8\sqrt{\frac{2}{\pi}} \frac{W}{\pi w_0^2 \tau^2}}. \tag{2.64}$$

Furthermore the reference [158] contains information about pulses beyond the TEM₀₀ mode, which are constructed by Hermite- and Laguerre-Gaussian modes.

Titanium-sapphire (Ti:sapphire) solid-state lasers have become one of the most popular high-intensity laser pulses. Titanium-doped Al₂O₃ crystals serve as the active medium, whereby Titanium ions (Ti³⁺) drive the fluorescence. An advantage is their fast generation of light pulses in the laser resonator, which allows operations in the femtosecond range. At the same time, it is inexpensive and simple in design. The Ti:sapphire works most efficiently at a wavelength of $\lambda = 800$ nm, but in principle its wavelength can be adjusted in the range from 660 nm to 1180 nm [180, 185–187].

Apollon at CILEX

At Centre Interdisciplinaire Lumière Extrême (CILEX) in Gif-sur-Yvette, France, the Apollon laser is currently under construction. This pulsed Ti:Sapphire laser should deliver pulses with the power of 10 PW. Furthermore, it aims to achieve a pulse duration of 18 fs and a pulse energy of 180 J. This would result in an intensity in the focus of 2×10^{22} W/cm² [188–190].

In addition to the main beam, there are other high-intensity lasers in this facility. Apart

from the fact that they can be used to perform independent experiments, they are used for adjustments or probing the main beam.

CoReLS

In contrast to Apollon, at the Center for Relativistic Laser Science (CoReLS), associated with Ultrashort Quantum Beam Facility (UQBF) in Gwangju, Republic of Korea, they have a 4 PW laser in operation since 2016. In 2020, an intensity of 10^{23} W/cm^2 was reached. The pulse duration is 20 fs and a statistical width of $1.2 \mu\text{m}$ was measured at the focus, which is very close to the diffraction limit; the wavelength is 800 nm. An additional 1 PW laser is available at the facility [191, 192].

ELI

One of the largest projects in laser research is the Extreme Light Infrastructure (ELI) which consists of three different pillars. ELI Beamlines is located in Dolní Břežany, Czech Republic, ELI Attosecond Light Pulse Source (ELI-ALPS) in Szeged, Hungary and ELI Nuclear Physics (ELI-NP) in Măgurele, Romania. ELI-ALPS is of less interest for the present work, since extremely short laser pulses are investigated there, which, however, have a lower pulse energy. These pulses consist of only a few cycles [193]. As it is the strongest laser of the ELI project, we concentrate on the high-intensity laser system of ELI-NP.

ELI-NP offers two 10 PW Ti:sapphire lasers with a wavelength of 800 nm. They are projected to achieve pulses with durations of 30 fs and pulse energy 300 J. On August 19th 2020, they measured a pulse energy of 230 J with a pulse duration of 22.7 fs. It was focused onto an area of $10 \mu\text{m}^2$ with a maximum intensity of 10^{23} W/cm^2 . This equals in a peak field strength of 10^{15} V/m . These lasers have a repetition rate of one shot per minute for an operation time of one hour. [138, 194–198].

With these features of ELI-NP, a variety of theoretical proposals get a possibility to be tested [141, 199].

Comparison of Different Facilities

In addition to the above mentioned facilities, there are several others that are candidates for sfQED experiments. These include the Advanced Ti:Sapphire Laser 3000 Terawatt (ATLAS-3000, shorted just ATLAS) at Center of Advanced Laser Applications (CALA) in Garching, Germany, the Jenaer Titan:Saphir 200 Terawatt (JETI-200) and the Petawatt Optical Laser Amplifier for Radiation Intensive Experiments (POLARIS) at Helmholtz Institute Jena (HI Jena) in Jena, Germany, the OMEGA Extended Performance (OMEGA EP) laser system at Laboratory for Laser Energetics (LLE) in Rochester, New York, U.S.A., and the Shen Guang-II (SG-II) at National Laboratory on High Power Lasers (NLHPL), cf. references [137, 200–206]. A comparison of their characteristics is shown in Tab. 2.1.

	APOLLON	ATLAS	CoReLS	ELI-NP
Affiliation	CILEX	CALA	UQBF	ELI
Location	Gif-sur-Yvette, France	Garching, Germany	Gwangju, Re- public of Korea	Măgurele, Romania
Power P in PW	10	3	4	2×10
Pulse energy W in J	180	60	55	300 (230)**
Intensity \mathcal{E}_0^2 in W/cm ²	2×10^{22}	$2 \times 10^{22*}$	10^{23}	10^{23}
Wavelength λ in nm	800	800	800	800
Pulse duration τ_{FWHM} in fs	18	20	20	22.7
Focus size $w_{0,\text{FWHM}}$ in μm	4.56*	4.6	1.1	3.56
Status	under construction	in operation	in operation	in operation

	JETI-200	OMEGA EP	POLARIS	SG-II
Affiliation	HI Jena	LLE	HI Jena	NLHPL
Location	Jena, Germany	Rochester, New York, USA	Jena, Germany	Shanghai, China
Power P in PW	0.2	0.7	0.2	5 (1.76***)
Pulse energy W in J	4	500	17	250 (37***)
Intensity \mathcal{E}_0^2 in W/cm ²	2×10^{20}	2×10^{22}	10^{21}	10^{21}
Wavelength λ in nm	800	1053	1030	808
Pulse duration τ_{FWHM} in fs	17	700	100	21
Focus size $w_{0,\text{FWHM}}$ in μm	4.08*	15	7.09	10
Status	in operation	in operation	in operation	under construction

Table 2.1.: *High-intensity laser facilities.* Listing of pulse characteristics of various high-intensity lasers including information about their facilities. The data are taken from the references [137, 138, 188–192, 194–198, 200–206]. *Estimated value by using Eq. (2.64). **Experimental measured pulse energy on Aug. 19th 2020. ***Current values given in [206]

3.

Probing the QED Vacuum Nonlinearities with Strong Electromagnetic Fields

“Dafür gibt es kein Wort. Denn unsre Sprache ist von den Etwas-Leuten gemacht; die Loch-Leute sprechen ihre eigne.”

— Kurt Tucholsky, *Zur soziologischen Psychologie der Löcher* [207]

In order to investigate the nonlinear response of the QED vacuum experimentally, it is inevitable to use strong electromagnetic fields as it follows from the derivation of the effective 1-loop Heisenberg-Euler Lagrangian, cf. Eq. (2.30) and Sec. 2.1. Here, strong fields are quantified by fractions of the critical field strength $\mathcal{E}_{cr} = \frac{m_e^2}{e}$, whereat we consider fields with an amplitude maximum value $\mathcal{E} = a \mathcal{E}_{cr}$ with $10^{-8} \leq a \leq 1$ to belong to the strong field regime. In particular, the fields accessible in high-intensity laser experiments are still weak enough compared to the critical field strength to justify field expansions of the full 1-loop Heisenberg-Euler Lagrangian Eq. (2.30) to the first nonlinear contributions, see Eq. (2.32).

Strong electromagnetic fields are hard to access directly in nature. At in small length scales, the atomic structure can provide strong fields, e.g. in ultra highly charged ions [20, 79, 126]. At large length scales we find strong fields near neutron stars; most notably the magnetars with extremely powerful field strength up to $\sim 10^{11}$ T [208–210]. The reference [211] deals with propagation of photons in a vacuum magnetized by the magnetosphere of a neutron star. Further, measurements of the neutron star RX J1856.5-3754 with a magnetic field about $\sim 10^9$ T indicate the possibility of birefringence [212, 213].

Beside these natural sources of extremely strong fields, humankind has developed techniques to achieve strong field strengths in the laboratory. Although laboratories manage to fabricate non-destructive pulsed magnetic fields over 90 T [214, 215] and pioneers experimentally studied quantum vacuum birefringence in the presents of constant magnetic fields [216], we want to focus on strong electromagnetic fields delivered by high-intensity laser pulses in the petawatt regime.

Therefore, in Sec. 3.1, we introduce the *vacuum emission picture*, a useful method to calculate photons which encode the signature of the nonlinearity of the QED vacuum. We refer to corresponding photons as signal photons. Equipped with this knowledge, we venture in Sec. 3.2 to investigate the signature of quantum vacuum nonlinearities under general use of high-intensity laser pulses. Thereby we develop a method to study the microscopic processes in detail by introducing the concept of so-called *channels*.

3.1. Vacuum Emission Picture

An efficient method to estimate the signal photons mediated by the quantum vacuum fluctuations is the *vacuum emission picture* (VEP). This method was developed for sfQED in 2015 by Felix Karbstein and Rashid Shaisultanov, see references [152, 217], while the basic idea was first given by Dmitry Galtsov in 1971 [218]. It was used explicitly for vacuum birefringence processes in [109]. Moreover, Karbstein applied it 2018 together with Holger Gies and Christian Kohlfürst for all-optical signatures of sfQED [155].

The VEP is based on the driving electromagnetic background fields $F^{\mu\nu}$ being treated as classical external fields, whereas the fields of the signature of quantum vacuum fluctuations are described as single signal photons using the methods of QFT. We describe a signal photon with the wave vector \mathbf{k} and polarization p by the state

$$|\gamma_{(p)}(\mathbf{k})\rangle = a_{(p),\mathbf{k}}^\dagger |0\rangle \quad (3.1)$$

in the Fock space. Thereby we used the representation of second quantization, where states are described by applying creation operators to the vacuum state $|0\rangle$. The operator $a_{(p),\mathbf{k}}^\dagger$ is the creator for the signal photon with its properties \mathbf{k} and p . Furthermore we can describe the polarization of the photon by the polarization four-vector $\varepsilon_{(p)}^\mu(\hat{\mathbf{k}}) = (0, \mathbf{e}_{(p)})$. The transverse vectors $\mathbf{e}_{(p)}$ with $p \in \{1, 2\}$ span the plane orthogonal to the propagation direction $\hat{\mathbf{k}} = \mathbf{k}/k$ of the photon with $k = |\mathbf{k}|$, therefore they fulfill $\hat{\mathbf{k}} \times \mathbf{e}_{(p)} = \mathbf{e}_{(p+1)}$ and $\mathbf{e}_{(3)} = -\mathbf{e}_{(1)}$.

Introducing the annihilation operator $a_{(p),\mathbf{k}}$ fulfilling $a_{(p),\mathbf{k}} |\gamma_{(p)}(\mathbf{k})\rangle = |0\rangle$ and the bosonic commutator relations

$$[a_{(p),\mathbf{k}}^\dagger, a_{(p),\mathbf{k}}^\dagger] = [a_{(p),\mathbf{k}}, a_{(p),\mathbf{k}}] = 0, \quad [a_{(p),\mathbf{k}}, a_{(p'),\mathbf{k}'}^\dagger] = \delta_{pp'} (2\pi)^3 \delta^3(\mathbf{k} - \mathbf{k}'), \quad (3.2)$$

we are able to write the gauge field for the signal photons in the Lorentz gauge in space coordinates as

$$a^\mu(x) = \sum_p \int \frac{d^3\mathbf{k}}{(2\pi)^3} \frac{1}{\sqrt{2k^0}} \left(\varepsilon_{(p)}^\mu(\mathbf{k}) e^{-ik^\nu x_\nu} a_{(p),\mathbf{k}} + \varepsilon_{(p)}^{*\mu}(\mathbf{k}) e^{ik^\nu x_\nu} a_{(p),\mathbf{k}}^\dagger \right), \quad (3.3)$$

where the component $k^0 = \omega = |\mathbf{k}| = k$. Also, by k we denote the modulus of the wave vector to avoid confusions with the four-vector $k = (k^\mu)$. The associated spacetime-dependent electromagnetic field strength tensor $f^{\mu\nu}$ for signal photons is given by

$$f_{\mu\nu}(x) = \partial_\mu a_\nu(x) - \partial_\nu a_\mu(x). \quad (3.4)$$

The total field strength tensor $F^{\mu\nu}(x) \rightarrow F^{\mu\nu}(x) + f^{\mu\nu}(x)$ decomposes into the background field $F^{\mu\nu}(x)$ and the dynamical field of the signal photons $f^{\mu\nu}(x)$. These fields are local; assuming high-intensity laser pulses as background fields $F^{\mu\nu}(x)$ is inhomogeneous. Moreover, the representation of $a^\mu(x)$ in Eq. (3.3) and Eq. (3.4) encodes the locality of the dynamical field $f^{\mu\nu}(x)$.

In Sec. 2.1 we derived the Heisenberg-Euler Lagrangian $\mathcal{L}_{\text{HE}} = \mathcal{L}_{\text{M}} + \mathcal{L}_{\text{NL}}$ in 1-loop order,

cf. Eq. (2.30). The Lagrangian

$$\mathcal{L}_{\text{NL}} = -\frac{1}{8\pi^2} \int_0^\infty \frac{d\tau}{\tau^3} e^{-\tau m_e^2} \left((e\tau)^2 \mathcal{G} \frac{\text{Re} \left\{ \cosh \left(e\tau \sqrt{2(\mathcal{F} + i\mathcal{G})} \right) \right\}}{\text{Im} \left\{ \cosh \left(e\tau \sqrt{2(\mathcal{F} + i\mathcal{G})} \right) \right\}} - \frac{2}{3} (e\tau)^2 \mathcal{F} - 1 \right) \quad (3.5)$$

describes the nonlinear contributions beyond classical physics encoded in the Maxwell Lagrangian \mathcal{L}_{M} . We have assumed that the external classical fields are constant, i.e. the relativistic invariants \mathcal{F} and \mathcal{G} dependent only on $F^{\mu\nu}$ and the dual field $\tilde{F}^{\mu\nu}$. Beyond constant fields derivatives $\partial_\alpha F^{\mu\nu}$ have to be taken into account for deriving \mathcal{L}_{NL} . These derivatives can be estimated by $\partial_\alpha F^{\mu\nu} \sim \omega_0 F^{\mu\nu}$ with the oscillation frequency ω_0 of the external inhomogeneous which is the (time) scale on which the field varies. The wave number $k_0 = |\mathbf{k}_0|$ corresponds to the spatial scale of the variation, whereas for laser beams $\omega_0 = |\mathbf{k}_0|$ is valid and therefore the frequency is sufficient as a comparison scale.

As long as we consider $\frac{\omega_0}{m_e} \ll 1$, which is satisfied for all-optical background fields, the derivatives $\partial_\alpha F^{\mu\nu}$ can still be neglected and we use the Lagrangian \mathcal{L}_{NL} even for inhomogeneous fields. Since $F^{\mu\nu}$ arises only with even powers, the inhomogeneous corrections are of the order $\mathcal{O}\left(\frac{\omega_0^2}{m_e^2}\right)$. This approximation is called locally constant field approximation (LCFA). Figuratively, the field strength supplied by the laser is constant on the scale of the vacuum fluctuations. Formally, the characteristic scales $\frac{1}{\omega_0}$ and $\lambda = \frac{2\pi}{k_0}$ are much bigger than the characteristic scales of the vacuum fluctuations, i.e. the Compton time $\tau_C = 1.29 \times 10^{-21}$ s and the electron Compton wave length $\lambda_C = 3.86 \times 10^{-13}$ m.

To describe the interaction between background fields $F^{\mu\nu}$ and fields of signal photons $f^{\mu\nu}$ we interpret the effect (1-loop) action $\Gamma_{\text{eff}}^{(1\text{-loop})} = -i \ln [\det(-i\not{D} + m_0)]$ as functional of the total field $F(x) \rightarrow F(x) + f(x)$,

$$\Gamma_{\text{eff}}^{(1\text{-loop})}[F(x)] = \int d^4x \mathcal{L}_{\text{eff}}[F(x)] . \quad (3.6)$$

Further, we are able to formulate the nonlinear contributions of the action Γ_{int} or the Lagrangian \mathcal{L}_{int} , respectively, in terms of interactions involving signal photons by expanding the effective action in terms of the quantum signal photons [152, 217]

$$\mathcal{L}_{\text{int}}(x) = f^{\mu\nu}(x) \frac{\partial \mathcal{L}_{\text{NL}}}{\partial F^{\mu\nu}}(x) + f^{\alpha\beta}(x) \frac{\partial^2 \mathcal{L}_{\text{NL}}}{\partial F^{\alpha\beta} \partial F^{\mu\nu}}(x) f^{\mu\nu}(x) + \dots \quad (3.7)$$

and $\Gamma_{\text{int}} = \int d^4x \mathcal{L}_{\text{int}}(x)$. The number of contributions of $f^{\mu\nu}$ in the terms of Eq. (3.7) indicates how many signal photons are involved in interaction processes with the background field. Using a diagrammatic representation, the Lagrangian is

$$\mathcal{L}_{\text{int}} \propto \text{diagram 1} + \text{diagram 2} + \dots$$

$$\begin{aligned}
 & + \gamma_{(p)}(\mathbf{k}) \text{ (diagram)} + \gamma_{(p)}(\mathbf{k}) \text{ (diagram)} + \dots \\
 & + \dots
 \end{aligned} \tag{3.8}$$

The wiggly lines represent photon fields while the solid lines refer to virtual fermionic particles, here the electron and the positron. See Sec. B.1 for a brief introduction in the language of Feynman diagrams. External electromagnetic fields are marked here by a cross at the end. Furthermore, the photon line with free end corresponds to the emission of a signal photon $\gamma_{(p)}(\mathbf{k})$. Obviously, the corresponding diagrams in Eq. (3.8) contain only even numbers of photon lines, according to Furry's theorem [219]. The interaction Lagrangian consists of the sum of infinite 1-loop contributions with even numbers (greater than or equal to four) of photon lines. Considering a loop dealing with an interaction of n photon lines, the contributions related to one signal photon are proportional to one signal photon and $n - 1$ background fields, contributions related to two signal photons are proportional to two signal photons and $n - 2$ background fields and so on.

The nonlinear Lagrangian $\mathcal{L}_{\text{NL}}(x)$ is determined only by the background fields, more specifically, it depends on the relativistic invariants \mathcal{F} , \mathcal{G} , see Eq. (3.5), with $\mathcal{F} = \frac{1}{4}F^{\mu\nu}F_{\mu\nu}$ and $\mathcal{G} = \frac{1}{4}F^{\mu\nu}\tilde{F}_{\mu\nu}$, cf. Eq. (2.16). We compute the derivatives

$$\frac{\partial \mathcal{L}_{\text{NL}}}{\partial F^{\mu\nu}} = \frac{\partial \mathcal{L}_{\text{NL}}}{\partial \mathcal{F}} \frac{\partial \mathcal{F}}{\partial F^{\mu\nu}} + \frac{\partial \mathcal{L}_{\text{NL}}}{\partial \mathcal{G}} \frac{\partial \mathcal{G}}{\partial F^{\mu\nu}} = \frac{1}{2} \left(\frac{\partial \mathcal{L}_{\text{NL}}}{\partial \mathcal{F}} F_{\mu\nu} + \frac{\partial \mathcal{L}_{\text{NL}}}{\partial \mathcal{G}} \tilde{F}_{\mu\nu} \right) \tag{3.9}$$

and

$$\begin{aligned}
 \frac{\partial^2 \mathcal{L}_{\text{NL}}}{\partial F^{\alpha\beta} \partial F^{\mu\nu}} &= \frac{1}{4} \left((\eta_{\alpha\mu} \eta_{\beta\nu} - \eta_{\alpha\nu} \eta_{\beta\mu}) \frac{\partial \mathcal{L}_{\text{NL}}}{\partial \mathcal{F}} + \epsilon_{\alpha\beta\mu\nu} \frac{\partial \mathcal{L}_{\text{NL}}}{\partial \mathcal{G}} + F_{\alpha\beta} F_{\mu\nu} \frac{\partial^2 \mathcal{L}_{\text{NL}}}{\partial \mathcal{F}^2} \right. \\
 &\quad \left. + \tilde{F}_{\alpha\beta} \tilde{F}_{\mu\nu} \frac{\partial^2 \mathcal{L}_{\text{NL}}}{\partial \mathcal{G}^2} + (F_{\alpha\beta} \tilde{F}_{\mu\nu} + \tilde{F}_{\alpha\beta} F_{\mu\nu}) \frac{\partial^2 \mathcal{L}_{\text{NL}}}{\partial \mathcal{F} \partial \mathcal{G}} \right)
 \end{aligned} \tag{3.10}$$

with respect to the tensor structure.

Since the number of signal photons is small, we do not have to take two signal photon interactions into account and neglect higher-order terms of $f = (f^\mu)$ in

$$\mathcal{L}_{\text{int}}(x) = f^{\mu\nu}(x) \frac{\partial \mathcal{L}_{\text{NL}}}{\partial F^{\mu\nu}}(x) + \mathcal{O}(f^2). \tag{3.11}$$

In Eq. (3.8) remains only the upper row to this order.

The amplitude for emission of a signal photon is [155, 217]

$$S_{(p)}(\mathbf{k}) \equiv \left\langle \gamma_{(p)}(\mathbf{k}) \left| \int d^4x \mathcal{L}_{\text{int}} \right| 0 \right\rangle. \tag{3.12}$$

It can be interpreted as a transition from the vacuum state to the signal photon state mediated by the action of the nonlinear interaction encoding the QED vacuum polarization. In the present thesis we will call it signal amplitude $S_{(p)}(\mathbf{k})$. This quantity contains all information

about the emission of the vacuum related to the nonlinearities. Moreover, $S_{(p)}(\mathbf{k})$ enables us to understand more about the quantum vacuum processes.

Before we determine Eq. (3.12) we take a look at the matrix element $\langle \gamma_{(p)}(\mathbf{k}) | f^{\mu\nu}(x) | 0 \rangle$ in spatial coordinates. Using Eq. (3.3) we obtain the derivative

$$\partial^\mu a^\nu(x) = \sum_{p'} \int \frac{d^3\mathbf{k}'}{(2\pi)^3} \frac{1}{\sqrt{2k'^0}} \left(-i\varepsilon_{(p')}^\mu(\mathbf{k}') k'^\nu e^{-ik'^\alpha x_\alpha} a_{(p'),\mathbf{k}'} + i\varepsilon_{(p')}^{*\mu}(\mathbf{k}') k'^\nu e^{ik'^\alpha x_\alpha} a_{(p'),\mathbf{k}'}^\dagger \right). \quad (3.13)$$

Furthermore, as the states $|0\rangle$ in the many-body system are orthonormal, i.e. $\langle 0|0\rangle = 1$, we calculate the matrix element by using a general complex number c fulfilling $cc^* = 1$,

$$\begin{aligned} \langle \gamma_{(p)}(\mathbf{k}) | c a_{(p'),\mathbf{k}'} + c^* a_{(p'),\mathbf{k}'}^\dagger | 0 \rangle &= \langle 0 | c a_{(p),\mathbf{k}} a_{(p'),\mathbf{k}'} + c^* a_{(p),\mathbf{k}} a_{(p'),\mathbf{k}'}^\dagger | 0 \rangle \\ &= \langle 0 | (2\pi)^3 c^* \delta_{pp'} \delta^3(\mathbf{k} - \mathbf{k}') | 0 \rangle + \langle 0 | c^* a_{(p),\mathbf{k}}^\dagger a_{(p'),\mathbf{k}'} | 0 \rangle \\ &= (2\pi)^3 c^* \delta_{pp'} \delta^3(\mathbf{k} - \mathbf{k}') , \end{aligned} \quad (3.14)$$

where we used $a_{(p),\mathbf{k}} | 0 \rangle = 0$ and the commutator in Eq. (3.2). Thus, we obtain with Eq. (3.4)

$$\begin{aligned} \langle \gamma_{(p)}(\mathbf{k}) | f^{\mu\nu}(x) | 0 \rangle &= \langle 0 | a_{(p),\mathbf{k}} (\partial^\mu a^\nu - \partial^\nu a^\mu) | 0 \rangle \\ &= i \sum_{p'} \int \frac{d^3\mathbf{k}'}{(2\pi)^3} \frac{(2\pi)^3}{\sqrt{2k'^0}} \\ &\quad \times \left(\varepsilon_{(p')}^{*\mu}(\mathbf{k}') k'^\nu - \varepsilon_{(p')}^{*\nu}(\mathbf{k}') k'^\mu \right) e^{ik'^\alpha x_\alpha} \delta_{pp'} \delta^3(\mathbf{k} - \mathbf{k}') \\ &= i \frac{1}{\sqrt{2k^0}} e^{ik^\alpha x_\alpha} \left(\varepsilon_{(p)}^{*\mu}(\mathbf{k}) k^\nu - \varepsilon_{(p)}^{*\nu}(\mathbf{k}) k^\mu \right). \end{aligned} \quad (3.15)$$

Now we calculate the signal amplitude by using the single signal photon interaction Lagrangian \mathcal{L}_{int} , cf. Eq. (3.11), with respect to the derivatives Eq. (3.9)

$$\begin{aligned} S_{(p)}(\mathbf{k}) &= \left\langle \gamma_{(p)}(\mathbf{k}) \left| \int d^4x f^{\mu\nu} \frac{\partial \mathcal{L}_{\text{NL}}}{\partial F_{\mu\nu}} \right| 0 \right\rangle \\ &= \left\langle \gamma_{(p)}(\mathbf{k}) \left| \int d^4x f^{\mu\nu} \frac{1}{2} \left(F_{\mu\nu} \frac{\partial \mathcal{L}_{\text{NL}}}{\partial \mathcal{F}} + \tilde{F}_{\mu\nu} \frac{\partial \mathcal{L}_{\text{NL}}}{\partial \mathcal{G}} \right) \right| 0 \right\rangle \\ &= i \frac{1}{2\sqrt{2k^0}} \int d^4x e^{ik^\alpha x_\alpha} \left[\left(\varepsilon_{(p)}^{*\mu}(\mathbf{k}) k^\nu F_{\mu\nu} - \varepsilon_{(p)}^{*\nu}(\mathbf{k}) k^\mu F_{\mu\nu} \right) \frac{\partial \mathcal{L}_{\text{NL}}}{\partial \mathcal{F}} \right. \\ &\quad \left. + \left(\varepsilon_{(p)}^{*\mu}(\mathbf{k}) k^\nu \tilde{F}_{\mu\nu} - \varepsilon_{(p)}^{*\nu}(\mathbf{k}) k^\mu \tilde{F}_{\mu\nu} \right) \frac{\partial \mathcal{L}_{\text{NL}}}{\partial \mathcal{G}} \right] \\ &= i \frac{\varepsilon_{(p)}^{*\mu}(\mathbf{k})}{\sqrt{2k^0}} \int d^4x e^{ik^\alpha x_\alpha} \left[k^\nu F_{\mu\nu} \frac{\partial \mathcal{L}_{\text{NL}}}{\partial \mathcal{F}} + k^\nu \tilde{F}_{\mu\nu} \frac{\partial \mathcal{L}_{\text{NL}}}{\partial \mathcal{G}} \right], \end{aligned} \quad (3.16)$$

where we used in the last step the antisymmetry of the field strength tensor $F_{\mu\nu} = -F_{\nu\mu}$.

Let us briefly summarize the most important properties of the signal amplitude $S_{(p)}(\mathbf{k})$. It is the transition amplitude for the emission of a signal photon with polarization p and wave vector \mathbf{k} from the quantum vacuum at 1-loop order. Thereby it is limited to single-particle emission processes. However, it can be determined for arbitrarily strong field strength of the

background field.

Meanwhile, it requires the determination of the derivatives $\frac{\partial \mathcal{L}_{\text{NL}}}{\partial \mathcal{F}}$ and $\frac{\partial \mathcal{L}_{\text{NL}}}{\partial \mathcal{G}}$. In the present work it is sufficient to restrict ourselves to weak electromagnetic fields. In the introduction of this chapter we already discussed weak fields with respect to the critical field strength $\mathcal{E}_{\text{cr}} \approx 1.3 \times 10^{18} \text{ V/m}$. From the critical field strength a critical intensity $\mathcal{E}_{\text{cr}}^2 \approx 10^{29} \text{ W/cm}^2$ follows; a comparison of the intensities of modern laser systems in Tab. 2.1 shows that they are far from reaching the Schwinger limit. For our purposes the restriction to weak fields is justified since the modern facilities reach $\mathcal{E}_0^2 \sim 10^{23} \text{ W/cm}^2$. Therefore, we consider the first nonlinear contribution in the weak-field expansion Eq. (2.32)

$$\mathcal{L}_{\text{HE}} = -\mathcal{F} + \frac{1}{45 \cdot 8\pi^2} \frac{e^4}{m_e^4} (4\mathcal{F}^2 + 7\mathcal{G}^2) + \mathcal{O}\left((F/\mathcal{E}_{\text{cr}})^6\right), \quad (3.17)$$

and obtain

$$\frac{\partial \mathcal{L}_{\text{NL}}}{\partial \mathcal{F}} = \frac{1}{45} \frac{e^2}{4\pi^2} \left(\frac{e}{m_e^2}\right)^2 4\mathcal{F}(x) \quad \text{and} \quad \frac{\partial \mathcal{L}_{\text{NL}}}{\partial \mathcal{G}} = \frac{1}{45} \frac{e^2}{4\pi^2} \left(\frac{e}{m_e^2}\right)^2 7\mathcal{G}(x) \quad (3.18)$$

straightforwardly to the relevant order of \mathcal{F} and \mathcal{G} . The derivatives beyond the weak-field expansion can be found in the references [152, 155]; furthermore, reference [152] contains the second derivatives for the two signal photon processes.

The expressions $k^\mu F_{\mu\nu}$ and $k^\mu \tilde{F}_{\mu\nu}$ with $|\mathbf{k}| = k = k^0$ from the signal photon amplitude Eq. (3.16) result in the four-vectors

$$k^\mu F_{\mu\nu} = k \left(\hat{\mathbf{k}} \cdot \mathbf{E}, -\hat{\mathbf{k}} \times \mathbf{B} - \mathbf{E} \right) \quad \text{and} \quad k^\mu \tilde{F}_{\mu\nu} = k \left(\hat{\mathbf{k}} \cdot \mathbf{B}, -\hat{\mathbf{k}} \times \mathbf{E} - \mathbf{B} \right). \quad (3.19)$$

Here, \mathbf{E} and \mathbf{B} denote the total external classical electric and magnetic field strengths. Applying the scalar product of the polarization four-vector $\varepsilon_{(p)}^\mu(\hat{\mathbf{k}}) = (0, \mathbf{e}_{(p)})$ with the property $\hat{\mathbf{k}} \times \mathbf{e}_{(p)} = \mathbf{e}_{(p+1)}$ and the four-vector $k^\mu F_{\mu\nu}$ or $k^\mu \tilde{F}_{\mu\nu}$ leads to a signal photon amplitude

$$S_{(p)}(\mathbf{k}) = \frac{1}{i} \frac{e}{4\pi^2} \frac{m_e^2}{45} \sqrt{\frac{k}{2}} \left(\frac{e}{m_e^2}\right)^3 \int d^4x e^{ik(\hat{\mathbf{k}} \cdot \mathbf{r} - t)} \left(4 \left[\mathbf{e}_{(p)} \cdot \mathbf{E} - \mathbf{e}_{(p+1)} \cdot \mathbf{B} \right] \mathcal{F} \right. \\ \left. + 7 \left[\mathbf{e}_{(p)} \cdot \mathbf{B} + \mathbf{e}_{(p+1)} \cdot \mathbf{E} \right] \mathcal{G} \right), \quad (3.20)$$

whereby we take advantage of the derivatives $\frac{\partial \mathcal{L}_{\text{NL}}}{\partial \mathcal{F}}$ and $\frac{\partial \mathcal{L}_{\text{NL}}}{\partial \mathcal{G}}$ in the weak field expansion, cf. Eq. (3.18).

The VEP leads to a signal photon amplitude $S_{(p)}(\mathbf{k})$ for the emission of one signal photon with polarization p and wave vector \mathbf{k} out of the vacuum. To achieve the differential number of signal photons $d^3 N_{(p)}(\mathbf{k})$ we consider the modulus square with respect to the infinitesimal volume given by the wave vector \mathbf{k} ,

$$d^3 N_{(p)}(\mathbf{k}) = \frac{k^2 dk d\Omega}{(2\pi)^3} |S_{(p)}(\mathbf{k})|^2. \quad (3.21)$$

For our purposes it is reasonable to express \mathbf{k} in spherical coordinates with $k = |\mathbf{k}|$, azimuthal

angle $\varphi \in [0, 2\pi)$ and polar angle $\vartheta \in [0, \pi]$ as emission angles fulfill $d\Omega = \sin \vartheta d\vartheta d\varphi$ for the differential solid angle $d\Omega$ around $\hat{\mathbf{k}}$.

By integrating the wave number k , which in the units used here corresponds to the energy or frequency, in the range k_{\min} to k_{\max} we define a polarization sensitive angular resolved signal-photon density

$$\rho_{(p)}(\varphi, \vartheta | k_{\min}, k_{\max}) = \frac{1}{(2\pi)^3} \int_{k_{\min}}^{k_{\max}} dk k^2 |S_{(p)}(\mathbf{k})|^2, \quad (3.22)$$

depending on the emission angles φ and ϑ and the frequency range k_{\min} to k_{\max} . Further, considering a given solid angle regime \mathcal{A} the total number of signal photons $N_{(p)}$ with polarization (p) yields

$$N_{(p)}(\mathcal{A} | k_{\min}, k_{\max}) = \int_{\mathcal{A}} d\Omega \rho_{(p)}(\varphi, \vartheta | k_{\min}, k_{\max}). \quad (3.23)$$

If we further assume an experiment where the measurement of the signal photons with frequency between k_{\min} and k_{\max} is polarization insensitive, we sum both polarization and obtain $\rho(\varphi, \vartheta | k_{\min}, k_{\max}) = \sum_{p=1}^2 \rho_{(p)}(\varphi, \vartheta | k_{\min}, k_{\max})$ as the photon density and $N(\mathcal{A} | k_{\min}, k_{\max}) = \sum_{p=1}^2 N_{(p)}(\mathcal{A} | k_{\min}, k_{\max})$ as the total number of emitted signal photons in the solid angle range \mathcal{A} .

3.2. Channel Analysis: Key to Optimization

Now, we want to analyze the signal-photon density that results from the collision of high-intensity Gaussian beams. Thereby, we derive a full analytical expression for the signal-photon density for arbitrary scenarios of laser pulse interactions. A key step here is the introduction of so-called channels. This new perspective gives access to us a microscopic interpretation of nonlinear vacuum processes. Moreover, it provides us with a method to optimize the design of laser pulse experiments to gain a measurable signature of QED nonlinearities that have not been observed in an experiment so far. The channel analysis was first used in the reference [160]; reference [164] deals with further developments.

To perform this analysis, we proceed step by step. First, in Sec. 3.2.1 we will discuss the laser pulses driving the emission of signal photons. In Sec. 3.2.2 we use these fields to calculate the signal photon amplitude. Afterwards we determine the signal-photon density by solving the temporal and spatial integral in Sec. 3.2.3. Furthermore, in Sec. 3.2.4, starting with the signal photon amplitude, we continue the derivation of signal-photon density. Subsequently, in Sec. 3.2.5 an interpretation of the resulting signal-photon density follows, including a discussion of the physical understanding of the channels. Moreover, we discuss the limitations of the channel analysis.

3.2.1. Collision of Several Arbitrary Pulses

First, let us comment on experiments with a single high-intensity laser pulse. In the paraxial approximation no signal photons as presented in Sec. 3.1 occur. The signal photon amplitude is proportional to the electromagnetic invariants \mathcal{F} and \mathcal{G} , cf. Eq. (3.20). Laser pulses fulfill

the property $\mathbf{E} \perp \mathbf{B} \perp \mathbf{k}$, which leads to $\mathcal{F} = \frac{1}{2}(\mathbf{B}^2 - \mathbf{E}^2) = 0$ and $\mathcal{G} = -\mathbf{B} \cdot \mathbf{E} = 0$. Accordingly, the signal amplitude $S_{(p)}(\mathbf{k})$ vanishes.

One way to obtain a non-vanishing signal is to use identical counter-propagating Gaussian beams. Assuming these beams are linearly polarized and their electric field vectors point in the same direction, their magnetic field vectors cancel each other and \mathcal{F} turns non-zero while $\mathcal{G} = 0$. If the polarization is shifted such that the electric fields are perpendicular to each other, the invariant \mathcal{F} vanishes since both fields have the same magnitudes, however, the invariant \mathcal{G} remains. If we assume the collision of two laser pulses whose optical axes differ, then contributions proportional to \mathcal{F} and \mathcal{G} are possible. In this case, the optical axes of these pulses span the collision plain.

In general, the interaction of several Gaussian pulses with arbitrary field strength maxima $\mathcal{E}_{0,i}$, oscillation frequency ω_i , propagation directions $\hat{\mathbf{k}}_i$, pulse durations τ_i , and beam waist sizes $w_{0,i}$ can be studied. At the same time, we have to keep in mind, that an experimental realization with several high-intensity laser pulses is quiet challenging. Besides the supply of the different Gaussian pulses it is desirable to synchronize the temporal and spatial focus to the same focus spot in order to maximize the local field strength. Nevertheless, from a theoretical perspective, the presence of several arbitrary Gaussian pulses gives us the opportunity to study the effects of their interaction. Therefore, in this section we will focus on multiple pulse interactions and consider n arbitrary pulses with elliptical cross section.

The field strength amplitude of the i th laser pulse is given by

$$\mathcal{E}_i(x) = \frac{1}{2}\mathcal{E}_{0,i} e^{-4\left(\frac{\zeta_i - t}{\tau_i}\right)^2} e^{-\left(\frac{\mathbf{r} \cdot \mathbf{e}_{1i}}{w_{0,1i}}\right)^2 - \left(\frac{\mathbf{r} \cdot \mathbf{e}_{2i}}{w_{0,2i}}\right)^2} \left(e^{i\omega_i(\zeta_i - t)} + e^{-i\omega_i(\zeta_i - t)} \right). \quad (3.24)$$

We assume that for the narrow interaction volume of the fields driving the quantum vacuum nonlinearity effects the use of the IRRA is justified, see Sec. 2.2.1. Furthermore, there is no shift of the different foci in time and space, all pulses have the same focus spot which we define as origin of the coordinate system, i.e. $t_0 = 0$ and $\mathbf{r}_0 = 0$ for all pulses. In addition, $\zeta_i = \hat{\mathbf{k}}_i \cdot \mathbf{r}$ parameterizes the optical axis of the i th beam pointing in $\hat{\mathbf{k}}_i$; the perpendicular axes are given by \mathbf{e}_{1i} and \mathbf{e}_{2i} which are in alignment with the semi-axes of the elliptical cross section. The different waist sizes are $w_{0,1i}$ and $w_{0,2i}$.

To compare several beams, we introduce dimensionless quantities related the the physical properties of the laser pulses. We consider frequencies of the lasers to be higher harmonics of a fundamental frequency $\omega_0 \equiv \min\{\omega_i\}$. The dimensionless oscillation frequency of the i th laser pulse is $\nu_i \equiv \frac{\omega_i}{\omega_0} \geq 1$. Further, we define $\tau_0 \equiv \max\{\tau_i\}$ as maximum pulse duration and $T_i \equiv \frac{\tau_i}{\tau_0} \leq 1$ as relative duration. As minimum beam waist we choose $w_0 \equiv \min\{w_{0,ji}\}$ where j indicates the semi-axis and i the i th beam; consequently, $\mu_{ji} \equiv \frac{w_{0,ji}}{w_0} \geq 1$ follows. For the pulse energies W_i we use $W_0 \equiv \max\{W_i\}$ and $A_i^2 \equiv \frac{W_i}{W_0} \leq 1$. These quantities specify the Gaussian pulses and lead to the maximum field strength amplitude $\mathcal{E}_{0,i}$ for the i th beam. Using Eq. (2.63) we define a general amplitude

$$\mathcal{E}_\star = \sqrt{8\sqrt{\frac{2}{\pi}} \frac{W_0}{\tau_0 w_0^2 \pi}} \quad (3.25)$$

and obtain

$$\mathcal{E}_{0,i} = \frac{A_i}{\sqrt{T_i \mu_{1i} \mu_{2i}}} \mathcal{E}_\star. \quad (3.26)$$

The field amplitude in Eq. (3.24) reads

$$\mathcal{E}_i(x) = \frac{A_i}{2\sqrt{T_i \mu_{1i} \mu_{2i}}} \mathcal{E}_\star e^{-4\left(\frac{\zeta_i - t}{\tau_0 T_i}\right)^2} e^{-\left(\frac{\mathbf{r} \cdot \mathbf{e}_{1i}}{w_0 \mu_{1i}}\right)^2 - \left(\frac{\mathbf{r} \cdot \mathbf{e}_{2i}}{w_0 \mu_{2i}}\right)^2} \left(e^{i\omega_0 \nu_i (\zeta_i - t)} + e^{-i\omega_0 \nu_i (\zeta_i - t)} \right). \quad (3.27)$$

With these field profiles and the field vectors

$$\mathbf{E}_i(x) = \mathcal{E}_i(x) \mathbf{e}_{E_i} \quad \text{and} \quad \mathbf{B}_i(x) = \mathcal{E}_i(x) \mathbf{e}_{B_i} \quad (3.28)$$

the external field yields

$$\mathbf{E}(x) = \sum_i \mathcal{E}_i(x) \mathbf{e}_{E_i} \quad \text{and} \quad \mathbf{B}(x) = \sum_i \mathcal{E}_i(x) \mathbf{e}_{B_i} \quad (3.29)$$

which we use to calculate the signal photon amplitude.

3.2.2. Signal Photon Amplitude and Channels

The VEP delivers the signal photon amplitude $S_{(p)}(\mathbf{k})$ given in Eq. (3.20). Here, the index p encodes the polarization of the photon emitted in direction $\hat{\mathbf{k}}$. Since the electromagnetic field of the signal photon is orthogonal to the direction of propagation, the polarization can be specified by an angle β . In Sec. 3.1 we have given the spatial polarization angle as $\mathbf{e}_{(p)}$. Including the direction of propagation and depending on the polarization angle β we write

$$\mathbf{e}_\beta(\hat{\mathbf{k}}) = \sin \beta \hat{\mathbf{k}} \Big|_{\varphi \rightarrow \varphi + \frac{\pi}{2}, \vartheta = \frac{\pi}{2}} + \cos \beta \hat{\mathbf{k}} \Big|_{\vartheta \rightarrow \vartheta + \frac{\pi}{2}}. \quad (3.30)$$

This corresponds to a parameterization of the rotation by β of a vector in the plane perpendicular to $\hat{\mathbf{k}}$. In the Cartesian coordinates it reads

$$\mathbf{e}_\beta(\hat{\mathbf{k}}) = \begin{pmatrix} \cos \beta \cos \varphi \cos \vartheta - \sin \beta \sin \varphi \\ \cos \beta \sin \varphi \cos \vartheta + \sin \beta \cos \varphi \\ -\cos \beta \sin \vartheta \end{pmatrix}. \quad (3.31)$$

Without loss of generality we associated $\mathbf{e}_{(1)} = \mathbf{e}_\beta$ with polarization $p = 1$; consequently, $\mathbf{e}_{(2)} = \mathbf{e}_{\beta + \frac{\pi}{2}}$ follows for the orthogonal direction. Fig. 3.1 shows the polarization vectors for a fixed choice of signal wave vector \mathbf{k} .

The signal photon amplitude appears for these two polarizations $S_{(1)}(\mathbf{k})$ and $S_{(2)}(\mathbf{k})$ with the relation $S_{(2)}(\mathbf{k}) = S_{(1)}(\mathbf{k}) \Big|_{\beta \rightarrow \beta + \frac{\pi}{2}}$. Therefore, we concentrate on the polarization $p = 1$ for the following computations.

Using the electric and magnetic fields introduced in Eq. (3.27), Eq. (3.29) we obtain for

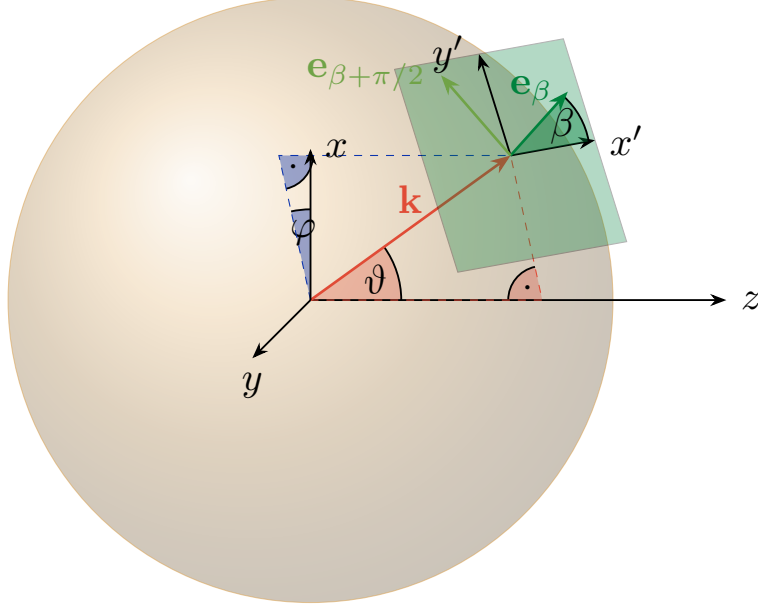


Figure 3.1.: *Vacuum emission direction and polarization.* The sphere symbolizes the full emission directions, with its radius indicating the corresponding frequency of the emitted signal photon. A fixed vector \mathbf{k} exemplifies an emission direction in (φ, ϑ) . Additionally, the polarization for this emission is illustrated: The field vectors of the signal photon at \mathbf{k} are orthogonal to the sphere in the green plane. The vectors \mathbf{e}_β and $\mathbf{e}_{\beta+\pi/2}$ show two polarization directions for a fixed choice of the angle β .

the relativistic invariants

$$\begin{aligned}
 \mathcal{F}(x) &= \frac{1}{2} (\mathbf{B}^2 - \mathbf{E}^2) \\
 &= \frac{1}{2} \left(\left(\sum_i \mathcal{E}_i(x) \mathbf{e}_{B_i} \right) \cdot \left(\sum_j \mathcal{E}_j(x) \mathbf{e}_{B_j} \right) - \left(\sum_i \mathcal{E}_i(x) \mathbf{e}_{E_i} \right) \cdot \left(\sum_j \mathcal{E}_j(x) \mathbf{e}_{E_j} \right) \right) \\
 &= \frac{1}{2} \sum_i \mathcal{E}_i(x) \mathcal{E}_j(x) (\mathbf{e}_{B_i} \cdot \mathbf{e}_{B_j} - \mathbf{e}_{E_i} \cdot \mathbf{e}_{E_j})
 \end{aligned} \tag{3.32}$$

and

$$\begin{aligned}
 \mathcal{G}(x) &= -\mathbf{B} \cdot \mathbf{E} = - \left(\sum_i \mathcal{E}_i(x) \mathbf{e}_{B_i} \right) \cdot \left(\sum_j \mathcal{E}_j(x) \mathbf{e}_{E_j} \right) \\
 &= -\frac{1}{2} \sum_i \mathcal{E}_i(x) \mathcal{E}_j(x) (\mathbf{e}_{B_i} \cdot \mathbf{e}_{E_j} + \mathbf{e}_{B_j} \cdot \mathbf{e}_{E_i}),
 \end{aligned} \tag{3.33}$$

where we used a symmetric representation in i and j in the last step. Determining the product of a polarization vector with a field vector and an invariant, e.g.

$$(\mathbf{e}_\beta \cdot \mathbf{E}) \mathcal{F} = \sum_{ijl} \mathcal{E}_i(x) \mathcal{E}_j(x) \mathcal{E}_l(x) (\mathbf{e}_\beta \cdot \mathbf{e}_{E_l}) (\mathbf{e}_{B_i} \cdot \mathbf{e}_{B_j} - \mathbf{e}_{E_i} \cdot \mathbf{e}_{E_j}), \tag{3.34}$$

the term in the parenthesis in Eq. (3.20) yields

$$\begin{aligned}
 & 4 \left[\mathbf{e}_\beta \cdot \mathbf{E} - \mathbf{e}_{\beta+\frac{\pi}{2}} \cdot \mathbf{B} \right] \mathcal{F} + 7 \left[\mathbf{e}_\beta \cdot \mathbf{B} + \mathbf{e}_{\beta+\frac{\pi}{2}} \cdot \mathbf{E} \right] \mathcal{G} \\
 &= \sum_{ijl} \mathcal{E}_i(x) \mathcal{E}_j(x) \mathcal{E}_l(x) \left[2 \left(\mathbf{e}_\beta \cdot \mathbf{e}_{E_l} - \mathbf{e}_{\beta+\frac{\pi}{2}} \cdot \mathbf{e}_{B_l} \right) \left(\mathbf{e}_{B_i} \cdot \mathbf{e}_{B_j} - \mathbf{e}_{E_i} \cdot \mathbf{e}_{E_j} \right) \right. \\
 &\quad \left. - \frac{7}{2} \left(\mathbf{e}_\beta \cdot \mathbf{e}_{B_l} + \mathbf{e}_{\beta+\frac{\pi}{2}} \cdot \mathbf{e}_{E_l} \right) \left(\mathbf{e}_{B_i} \cdot \mathbf{e}_{E_j} + \mathbf{e}_{B_j} \cdot \mathbf{e}_{E_i} \right) \right] \quad (3.35)
 \end{aligned}$$

for the polarization $p = 1$.

For a fixed choice of components i, j , and l , the terms in Eq. (3.35) can be decomposed in a natural manner: The product of the three corresponding field amplitudes contains all the information about the local dependence, whereas the part in the square brackets is determined exclusively by the geometrical arrangement of the driving laser pulses and the measured signal. Because of their different dependencies and physical meaning we separate these contributions and define the Fourier integral

$$\mathcal{I}_{ijl}(\mathbf{k}) \equiv \int d^4x e^{ik_\mu x^\mu} \mathcal{E}_i(x) \mathcal{E}_j(x) \mathcal{E}_l(x) \quad (3.36)$$

as well as the geometric function

$$\begin{aligned}
 g_{\beta;ijl}(\varphi, \vartheta) &\equiv 2 \left(\mathbf{e}_\beta \cdot \mathbf{e}_{E_l} - \mathbf{e}_{\beta+\frac{\pi}{2}} \cdot \mathbf{e}_{B_l} \right) \left(\mathbf{e}_{B_i} \cdot \mathbf{e}_{B_j} - \mathbf{e}_{E_i} \cdot \mathbf{e}_{E_j} \right) \\
 &\quad - \frac{7}{2} \left(\mathbf{e}_\beta \cdot \mathbf{e}_{B_l} + \mathbf{e}_{\beta+\frac{\pi}{2}} \cdot \mathbf{e}_{E_l} \right) \left(\mathbf{e}_{B_i} \cdot \mathbf{e}_{E_j} + \mathbf{e}_{B_j} \cdot \mathbf{e}_{E_i} \right). \quad (3.37)
 \end{aligned}$$

For $\mathcal{I}_{ijl}(\mathbf{k})$ we have used that the integral and summation over i, j, l are invariant under index permutations; additionally we have included the exponential function in the definition. This contribution corresponds to the Fourier transform of the product of the field amplitudes of three laser modes. We call the combination of fixed i, j and l *channels* and use the tuple (ijl) to indicate it. In Sec. 3.2.5 we interpret the physical meaning of these channels.

To determine the signal photon amplitude $S_{(1)}(\mathbf{k})$ with $p = 1$ we sum over the contributions of all channels, using Eq. (3.20), Eq. (3.35), Eq. (3.36), and Eq. (3.37),

$$S_{(1)}(\mathbf{k}) = \frac{1}{i} \frac{e}{4\pi^2} \frac{m_e^2}{45} \sqrt{\frac{k}{2}} \left(\frac{e}{m_e^2} \right)^3 \sum_{ijl} \mathcal{I}_{ijl}(\mathbf{k}) g_{\beta;ijl}(\varphi, \vartheta) \quad (3.38)$$

follows. Analogously, for the second polarization $p = 2$, we obtain

$$S_{(2)}(\mathbf{k}) = \frac{1}{i} \frac{e}{4\pi^2} \frac{m_e^2}{45} \sqrt{\frac{k}{2}} \left(\frac{e}{m_e^2} \right)^3 \sum_{ijl} \mathcal{I}_{ijl}(\mathbf{k}) g_{\beta+\frac{\pi}{2};ijl}(\varphi, \vartheta). \quad (3.39)$$

For n different laser pulses n^3 different channels occur. However, according to the properties of \mathcal{I}_{ijl} and $g_{\beta;ijl}$, we can reduce them to $n^3 - n^2$. For $i = j$ the function $g_{\beta;iil}(\varphi, \vartheta)$ vanishes since both second parentheses in Eq. (3.37) yield zero. Moreover, $g_{\beta;ijl}(\varphi, \vartheta)$ has a symmetry in i and j , but not in l , $g_{\beta;ijl} = g_{\beta;jil}$; in contrast to \mathcal{I}_{ijl} which is completely symmetric in its indices. This leads to $\frac{n^3 - n^2}{2}$ independent channels. In order to calculate the Fourier

integrals \mathcal{I}_{ijl} it reduces to $\frac{1}{6}(n-1)(4n+n^2)$ independent channels. Considering an example with $n=2$ laser pulses, there are two relevant independent Fourier integrals $\mathcal{I}_{121} = \mathcal{I}_{211}$ and $\mathcal{I}_{212} = \mathcal{I}_{122}$ and two independent different geometric functions $g_{\beta;121} = g_{\beta;211}$ and $g_{\beta;212} = g_{\beta;122}$. The substitution $\sum_{ijl} \rightarrow 2 \sum_{\substack{ijl \\ i \leftrightarrow j}}$ takes these equalities into account.

Furthermore, we define the channel contributions for the signal photon amplitude

$$\frac{1}{i} S_{(1);ijl}(\mathbf{k}) \equiv \frac{1}{i} \frac{e}{4\pi^2} \frac{m_e^2}{45} \sqrt{\frac{k}{2}} \left(\frac{e}{m_e^2} \right)^3 \mathcal{I}_{ijl}(\mathbf{k}) g_{\beta;ijl}(\varphi, \vartheta) \quad (3.40)$$

and

$$\frac{1}{i} S_{(2);ijl}(\mathbf{k}) \equiv \frac{1}{i} \frac{e}{4\pi^2} \frac{m_e^2}{45} \sqrt{\frac{k}{2}} \left(\frac{e}{m_e^2} \right)^3 \mathcal{I}_{ijl}(\mathbf{k}) g_{\beta+\frac{\pi}{2};ijl}(\varphi, \vartheta) . \quad (3.41)$$

The definitions are chosen in a way that $S_{(1);ijl}(\mathbf{k})$ and $S_{(2);ijl}(\mathbf{k})$ are real, this will be clarified in section 3.2.4. Correspondingly, the total signal photon amplitude is

$$S_{(1,2)}(\mathbf{k}) = 2 \sum_{\substack{ijl \\ i \leftrightarrow j}} \frac{1}{i} S_{(1,2);ijl}(\mathbf{k}) . \quad (3.42)$$

Since the polarization of the signal exclusively affects the function $g_{\beta;ijl}(\varphi, \vartheta)$ in $S_{(p)}(\mathbf{k})$, the polarization insensitive signal photon amplitude follows from the sum of two geometric functions with orthogonal polarization angle,

$$\frac{1}{i} S_{ijl}(\mathbf{k}) = \frac{1}{i} \frac{e}{4\pi^2} \frac{m_e^2}{45} \sqrt{\frac{k}{2}} \left(\frac{e}{m_e^2} \right)^3 \mathcal{I}_{ijl}(\mathbf{k}) \left(g_{\beta;ijl}(\varphi, \vartheta) + g_{\beta+\frac{\pi}{2};ijl}(\varphi, \vartheta) \right) . \quad (3.43)$$

In order to estimate the contributions of each channel we have to perform the Fourier integral.

3.2.3. Performing the Fourier Integral

So far, we have exclusively exploited the $\mathbf{e}_{E_i} \perp \mathbf{e}_{B_i}$ property of laser pulses. The determination of the signal amplitude according to Eq. (3.40), Eq. (3.41), and Eq. (3.42) is independent of the kind of the profiles $\mathcal{E}_i(x)$. However, to evaluate the Fourier integral $\mathcal{I}_{ijl}(\mathbf{k})$, we must consider the shape of the functions $\mathcal{E}_i(x)$. Here we concentrate on the Gaussian pulses introduced in Sec. 2.2.1, as described in (3.27).

In order to determine the spacetime integral $\int d^4x = \int dt \int d^3\mathbf{r}$, we first perform the temporal integral. In a second step we will consider the spatial dimensions.

Performing the temporal integral

We start by introducing a short-hand notation \mathcal{J}_{ijl} for the time-dependent contributions in \mathcal{I}_{ijl} ,

$$\mathcal{J}_{ijl} = \int_{-\infty}^{\infty} dt e^{-ikt} e^{-4 \left[\left(\frac{\zeta_i - t}{\tau_0 T_i} \right)^2 - \left(\frac{\zeta_j - t}{\tau_0 T_j} \right)^2 - \left(\frac{\zeta_l - t}{\tau_0 T_l} \right)^2 \right]} \left(e^{i\omega_0 \nu_i (\zeta_i - t)} + e^{-i\omega_0 \nu_i (\zeta_i - t)} \right)$$

$$\begin{aligned}
 & \times \left(e^{i\omega_0\nu_j(\zeta_j-t)} + e^{-i\omega_0\nu_j(\zeta_j-t)} \right) \left(e^{i\omega_0\nu_l(\zeta_l-t)} + e^{-i\omega_0\nu_l(\zeta_l-t)} \right) \\
 & = \sum_{\xi, \eta, \chi \in \mathcal{S}} \int_{-\infty}^{\infty} dt e^{-ikt} e^{-4 \left[\left(\frac{\zeta_i-t}{\tau_0 T_i} \right)^2 - \left(\frac{\zeta_j-t}{\tau_0 T_j} \right)^2 - \left(\frac{\zeta_l-t}{\tau_0 T_l} \right)^2 \right]} e^{i\omega_0(\xi\nu_i(\zeta_i-t) + \eta\nu_j(\zeta_j-t) + \chi\nu_l(\zeta_l-t))}.
 \end{aligned} \tag{3.44}$$

Here, by definition $\xi = \pm 1$, $\eta = \pm 1$, $\chi = \pm 1$, we have replaced the products of the sums of exponential functions with a single exponential function; the corresponding summation can be performed after integration. With the set $\mathcal{S} = \{-1, +1\}$ we cover all possible combinations of the products of the sums. The contributions $\xi\nu_i = \pm\nu_i$ correspond to an addition or subtraction of the relative frequencies of the i th driving laser pulse. By representing the exponent as a second order polynomial in t the integral

$$\begin{aligned}
 \mathcal{J}_{ijl} &= \sum_{\xi, \eta, \chi \in \mathcal{S}} \int_{-\infty}^{\infty} dt e^{-\frac{4}{\tau_0^2} \left(\frac{1}{T_i^2} + \frac{1}{T_j^2} + \frac{1}{T_l^2} \right) t^2 + \left(\frac{8}{\tau_0^2} \left(\frac{\zeta_i}{T_i^2} + \frac{\zeta_j}{T_j^2} + \frac{\zeta_l}{T_l^2} \right) - i(k + \omega_0(\xi\nu_i + \eta\nu_j + \chi\nu_l)) \right) t} \\
 & \quad \times e^{-\left(\frac{4}{\tau_0^2} \left(\frac{\zeta_i^2}{T_i^2} + \frac{\zeta_j^2}{T_j^2} + \frac{\zeta_l^2}{T_l^2} \right) - i\omega_0(\xi\nu_i\zeta_i + \eta\nu_j\zeta_j + \chi\nu_l\zeta_l) \right)} \\
 &= \sum_{\xi, \eta, \chi \in \mathcal{S}} \tau_0 \frac{T_i T_j T_l}{2} \sqrt{\frac{\pi}{T_j^2 T_l^2 + T_i^2 T_l^2 + T_i^2 T_j^2}} \\
 & \quad \times e^{\frac{\tau_0^2}{16} \frac{T_i^2 T_j^2 T_l^2}{T_j^2 T_l^2 + T_i^2 T_l^2 + T_i^2 T_j^2} \left(\frac{8}{\tau_0^2} \left(\frac{\zeta_i}{T_i^2} + \frac{\zeta_j}{T_j^2} + \frac{\zeta_l}{T_l^2} \right) - i(k + \omega_0(\xi\nu_i + \eta\nu_j + \chi\nu_l)) \right)^2}
 \end{aligned} \tag{3.45}$$

$$\times e^{-\left(\frac{4}{\tau_0^2} \left(\frac{\zeta_i^2}{T_i^2} + \frac{\zeta_j^2}{T_j^2} + \frac{\zeta_l^2}{T_l^2} \right) - i\omega_0(\xi\nu_i\zeta_i + \eta\nu_j\zeta_j + \chi\nu_l\zeta_l) \right)} \tag{3.46}$$

is a Gauss integral.

Using \mathcal{J}_{ijl} , only the spatial integral

$$\begin{aligned}
 \mathcal{I}_{ijl}(\mathbf{k}) &= \frac{A_i A_j A_l}{8\sqrt{T_i T_j T_l}} \frac{\mathcal{E}_\star^3}{\sqrt{\mu_{1i}\mu_{2i}\mu_{1j}\mu_{2j}\mu_{1l}\mu_{2l}}} \int d^3\mathbf{r} e^{i\mathbf{k}\cdot\mathbf{r}} \mathcal{J}_{ijl} \\
 & \quad \times e^{-\left(\frac{\mathbf{r}\cdot\mathbf{e}_{1i}}{w_0\mu_{1i}} \right)^2 - \left(\frac{\mathbf{r}\cdot\mathbf{e}_{2i}}{w_0\mu_{2i}} \right)^2 - \left(\frac{\mathbf{r}\cdot\mathbf{e}_{1j}}{w_0\mu_{1j}} \right)^2 - \left(\frac{\mathbf{r}\cdot\mathbf{e}_{2j}}{w_0\mu_{2j}} \right)^2 - \left(\frac{\mathbf{r}\cdot\mathbf{e}_{1l}}{w_0\mu_{1l}} \right)^2 - \left(\frac{\mathbf{r}\cdot\mathbf{e}_{2l}}{w_0\mu_{2l}} \right)^2}
 \end{aligned} \tag{3.47}$$

remains.

Performing the space integral

From Eq. (3.46) it can be seen that \mathcal{J}_{ijl} has position-dependent contributions encoded in the corresponding propagation directions ζ_i , ζ_j , and ζ_l . Furthermore, the transverse Gaussian decays in Eq. (3.47) add further functions depending on \mathbf{r} .

First, we define $\mathcal{W}_{ijl}^{\xi\eta\chi}$ as a solution of the spatial integral for corresponding sign combination

ξ , η , and χ . Thus it follows for the Fourier integral

$$\begin{aligned} \mathcal{I}_{ijl}(\mathbf{k}) = & \frac{A_i A_j A_l}{16} \frac{\mathcal{E}_*^3 \tau_0}{\sqrt{\mu_{1i} \mu_{2i} \mu_{1j} \mu_{2j} \mu_{1l} \mu_{2l}}} \sqrt{\frac{\pi \mathsf{T}_i \mathsf{T}_j \mathsf{T}_l}{\mathsf{T}_j^2 \mathsf{T}_l^2 + \mathsf{T}_i^2 \mathsf{T}_l^2 + \mathsf{T}_i^2 \mathsf{T}_j^2}} \\ & \times \sum_{\xi, \eta, \chi \in \mathcal{S}} \mathcal{W}_{ijl}^{\xi\eta\chi} e^{-\frac{\tau_0^2}{16} \frac{\mathsf{T}_i^2 \mathsf{T}_j^2 \mathsf{T}_l^2}{\mathsf{T}_j^2 \mathsf{T}_l^2 + \mathsf{T}_i^2 \mathsf{T}_l^2 + \mathsf{T}_i^2 \mathsf{T}_j^2} [\mathbf{k} + \omega_0(\xi \nu_i + \eta \nu_j + \chi \nu_l)]^2}. \end{aligned} \quad (3.48)$$

The integral to be solved is

$$\begin{aligned} \mathcal{W}_{ijl}^{\xi\eta\chi} = & \int d^3 \mathbf{r} e^{i\mathbf{k} \cdot \mathbf{r}} e^{-\left(\frac{\mathbf{r} \cdot \mathbf{e}_{1i}}{w_0 \mu_{1i}}\right)^2 - \left(\frac{\mathbf{r} \cdot \mathbf{e}_{2i}}{w_0 \mu_{2i}}\right)^2 - \left(\frac{\mathbf{r} \cdot \mathbf{e}_{1j}}{w_0 \mu_{1j}}\right)^2 - \left(\frac{\mathbf{r} \cdot \mathbf{e}_{2j}}{w_0 \mu_{2j}}\right)^2 - \left(\frac{\mathbf{r} \cdot \mathbf{e}_{1l}}{w_0 \mu_{1l}}\right)^2 - \left(\frac{\mathbf{r} \cdot \mathbf{e}_{2l}}{w_0 \mu_{2l}}\right)^2} \\ & \times e^{\frac{4}{\tau_0^2} \left[\left(\frac{\mathsf{T}_{ijl}}{\mathsf{T}_i^2} - 1 \right) \frac{\zeta_i^2}{\mathsf{T}_i^2} + \left(\frac{\mathsf{T}_{ijl}}{\mathsf{T}_j^2} - 1 \right) \frac{\zeta_j^2}{\mathsf{T}_j^2} + \left(\frac{\mathsf{T}_{ijl}}{\mathsf{T}_l^2} - 1 \right) \frac{\zeta_l^2}{\mathsf{T}_l^2} + 2\mathsf{T}_{ijl} \frac{\zeta_j \zeta_l}{\mathsf{T}_j^2 \mathsf{T}_l^2} + 2\mathsf{T}_{ijl} \frac{\zeta_i \zeta_l}{\mathsf{T}_i^2 \mathsf{T}_l^2} + 2\mathsf{T}_{ijl} \frac{\zeta_i \zeta_j}{\mathsf{T}_i^2 \mathsf{T}_j^2} \right]} \\ & \times e^{-i\omega_0 \left[\mathsf{T}_{ijl} \left(\frac{\zeta_i}{\mathsf{T}_i^2} + \frac{\zeta_j}{\mathsf{T}_j^2} + \frac{\zeta_l}{\mathsf{T}_l^2} \right) (\xi \nu_i + \eta \nu_j + \chi \nu_l) - \xi \nu_i \zeta_i - \eta \nu_j \zeta_j - \chi \nu_l \zeta_l \right]} \\ & \times e^{-i\mathbf{k} \mathsf{T}_{ijl} \left(\frac{\zeta_i}{\mathsf{T}_i^2} + \frac{\zeta_j}{\mathsf{T}_j^2} + \frac{\zeta_l}{\mathsf{T}_l^2} \right)} \\ = & \int d^3 \mathbf{r} e^{-\frac{1}{2} \mathbf{r} \cdot \mathcal{M}_{ijl} \mathbf{r} + i \mathbf{K}_{ijl}^{\xi\eta\chi} \cdot \mathbf{r}}, \end{aligned} \quad (3.49)$$

where we use $\mathsf{T}_{ijl} = \mathsf{T}_i^2 \mathsf{T}_j^2 \mathsf{T}_l^2 / (\mathsf{T}_i^2 \mathsf{T}_j^2 + \mathsf{T}_j^2 \mathsf{T}_l^2 + \mathsf{T}_i^2 \mathsf{T}_l^2)$ as abbreviation. In the last step in Eq. (3.49), we summarized the arguments of the exponential functions. Here the contributions proportional to the product of two spatial variables are mapped to the matrix \mathcal{M}_{ijl} ; the contributions linear in the spatial coordinates can be formed over the scalar product of \mathbf{r} with vector $\mathbf{K}_{ijl}^{\xi\eta\chi}$. Since the generalized Gaussian integral from Eq. (3.49) can be solved according to

$$\mathcal{W}_{ijl}^{\xi\eta\chi} = \sqrt{\frac{(2\pi)^3}{\det \mathcal{M}_{ijl}}} e^{-\frac{1}{2} \mathbf{K}_{ijl}^{\xi\eta\chi} \cdot \mathcal{M}_{ijl}^{-1} \mathbf{K}_{ijl}^{\xi\eta\chi}}, \quad (3.50)$$

only the determination of the matrix \mathcal{M}_{ijl} and the vector $\mathbf{K}_{ijl}^{\xi\eta\chi}$ remains.

The vector $\mathbf{K}_{ijl}^{\xi\eta\chi}$ decomposes into a contribution proportional to the minimum frequency ω_0 and a contribution proportional to the frequency of the signal photon \mathbf{k} ,

$$\mathbf{K}_{ijl}^{\xi\eta\chi} = \omega_0 \mathbf{K}_{1,ijl}^{\xi\eta\chi} + \mathbf{k} \mathbf{K}_{2,ijl}, \quad (3.51)$$

where the signs ξ , η , and χ exclusively influence the contribution $\mathbf{K}_{1,ijl}^{\xi\eta\chi}$ proportional to the minimum frequency ω_0 . This contribution is determined by the interaction of the different laser modes. Eq. (3.49) and the property $\zeta_i = \hat{\mathbf{k}}_i \cdot \mathbf{r}$ result in the vectors

$$\mathbf{K}_{1,ijl}^{\xi\eta\chi} = \xi \nu_i \hat{\mathbf{k}}_i + \eta \nu_j \hat{\mathbf{k}}_j + \chi \nu_l \hat{\mathbf{k}}_l - \mathsf{T}_{ijl} \left(\frac{\hat{\mathbf{k}}_i}{\mathsf{T}_i^2} + \frac{\hat{\mathbf{k}}_j}{\mathsf{T}_j^2} + \frac{\hat{\mathbf{k}}_l}{\mathsf{T}_l^2} \right) \quad (3.52)$$

and

$$\mathbf{K}_{2,ijl} = \hat{\mathbf{k}} - \tau_{ijl} \left(\frac{\hat{\mathbf{k}}_i}{T_i^2} + \frac{\hat{\mathbf{k}}_j}{T_j^2} + \frac{\hat{\mathbf{k}}_l}{T_l^2} \right). \quad (3.53)$$

Furthermore, the matrix

$$\begin{aligned} \mathcal{M}_{ijl} = & \frac{2}{w_0^2} \left(\frac{\mathbf{e}_{1i} \otimes \mathbf{e}_{1i}}{\mu_{1i}^2} + \frac{\mathbf{e}_{2i} \otimes \mathbf{e}_{2i}}{\mu_{2i}^2} + \frac{\mathbf{e}_{1j} \otimes \mathbf{e}_{1j}}{\mu_{1j}^2} + \frac{\mathbf{e}_{2j} \otimes \mathbf{e}_{2j}}{\mu_{2j}^2} + \frac{\mathbf{e}_{1l} \otimes \mathbf{e}_{1l}}{\mu_{1l}^2} + \frac{\mathbf{e}_{2l} \otimes \mathbf{e}_{2l}}{\mu_{2l}^2} \right) \\ & - \frac{8}{\tau_0^2} \left[\left(\frac{\tau_{ijl}}{T_i^2} - 1 \right) \frac{\hat{\mathbf{k}}_i \otimes \hat{\mathbf{k}}_i}{T_i^2} + \left(\frac{\tau_{ijl}}{T_j^2} - 1 \right) \frac{\hat{\mathbf{k}}_j \otimes \hat{\mathbf{k}}_j}{T_j^2} + \left(\frac{\tau_{ijl}}{T_l^2} - 1 \right) \frac{\hat{\mathbf{k}}_l \otimes \hat{\mathbf{k}}_l}{T_l^2} \right] \\ & - \frac{16\tau_{ijl}}{\tau_0^2} \left(\frac{\hat{\mathbf{k}}_j \otimes \hat{\mathbf{k}}_l}{T_j^2 T_l^2} + \frac{\hat{\mathbf{k}}_l \otimes \hat{\mathbf{k}}_i}{T_l^2 T_i^2} + \frac{\hat{\mathbf{k}}_i \otimes \hat{\mathbf{k}}_j}{T_i^2 T_j^2} \right) \end{aligned} \quad (3.54)$$

follows from Eq. (3.49) and the property $\zeta_i \zeta_j = \mathbf{r} \cdot (\hat{\mathbf{k}}_i \otimes \hat{\mathbf{k}}_j) \mathbf{r}$. The first parenthesis dominates the contribution by decay of the Gaussian functions perpendicular to the optical axes of each laser pules. Moreover, the remaining contributions are governed by the propagation directions of the driving lasers. Additionally, the convergence is ensured by the pulse durations for the propagation contribution and by the waist sizes for the perpendicular terms.

3.2.4. From the Channel Signal Photon Amplitude to the Density

With the determination of the Fourier integral $\mathcal{I}_{ijl}(\mathbf{k})$ the signal photon amplitude for a fixed channel can be calculated. For this we insert Eq. (3.48) and Eq. (3.50) into Eq. (3.40) and obtain

$$\begin{aligned} S_{(1);ijl}(\mathbf{k}) = & \frac{e}{4\pi^2} \frac{m_e^2}{45} \left(\frac{e}{m_e^2} \right)^3 \sqrt{\frac{\mathbf{k}}{2}} \mathcal{E}_*^3 \tau_0 \sqrt{\frac{\tau_{ijl}}{T_i T_j T_l}} \frac{A_i A_j A_l}{16 \sqrt{M_{ijl}}} \frac{g_{\beta;ijl}(\varphi, \vartheta)}{\sqrt{\det \mathcal{M}_{ijl}}} \sqrt{\pi (2\pi)^3} \\ & \times \sum_{\xi, \eta, \chi \in \mathcal{S}} e^{-\frac{\tau_0^2}{16} \tau_{ijl} [\mathbf{k} + \omega_0 (\xi \nu_i + \eta \nu_j + \chi \nu_l)]^2 - \frac{1}{2} \mathbf{K}_{ijl}^{\xi \eta \chi} \cdot \mathcal{M}_{ijl}^{-1} \mathbf{K}_{ijl}^{\xi \eta \chi}}, \end{aligned} \quad (3.55)$$

using $M_{ijl} \equiv \mu_{1i} \mu_{2i} \mu_{1j} \mu_{2j} \mu_{1l} \mu_{2l}$ for a compact notation. From Eq. (3.55) it can be seen that $S_{(1);ijl}(\mathbf{k})$ is real due to the definition of $S_{(1);ijl}(\mathbf{k})$ in Eq. (3.40) without prefactor $-i$.

To receive the differential number of signal photons from the signal photon amplitude, the absolute square of this is required. This includes a summation over all channels; due to the real amplitude $S_{(1);ijl}(\mathbf{k})$ of each channel, the modulus square follows from

$$\left| S_{(1)}(\mathbf{k}) \right|^2 = \left(2 \sum_{\substack{ijl \\ i \leftrightarrow j}} \frac{1}{i} S_{(1);ijl}(\mathbf{k}) \right) \left(2 \sum_{\substack{ijl \\ i \leftrightarrow j}} \frac{1}{i} S_{(1);ijl}(\mathbf{k}) \right)^* = 4 \sum_{\substack{ijl i' j' l' \\ i \leftrightarrow j, i' \leftrightarrow j'}} S_{(1);ijl}(\mathbf{k}) S_{(1);i' j' l'}(\mathbf{k}). \quad (3.56)$$

Here we have used the symmetry concerning the interchange of i and j . The differential number of signal photons per energy dk and solid angle $d\Omega$ thus results in

$$d^3 N = dk d\Omega \frac{e^2}{16\pi^4} \frac{m_e^4}{45^2} \left(\frac{e}{m_e^2} \right)^6 \frac{k^3}{2} \mathcal{E}_*^6 \tau_0^2 \frac{\pi}{16^2} 4$$

$$\begin{aligned}
 & \times \sum_{\substack{ijl, i'j'l' \\ i \leftrightarrow j, i' \leftrightarrow j'}} \left[\frac{A_i A_j A_l A_{i'} A_{j'} A_{l'}}{\sqrt{M_{ijl} M_{i'j'l'}}} \sqrt{\frac{\tau_{ijl} \tau_{i'j'l'}}{T_i T_j T_l T_{i'} T_{j'} T_{l'}}} \frac{g_{\beta;ijl}(\varphi, \vartheta) g_{\beta\phi; i'j'l'}(\varphi, \vartheta)}{\sqrt{\det \mathcal{M}_{ijl} \det \mathcal{M}_{i'j'l'}}} \right. \\
 & \times \sum_{\substack{\xi, \eta, \chi \in \mathcal{S} \\ \xi', \eta', \chi' \in \mathcal{S}}} \left(e^{-\frac{\tau_0^2}{16} \left(\tau_{ijl} [k + \omega_0 (\xi \nu_i + \eta \nu_j + \chi \nu_l)]^2 + \tau_{i'j'l'} [k + \omega_0 (\xi' \nu_{i'} + \eta' \nu_{j'} + \chi' \nu_{l'})]^2 \right)} \right. \\
 & \left. \left. \times e^{-\frac{1}{2} \mathbf{K}_{ijl}^{\xi\eta\chi} \cdot \mathcal{M}_{ijl}^{-1} \mathbf{K}_{ijl}^{\xi\eta\chi} - \frac{1}{2} \mathbf{K}_{i'j'l'}^{\xi'\eta'\chi'} \cdot \mathcal{M}_{i'j'l'}^{-1} \mathbf{K}_{i'j'l'}^{\xi'\eta'\chi'}} \right) \right]. \quad (3.57)
 \end{aligned}$$

Again, the different signs ξ, η, χ have to be taken into account. By squaring the amplitude, the sum has to be expanded with the signs marked by a prime. Apart from the general prefactor k^3 the energy dependence is given exclusively in the exponential function. By separating the k -dependent contribution from the ω_0 -dependent contribution in $\mathbf{K}_{ijl}^{\xi\eta\chi}$, see Eq. 3, it follows for the exponential function

$$\begin{aligned}
 e^{-\frac{1}{2} \mathbf{K}_{ijl}^{\xi\eta\chi} \cdot \mathcal{M}_{ijl}^{-1} \mathbf{K}_{ijl}^{\xi\eta\chi}} &= e^{-\frac{1}{2} \mathbf{K}_{2,ijl} \cdot \mathcal{M}_{ijl}^{-1} \mathbf{K}_{2,ijl} k^2 - \frac{1}{2} \omega_0 \left(\mathbf{K}_{1,ijl}^{\xi\eta\chi} \cdot \mathcal{M}_{ijl}^{-1} \mathbf{K}_{2,ijl} + \mathbf{K}_{2,ijl} \cdot \mathcal{M}_{ijl}^{-1} \mathbf{K}_{1,ijl}^{\xi\eta\chi} \right) k} \\
 &\times e^{-\frac{1}{2} \omega_0^2 \mathbf{K}_{1,ijl}^{\xi\eta\chi} \cdot \mathcal{M}_{ijl}^{-1} \mathbf{K}_{1,ijl}^{\xi\eta\chi}}. \quad (3.58)
 \end{aligned}$$

For further steps we want to introduce the abbreviations $\ell_{ijl}^{\xi\eta\chi} \equiv \xi \nu_i + \eta \nu_j + \chi \nu_l$ and $\ell_{i'j'l'}^{\xi'\eta'\chi'} \equiv \xi' \nu_{i'} + \eta' \nu_{j'} + \chi' \nu_{l'}$. They correspond to the sum of the relative frequencies ν_i of the driving lasers with respect to the choice of the signs ξ, η, χ . Within Eq. (3.57) $\ell_{ijl}^{\xi\eta\chi}$ appears always with the prefactor ω_0 and is therefore interpreted as a frequency given by the driving laser pulses, which is related to the signal frequency k by the exponential function.

Accordingly, we consider the k dependence in Eq. (3.57) by formulating the argument of the exponential function as a second-order polynomial in k explicitly according to

$$d^3 N \propto k^3 e^{-\Xi_{ijli'i'j'l'}^{\xi\eta\chi\xi'\eta'\chi'} k^2 + \omega_0 \Sigma_{ijli'i'j'l'}^{\xi\eta\chi\xi'\eta'\chi'} k}. \quad (3.59)$$

Here we have introduced the quantities

$$\Xi_{ijli'i'j'l'}^{\xi\eta\chi\xi'\eta'\chi'} \equiv \frac{1}{2} \left[\mathbf{K}_{2,ijl} \mathcal{M}_{ijl}^{-1} \mathbf{K}_{2,ijl} + \mathbf{K}_{2,i'j'l'} \mathcal{M}_{i'j'l'}^{-1} \mathbf{K}_{2,i'j'l'} + \frac{\tau_0^2}{8} (\tau_{ijl} + \tau_{i'j'l'}) \right] \quad (3.60)$$

and

$$\begin{aligned}
 \Sigma_{ijli'i'j'l'}^{\xi\eta\chi\xi'\eta'\chi'} &\equiv -\frac{1}{2} \left[\mathbf{K}_{1,ijl}^{\xi\eta\chi} \mathcal{M}_{ijl}^{-1} \mathbf{K}_{2,ijl} + \mathbf{K}_{2,ijl} \mathcal{M}_{ijl}^{-1} \mathbf{K}_{1,ijl}^{\xi\eta\chi} + \mathbf{K}_{1,i'j'l'}^{\xi'\eta'\chi'} \mathcal{M}_{i'j'l'}^{-1} \mathbf{K}_{2,i'j'l'} \right. \\
 &\quad \left. + \mathbf{K}_{2,i'j'l'} \mathcal{M}_{i'j'l'}^{-1} \mathbf{K}_{1,i'j'l'}^{\xi'\eta'\chi'} + \frac{\tau_0^2}{4} (\tau_{ijl} \ell_{ijl}^{\xi\eta\chi} + \tau_{i'j'l'} \ell_{i'j'l'}^{\xi'\eta'\chi'}) \right]. \quad (3.61)
 \end{aligned}$$

Besides the relative sizes of the laser parameters like τ_{ijl} or $\ell_{ijl}^{\xi\eta\chi}$ they also contain the absolute parameters τ_0 and w_0 , the latter being encoded within the inverse matrix \mathcal{M}_{ijl}^{-1} . Using this representation, the spectrum of the signal photon can be assigned to the corresponding channels (ijl) . The sum over all signs ξ, η, χ at fixed channels and solid angles (φ, ϑ) leads to the distribution of the differential photon number per emission frequency or energy k . Therefore,

an understanding of the channels leads to a deeper understanding of the emission frequency and microscopic processes in these effects of the nonlinearity of the quantum vacuum. Further comments follow in Sec. 3.2.5 on interpretation.

Next, we want to derive a solid angle resolved density $\rho_{(1);ijli'j'l'}(\varphi, \vartheta|\omega_i, \omega_f)$ from the differential signal-photon number d^3N with respect to the channels (ijl) and $(i'j'l')$. Eq. (3.22) shows the formal relation. According to this, an integration over the frequency of the signal photon is necessary. We can reduce the density to signal photons from a fixed frequency interval from ω_i to ω_f . To determine this we calculate the integral

$$\begin{aligned} \Gamma_{ijli'j'l'}^{\xi\zeta\chi\xi'\zeta'\chi'} \Big|_{\omega_i}^{\omega_f}(\varphi, \vartheta) &\equiv \int_{\omega_i}^{\omega_f} dk k^3 e^{-\Xi_{ijli'j'l'}^{\xi\eta\chi\xi'\eta'\chi'} k^2 + \omega_0 \Sigma_{ijli'j'l'}^{\xi\eta\chi\xi'\eta'\chi'} k} \\ &= e^{-\omega_i^2 \Xi + \omega_0 \omega_i \Sigma} \frac{4\Xi(1 + \omega_i^2 \Xi) + 2\omega_0 \omega_i \Xi \Sigma + \omega_i^2 \Sigma^2}{8\Xi^3} \\ &\quad - e^{-\omega_f^2 \Xi + \omega_0 \omega_f \Sigma} \frac{4\Xi(1 + \omega_f^2 \Xi) + 2\omega_0 \omega_f \Xi \Sigma + \omega_f^2 \Sigma^2}{8\Xi^3} \\ &\quad + \sqrt{\pi} \frac{\omega_0 \Sigma (6\Xi + \omega_0^2 \Sigma^2)}{16\Xi^{\frac{7}{2}}} e^{\frac{\omega_0^2 \Sigma^2}{4\Xi}} \\ &\quad \times \left(\operatorname{erf}\left(\frac{2\omega_f \Xi - \omega_0 \Sigma}{2\sqrt{\Xi}}\right) - \operatorname{erf}\left(\frac{2\omega_i \Xi - \omega_0 \Sigma}{2\sqrt{\Xi}}\right) \right), \end{aligned} \quad (3.62)$$

where the expression $\Gamma_{ijli'j'l'}^{\xi\zeta\chi\xi'\zeta'\chi'} \Big|_{\omega_i}^{\omega_f}(\varphi, \vartheta)$ is used in the following as abbreviation of the solution. In order to preserve a more compact notation, we omit the indices of $\Xi \equiv \Xi_{ijli'j'l'}^{\xi\eta\chi\xi'\eta'\chi'}$ and $\Sigma \equiv \Sigma_{ijli'j'l'}^{\xi\eta\chi\xi'\eta'\chi'}$ here and in the following. Since the integral is Gaussian with finite limits, the Gaussian error function erf is part of the solution. If we consider the frequency range $\omega_i = 0$ to $\omega_f = \infty$, we get

$$\Gamma_{ijli'j'l'}^{\xi\zeta\chi\xi'\zeta'\chi'} \equiv \Gamma_{ijli'j'l'}^{\xi\zeta\chi\xi'\zeta'\chi'} \Big|_0^\infty = \frac{4\Xi + \omega_0^2 \Sigma}{8\Xi^3} + \sqrt{\pi} \frac{\omega_0 \Sigma (6\Xi + \omega_0^2 \Sigma^2)}{16\Xi^{\frac{7}{2}}} e^{\frac{\omega_0^2 \Sigma^2}{4\Xi}} \left(1 + \operatorname{erf}\left(\frac{\omega_0 \Sigma}{2\sqrt{\Xi}}\right) \right). \quad (3.63)$$

If the spectrum indicates that there are no further contributions to the signal beyond a compact region $[\omega_i, \omega_f] \subset [0, \infty)$, then $\Gamma_{ijli'j'l'}^{\xi\zeta\chi\xi'\zeta'\chi'}$ can be used in general for the calculation.

The total signal-photon density after summation over all channels is

$$\begin{aligned} \rho_{(1)}(\varphi, \vartheta|\omega_i, \omega_f) &= \frac{e^2}{16\pi^4} \frac{m_e^4}{45^2} \left(\frac{e}{m_e^2} \right)^6 \frac{\pi \mathcal{E}_*^6 \tau_0^2}{128} \sum_{\substack{ijli'j'l' \\ i \leftrightarrow j, i' \leftrightarrow j'}} \left[\frac{A_i A_j A_l A_{i'} A_{j'} A_{l'}}{\sqrt{M_{ijl} M_{i'j'l'}}} \sqrt{\frac{\Gamma_{ijl} \Gamma_{i'j'l'}}{\Gamma_i \Gamma_j \Gamma_l \Gamma_{i'} \Gamma_{j'} \Gamma_{l'}}} \right. \\ &\quad \times \frac{g_{\beta;ijl}(\varphi, \vartheta) g_{\beta\phi;i'j'l'}(\varphi, \vartheta)}{\sqrt{\det \mathcal{M}_{ijl} \det \mathcal{M}_{i'j'l'}}} \sum_{\substack{\xi, \eta, \chi \in \mathcal{S} \\ \xi', \eta', \chi' \in \mathcal{S}}} \left(e^{-\frac{1}{2} \omega_0^2 \mathbf{K}_{1,ijl}^{\xi\eta\chi} \cdot \mathcal{M}_{ijl}^{-1} \mathbf{K}_{1,ijl}^{\xi\eta\chi}} \right. \\ &\quad \times e^{-\frac{1}{2} \omega_0^2 \mathbf{K}_{1,i'j'l'}^{\xi'\eta'\chi'} \cdot \mathcal{M}_{i'j'l'}^{-1} \mathbf{K}_{1,i'j'l'}^{\xi'\eta'\chi'} - \frac{\tau_0^2}{16} \omega_0^2 \left(\Gamma_{ijl} (\ell_{ijl}^{\xi\eta\chi})^2 + \Gamma_{i'j'l'} (\ell_{i'j'l'}^{\xi'\eta'\chi'})^2 \right)} \\ &\quad \left. \left. \times \Gamma_{ijli'j'l'}^{\xi\zeta\chi\xi'\zeta'\chi'} \Big|_{\omega_i}^{\omega_f}(\varphi, \vartheta) \right) \right]. \end{aligned} \quad (3.64)$$

3.2.5. Physical Interpretation of the Channels

Considering separate contributions of several driving laser pulses, the channels (ijl) appear in the VEP. By summing up all channels the total polarization-dependent signal amplitude $S_{(p),ijl}(\mathbf{k})$ can be determined. For a consideration of the differential signal-photon number d^3N or the angular resolved density $\rho_{(p)}(\varphi, \vartheta|\omega_i, \omega_f)$ the product of the summation over the channels is necessary.

Initially, we understood the signal-photon density only as the result after performing the multiple sums over all channels. In the following we want to elaborate whether also a signal-photon density for corresponding channels can be interpreted as a physical density, analogous to the signal photon amplitude. For this we first decompose the density into contributions of the channel combinations (ijl) and $(i'j'l')$,

$$\rho_{(p)}(\varphi, \vartheta|\omega_i, \omega_f) = \sum_{\substack{ijl \\ i'j'l'}} \rho_{(p);ijli'j'l'}(\varphi, \vartheta|\omega_i, \omega_f). \quad (3.65)$$

Here, we do not exploit the symmetry in i and j or i' and j' , i.e. we sum over the full sum $\sum_{\substack{ijl \\ i'j'l'}}$. In this representation $\rho_{(p);ijli'j'l'}(\varphi, \vartheta|\omega_i, \omega_f)$ can be understood as an element of a $(ijl) \times (i'j'l')$ -matrix. From Eq. 4 these elements result in

$$\begin{aligned} \rho_{(1);ijli'j'l'}(\varphi, \vartheta|\omega_i, \omega_f) &= \frac{e^2}{16\pi^4} \frac{m_e^4}{45^2} \left(\frac{e}{m_e^2} \right)^6 \frac{\pi \mathcal{E}_*^6 \tau_0^2}{512} \frac{A_i A_j A_l A_{i'} A_{j'} A_{l'}}{\sqrt{M_{ijl} M_{i'j'l'}}} \sqrt{\frac{\mathcal{T}_{ijl} \mathcal{T}_{i'j'l'}}{\mathcal{T}_i \mathcal{T}_j \mathcal{T}_l \mathcal{T}_{i'} \mathcal{T}_{j'} \mathcal{T}_{l'}}} \\ &\times \frac{g_{\beta;ijl}(\varphi, \vartheta) g_{\beta\phi;i'j'l'}(\varphi, \vartheta)}{\sqrt{\det \mathcal{M}_{ijl} \det \mathcal{M}_{i'j'l'}}} \\ &\times \sum_{\substack{\xi, \eta, \chi \in \mathcal{S} \\ \xi', \eta', \chi' \in \mathcal{S}}} \left(e^{-\frac{1}{2} \omega_0^2 \left(\mathbf{K}_{1,ijl}^{\xi\eta\chi} \cdot \mathcal{M}_{ijl}^{-1} \mathbf{K}_{1,ijl}^{\xi\eta\chi} + \mathbf{K}_{1,i'j'l'}^{\xi'\eta'\chi'} \cdot \mathcal{M}_{i'j'l'}^{-1} \mathbf{K}_{1,i'j'l'}^{\xi'\eta'\chi'} \right)} \right. \\ &\quad \left. \times e^{-\frac{\tau_0^2}{16} \omega_0^2 \left(\mathcal{T}_{ijl} (\ell_{ijl}^{\xi\eta\chi})^2 + \mathcal{T}_{i'j'l'} (\ell_{i'j'l'}^{\xi'\eta'\chi'})^2 \right)} \Gamma_{ijli'j'l'}^{\xi\zeta\chi\xi'\zeta'\chi'} \Big|_{\omega_i}^{\omega_f}(\varphi, \vartheta) \right) \end{aligned} \quad (3.66)$$

with respect to the polarization $p = 1$.

The diagonal elements $(ijl) = (i'j'l')$ are all nonnegative, since all contributions except $g_{\beta;ijl}(\varphi, \vartheta)$ are nonnegative and the diagonal elements are each proportional to the term $g_{\beta;ijl}^2(\varphi, \vartheta) \geq 0$. This statement does not hold for off-diagonal elements; as $g_{\beta;ijl}(\varphi, \vartheta) < 0$ is possible, contributions with $g_{\beta;ijl}(\varphi, \vartheta) g_{\beta\phi;i'j'l'}(\varphi, \vartheta) < 0$ may occur. Consequently, these channel contributions cannot be understood as a pure physical density, since densities are always nonnegative. Further these considerations show that the interference terms, i.e. the off-diagonal terms $(ijl) \neq (i'j'l')$, of the signal-photon density can have a non-negligible influence on the physical density.

Microscopic Interpretation

Let us trace the microscopic origin of the signal photon emission. For this we consider the spectrum which results from the differential particle number d^3N , see Eq. (3.57). Apart from the global prefactor k^3 , this consists of sums of Gaussian functions, as already shown in Eq. (3.59). Here we sum over all sign combinations $\xi, \eta, \chi, \xi', \eta',$ and χ' and channel combinations (ijl) and $(i'j'l')$.

In what follows, we use assumption $\tau_i \gg \omega_i$ consequently also $\tau_0 \gg \omega_0$. This may be in conflict with the assumption $\tau_i \ll \zeta_{R,ji} = \frac{1}{2}w_{0,ji}^2\omega_0$ for the IRRA; this problem can be avoided by demanding that the IRRA is ensured by the geometrical properties $\frac{w_{0,ji}}{\zeta_{R,ml}} \ll |\sin \theta_{il}|$ of the optical laser pulses i and l with the selected semi-axis j and m , respectively, see Eq. (2.51). Furthermore, in the following we want to neglect the terms proportional to \mathcal{M}_{ijl}^{-1} , since we are interested here in the qualitative behavior of the spectrum. Their contributions change the argument of the exponential function only quantitatively for fixed solid angles (φ, ϑ) . In a quantitative analysis, as we discuss in Sec. 4.2, these contributions are taken into account again. In addition, let the pulse durations of all involved laser pulses be identical, i.e. $\tau_i = \tau_0$ and $T_i = 1$, respectively, and consequently $\mathsf{T}_{ijl} = \frac{1}{3}$.

The remaining contribution to the spectrum for fixed channels (ijl) and $(i'j'l')$ is the sum

$$d^3N \propto k^3 \sum_{\substack{\xi, \eta, \chi \in \mathcal{S} \\ \xi', \eta', \chi' \in \mathcal{S}}} e^{-\frac{\tau_0^2}{3 \times 16} [k + \omega_0 \ell_{ijl}^{\xi\eta\chi}]^2} \times e^{-\frac{\tau_0^2}{3 \times 16} [k + \omega_0 \ell_{i'j'l'}^{\xi'\eta'\chi'}]^2}. \quad (3.67)$$

If we consider a fixed choice of signs, we observe that they only give a contribution if $\ell_{ijl}^{\xi\eta\chi} \approx \ell_{i'j'l'}^{\xi'\eta'\chi'}$ is valid. This can be explained by the fact that $\omega_0\tau \gg 1$, or equivalently $1/\tau \ll \omega_0$, which holds for optical pulses. The spectral width of these Gaussian peaks generated by $\exp\left(-\frac{\tau_0^2}{3 \times 16} [k + \omega_0 \ell_{ijl}^{\xi\eta\chi}]^2\right)$ is much smaller than the spectral separation to the second Gaussian peak $\exp\left(-\frac{\tau_0^2}{3 \times 16} [k + \omega_0 \ell_{i'j'l'}^{\xi'\eta'\chi'}]^2\right)$ with different maximum position encoded by $\ell_{ijl}^{\xi\eta\chi}$ or $\ell_{i'j'l'}^{\xi'\eta'\chi'}$, respectively. Therefore the product of these functions is again Gaussian, but the maximum is strongly suppressed compared to contributions where $\ell_{ijl}^{\xi\eta\chi} \approx \ell_{i'j'l'}^{\xi'\eta'\chi'}$ is satisfied. The proportionality of the spectrum is consequently

$$d^3N \propto k^3 \sum_{\substack{\xi, \eta, \chi \in \mathcal{S} \\ \xi', \eta', \chi' \in \mathcal{S}}} e^{-\frac{2\tau_0^2}{3 \times 16} [k + \omega_0 \ell_{ijl}^{\xi\eta\chi}]^2}. \quad (3.68)$$

With this Gaussian distribution we can define a spectral width $\sigma = \frac{2\sqrt{3}}{\tau_0}$. It determines the possibility of contributions with different channels and signs. In the following we will establish a transition rule, whether two channels provide a contribution, by using limit considerations.

We focus on the channel with fixed (ijl) but unspecified ξ, η, χ , in order to identify the signal photon frequency associated with this channel. Considering the formal limit of $\tau \rightarrow \infty$ corresponding to the collision of monochromatic optical laser beams the temporal integration in \mathcal{I}_{ijl} , cf. Sec. 3.2.3, results in a delta function ensuring the signal photon energy k to be

fully determined by the oscillation frequencies $\omega_i = \nu_i \omega_0$ of the driving laser beams, see [164]. Therefore we obtain

$$k = \omega_0 |\pm \nu_i \pm \nu_j \pm \nu_l|, \quad (3.69)$$

where each sign can occur separately. Microscopically, a positive sign indicates the emission of a photon of the corresponding driving laser beam, whereas a negative sign represents the absorption of the photon. For example, if we consider a channel with the involved laser beam frequencies $\omega_1 = \omega_0$, $\omega_2 = 3\omega_0$, and $\omega_3 = 5\omega_0$ then $k = \omega_0$, $k = 3\omega_0$, $k = 7\omega_0$, and $k = 9\omega_0$ result as possible frequencies of the signal. In general, for a fixed channel maximum four different signal frequencies connected with the signal amplitude are possible; if all oscillation frequencies are equal only ω_0 and $3\omega_0$ remains. We emphasize that both factors $S_{(p);ijl}$ and $S_{(p);i'j'l'}^*$ in Eq. (3.66) must support the same frequency to obtain an appreciable contribution from signal photons at a given frequency.

In collision experiments with laser pulses, the pulse durations are finite τ_i and the selection rules in Eq. (3.69) hold only approximately. However, this approximation is adequate as long as the propagation directions of the driving beams differ sufficiently and $\tau\omega_0 \gg 1$. Moreover, the delta peaks in the limit $\tau \rightarrow \infty$ resulting from the temporal integration in \mathcal{I}_{ijl} have to be replaced by Gaussian peaks including a finite spectral width scaling $\sim \tau_0^{-1}$, as shown before.

In addition, if we consider constellations where the scale of the change of the scalar product between the directed mean of the intensity profiles and the optical axis of all other beams is significantly larger than the wavelength of corresponding beams, then the wave vector of the signal can be approximated by the wave vectors of the driving lasers. This is the plane-wave limit and it delivers

$$\mathbf{k} \approx \mathbf{k}_{\text{PW}} = \pm \mathbf{k}_i \pm \mathbf{k}_j \pm \mathbf{k}_l, \quad (3.70)$$

which is formally performed by $\{\tau_i, w_{0,ji}\} \rightarrow \infty$ and it neglects focussing effects. Again, each sign can occur separately, depending on the microscopic emission and absorption processes given by the signs ξ , η , and χ .

From the limit considerations, the selection rule follows whether the combination of two channels (ijl) and $(i'j'l')$ contributes to the signature of the quantum vacuum. By blurring the limits, also the selection rule becomes fuzzy. A possibility to estimate whether a combination of signs leads to a contribution is the comparison of the modulus of the wave vector of the signal in the plane-wave limit $|\mathbf{k}_{\text{PW}}|$ with the signal frequency k from (3.69) under consideration of the spectral width σ . If

$$|\mathbf{k}_{\text{PW}}| \in [\omega_S - \Delta\omega, \omega_S + \Delta\omega] \quad (3.71)$$

with $\omega_S = \omega_0 |\pm \nu_i \pm \nu_j \pm \nu_l|$ holds, where $\Delta\omega = 4\sqrt{\ln 100} \sigma$ is the σ associated full peak-width measured at 1% of the peak maximum, then a polarization insensitive signal $\rho(\varphi_S, \vartheta_S | \omega_S - \Delta\omega, \omega_S + \Delta\omega)$ is detectable. Here the angles (φ_S, ϑ_S) are determined by the normalized wave vector $\hat{\mathbf{k}}_{\text{PW}}$, or are in its immediate vicinity; the signal points in the direction of \mathbf{k}_{PW} . This signal is associated with the channels used to estimate \mathbf{k}_{PW} and ω_S , therefore it can be interpreted as the absorption-emission process of the photons of the corresponding channels.

Nevertheless, most variants of $\rho_{(p);ijl'i'j'l'}(\varphi, \vartheta|\omega_i, \omega_f)$ are suppressed.

At this point, it should be pointed out once again that the properties derived here are based on various assumptions. For example, we have neglected the contributions proportional to \mathcal{M}_{ijl}^{-1} on the spectrum. A numerically comprehensive analysis requires the consideration of these contributions. In Ch. 4 we consider two example scenarios for the detection of the signature of quantum vacuum nonlinearities. Among them is an experiment in Sec. 4.2, where we apply these selection rules using finite pulse durations and beams waists and taking into account the full contribution in d^3N , see (3.57). Thereby these full results confirm the selection rule estimated here.

Proto-physical Channels

We have shown that only $\rho(\varphi, \vartheta|\omega_i, \omega_f)$ is a physical density and not its single contributions given by $\rho_{ijl'i'j'l'}(\varphi, \vartheta|\omega_i, \omega_f)$. Furthermore, we have found constraints for sizable contributions $\rho_{(p);ijl'i'j'l'}(\varphi, \vartheta|\omega_i, \omega_f)$ deduced by the signal photon amplitudes $S_{(p);ijl}$ and $S_{(p);i'j'l'}^*$ related to the channels (ijl) and $(i'j'l')$. These contributions give rise to special properties of the signal such as oscillation frequency or direction. Consequently, the question arises if there is a set of channel contributions $\{(ijl), (i'j'l')\}$ leading to a *proto-physical* density. Affirming this question implies that the total density $\rho(\varphi, \vartheta|\omega_i, \omega_f)$ separates into all proto-physical densities $\rho_{\{ijl\}}(\varphi, \vartheta|\omega_i, \omega_f)$,

$$\rho(\varphi, \vartheta|\omega_i, \omega_f) = \sum_{\{ijl\} \in \text{proto-physical}} \rho_{\{ijl\}}(\varphi, \vartheta|\omega_i, \omega_f), \quad (3.72)$$

where all other contributions beyond the proto-physical channel combinations are negligible.

One way to illustrate the existence of these proto-physical channels is to consider a two-beam collision scenario, as we analyze it accurately in Sec. 4.1. In this case, the channel indices are $i, j, l \in \{1, 2\}$. Consequently, only (121), (211), (122), (212) are contributing channels for the signal photon amplitude since for $i = j$ the geometrical function vanishes, $g_{(p);11l} = g_{(p);22l} = 0$. The direction of the signal can be estimated by \mathbf{k}_{PW} , see Eq. (3.70), in the plane-wave limit. We observe that the signals point mainly in the direction of the driving laser pulses, i.e. $\hat{\mathbf{k}} \approx \hat{\mathbf{k}}_1$ or $\hat{\mathbf{k}} \approx \hat{\mathbf{k}}_2$. The references [101, 155, 220, 221] demonstrate this for the collision of two pulses. However, the angle-dependent decay of the signal varies compared to the angle-dependent decay of the background of the driving laser pulses; this is part of the analysis in Sec. 4.1.

Restricting to the signal pointing in the direction of $\hat{\mathbf{k}}_1$ and using Eq. (3.70), it follows that only channels with two contributions of pulse 2 and only one contribution of pulse 1, i.e. (212) and (122), can provide the wave vector $\hat{\mathbf{k}}_{PW} \approx \hat{\mathbf{k}}_1$ in the plane-wave limit. Moreover, this behavior can be explained by microscopic absorption and emission of photons belonging to pulse 2, which we call in this situation *pump* pulse, beam or field. The pump field stimulates the quantum vacuum and the *probe* field, as we call the pulse pointing in the direction of observation, interrogates it.

Assuming sufficiently separated propagation directions of the two colliding high-intensity

laser pulses, the physical signal-photon density for appropriate solid angles (φ_S, ϑ_S) related to the vicinity of the $\hat{\mathbf{k}}_1$ direction yields

$$\begin{aligned}\rho(\varphi_S, \vartheta_S | \omega_i, \omega_f) &= \rho_{212212}(\varphi_S, \vartheta_S | \omega_i, \omega_f) + \rho_{212122}(\varphi_S, \vartheta_S | \omega_i, \omega_f) \\ &\quad + \rho_{122212}(\varphi_S, \vartheta_S | \omega_i, \omega_f) + \rho_{122122}(\varphi_S, \vartheta_S | \omega_i, \omega_f) \\ &= 4\rho_{212212}(\varphi_S, \vartheta_S | \omega_i, \omega_f) \\ &\equiv \rho_{\{212\}}(\varphi_S, \vartheta_S | \omega_i, \omega_f) .\end{aligned}\tag{3.73}$$

The combination $\{212\}$ indicates the use of all permutations $\{(212), (121)\}$ for (ijl) and $(i'j'l')$. Eq. (3.73) shows that obviously a proto-physical density can be an actual physical density in a restricted solid angle region. In other words, the equality in Eq. (3.73) ensures that the observed signal in the corresponding region and frequency domain is originated by the physics behind the respective channels. Furthermore, the proto-physical channels $\{212\}$ explain the microscopic processes for the measured signal. This perception can be utilized to enhance signal contributions with requested special properties like oscillation frequency or propagation direction.

Analogously, the proto-physical channel $\{121\}$ leads to the signal in the vicinity of $\hat{\mathbf{k}}_2$. Additionally, the interference terms of mixing channels, e.g. $(ijl) = (121)$ and $(i'j'l') = (212)$ are comparatively small and can be neglected.

In general we characterize proto-physical channel combinations by $\{i''j''l''\}$ which implies $(ijl) \in \text{permut}(\{i'', j'', l''\})$ and $(i'j'l') \in \text{permut}(\{i'', j'', l''\})$, where $\text{permut}(A)$ gives all permutations of the ordered set A . Considering the collision of n different laser pulses, we count $\frac{1}{6}(n-1)(4n+n^2)$ different proto-physical channels $\{ijl\}$. For example, $n = 2$ leads to the two independent proto-physical channels $\{121\}$ and $\{212\}$, while for $n = 3$ we already count seven different proto-physical channels.

Limits of the Channel Analysis

The channel analysis provides an overview of the microscopic processes involved in multi-laser interactions. In particular, in scenarios where more than two high-intensity laser pulses collide with each other, the determination of the signal photons becomes much more challenging. By studying the channels discussed here, a deeper understanding of microscopic processes is achieved. In addition, the entire signal can be divided in its properties such as frequency or direction and traced back to corresponding channels. Another advantage of the channel analysis is that it has no upper threshold of laser pulses involved. This distinguishes it from similar approaches that are limited to three laser pulses, cf. [102, 122]. Although the channel analysis has these advantages, it is restricted by the underlying assumptions.

First of all, in the VEP, see Sec. 3.1, we only considered single signal photon processes and neglected all higher-order terms of f^2 . Furthermore, in Eq. (3.17) we used the weak-field expansion. Nevertheless, the derivation in Sec. 3.1 reveals how to extend the signal photon amplitude for higher order contributions. For the state-of-the-art high-intensity laser pulses, however, the used field approximations are sufficient.

With the choice of the electromagnetic field profile in Eq. (3.24), we developed the channel analysis for Gaussian fields in the IRRA. Consequently, the deduced results are valid for pulses of this shape. Still, it is possible to conceive a channel analysis for laser pulses of arbitrary profile, e.g. TEM_{xy} modes beyond the TEM₀₀ mode or flat top beams. In Sec. 3.1 it has been shown that the signal amplitude for a fixed channel (ijl) is proportional to the product of the Fourier integral $\mathcal{I}_{ijl}(\mathbf{k})$ with the geometric function $g_{\beta;ijl}(\varphi, \vartheta)$,

$$S_{(p);ijl}(\mathbf{k}) \propto \mathcal{I}_{ijl}(\mathbf{k}) g_{\beta;ijl}(\varphi, \vartheta). \quad (3.74)$$

It should be emphasized here that the geometric function depends exclusively on the geometry of the driving lasers and the observed signal. The Fourier integral is determined by the field amplitudes of the corresponding three laser fields of the channel. For arbitrary choice of field profiles $\mathcal{E}_i(x)$ the Fourier integral $\mathcal{I}_{ijl}(\mathbf{k})$ can be estimated by performing the Fourier transformation over $\mathcal{E}_i(x) \mathcal{E}_j(x) \mathcal{E}_l(x)$ numerically. This gives rise to extensions beyond Gaussian pulses. However, the geometric function $g_{\beta;ijl}(\varphi, \vartheta)$ is not influenced by the profiles and still provides constraints for channel constellations like the forbidden channel $i = j$.

Further limitations are given by the IRRA which is satisfied for short-pulse frequencies compared to the Rayleigh range, $\tau_i \ll \zeta_{R,ji}$ with $j = 1$ and $j = 2$, or geometrical restrictions $\frac{w_{0,ji}}{\zeta_{R,ml}} \ll |\sin \theta_{il}|$ with θ_{il} , where the angle included by the two pulses i and l . Here, due to the elliptic cross section of the driving laser beams in the focus spot, we have to consider Rayleigh ranges for each focus waist $w_{0,1i}$ and $w_{0,2i}$, i.e. $\zeta_{R,ji} = \frac{\pi w_{0,ji}^2}{\lambda} = \frac{1}{2} w_{0,ji}^2 \omega_i$. The assumptions $\tau_i \ll \zeta_{R,ij}$ with $j = 1$ and $j = 2$ stand in conflict with the assumption $\tau_0 \gg \omega_0$ which we used to deduce a microscopic interpretation. In addition, the laser pulses provided by modern facilities contain several cycles, cf. Sec. 2.2.2 and Tab. 2.1.

Furthermore, we have used the plane-wave limit $w_{0,ji} \rightarrow \infty$ to obtain information about the momentum transfer from the driving laser pulses to the signal, see (3.70). For laboratory scenarios, this limit is certainly not applicable. However, even if the plane-wave limit is not suitable for calculations, the direction of the signal is determined in the full physical signal-photon density $\rho(\varphi, \vartheta | \omega_i, \omega_f)$ for the signal in the frequency domain $\omega_i \leq k \leq \omega_f$. In our approach, this density is calculated analytically. Moreover, using the proto-physical density $\rho_{\{ijl\}}(\varphi, \vartheta | \omega_i, \omega_f)$, information about direction and frequency is available without using the plane-wave limit. Therefore, the plane-wave limit is useful to understand the microscopic processes and to estimate the relevant channels for the signal photon emission, but it is not necessary to achieve results since a numerical determination does not use it.

4.

Discernible Signal of QED Vacuum in Exemplary Scenarios

*“Dass ich erkenne, was die Welt
Im Innersten zusammenhält.”*

— Johann Wolfgang von Goethe, *Faust* [222]

Having deepened our understanding of the signature of the nonlinearity of the QED vacuum from Ch. 2 and Ch. 3, in the present chapter we apply that knowledge to conceptualize experiments that may provide the detection of signals mediated by the quantum vacuum that has been missing so far. Previous experiments, such as PVLAS, mostly used constant fields making long path lengths possible, such as cavities in strong magnetic fields [107, 116, 216]. Here we will focus on experimental setups with optical laser pulses, as illustrated in Sec. 2.2.1 and Sec. 3.2. Laser pulses, in particular with a Gaussian profile, allow well-controlled parameters of the signal. The channel analysis has shown how the frequency and direction of the signal can be predicted from the characteristics of the driving lasers. This method allows a fundamentally new approach to design collision geometries with detectable signal.

The main difficulty in the detection of signal photons encoding the physics of nonlinearity of the quantum vacuum is to distinguish them from enormous background of the driving lasers. However, by the aforementioned control of the signal, it is possible to measure results of quantum vacuum physics beyond the background. Admittedly, the yield of measurable signal photons is significantly lower than the total numbers of emitted photons, but it is still sufficiently large such that currently available detectors can register [148].

To detect the signal beyond the background it is necessary to describe the background quantitatively in the far field where the signal photons are detected. Analogously to the signal photon number $N_{(p)}(\mathcal{A}|\omega_i, \omega_f)$ and density $\rho_{(p)}(\varphi, \vartheta|\omega_i, \omega_f)$, cf. Eq. (3.23) and Eq. (3.22), we count the number of background photons $\mathcal{N}_i(\mathcal{A})$ of the i th driving laser pulse in the solid angle region \mathcal{A} by

$$\mathcal{N}_i(\mathcal{A}) = \int_{\mathcal{A}} d\Omega \varrho_i(\varphi, \vartheta) , \quad (4.1)$$

where $\varrho_i(\varphi, \vartheta)$ is the solid angle resolved density of the corresponding driven laser photons in the far field. Compared to the signal of emitted photons in the VEP, $\varrho_i(\varphi, \vartheta)$ and $\mathcal{N}_i(\mathcal{A})$ are not given with specified polarization and spectral width of related photons. Since we assume linearly polarized driving laser pulses with their spectral distribution assembled around

the oscillation frequency ω_i without further consideration of the spectral width, information about polarization and spectrum of the background is already preserved with reference to the i th laser pulse in $\mathcal{N}_i(\mathcal{A})$. Nevertheless, for polarization-sensitive measurements the specification of the purity \mathcal{P} of the polarization of the driving pulse is essential to characterize the background of photons with corresponding polarization.

The total number of photons $\mathcal{N}_i(4\pi)$ of a driving laser pulse can be estimated via the pulse energy W_i and oscillation frequency ω_i , $\mathcal{N}_i(4\pi) = \frac{W_i}{\omega_i}$, as already described in Sec. 2.2.2. Here $\mathcal{A} = 4\pi$ indicates the full solid angle. Furthermore, the sum of the numbers of all pulses results in the total number of laser photons, $\mathcal{N}^{\text{tot}} = \sum_i \mathcal{N}_i(4\pi)$.

Now the solid angle resolved distribution of the background photons of the i th laser pulse in the far field is to be estimated. Since the solid angles (φ, ϑ) were chosen for the signal with wave vector \mathbf{k} , they are not necessarily suitable for the description of the i th laser. Therefore we use here the solid angles $(\phi_i(\varphi, \vartheta), \theta_i(\varphi, \vartheta))$; these come from the coordinate system in spherical coordinates, where the space vector $\mathbf{r}|_{\theta_i=0}$ points in the propagation direction of the laser pulse, thus collinear with the optical axis. In the following steps the specification of the dependence on the angles φ and ϑ , i.e. $\phi_i \equiv \phi_i(\varphi, \vartheta)$ and $\theta_i \equiv \theta_i(\varphi, \vartheta)$ is not needed. A parameterization of these angles requires a geometry of laser propagation. Later in this chapter we introduce two collision geometries in Sec. 4.1 and Sec. 4.2 including the parameterizations based on these examples.

Because of the Gaussian structure of the beams we also deduce a Gaussian distribution in the far field, so that we choose the ansatz

$$\varrho_i(\phi_i, \theta_i) = \tilde{\mathcal{N}}_i e^{-\frac{\theta_i^2 \cos^2 \phi_i}{2\sigma_{1i}^2} - \frac{\theta_i^2 \sin^2 \phi_i}{2\sigma_{2i}^2}} \quad (4.2)$$

for the background photon density with normalization $\tilde{\mathcal{N}}_i$. Here we assume beams with elliptical cross section, where the parametrization ϕ_i is chosen such that in the near field along $\phi_i = 0$ the semi-axis is described with the focus waist $w_{0,1i}$. Consequently $\phi_i = \frac{\pi}{2}$ points to the other semi-axis with $w_{0,2i}$. Furthermore, σ_{1i} and σ_{2i} describe the variance of the Gaussian distribution in the far field in the directions of the corresponding semi-axes as function of Θ_{ij} . With the opening angles $\Theta_{ji} = 2\frac{w_{0,ji}}{\zeta_{R,ji}} = \frac{4}{w_{0,ji}\omega_i}$ in the far field, cf. Eq. (2.44), these variances can be determined from $\varrho_i\left(0, \frac{1}{2}\Theta_{1i}\right) = \tilde{\mathcal{N}}_i e^{-2}$ and $\varrho_i\left(\frac{\pi}{2}, \frac{1}{2}\Theta_{2i}\right) = \tilde{\mathcal{N}}_i e^{-2}$ to $\sigma_{1i} = \frac{1}{w_{0,1i}\omega_i}$ and $\sigma_{2i} = \frac{1}{w_{0,2i}\omega_i}$, respectively, cf. [179].

Following the ansatz Eq. (4.2) together with $\mathcal{N}_i(4\pi) = \frac{W_i}{\omega_i}$ we determine the normalization $\tilde{\mathcal{N}}_i$. Therefore we solve the integral

$$\frac{W_i}{\omega_i} = \int_{4\pi} d\Omega \tilde{\mathcal{N}}_i e^{-\frac{1}{2}\theta_i^2 \omega_i^2 (w_{0,1i}^2 \cos^2 \phi_i + w_{0,2i}^2 \sin^2 \phi_i)}. \quad (4.3)$$

Using the solid angles (ϕ_i, θ_i) and the identities $\sin^2 \phi_i = 1 - \cos^2 \phi_i$ and $\cos^2 \phi_i = \frac{1}{2}(1 + \cos 2\phi_i)$,

$$\frac{W_i}{\omega_i} = \int_0^\pi d\theta_i \sin \theta_i \tilde{\mathcal{N}}_i e^{-\frac{1}{2}\theta_i^2 \omega_i^2 \frac{w_{0,1i}^2 + w_{0,2i}^2}{2}} \int_0^{2\pi} d\phi_i e^{-\frac{1}{2}\theta_i^2 \omega_i^2 \frac{w_{0,1i}^2 - w_{0,2i}^2}{2} \cos 2\phi_i} \quad (4.4)$$

follows. Next, we substitute $\psi_i = 2\phi_i$ and, applying the symmetry property $\int_0^{4\pi} d\psi_i e^{\cos \psi_i} = 4 \int_0^\pi d\psi_i e^{\cos \psi_i}$, we obtain the integrals

$$\frac{W_i}{\omega_i} = \int_0^\pi d\theta_i \sin \theta_i \tilde{N}_i e^{-\frac{1}{2}\theta_i^2 \omega_i^2 \frac{w_{0,1i}^2 + w_{0,2i}^2}{2}} 2\pi \frac{1}{\pi} \int_0^\pi d\psi_i e^{-\frac{1}{2}\theta_i^2 \omega_i^2 \frac{w_{0,1i}^2 - w_{0,2i}^2}{2} \cos \psi_i}, \quad (4.5)$$

where we introduced the factor $\frac{\pi}{\pi}$ to identify the modified Bessel function $I_0(z) = \frac{1}{\pi} \int_0^\pi d\psi e^{z \cos \psi}$ [223]. With $a_{+,i} \equiv \frac{1}{2}\omega_i^2 \frac{w_{0,1i}^2 + w_{0,2i}^2}{2}$ and $a_{-,i} \equiv \frac{1}{2}\omega_i^2 \frac{w_{0,1i}^2 - w_{0,2i}^2}{2}$, where obviously $a_{+,i} > a_{-,i}$, we get

$$\frac{W_i}{\omega_i} = 2\pi \int_0^\pi d\theta_i \sin \theta_i \tilde{N}_i e^{-a_{+,i}\theta_i^2} I_0(a_{-,i}\theta_i^2). \quad (4.6)$$

To solve the θ_i integral we first resubstitute the modified Bessel function again. Furthermore we approximate $\sin \theta_i \approx \theta_i$ for small angles, this is ensured by the fact that θ_i is parameterized in such a way that the distribution $\varrho_i(\theta_i, \phi_i = \text{const.})$ is maximal at $\theta_i = 0$. At the same time the distribution decreases sufficiently fast towards zero with increasing θ_i that we can formally extend the upper integration limit $\theta_i \rightarrow \infty$,

$$\begin{aligned} \frac{W_i}{\omega_i} &\approx 2 \int_0^\pi d\psi_i \int_0^\infty d\theta_i \theta_i \tilde{N}_i e^{-(a_{+,i} + a_{-,i} \cos \psi) \theta_i^2} \\ &= \frac{1}{a_{+,i}} \int_0^\pi d\psi_i \frac{\tilde{N}_i}{1 - a_{-,i}/a_{+,i}} \cos \psi_i \\ &= \frac{\pi}{\sqrt{a_{+,i}^2 - a_{-,i}^2}} \tilde{N}_i. \end{aligned} \quad (4.7)$$

Here, the Gauss integral was solved first. The remaining integral over ψ_i can be performed with the help of the identity $\int_0^\pi d\psi \frac{1}{1+c \cos \psi} = \frac{\pi}{\sqrt{1-c^2}}$ [224]. With the resubstitution of $a_{+,i}$ and $a_{-,i}$ we solve Eq. (4.7) for \tilde{N}_i and get

$$\tilde{N}_i = \frac{w_{0,1i} w_{0,2i} \omega_i}{2\pi} W_i = \mu_{1i} \mu_{2i} \nu_i A_i^2 \mathcal{N}_\star, \quad (4.8)$$

where in the last step the normalization was expressed in relative laser parameters, see Sec. 3.2.1. Thereby we use

$$\mathcal{N}_\star = \frac{w_{0,1i}^2 \omega_i^2}{2\pi} W_0. \quad (4.9)$$

Using this normalization, we can describe the angularly resolved density of background photons for any driving laser by

$$\varrho_i(\varphi, \vartheta) = \mu_{1i} \mu_{2i} \nu_i A_i^2 \mathcal{N}_\star e^{-\frac{1}{2}\nu_i^2 \omega_0^2 w_0^2 \theta_i^2(\varphi, \vartheta) (\mu_{1i}^2 \cos^2 \phi_i(\varphi, \vartheta) + \mu_{2i}^2 \sin^2 \phi_i(\varphi, \vartheta))}. \quad (4.10)$$

The general description allows us to determine the background in arbitrary scenarios with Gaussian beams. If we consider the angularly resolved density of background photons of all driving lasers we write $\varrho(\varphi, \vartheta) = \sum_i^n \varrho_i(\varphi, \vartheta)$. In addition, the corresponding number of all background photons in the solid angle region \mathcal{A} is $\mathcal{N}_i(\mathcal{A}) = \sum_i^n \mathcal{N}(\mathcal{A})$, cf Eq. (4.1).

For completeness, however, it should be noted that the difficulty of an absolutely background-free measurement in a real experimental setup involves more than just the background of the forward direction of the driving lasers. Beside the photons of the driving laser fields, there are also indirect photons by scattering effects present in the vacuum chamber. Any practical imperfection such as a non-ideal vacuum in the vacuum chamber coming along with residual atoms and molecules in the interaction region may give rise to higher-harmonic backgrounds. Such scattering can take place at the walls and optical apertures, such as mirrors. Furthermore (relativistic) Thomson and (relativistic) Rayleigh scattering by residual gas ions and their electrons can occur [225]. The full quantitative incorporation of such effects is outside the scope of the present idealized analysis. Still, these backgrounds can, in principle, be monitored (e.g. by rest-gas measurements, or geometric adjustments) and thus parametrically controlled to a large degree. The study [149] deals in detail with a strong field setup of a PW laser pulse and how this background can be reduced.

In this chapter, two experimental scenarios are discussed. The presented concept and results are mainly content of the reference [160, 162, 164]. First, in Sec. 4.1 we consider the collision of two Gaussian pulses. Some previous work has already investigated this setup [221]. Among other things, the references [155, 165] studied the influence of the relative shift of the laser foci. Furthermore, the focus here lies on the discernibility of the signal from the background. The use of different beam waist sizes with both kind of cross sections, circular and elliptical, is the key to obtain a measurable signal [162]. Moreover, we deduce the predicted signal with respect to the background of the driving laser pulses and calculate the regions of signal photon emissions discernible from the background.

In the second part of this chapter, Sec. 4.2, the results of the channel analysis are applied to an experimental scenario. Here the main idea was elaborated in the publication [160], while the reference [164] contains a more comprehensive study of the relationship between the predicted signal and the channel analysis. Contrary to the considerations in Sec. 4.1, the collision of multiple laser pulses of different oscillation frequencies and propagation directions is considered in Sec. 4.2. More specifically, we consider an example scenario involving the collision of four laser pulses in fixed geometry, which is described in Sec. 4.2.1. All pulses are originated from a single laser pulse, while we use beam splitting and sum-difference frequency generation techniques to obtain different oscillation frequencies. We focus on the signal emitted in directions outside the forward cones of the driving lasers. At the end, we discuss the results from the perspective of channel analysis. This is achieved in particular by distinguishing between so-called *elastic* and *inelastic* channels.

4.1. Signature of QED Vacuum Nonlinearities in a Two-Beam Collision

In a first exemplary scenario, we study the perspectives of inducing a discernible quantum vacuum signal in a two beam pump-probe setup with optical ultrashort PW laser pulses. We focus on the determination of the detectable signal and an optimization of laser parameters of

the pump and probe beam. The key parameter to enhance the signal is the choice of optimal beam waists.

In Sec. 4.1.1 we introduce the experimental scenario, based on the parameters available at state-of-the-art strong laser facilities. Further, we will fix the collision geometry. Then, in Sec. 4.1.2, we define the discernible signal and present a numerical method for determining the solid angle region of the discernible signal for the selected collision geometry. In Sec. 4.1.3 this is followed by an analysis of the effects of different focusing on the polarization insensitive yield at different collision angles between the pump and probe beams. First, we consider a probe beam with circular cross section followed by calculations with a probe beam with elliptical cross section. Finally, in Sec. 4.1.4, we discuss the effect of vacuum birefringence based on the analyzed geometries.

This section is strongly oriented along our results published in [162] and explicitly reproduces its contents.

4.1.1. Collision Geometry and Pulse Properties

For our investigations we use high-intensity laser pulses in the all-optical regime. Here, we consider two pulses with almost identical properties and we refer to one laser as the probe field, labeled by subscript 1, and the other as the pump field, labeled by the subscript 2. Both have the pulse energy $W_1 = W_2 = W_0 = 25 \text{ J}$ and duration $\tau_1 = \tau_2 = \tau_0 = 42.4 \text{ fs}$. However, to compare to experiments, this pulse duration is $\tau = 25 \text{ fs}$ measured at FWHM of the intensity, see Sec. 2.2.1 and Sec. 2.2.2. As oscillation frequency and thus photon energy of the laser we choose $\omega_1 = \omega_2 = \omega_0 = 1.55 \text{ eV}$. This frequency is available with Ti:Sapphire lasers and is used in many high-intensity laser laboratories. The corresponding wavelength is $\lambda = 800 \text{ nm}$. According to the choice of these parameters, the use of these relative parameters $A_1 = A_2 = 1$, $\nu_1 = \nu_2 = 1$, and $T_1 = T_2 = 1$ is not necessary. Furthermore, by focusing the field on $w_0 = \lambda$, the maximum general field amplitude \mathcal{E}_\star , see Eq. (3.25), reaches a field strength $\mathcal{E}_\star \approx 8.5 \times 10^{15} \text{ V/m}$.

Tab. 2.1 in Sec. 2.2.2 shows that these parameters are achievable with the current state-of-the-art facilities. The ATLAS laser, CoReLas or Apollon are suitable for realizing this setup [188–192, 200, 201]. Since two pulses each with an energy of $W = 25 \text{ J}$ meet in a collision, a total pulse energy $W_{\text{tot}} = 50 \text{ J}$ must be provided by the laser facility. With the selected pulse duration $\tau = 25 \text{ fs}$ (FWHM), this corresponds to a 2 PW class laser. The above facilities all support higher power lasers, but it must be kept in mind that power is lost by splitting the original laser beam into two equal beams. Using mirror techniques, the two laser pulses can be focused to collide at the same point.

In this study, we consider the collision of two Gaussian laser pulses under the angle ϑ_{col} . For our calculations we investigate different collision angles ϑ_{col} varying in the range from 100° to 160° in 10° steps. Previous work indicates that for head-on collisions, i.e. $\vartheta_{\text{col}} = 180^\circ$, the signal photon yield encoding the quantum vacuum nonlinearities is maximized [155, 156]. Note that we explicitly avoid head-on collisions because head-on collisions are experimentally very challenging and often not practically accessible due to experimental constraints. For

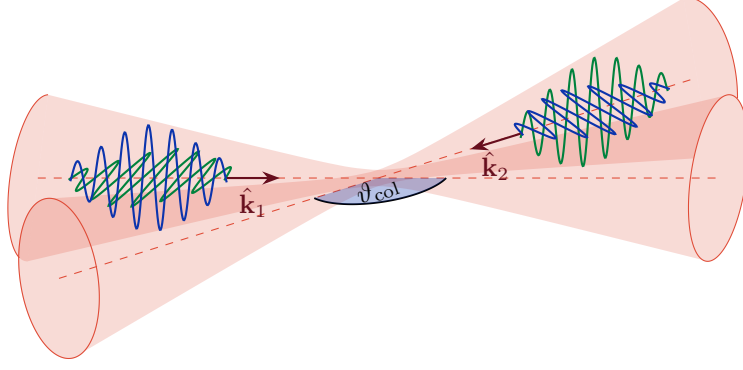


Figure 4.1.: *Collision of two high-intensity laser pulses.* The red shades illustrate the forward/backward cones of two laser pulses colliding under the collision angle ϑ_{col} with a circular focus cross section. Their optical axes are marked by the red dash lines. Additionally, the green (blue) lines represent a typical course of the electric (magnetic) field amplitude in a pulse.

example, a minimally focused laser requires a maximum half opening angle of $\frac{1}{2}\Theta_{\text{max}} \approx 18.24^\circ$. This region is then occupied by the optical apparatuses, see Eq. (2.45).

The purpose of the pump beam is to stimulate the quantum vacuum and provide a localized strong field region inducing the signal which is probed by the probe beam. Here, we define the propagation directions of the laser pulses by

$$\hat{\mathbf{k}}_1 = \hat{\mathbf{e}}_z \quad \text{and} \quad \hat{\mathbf{k}}_2 = \sin \vartheta_{\text{col}} \hat{\mathbf{e}}_x + \cos \vartheta_{\text{col}} \hat{\mathbf{e}}_z, \quad (4.11)$$

respectively. Together they span the collision plane; in our choice of coordinates it is the x - z plane. Fig. 4.1 illustrates this experimental scenario and shows the forward and backward cones of these driving lasers. Their wave vectors are $\mathbf{k}_1 = \omega_1 \hat{\mathbf{k}}_1$ and $\mathbf{k}_2 = \omega_2 \hat{\mathbf{k}}_2$ with $\omega_1 = \omega_2 = \omega_0 = \frac{2\pi}{\lambda} = 1.55 \text{ eV}$. The origin of our coordinate system is defined by the collision point of the two pulses at their focal spots at $\mathbf{r} = 0$. Further we assume that both pulses reach their peak fields at the focus at time $t = 0$, i.e. $\mathbf{r}_0 = 0$ and $t_0 = 0$ for both pulses.

Modern facilities deliver linear polarized high-intensity pulses. For the probe, we choose a fixed polarization in such a way that the electric field $\mathbf{E}_1(x) = \mathcal{E}_1(x) \mathbf{e}_{E_1}$ is orientated along the x direction; correspondingly the magnetic field $\mathbf{B}_1(x) = \mathcal{E}_1(x) \mathbf{e}_{B_1}$ points in the y axis. In the calculations in Sec. 4.1.3 we choose a different polarization direction for the pump than in Sec. 4.1.4, because in Sec. 4.1.4 we study vacuum birefringence, which maximizes with a different relative polarization compared to polarization insensitive measurements. Therefore, we introduce β_2 describing the angle between \mathbf{e}_{E_1} and \mathbf{e}_{E_2} with pump field $\mathbf{E}_2(x) = \mathcal{E}_2 \mathbf{e}_{E_2}$ for a hypothetical collision with $\vartheta_{\text{col}} = 0^\circ$. For a general choice of the collision angle ϑ_{col} the polarization is given by

$$\mathbf{e}_{E_2}(x) = \cos \beta_2 \cos \vartheta_{\text{col}} \mathbf{e}_x + \sin \beta_2 \mathbf{e}_y - \cos \beta_2 \sin \vartheta_{\text{col}} \mathbf{e}_z \quad (4.12)$$

and

$$\mathbf{e}_{B_2}(x) = -\sin \beta_2 \cos \vartheta_{\text{col}} \mathbf{e}_x + \cos \beta_2 \mathbf{e}_y + \sin \beta_2 \sin \vartheta_{\text{col}} \mathbf{e}_z \quad (4.13)$$

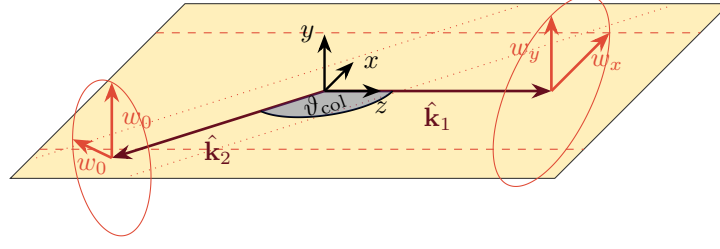


Figure 4.2.: *Pump-probe-collision with elliptical focused probe in IRRA.* The wave vectors of probe $\hat{\mathbf{k}}_1$ and pump $\hat{\mathbf{k}}_2$ illustrates the propagation directions. Further, the red dashed (dotted) lines show the focus radius of the probe (pump) in the yellow marked collision plane. The solid curve illustrates the radii of the waists in three dimensions. The rotationally symmetric pump has a waist size of w_0 while the probe with elliptical cross section has the waists w_x in the collision plane and w_y perpendicular to it.

where the relation $\mathbf{e}_{B_2} = \hat{\mathbf{k}}_2 \times \mathbf{e}_{E_2}$ is satisfied and $\mathbf{B}_2(x) = \mathcal{E}_2(x) \mathbf{e}_{B_2}$.

In all beam collision scenarios, we consider a rotationally symmetric pump. Further, we assume that the pump is always minimally focused. Consequently, $w_{0,12} = w_{0,22} = w_0 = \frac{2\pi}{\omega_0}$ with $\mu_{12} = \mu_{22} = 1$ is valid and together with Eq. (3.27) the profile of the pump simplifies in the IRRA to

$$\mathcal{E}_2(x) = \mathcal{E}_\star e^{-\left(\frac{\mathbf{r} \cdot \hat{\mathbf{k}}_2 - t}{\tau_0/2}\right)^2 - \frac{\mathbf{r}^2 - (\mathbf{r} \cdot \hat{\mathbf{k}}_2)^2}{w_0^2}} \cos(\omega_0(\mathbf{r} \cdot \hat{\mathbf{k}}_2 - t)). \quad (4.14)$$

Here we used $\zeta_2 = \mathbf{r} \cdot \hat{\mathbf{k}}_2$.

On the other hand, we use a circular and elliptical focus cross sections for the probe laser. First we investigate the influence of a rotationally symmetric probe and then we study setups with a probe with an elliptical cross section. We require that for an elliptical cross section, the semi-axes point in the polarization direction of the probe or orthogonal to it. Thus, the two independent beam waists are $w_{0,11} = w_x$ in the collision plane and $w_{0,21} = w_y$ in the direction perpendicular to it. Using relative parameters, for a probe with circular cross section we parameterize the waists $w_x = w_y = \mu w_0$ with $\mu \geq 1$. In the case of elliptical cross sections we analogously introduce $w_x = \mu_x w_0$ and $w_y = \mu_y w_0$ with $\{\mu_x, \mu_y\} \geq 1$. This choice simplifies the parameterization, because $\mu_{11} = \mu_x$ and $\mu_{21} = \mu_y$, so that we write

$$\mathcal{E}_1(x) = \frac{\mathcal{E}_\star}{\sqrt{\mu_x \mu_y}} e^{-\left(\frac{z-t}{\tau_0/2}\right)^2 - \frac{x^2}{w_x^2} - \frac{y^2}{w_y^2}} \cos(\omega_0(z-t)) \quad (4.15)$$

for the profile of the probe in IRRA. Additionally, Fig. 4.2 illustrates the beam radii in the IRRA with a rotationally symmetric pump and a probe beam with elliptical cross section.

Using IRRA is justified because $\frac{w_0}{\zeta_{R,x}} = \frac{1}{\pi} \approx 0.318 \lesssim |\sin \vartheta_{\text{col}}| \approx 0.342$, where here $\vartheta_{\text{col}} = 160^\circ$ gives the smallest possible value of $|\sin \vartheta_{\text{col}}|$ and $\mu_x = 1$ gives the largest possible value of $w_0/\zeta_{R,x}$ with $\zeta_{R,x} = \frac{1}{2} w_x^2 w_0$. For higher values of w_x or w_y , this uncertainty holds and the difference becomes even bigger.

In order to describe the background of the driving laser fields we introduced the parameterization $\phi_i(\varphi, \vartheta)$ and $\theta_i(\varphi, \vartheta)$ at the beginning of Sec. 4. With these coordinates we describe

the system in spherical coordinates, where the space vector $\mathbf{r}|_{\theta_i=0}$ points in the propagation direction of the laser pulses. Here, for the far-field distribution of a Gaussian beam, we use the background photon density $\varrho(\varphi, \vartheta)$, cf. Eq. (4.10). We use

$$\phi_1 = \varphi \quad \text{and} \quad \phi_2 = \arctan(\cos \varphi \sin \vartheta \cos \vartheta_{\text{col}} - \sin \varphi \sin \vartheta \sin \vartheta_{\text{col}}) \quad (4.16)$$

to parameterize the rotations around the beam axis. Further,

$$\theta_1 = \vartheta \quad \text{and} \quad \theta_2 = \arccos(\cos \varphi \sin \vartheta \sin \vartheta_{\text{col}} + \cos \vartheta \cos \vartheta_{\text{col}}) \quad (4.17)$$

are the polar angles measured from the forward beam axis; φ and ϑ are azimuthal and polar angles used to parameterize the emission direction in a spherical coordinate system with the north pole along the outgoing direction of the probe laser \mathbf{k}_1 .

4.1.2. Region of Discernible Signal

In Sec. 3.2.4 we have introduced how to calculate the angular resolved signal-photon density $\rho(\varphi, \vartheta|\omega_i, \omega_f)$. Since the signal here has only one peak assembled around $\mathbf{k} = \omega_0$ in the spectrum, we omit the specification of the spectral interval for the density and write $\rho(\varphi, \vartheta)$ instead. To this end, in Sec. 4.1.3 and Sec. 4.1.4 we estimate the corresponding signal photon densities. Additionally, we describe the full background density of the driving laser fields by $\varrho(\varphi, \vartheta)$.

In this section, we use these densities $\rho(\varphi, \vartheta)$ and $\varrho(\varphi, \vartheta)$ to introduce a numerical method to determine the solid angle region, where the signal surpasses the background. Within these regions we speak of a *discernible signal*. The solid angle region where the signal dominates is defined formally as

$$\mathcal{A}_{\text{d},\bar{\mu}} = \{(\varphi, \vartheta) \in [0, 2\pi) \times [0, \pi] \mid \rho(\varphi, \vartheta) \geq \varrho(\varphi, \vartheta)\} , \quad (4.18)$$

where we use the index $\bar{\mu}$ which indicates the used beam waist parameter. The shape of this region depends on the parameters of the interacting lasers, in particular the choice of the beam waists, represented by $\bar{\mu}$ for any kind of cross section, and the collision angle ϑ_{col} . This region can be of variable shape and is not simply connected in general. If the signal does not become dominant anywhere, then $\mathcal{A}_{\text{d},\bar{\mu}} = \{ \}$ results and we cannot measure a signal against the background. In addition, we denote the boundary of the region $\mathcal{A}_{\text{d},\bar{\mu}}$ by

$$\partial\mathcal{A}_{\text{d},\bar{\mu}} = \{(\varphi, \vartheta) \in [0, 2\pi) \times [0, \pi] \mid \rho(\varphi, \vartheta) = \varrho(\varphi, \vartheta)\} . \quad (4.19)$$

For simply connected regions, the boundary can be parameterized by two functions $\vartheta_l(\varphi) \leq \vartheta_u(\varphi)$ depending on the azimuthal angle φ , where $\vartheta_l(\varphi)$ denotes the lower bound and $\vartheta_u(\varphi)$ the upper bound for a solid angle region of the discernible signal. These functions are defined in the interval $[\varphi_i, \varphi_f]$ with φ_i and φ_f implicitly determined by $\vartheta_l(\varphi_i) = \vartheta_u(\varphi_i)$ and $\vartheta_l(\varphi_f) = \vartheta_u(\varphi_f)$ for $\varphi_i > 0$ and $\varphi_f < 2\pi$. If the latter condition is violated, $\vartheta_l(0) = \vartheta_l(2\pi)$ applies in both cases, where the values of the two functions on the boundary may now be unequal.

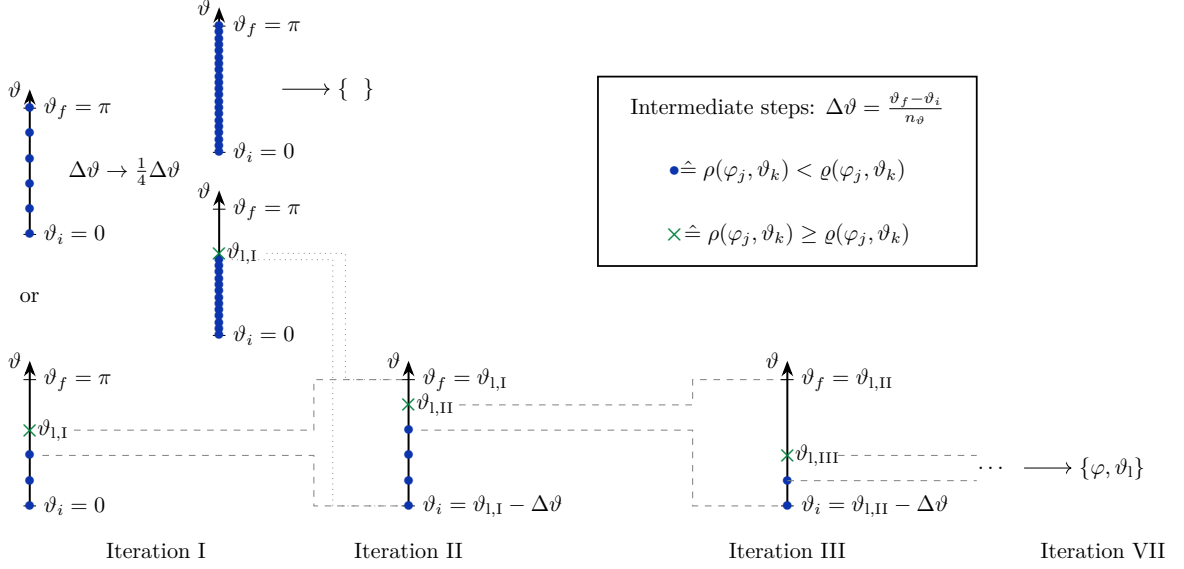


Figure 4.3.: Scheme for numerical determination of the lower bound of ϑ_1 at constant φ for the region of discernible signal. The evaluated functions $\rho(\varphi, \vartheta)$ (signal-photon density) and $\varrho(\varphi, \vartheta)$ (background photon density) are compared at fixed φ on the interval $[\vartheta_i, \vartheta_f]$, starting in steps $\Delta\vartheta$ ascending from ϑ_i . In the first iteration $s = I$ we define $\vartheta_i \equiv 0$ and $\vartheta_f \equiv \pi$. If always $\rho(\varphi, \vartheta) < \varrho(\varphi, \vartheta)$ is valid, the interval is scanned again with a quarter of the step size. If there is no finding for given φ the signal is classified as hidden in this region. If the signal is dominant at $\vartheta_{1,s}$, then the run is terminated prematurely and the next iteration step $s \rightarrow s + 1$ begins. Here, the interval boundaries are adjusted to $\vartheta_i \equiv \vartheta_{1,s-1} - \Delta\vartheta$ and $\vartheta_f \equiv \vartheta_{1,s-1}$ according to the previous iteration step. The step size is redetermined and the procedure starts again. After seven iterations, the result $\vartheta_1 = \vartheta_{1,VII}$ is used.

Therefore $\partial\mathcal{A}_{d,\bar{\mu}} = \{\vartheta_1(\varphi) \mid \varphi \in [\varphi_i, \varphi_f]\} \cup \{\vartheta_u(\varphi) \mid \varphi \in [\varphi_i, \varphi_f]\}$ is valued.

If the region $\mathcal{A}_{d,\bar{\mu}}$ is not simply connected, but at most two mappings to ϑ can be found for any given value of φ , then the φ domain can be divided into M connected intervals $[\varphi_i^{(m)}, \varphi_f^{(m)}]$ labeled by $m = 1, 2, \dots, M$, where lower and upper bound $\vartheta_{l/u}^{(m)}(\varphi)$ can be defined such that

$$\partial\mathcal{A}_{d,\bar{\mu}} = \bigcup_{m=1}^M \left(\left\{ \vartheta_l^{(m)}(\varphi) \mid \varphi \in [\varphi_i^{(m)}, \varphi_f^{(m)}] \right\} \cup \left\{ \vartheta_u^{(m)}(\varphi) \mid \varphi \in [\varphi_i^{(m)}, \varphi_f^{(m)}] \right\} \right). \quad (4.20)$$

It is possible to discuss further more complicated shapes of $\mathcal{A}_{d,\bar{\mu}}$ and $\partial\mathcal{A}_{d,\bar{\mu}}$, respectively, but this is not necessary in the present case, cf. the results in Sec. 4.1.3.

To evaluate $\mathcal{A}_{d,\bar{\mu}}$ we first calculate $\partial\mathcal{A}_{d,\bar{\mu}}$ by determining all possible functions $\vartheta(\varphi)$, which solve the equation $\rho(\varphi, \vartheta) = \varrho(\varphi, \vartheta)$ on $(\varphi, \vartheta) \in [0, 2\pi] \times [0, \pi]$. Since $\rho(\varphi, \vartheta)$ in general exhibits a complicated dependency on the solid angles ϑ and φ we aim at solving equation numerically.

Being aware of potential shortcomings of this approach we determine both a lower bound $\vartheta_l(\varphi)$ and upper bound $\vartheta_u(\varphi) \geq \vartheta_l(\varphi)$ in a first step. Therefore, we sample the interval $\varphi_j \in [0, 2\pi]$ by n_φ sampling points, usually using $n_\varphi = 300$ or bigger. For these fixed

values of φ , we then determine the lower/upper bounds $\vartheta_{l/u}(\varphi)$ using the iterative procedure illustrated schematically in Fig. 4.3. In iteration I the interval $\vartheta_k \in [0, \pi)$ is divided into n_ϑ points with $\Delta\vartheta = \frac{\pi}{n_\vartheta}$, using $n_\vartheta = 70$ or bigger. Depending on whether we are looking for the upper or lower bound we start with $\vartheta_{k=1} = \pi$ or $\vartheta_{k=1} = 0$. In the following we concentrate on the determination of the lower bound. For this purpose, we evaluate both $\rho(\varphi_j, \vartheta_k)$ and $\varrho(\varphi_j, \vartheta_k)$ at each sampling point (φ_j, ϑ_k) with ascending value of $\vartheta_{k+1} \rightarrow \vartheta_k + \Delta\vartheta$ from the initial value $\vartheta_{k=1} = 0$ and compare them. If $\rho(\varphi_j, \vartheta_k) < \varrho(\varphi_j, \vartheta_k)$ holds, we increase ϑ_k by $\Delta\vartheta$ and compare again. If the signal density becomes larger or equal to the background density, we terminate the procedure and register this value as $\vartheta_{l,I}$. If the first iteration did not result in a positive outcome, we decrease the step size $\Delta\vartheta$ by one-fourth, $\Delta\vartheta \rightarrow \frac{1}{4}\Delta\vartheta$, and repeat iteration I. If this also does not yield a result, we assume an empty solution for this value of φ_j . We continue with the next iteration step, see iteration II.

In iteration II, we refine the outcome of iteration I by adjusting the bounds of the ϑ domain to be studied. As initial value we now use $\vartheta_i = \vartheta_{l,I} - \Delta\vartheta$, as final value $\vartheta_f = \vartheta_{l,I}$. From these two values a new step size $\Delta\vartheta = \frac{\vartheta_f - \vartheta_i}{n_\vartheta}$ is calculated. Starting with $\vartheta_{k=1} = \vartheta_i$ the values of $\rho(\varphi_j, \vartheta_k)$ and $\varrho(\varphi_j, \vartheta_k)$ are compared again until the signal dominates. The corresponding value is registered and $\vartheta_{l,II}$ is used as input for the next iteration III which resembles iteration II with $\vartheta_{l,I} \rightarrow \vartheta_{l,II}$.

After seven iterations we stop and use $\vartheta_{l,VII} = \vartheta_l$. By successively decreasing the intervals and step sizes, this value has a maximum error of πn_ϑ^{-7} , which is negligible in the context of the accuracy of the applied approximations.

Applying this procedure to all sampling points φ_j of φ we obtain a table of mappings $\{\varphi, \vartheta_l\}$. We use this table to interpolate a function $\vartheta_l(\varphi)$ (or several functions for regions which are not simply connected). For this interpolation we fit third-degree polynomial curves between successive data points. Analogously, we obtain the interpolation $\vartheta_u(\varphi)$ of the upper bound. These results allow us to determine the solid angle region where the signal dominates the background as $\mathcal{A}_{d,\bar{\mu}} = \mathcal{A}_{l,\bar{\mu}} \cap \mathcal{A}_{u,\bar{\mu}}$ with

$$\mathcal{A}_{l,\bar{\mu}} = \{(\varphi, \vartheta) \in [0, 2\pi) \times [0, \pi] \mid \vartheta(\varphi) \geq \vartheta_l(\varphi)\} \quad (4.21)$$

and

$$\mathcal{A}_{u,\bar{\mu}} = \{(\varphi, \vartheta) \in [0, 2\pi) \times [0, \pi] \mid \vartheta(\varphi) \leq \vartheta_u(\varphi)\} . \quad (4.22)$$

Nevertheless, as already mentioned in the introduction of the numerical method, our iterative numerical algorithm may provide us with an erroneous result for $\mathcal{A}_{d,\bar{\mu}}$. Figure 4.4 shows a potential source of error: if for a fixed value of φ_j more than two values of $\vartheta_{l/u}$ exist, then the numerical method presented above fails. However, it nevertheless makes sense to adopt this method for the following reasons: first, this algorithm is much faster than an alternative method resolving distinguished regions with multiple values of ϑ for fixed values of φ . Second, we aim for regions fulfilling $\int_{\mathcal{A}} d\Omega [\rho(\varphi, \vartheta) - \varrho(\varphi, \vartheta)] > 0$. As long as the total integral over \mathcal{A} is positive, the signal dominates the background, regardless of whether this is also the case locally in \mathcal{A} . Third, we can make sure that region $\mathcal{A}_{d,\bar{\mu}}$ satisfies the condition

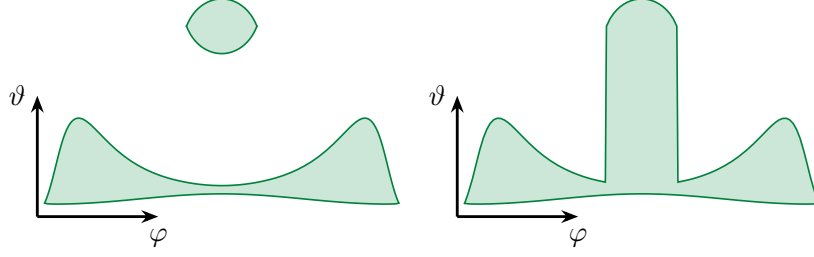


Figure 4.4.: *Potential source of error of the numerical method for determining the solid angle region of the region of discernible signal.* The frames show the range where $\rho(\varphi, \vartheta) = \varrho(\varphi, \vartheta)$. The real desired region is shown in the left panel; on the other hand, the right panel shows the result according to the numerical method used. Since the numerical method always assumes exactly one upper and one lower bound, the multiple mappings of φ to ϑ , as visible left, cannot be detected. This region was observed at a collision angle $\vartheta_{\text{col}} = 90^\circ$ (which we do not study further) and circular focusing $\mu = 5$ of the probe beam.

by using numerical programs to plot the function $\rho(\varphi, \vartheta) - \varrho(\varphi, \vartheta) > 0$ and compare it with the graph of region $\mathcal{A}_{\text{d}, \bar{\mu}}$.

Using the numerical method presented here, we will determine the regions of discernible signals in the following sections. Furthermore, performing the solid angle integration over these regions $\mathcal{A}_{\text{d}, \bar{\mu}}$ allows us to determine the discernible signal-photon number and the corresponding number of background photons of the driving lasers.

4.1.3. Discernible Polarization Insensitive Signal

In this section, we aim to estimate the discernible signal-photon number for polarization insensitive measurements. Therefore we vary the probe waist sizes, first with rotationally symmetric probe, later using to independent values w_x, w_y . Further, we have to sum both polarization densities $\rho_{(p)}(\varphi, \vartheta)$ for the polarization insensitive signal-photon density $\rho(\varphi, \vartheta) = \sum_{p=1}^2 \rho_{(p)}(\varphi, \vartheta)$, see Sec. 3.1.

The channel analysis, see Sec. 3.2, delivers a straightforward analytical result for the signal density $\rho(\varphi, \vartheta)$, e.g. see (3.64) and apply the sum over both polarizations. Applying the channel analysis to the two-beam collision, the only relevant proto-physical channels are $\{121\}$ and $\{212\}$. Consequently, the signal photon amplitude in Eq. (3.38) for polarization $p = 1$ corresponding to β yields

$$S_{(1)}(\mathbf{k}) = \frac{1}{i} \frac{e}{4\pi^2} \frac{m_e^2}{45} \sqrt{\frac{k}{2}} \left(\frac{e}{m_e^2} \right)^3 2 (\mathcal{I}_{121}(\mathbf{k}) g_{\beta;121}(\varphi, \vartheta) + \mathcal{I}_{212}(\mathbf{k}) g_{\beta;212}(\varphi, \vartheta)) . \quad (4.23)$$

According to (3.36) and (3.48), the probe waist sizes w_x and w_y only influence the Fourier integrals \mathcal{I}_{121} and \mathcal{I}_{212} . Furthermore, the polarization in $S_{(p)}(\mathbf{k})$ is only encoded in the geometrical functions $g_{\beta;121}(\varphi, \vartheta)$ and $g_{\beta;212}(\varphi, \vartheta)$, while the corresponding functions for the

second polarization are achieved by $\beta \rightarrow \beta + \frac{\pi}{2}$; the relevant contributions read

$$g_{\beta;121}(\varphi, \vartheta) = \frac{1}{4} (1 - \cos \vartheta) (1 - \cos \vartheta_{\text{col}}) [3 \cos(\beta + \beta_2 - \varphi) - 11 \cos(\beta - \beta_2 - \varphi)] \quad (4.24)$$

and

$$g_{\beta;212}(\varphi, \vartheta) = \left([11 \cos \beta - 3 \cos(\beta + 2\beta_2)] [(\cos \vartheta \cos \vartheta_{\text{col}} - 1) \cos \varphi + \sin \vartheta \sin \vartheta_{\text{col}}] \right. \\ \left. + [11 \sin \beta - 3 \sin(\beta + 2\beta_2)] (\cos \vartheta - \cos \vartheta_{\text{col}}) \sin \varphi \right) \frac{1}{4} (1 - \cos \vartheta_{\text{col}}), \quad (4.25)$$

see Eq. (3.37). Though it can be shown straightforwardly that a maximum of the total polarization insensitive signal is observable at an angle $\beta_2 = 90^\circ$, we will choose this angle in the following calculations.

To determine the signal-photon density $\rho(\varphi, \vartheta)$ we calculate $S_{(p)} S_{(p)}^*$ without resolving their polarization and frequency and obtain

$$\rho(\varphi, \vartheta) = \frac{1}{(2\pi)^7} \frac{2}{45^2} \left(\frac{e}{m_e} \right)^8 \int_0^\infty dk k^3 \sum_{p=1}^2 \left(\mathcal{I}_{121} g_{(p);121} + \mathcal{I}_{212} g_{(p);212} \right)^2. \quad (4.26)$$

We omit constraints on the frequency regime of the signal because the signal is dominated by the frequency range around ω_0 in this setup, see also the detailed analysis in Sec. 3.2 and mainly the discussion in Sec. 3.2.5. All contributions $\mathcal{I}_{121} g_{(p);121}$ and $\mathcal{I}_{212} g_{(p);212}$ give rise to non-vanishing contributions for complementary values of (φ, ϑ) . The interference term $2\mathcal{I}_{121}\mathcal{I}_{212}g_{(p);121}g_{(p);212}$ is exponentially suppressed in comparison to the proto-physical channels $\{121\}$, $\{212\}$ and can be safely neglected. Therefore, we neglect the interference term in the remainder.

Since the polarization occurs exclusively in the functions $g_{(p);iji}$, we can already perform this summation and Eq. (4.26) can be expressed as

$$\rho(\varphi, \vartheta) = \frac{1}{(2\pi)^7} \frac{2}{45^2} \left(\frac{e}{m_e} \right)^8 \left[\left(\sum_{p=1}^2 g_{(p);121}^2(\varphi, \vartheta) \right) \int_0^\infty dk k^3 \mathcal{I}_{121}^2(\mathbf{k}) \right. \\ \left. + \left(\sum_{p=1}^2 g_{(p);212}^2(\varphi, \vartheta) \right) \int_0^\infty dk k^3 \mathcal{I}_{212}^2(\mathbf{k}) \right]. \quad (4.27)$$

Subsequently we use $\beta_2 = \frac{\pi}{2}$, which implies

$$\sum_{p=1}^2 g_{121}^2(\varphi, \vartheta) \Big|_{\beta_2=\frac{\pi}{2}} = 196 \sin^4 \frac{\vartheta}{2} \sin^4 \frac{\vartheta_{\text{col}}}{2} \quad (4.28)$$

and

$$\sum_{p=1}^2 g_{212}^2(\varphi, \vartheta) \Big|_{\beta_2=\frac{\pi}{2}} = 49 \sin^4 \frac{\vartheta_{\text{col}}}{2} \left[\cos \vartheta \cos \vartheta_{\text{col}} - 1 + \cos \varphi \sin \vartheta \sin \vartheta_{\text{col}} \right]^2. \quad (4.29)$$

Finally, we determine the signal-photon density completely analytically

$$\begin{aligned} \rho(\varphi, \vartheta) = & \frac{e^2}{16\pi^4} \frac{m_e^4}{45^2} \left(\frac{e}{m_e^2} \right)^6 \frac{\pi \mathcal{E}_*^6 \tau_0^2}{128} \frac{1}{3} \left[\left(\sum_{p=1}^2 g_{(p);121}^2(\varphi, \vartheta) \right) \frac{1}{\mu_x \mu_y} \frac{4}{\det \mathcal{M}_{121}} \right. \\ & \times e^{-\frac{4}{9} \omega_0^2 (\hat{\mathbf{k}}_2 - \hat{\mathbf{k}}_1) \cdot \mathcal{M}_{121}^{-1} (\hat{\mathbf{k}}_2 - \hat{\mathbf{k}}_1) - \frac{\tau_0^2 \omega_0^2}{24}} \Gamma_{121121}^{+---+---}(\varphi, \vartheta) + \left(\sum_{p=1}^2 g_{(p);212}^2(\varphi, \vartheta) \right) \\ & \times \left. \frac{1}{\sqrt{\mu_x \mu_y}} \frac{4}{\det \mathcal{M}_{212}} e^{-\frac{4}{9} \omega_0^2 (\hat{\mathbf{k}}_1 - \hat{\mathbf{k}}_2) \cdot \mathcal{M}_{212}^{-1} (\hat{\mathbf{k}}_1 - \hat{\mathbf{k}}_2) - \frac{\tau_0^2 \omega_0^2}{24}} \Gamma_{212212}^{+---+---}(\varphi, \vartheta) \right] \end{aligned} \quad (4.30)$$

in the IRRA, see (3.64). Here we use the matrices

$$\mathcal{M}_{121} = 2 \begin{pmatrix} \frac{2}{\mu_x^2 w_0^2} + \frac{\cos^2 \vartheta_{\text{col}}}{w_0^2} + \frac{8 \sin^2 \vartheta_{\text{col}}}{3 \tau_0^2} & 0 & \left(\frac{8}{\tau_0^2} - \frac{3}{w_0^2} \right) \frac{\sin \vartheta_{\text{col}} \cos \vartheta_{\text{col}}}{3} \\ 0 & \frac{1}{w_0^2} \left(\frac{2}{\mu_y^2} + 1 \right) & 0 \\ \frac{\sin \vartheta_{\text{col}}}{3} \left(\left(\frac{8}{\tau_0^2} - \frac{3}{w_0^2} \right) \cos \vartheta_{\text{col}} - \frac{16}{\tau_0^2} \right) & 0 & \frac{\sin^2 \vartheta_{\text{col}}}{w_0^2} + \frac{8(\cos \vartheta_{\text{col}} - 1)^2}{3 \tau_0^2} \end{pmatrix} \quad (4.31)$$

and

$$\mathcal{M}_{212} = 2 \begin{pmatrix} \frac{1+2\mu_x^2 \cos^2 \vartheta_{\text{col}}}{\mu_x^2 w_0^2} + \frac{8 \sin^2 \vartheta_{\text{col}}}{3 \tau_0^2} & 0 & \frac{2 \sin \vartheta_{\text{col}} ((4w_0^2 - 3\tau_0^2) \cos \vartheta_{\text{col}} - 8w_0^2)}{3 \tau_0^2 w_0^2} \\ 0 & \frac{1}{w_0^2} \left(\frac{1}{\mu_y^2} + 2 \right) & 0 \\ \left(\frac{8}{\tau_0^2} - \frac{6}{w_0^2} \right) \frac{\sin \vartheta_{\text{col}} \cos \vartheta_{\text{col}}}{3} & 0 & \frac{2 \sin^2 \vartheta_{\text{col}}}{w_0^2} + \frac{8(\cos \vartheta_{\text{col}} - 1)^2}{3 \tau_0^2} \end{pmatrix}, \quad (4.32)$$

as well as the solution of the integral over the spectrum $\Gamma_{ijii'j'i'}^{+---+---}(\varphi, \vartheta)$, see Eq. (3.63), which results from the vectors $\mathbf{K}_{1,iji}^{+---} = -\frac{2}{3} (\hat{\mathbf{k}}_j - \hat{\mathbf{k}}_i)$, $\mathbf{K}_{2,iji} = \hat{\mathbf{k}} - \frac{1}{3} (2\hat{\mathbf{k}}_i + \hat{\mathbf{k}}_j)$ and the matrix \mathcal{M}_{iji} . This is shown in Sec. 3.2.3 and Sec. 3.2.4. Furthermore, we have used the insight from the channel analysis to perform the summation over the signs ξ, η, χ , where only contributions that satisfy $\xi + \eta + \chi = 1$ are relevant. The factor 4 in Eq. (4.30) follows from applying the symmetries in this summation.

So far, all calculations could be performed analytically. The number of signal photons $N(\mathcal{A})$ emitted into a given solid angle region \mathcal{A} is finally evaluated by a numerical integration over \mathcal{A} as

$$N(\mathcal{A}) = \int_{\mathcal{A}} d\Omega \rho(\varphi, \vartheta). \quad (4.33)$$

which closely resembles Eq. (3.23). For convenience, we define the area of a given solid angle region \mathcal{A} as

$$A(\mathcal{A}) = \int_{\mathcal{A}} d\Omega. \quad (4.34)$$

We note here that the choice of focus width (along both orthogonal axes) of the probe is a quantity of interest for following investigations. In addition to the density, this also affects the region of discernible signal photons $\mathcal{A}_{d,\bar{\mu}}$, where the parameter tuple $\bar{\mu}$ explicitly indicate both waist sizes w_x and w_y . In the following, we will study the effects of these two different probe waists one by one.

Rotationally Symmetric Probe

First, we study the collision of pump and probe laser pulses with circular cross section. In addition, we first turn our attention to the collision under the angle $\vartheta_{\text{col}} = 160^\circ$, because here we expect the largest signal of the collision angles considered. As already mentioned, the pump laser is focused to its diffraction limit with $w_0 = 2\pi/\omega_0$, whereas the probe beam has a variable radially symmetric waist of size $w_x = w_y = \mu w_0$ with $\mu \in [1, 10]$. The lower bound is physically motivated by the diffraction laws, while the upper bound can be chosen arbitrarily high. For the upper bound we chose $\mu = 10$, however, already before $\mu = 10$ a saturation is observed.

At first we determine the area of solid angle regions $A(\mathcal{A}_{d,\mu})$ where the signal is discernible; see Sec. 4.1.2,. Here, we use the parameter μ as index of the dominant region $\mathcal{A}_{d,\mu}$. The dependence of the area on the parameter $\mu = w/w_0$ is shown in the Fig. 4.5. From Fig. 4.5 we infer that there is no discernible signal for $\mu \leq 1.6$. For $1.6 \leq \mu \lesssim 4$ the area of \mathcal{A}_d grows very strongly, but beyond $\mu \approx 4$ the increase with μ becomes much slower.

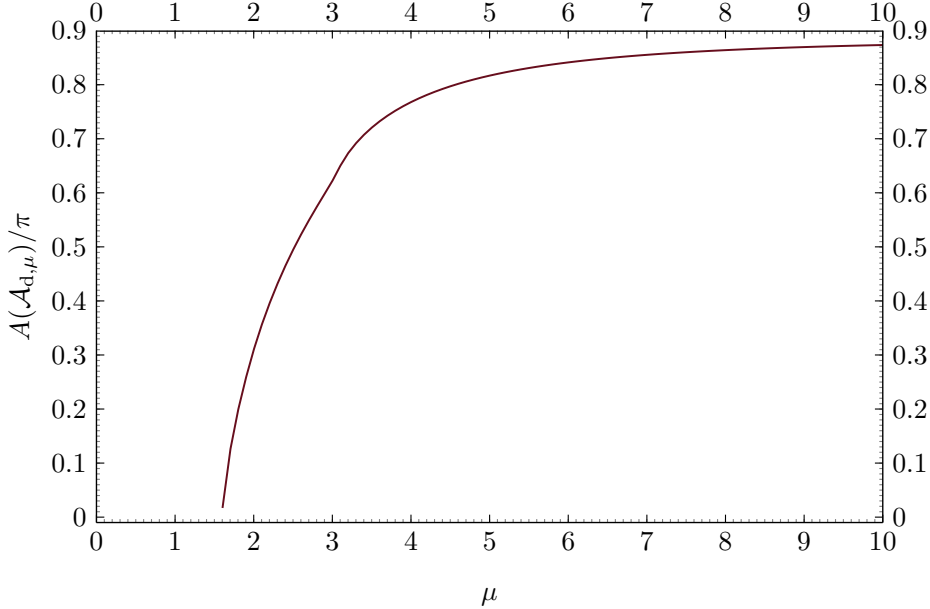


Figure 4.5.: Area of the solid angle region $\mathcal{A}_{d,\mu}$ of discernible signal over μ for two-beam (circular probe) collision with $\vartheta_{\text{col}} = 160^\circ$. Here we consider the collision of two beams of equal frequency $\omega_0 = 1.55 \text{ eV}$, pulse duration $\tau = 25 \text{ fs}$ (FWHM), and pulse energy $W = 25 \text{ J}$. The pump (probe) beam has a circular cross section with waist size $w_0 = \frac{2\pi}{\omega_0}$ ($w_x = w_y = \mu w_0$).

In Figure 4.6 we highlight the photon density for the full solid angle region of 4π for the example $\mu = 5$. The region where the signal dominates the background is framed. Inside this region the density of the signal photons is shown in the corresponding color scale (black over green to yellow). Outside of this area the background of the driving photons is shown, for this a different logarithmic color scale (black over purple to ocher) is used. To map the sphere surface on a two-dimensional surface we use a Mollweide projection. This projection conserves the relevant areas of surfaces but is not angle conserving. Therefore, this representation helps

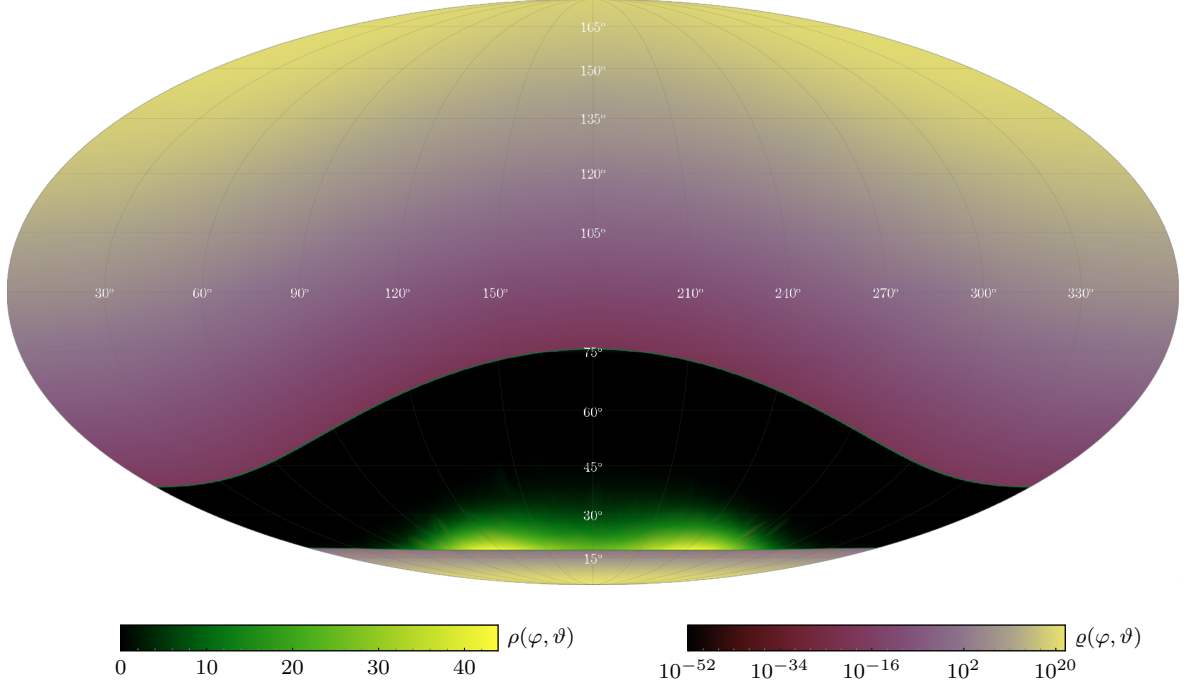


Figure 4.6.: Mollweide plot of signal and background density for two-beam (circular probe) collision with $\vartheta_{\text{col}} = 160^\circ$ and $\mu = 5$. The Mollweide plot (longitude φ , latitude ϑ) gives the signal-photon density $\rho(\varphi, \vartheta)$ and the density of the background $q(\varphi, \vartheta)$. The region where $\rho(\varphi, \vartheta) = q(\varphi, \vartheta)$ is highlighted by the green frame, $\rho(\varphi, \vartheta) > q(\varphi, \vartheta)$ is illustrated with the green linear color function and for the complementary region $\rho(\varphi, \vartheta) < q(\varphi, \vartheta)$ the purple logarithmic color function is chosen. We consider the collision of two beams of equal frequency $\omega_0 = 1.55$ eV, pulse duration $\tau = 25$ fs (FWHM), and pulse energy $W = 25$ J for $\vartheta_{\text{col}} = 160^\circ$. The pump (probe) beam has a circular cross section with waist radius $w_0 = \frac{2\pi}{\omega_0}$ ($w_x = w_y = 5w_0$).

to compare areas on the sphere.

Fig. 4.6 marks the region of the detectable signal. In the considered case $\mu = 5$ this region is simply connected and we can assign to it, as introduced in Sec. 4.1.2, a lower and an upper bound $\vartheta_{l/u}(\varphi)$ where $\rho(\varphi, \vartheta_{l/u}(\varphi)) = q(\varphi, \vartheta_{l/u}(\varphi))$ holds. The lower bound $\vartheta_l(\varphi)$ is almost constant because on the one hand this region is close to the forward beam axis of the probe beam $\vartheta = 0$, on the other hand the probe beam has a circular cross section. In contrast, the upper bound $\vartheta_u(\varphi)$ shows a more pronounced φ dependence. It becomes minimal in the collision plane of the driving lasers at $\varphi = 0$. The maximum of $\vartheta_u(\varphi)$ is reached at $\varphi = 180^\circ$. Between these two extrema the $\vartheta_u(\varphi)$ increases monotonically. The color scale encodes the distribution of the signal photons. The highest values of the discernible signal are reached close to $\vartheta_l(\varphi)$. Furthermore, we observe pronounced maxima for $\vartheta \approx 17.5^\circ$ and $\varphi \approx 114.54^\circ$ and $\varphi \approx 245.46^\circ$, respectively.

In the next step we analyze the number of discernible signal photons $N(\mathcal{A}_{d,\mu})$ as a function of μ . The results of this study are shown in Fig. 4.7. Only for $\mu \gtrsim 1.6$ a discernible signal can be identified. A beginning of the increase of the photon number with increasing parameter μ at $N(\mathcal{A}_{d,\mu}) = 0$ indicates that the numerical procedure has not omit any relevant region.

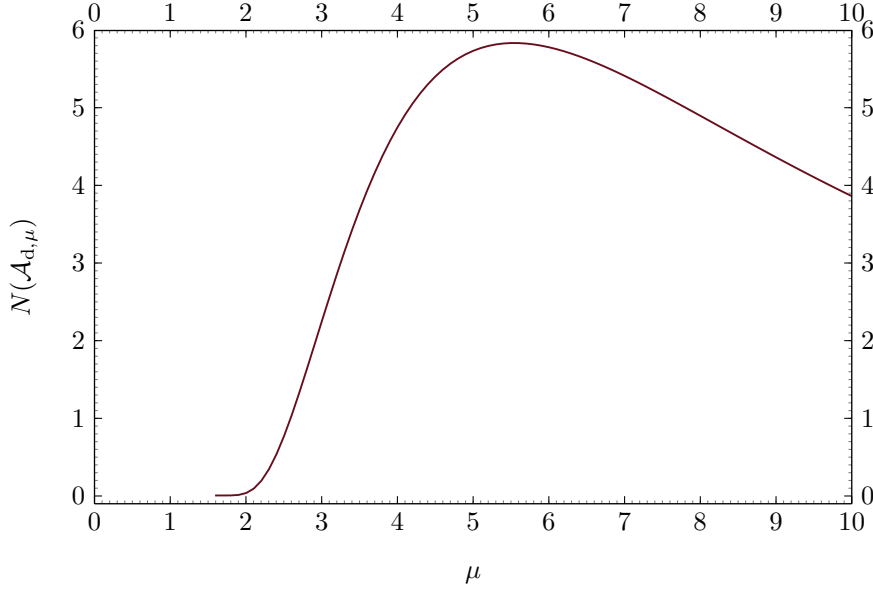


Figure 4.7.: Number of discernible signal photons $N(\mathcal{A}_{d,\mu})$ over μ for two-beam (circular probe) collision with $\vartheta_{\text{col}} = 160^\circ$. The maximum number of background photons $N(\mathcal{A}_{d,3.8}) \approx 0.16$ is reached at $\mu = 3.8$. See Figure 4.5 for the laser parameters employed here.

The increase of N differs visibly from the growth of $\mathcal{A}_{d,\mu}$ with μ , cf. Fig. 4.5. At $\mu \approx 5.5$ we encounter a pronounced maximum with $N(\mathcal{A}_{d,5.5}) \approx 5.84$ signal photons per shot. For comparison, the associated number of background photons yields $N(\mathcal{A}_{d,5.5}) \approx 0.12$ photons per shot. For $\mu \gtrsim 5.5$ the number of discernible signal photons decreases approximately linearly with μ . A similar behavior was identified in the head-on collision of optical and x-ray laser pulses in [118].

The appearance of a local maximum in $N(\mathcal{A}_{d,\mu})$ for $\vartheta_{\text{col}} = 160^\circ$ shows that the probe waist provides a handle to amplify or decrease the signal for given other parameters. Since the pulse energy and duration are kept constant, the probe density decreases when using a wider focus. At the same time, a wider focus tends to increase $\mathcal{A}_{d,\mu}$ because the probe divergence diminishes. Even if the area $A(\mathcal{A}_{d,\mu})$ does not change too much, the value of the lower limit ϑ_1 changes significantly; this can be seen in the Fig. 4.8. However, at some point the intensity of the probe eventually becomes too weak for large values of μ such that the number of signal photons decreases.

In Fig. 4.8 we highlight our results for the boundaries of $\mathcal{A}_{d,\mu}$ for other collision angles ϑ_{col} . Here we analyze the collision angles 100° to 160° in 10° steps. This figure shows the boundaries $\vartheta_1(\varphi)$ and $\vartheta_d(\varphi)$ of the regions $\mathcal{A}_{d,\mu}$, i.e. $\rho(\varphi, \vartheta) = \varrho(\varphi, \vartheta)$. Besides, the directions of the driving lasers are indicated: the colored shading indicates the direction of the pump laser, the black one the direction of the probe beam. For each value of ϑ_{col} we plot $\partial\mathcal{A}_{d,\mu}$ for six different values of $\mu \in \{2, 3, 4, 5, 6, 7\}$. These are indicated by the spacing of the dashed; the larger μ , the smaller the spacing of the dashes.

We observe that for $\vartheta_{\text{col}} > 100^\circ$ the upper bound $\vartheta_u(\varphi)$ is almost independent of μ . The reason for this is that the choice of μ only affects the focusing of the probe laser propagating

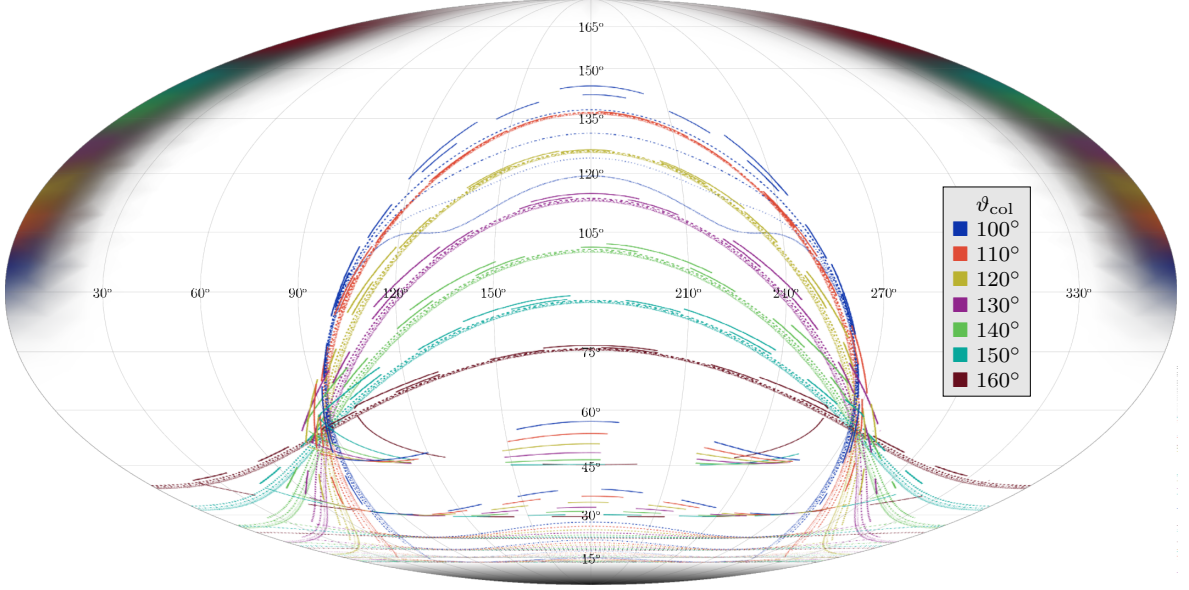


Figure 4.8.: *Mollweide plot for equal signal and background density for two-beam (circular probe) collision with different angle ϑ_{col} and probe waists.* The Mollweide plot (longitude φ , latitude ϑ) is showing the different forward beam axis of the pump laser pulses for different collision angles ϑ_{col} marked with different colors, see legend. Moreover, the direction of the probe is given by the black shade. The boundaries $\vartheta_1(\varphi)$ and $\vartheta_u(\varphi)$ highlighting $\rho(\varphi, \vartheta) = \varrho(\varphi, \vartheta)$ are marked by colored lines for different values of μ : 2, 3, 4, 5, 6, 7. The value of μ is encoded by the lines style. Larger μ means smaller spacing between dashes. The pump (probe) is focused to a waist of $w_0 = \frac{2\pi}{\omega_0}$ ($w_x = w_y = \mu\omega_0$). Both lasers have the same frequencies $\omega_0 = 1.55$ eV, pulse energy $W = 25$ J, and duration $\tau = 25$ fs (FWHM).

along $\vartheta = 0$. At the same time, we find that the lower bound ϑ_1 becomes smaller, i.e. $A(\mathcal{A}_{d,\mu})$ grows with increasing μ . Considering $\vartheta_{\text{col}} = 100^\circ$, the upper bound $\vartheta_u(\varphi)$ varies with μ since the background of the pump $\varrho_2(\varphi, \vartheta)$ is less relevant for higher angle ϑ .

Analogous to Fig. 4.7 for $\vartheta_{\text{col}} = 160^\circ$, in Fig. 4.9 we plot the number of discernible signal $N(\mathcal{A}_{d,\mu})$ and background photons $\mathcal{N}(\mathcal{A}_{d,\mu})$ per shot in the regions $\mathcal{A}_{d,\mu}$ as a function of μ . Here the different photon numbers are compared adapting a logarithmic scale. In each case, the number of signal photons (solid) surpasses the number of background photons (dashed) in line with the discernibility criterion adopted to determine $\mathcal{A}_{d,\mu}$, see Sec. 4.1.2 and especially Eq. (4.18). For each value of ϑ_{col} considered here, a local maximum in the numbers of signal photons at $\mu_{\text{max}N}$ or background photons at $\mu_{\text{max}N}$ is observed. The positions μ_{max} of these maxima shift to smaller values of μ as the collision angle ϑ_{col} increases. Moreover, we find that the position of the maximum of the background varies slower with μ than that for the signal when changing ϑ_{col} . In addition, $\mu_{\text{max}N} < \mu_{\text{max}N}$ always holds in the considered cases.

Tab. 4.1 and Tab. 4.2 list the numbers of signal and background photons per shot at the corresponding values $\mu_{\text{max}N}$ and $\mu_{\text{max}N}$, respectively. A comparison of these values confirms that the number of discernible signal photons increases with ϑ_{col} . Furthermore, the two tables confirm that the maximum of discernible signal photons for a fixed choice of ϑ_{col} is always

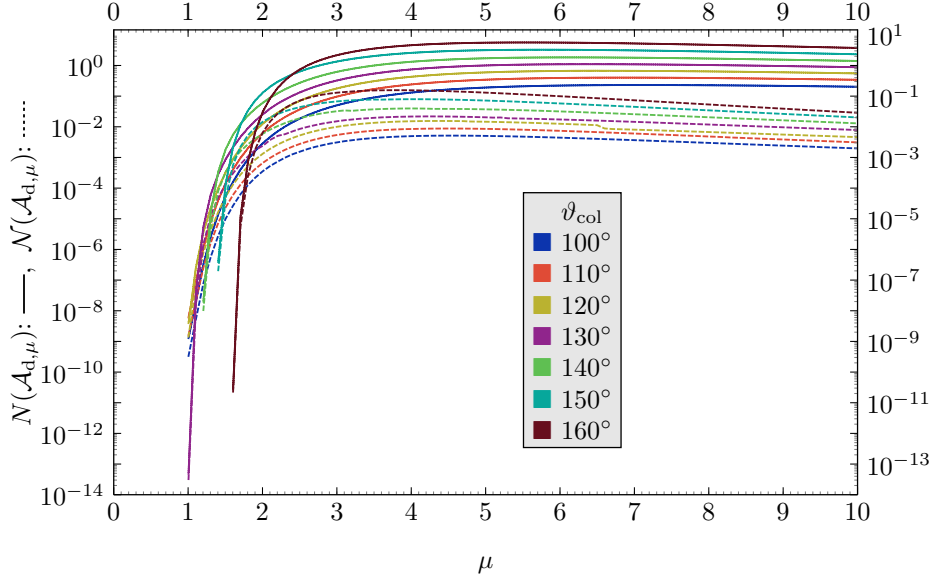


Figure 4.9.: Number of discernible signal photons $N(\mathcal{A}_{d,\mu})$ and corresponding background photons $N(\mathcal{A}_{d,\mu})$ over μ for two-beam (circular probe) collisions. Number of signal (solid) and background photons (dashed) in solid angle region $\mathcal{A}_{d,\mu}$ as a function of $\mu = w_x/w_0 = w_y/w_0$ for different collision angles ϑ_{col} . Both lasers have the same frequencies $\omega_0 = 1.55 \text{ eV}$, pulse energy $W = 25 \text{ J}$, and duration $\tau = 25 \text{ fs}$ (FWHM). The pump has a waist size $w_0 = \frac{2\pi}{\omega_0}$.

ϑ_{col}	$\mu = \mu_{\text{max}N}$	$N(\mathcal{A}_{d,\mu_{\text{max}N}})$	$N(\mathcal{A}_{d,\mu_{\text{max}N}})$
100°	7.1	0.237	0.004
110°	6.9	0.414	0.006
120°	6.5	0.694	0.012
130°	6.4	1.139	0.017
140°	6.1	1.898	0.032
150°	5.8	3.376	0.062
160°	5.5	5.839	0.118

Table 4.1.: Maximum numbers of discernible signal photons $N(\mathcal{A}_{d,\mu_{\text{max}N}})$ and its corresponding relative probe waist size $\mu_{\text{max}N}$ for two-beam (circular probe) collision. The maximum of the signal is determined for different collision angles ϑ_{col} at $\mu = \mu_{\text{max}N}$ for the corresponding region of discernible signal $\mathcal{A}_{d,\mu_{\text{max}N}}$. For comparison, the corresponding number of background photons $N(\mathcal{A}_{d,\mu_{\text{max}N}})$ is also given here. See Fig. 4.9 for the laser parameters employed here.

found at higher values of μ than the maximum of the background, determined in the region of the dominant signal $\mathcal{A}_{d,\mu}$. By definition of the studied region, the signal in Tab. 4.1 and Tab. 4.2 is always higher than the corresponding background.

To contextualize the observed maxima of discernible signal photons to the area of the corresponding region, we plot the areas as a function of width, analogously as in Fig. 4.5 for $\vartheta_{\text{col}} = 160^\circ$. Fig. 4.10 illustrates these areas for different collision angles ϑ_{col} . Interestingly, the area of the regions $\mathcal{A}_{d,\mu}$ decreases with increasing angle ϑ_{col} – except for the results with collision angle $\vartheta_{\text{col}} = 100^\circ$. For example, with $\vartheta_{\text{col}} = 130^\circ$ at $\mu_{\text{max}}^{\text{Sig}} = 6.4$ we find

4.1. Signature of QED Vacuum Nonlinearities in a Two-Beam Collision

ϑ_{col}	$\mu = \mu_{\text{max}N}$	$N(\mathcal{A}_{\text{d},\mu_{\text{max}N}})$	$\mathcal{N}(\mathcal{A}_{\text{d},\mu_{\text{max}N}})$
100°	4.5	0.169	0.005
110°	4.5	0.309	0.009
120°	4.4	0.524	0.016
130°	4.2	0.838	0.022
140°	4.0	1.367	0.041
150°	4.0	2.669	0.082
160°	3.8	4.340	0.161

Table 4.2.: Maximum numbers of background photons $\mathcal{N}(\mathcal{A}_{\text{d},\mu_{\text{max}N})$ and its corresponding relative probe waist size $\mu_{\text{max}N}$ for two-beam (circular probe) collision. The maximum of the background is determined for different collision angles ϑ_{col} at $\mu = \mu_{\text{max}N}$ for the corresponding region of discernible signal $\mathcal{A}_{\text{d},\mu_{\text{max}N}}$. For comparison, the corresponding number of signal photons $N(\mathcal{A}_{\text{d},\mu_{\text{max}N})$ is also given here. See Fig. 4.9 for the laser parameters employed here.

$A(\mathcal{A}_{\text{d},6.4}) \approx 1.10\pi$, whereas for $\vartheta_{\text{col}} = 160^\circ$ we have $A(\mathcal{A}_{\text{d},6.4}) \approx 0.85\pi$. This indicates that the strength of the signal is more important than the size of the region where the signal surpasses the background. The fact that the area $A(\mathcal{A}_{\text{d},\mu})$ has a qualitatively different trend determined at the angle $\vartheta_{\text{col}} = 100^\circ$ is due to the direction of the pump laser and the associated higher influence of the probe waist on the upper bound $\vartheta_{\text{u}}(\varphi)$.

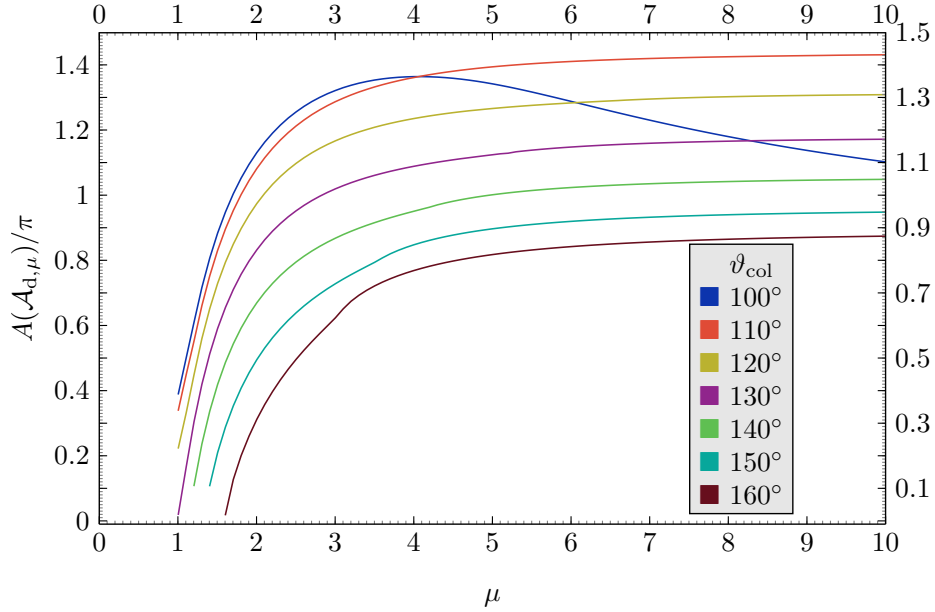


Figure 4.10.: Area of the solid angle region $\mathcal{A}_{\text{d},\mu}$ of discernible signal over μ for two-beam (circular probe) collision with different $\vartheta_{\text{col}} = 160^\circ$. The collision angles ϑ_{col} are given in the legend. See Fig. 4.9 for the laser parameters employed here.

To conclude the analysis using a probe with circular cross section, a summary of the main finding follows. In the collision of two equal laser pulses under a set of angles from $\vartheta_{\text{col}} = 100^\circ$ to $\vartheta_{\text{col}} = 160^\circ$, which differ only in the width of their rotationally symmetric beam waists, solid angle regions $\mathcal{A}_{\text{d},\mu}$ can be observed where the number of signal photons surpasses the number of background photons. Contrary to the observations of previous work

in the all-optical regime, which essentially focused on the signal intensity and did not make any quantitative comparison with the background, minimal focusing of the probe laser does not lead to a maximum yield of discernible signal photons. The analysis presented here shows how the signal becomes both discernible and maximized.

Probe With Elliptical Cross Section

In a next step we turn to a probe beam with an elliptical cross section. To this end we chose two independent waist sizes $w_x = \mu_x w_0$ and $w_y = \mu_y w_0$ for the probe beam. These values determine the two semi-axes of the elliptic cross section, where w_x lies in the collision plane.

From the analysis of circular cross sections discussed in the previous subsection, we know that the signal $N(\mathcal{A}_{d,\mu})$ becomes maximal for $w_x = w_y = \mu_{\max N}$. The tighter the focusing, the larger the intensity, which results in a stronger signal. However, at the same time the divergence of the beam is increased, so that the discernible signal generically decreases. If this beam is now focused harder only along the one of the semi-axes of the ellipsis, the signal is still expected to increase, whereas it remains discernible in the perpendicular direction characterized by keeping the value $\mu_{\max N}$ fixed. For given other parameters such an elliptical cross section is expected to result in a larger yield of discernible signal photons $N(\mathcal{A}_{d,\mu})$ [108, 163]. This effect is shown schematically in Fig. 4.11.

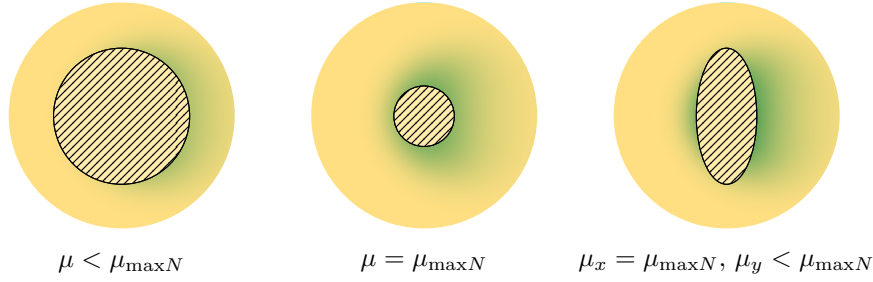


Figure 4.11.: *Schematic of the possible increase in the yield of discernible signal photons by an elliptical probe beam.* The color gradient from yellow to green qualitatively indicates the strength of the signal in the far field, where yellow means no signal and the hatched area represents the region in the far field where the background of the probe dominates. On the left, the sample has a circular cross section with relative waist size $\mu < \mu_{\max N}$, in the center the waist is larger, $\mu = \mu_{\max N}$, so that the discernible photon number becomes maximal. On the right, a probe with elliptical cross section with $\mu_x = \mu_{\max N}$ and $\mu_y < \mu_{\max N}$ is selected. With $\mu < \mu_{\max N}$ the signal density increases but the region of detectable signal becomes larger. The signal-photon densities are estimated for a collision of two beams with $\vartheta_{\text{col}} = 160^\circ$.

For generic choices of μ_x and μ_y the parameter space is significantly increased in comparison to the case of the rotationally symmetric case characterized by a single parameter $\mu = \mu_x = \mu_y$. For convenience and to simplify the following discussion we fix the parameter μ_x to the value maximizing the signal in the case for a probe with circular cross section for the corresponding collision angle ϑ_{col} , i.e. set $\mu_x = \mu_{\max N}(\vartheta_{\text{col}})$, cf. Tab. 4.1. The other parameter μ_y is varied in the range $\mu_y(\vartheta_{\text{col}}) \in [1, \mu_{\max N}(\vartheta_{\text{col}})]$. We choose μ_y as free parameter,

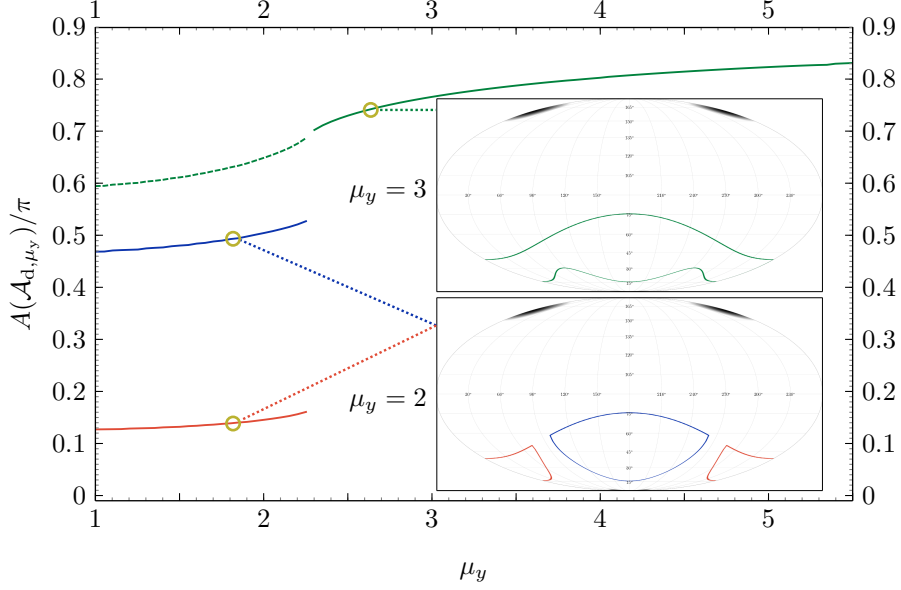


Figure 4.12.: Area of the solid angle region \mathcal{A}_{d,μ_y} of discernible signal over μ_y for two-beam (elliptic probe, $\mu_x = \mu_{\max N}$) collision with $\vartheta_{\text{col}} = 160^\circ$. For low values of μ_y the region \mathcal{A}_{d,μ_y} is separated into two parts, as illustrated by the red and blue colored curves. Their sum yields the dashed green curve. The inlays show Mollweide plots of the areas for the example values of $\mu_y = 2$ and $\mu_y = 3$. For $\mu_y = 3$ the region is simply connected (green solid line). Here we consider the collision of two beams of equal frequency $\omega_0 = 1.55 \text{ eV}$, pulse duration $\tau = 25 \text{ fs}$ (FWHM), and pulse energy $W = 25 \text{ J}$. The pump (probe) has a circular (elliptical) cross section with focus waist size $w_0 = \frac{2\pi}{\omega_0}$ ($w_x = \mu_{\max N}$, $w_y = \mu w_0$).

since this leads to the maximum possible value of discernible signal photons at $\vartheta_{\text{col}} = 160^\circ$.

In a first step, we focus on a collision of angle $\vartheta_{\text{col}} = 160^\circ$. Previously, we established for this angle that the choice of $\mu_{\max N} = 5.5$ maximizes the discernible signal for a rotationally symmetric probe. Therefore we set $\mu_x = 5.5$ and keep μ_y as a free parameter. At the same time, the other parameters, of course, remain unchanged.

First we consider the angular regions \mathcal{A}_{d,μ_y} where the signal dominates the background. Here the index μ_y indicates the parameter to be varied. In Fig. 4.12 we study the discernible solid angle area $A(\mathcal{A}_{d,\mu_y})$ as function of μ_y . We observe something which has not appeared before: For small values of μ_y there exist two distinct angular regions where the signal becomes discernible. This is illustrated in the Fig. 4.12 by the red and blue curves representing the areas of these two regions; the red (blue) curve measures the area around $\varphi = 0$, we denote the region by $\mathcal{A}_{d,\mu_y}^{(1)}$, and the blue curve indicates the area of the region $\mathcal{A}_{d,\mu_y}^{(2)}$, located around $\varphi = 180^\circ$. In Fig. 4.12 the third, dashed green curve indicates the sum of both areas, $A(\mathcal{A}_{d,\mu_y}^{(1)} \cup \mathcal{A}_{d,\mu_y}^{(2)}) = A(\mathcal{A}_{d,\mu_y})$. For $\mu_y \approx 2.3$ the two regions unite and beyond this value only a single angular region where the signal is discernible persists; cf. the green solid line. Interestingly, the location of μ_y where the two regions merge amounts to an inflection point in the angular area. Fig. 4.12 also shows two representative Mollweide projections of the boundaries of these regions for $\mu_y = 2$ and $\mu_y = 3$.

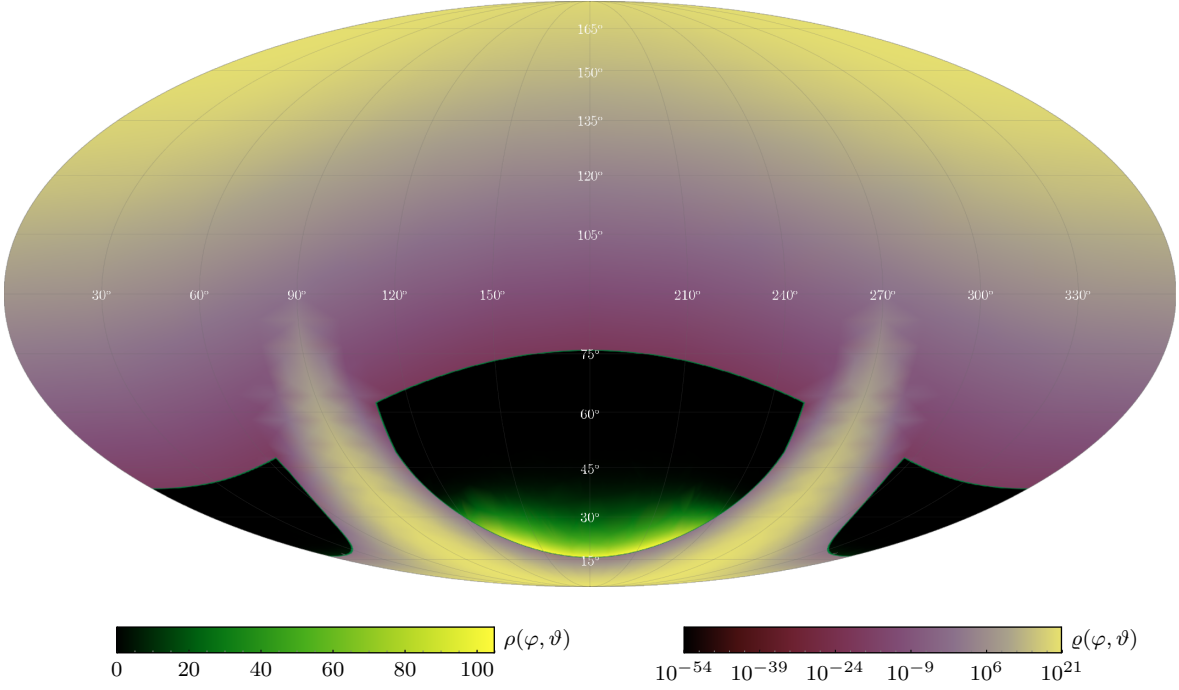


Figure 4.13.: *Mollweide plot of signal and background density for a two-beam (elliptical probe) collision with $\vartheta_{\text{col}} = 160^\circ$ and $\mu_x = 5.5$, $\mu_y = 1$.* The Mollweide plot (longitude φ , latitude ϑ) gives the signal-photon density $\rho(\varphi, \vartheta)$ and the density of the background $\varrho(\varphi, \vartheta)$. The region where $\rho(\varphi, \vartheta) = \varrho(\varphi, \vartheta)$ is highlighted by the green frame, $\rho(\varphi, \vartheta) > \varrho(\varphi, \vartheta)$ is illustrated with the green linear color function and for the complementary region $\rho(\varphi, \vartheta) < \varrho(\varphi, \vartheta)$ the purple logarithmic color function is chosen. We consider the collision of two beams of equal frequency $\omega_0 = 1.55$ eV, pulse duration $\tau = 25$ fs (FWHM) and pulse energy $W = 25$ J for $\vartheta_{\text{col}} = 160^\circ$. The pump (probe) beam has a circular (elliptical) cross section with waist radius $w_0 = \frac{2\pi}{\omega_0}$ ($w_x = w_0$, $w_y = 5.5w_0$).

Tracing these areas in Mollweide projections as a function of μ_y , it can be observed how the two regions $\mathcal{A}_{\text{d},\mu_y}^{(1)}$ and $\mathcal{A}_{\text{d},\mu_y}^{(2)}$ slowly converge and finally merge. In this process the upper bounds $\vartheta_{\text{u}}^{(m)}(\varphi)$ do not change significantly; only the lower bounds $\vartheta_{\text{l}}^{(m)}(\varphi)$ visibly change with μ_y predominantly in the vicinity of $\varphi = 90^\circ$ and $\varphi = 270^\circ$. These angles indicate here the semi-axis of the probe waist w_x .

In addition, we compare the properties of the two disjoint regions for the example value of $\mu_y = 2$. It is obvious that the area $A(\mathcal{A}_{\text{d},2}^{(1)})$ is much larger than $A(\mathcal{A}_{\text{d},2}^{(2)})$, since $A(\mathcal{A}_{\text{d},2}^{(2)})$ is only $\sim 22.3\%$ of the total area $A(\mathcal{A}_{\text{d},2})$. Interestingly, only 3.0% of the background photons and 0.5% of the signal photons are located in this 22.3% of the total area. In absolute numbers, we count around 0.02 signal photons per shot in $\mathcal{A}_{\text{d},2}^{(2)}$ and 7.22 in $\mathcal{A}_{\text{d},2}^{(1)}$. An analogous behavior is observed for beams with elliptical average, even more, the effect is amplified by the different beam waists.

Fig. 4.13 illustrates the density of the discernible signal photons $\rho(\varphi, \vartheta)$ in the region where the signal surpasses the background. Additionally, the Mollweide projection in Fig. 4.13 shows the density of the background photons $\varrho(\varphi, \vartheta)$. Both densities are given for exemplary parameter choice $\mu_x = 5.5$, $\mu_y = 1$ and $\vartheta_{\text{col}} = 160^\circ$. In Fig. 4.13 it can be easily seen how the

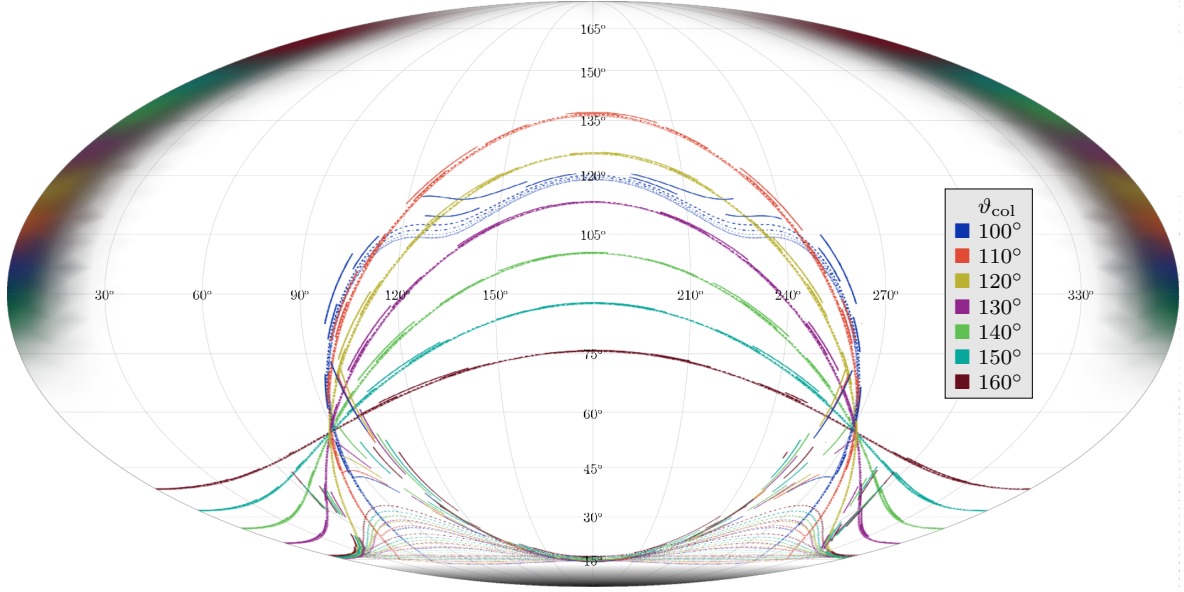


Figure 4.14.: Mollweide plot for equal signal and background density for two-beam (elliptical probe) collision with different angle ϑ_{col} and probe waists. The Mollweide plot (longitude φ , latitude ϑ) is showing the different forward beam axis of the pump laser pulses for different collision angles ϑ_{col} marked with different colors, see legend. Moreover, the direction of the probe is given by the black shade. The bounds $\vartheta_1(\varphi)$ and $\vartheta_u(\varphi)$ highlighting $\rho(\varphi, \vartheta) = \varrho(\varphi, \vartheta)$ are marked by colored lines for different values of $\mu_x = \mu_{\text{max}N}(\vartheta_{\text{col}})$, cf. Tab. 4.1, and $\mu_y = \frac{1}{5}(5 + l(\mu_{\text{max}N}(\vartheta_{\text{col}}) - 1))$ with $l \in \mathbb{N}^{[0,5]}$. The value of μ_y is encoded by the lines style. Larger μ_y means smaller spacing between dashes. The pump is focused to a waist of $w_0 = \frac{2\pi}{\omega_0}$ ($w_x = w_y = \mu\omega_0$) and the probe waists are $w_x = \mu_x w_0$ and $w_y = \mu_y w_0$. Both lasers have the same frequencies $\omega_0 = 1.55$ eV, pulse energy $W = 25$ J and duration $\tau = 25$ fs (FWHM).

the elliptical probe cross section affects the discernible signal; the other colored area in the lower half sphere reflects the elliptical probe cross section. In the region around $\theta = 180^\circ$ the signal is much stronger than in the region around $\varphi = 0$ separated from it. This is consistent with previous observations at $\mu_y = 2$: the former region accounts for 21.2% of the total area and contains only 3% of the background and 0.5% of the discernible signal photons. However, considering $\mu_y = 5.5$ which implies the union of both regions where the signal dominates the background, 11.63 signal photons per shot and 0.25 background photons per shot can be counted.

In Fig. 4.14 the bounds of the regions of the dominant signals for different collision angles ϑ_{col} are highlighted; there $\rho(\varphi, \vartheta) = \varrho(\varphi, \vartheta)$ holds. The parameter $\mu_x = \mu_{\text{max}N}(\vartheta_{\text{col}})$ is fixed for each collision angle ϑ_{col} to respective value in Tab. 4.1. At the same time, the parameter μ_y is varied in the interval $[1, \mu_{\text{max}N}(\vartheta_{\text{col}})]$. Fig. 4.14 clearly shows that the upper bound $\vartheta_u(\varphi)$ typically does not change appreciably with μ_y for constant ϑ_{col} . The only exception is the angle $\vartheta_{\text{col}} = 100^\circ$. Here the collision angle is close to $\vartheta_{\text{col}} \approx 90^\circ$; thus the influence of the waist of the probe beam on the upper bound $\vartheta_u(\varphi)$ is stronger.

At the same time the lower boundary $\vartheta_1(\varphi)$ changes strongly with ϑ_{col} . Here we observe that

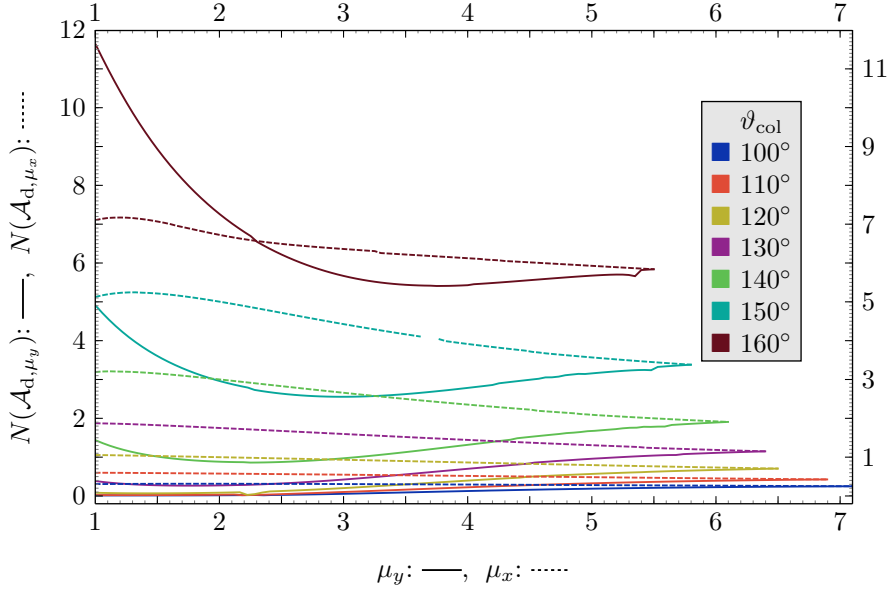


Figure 4.15.: Number of discernible signal photons $N(\mathcal{A}_{d,\mu_y})$ over μ_y and $N(\mathcal{A}_{d,\mu_x})$ over μ_x for two-beam (elliptical probe) collisions. The number of signal photons in the solid angle region \mathcal{A}_{d,μ_y} or \mathcal{A}_{d,μ_x} are determined for different collision angles ϑ_{col} , see legend. The solid (dashed) lines indicate the number where $\mu_x = \mu_{\text{max}N}(\vartheta_{\text{col}})$ ($\mu_y = \mu_{\text{max}N}(\vartheta_{\text{col}})$) is fixed and μ_y (μ_x), i.e. the waist size orthogonal to (in) the collision plane, is the free parameter. Both lasers have the same pulse frequencies $\omega_0 = 1.55$ eV energy $W = 25$ J and duration $\tau = 25$ fs (FWHM). The pump has a waist size $w_0 = \frac{2\pi}{\omega_0}$ and the probe waists are $w_x = \mu_{\text{max}N}(\vartheta_{\text{col}})$, cf. Tab. 4.1, and $w_y = \mu_y w_0$ (solid) or $w_y = \mu_{\text{max}N}(\vartheta_{\text{col}})$, cf. Tab. 4.1, and $w_x = \mu_y w_0$ (dashed).

with decreasing μ_y pronounced local maxima around $\varphi = 90^\circ$ and $\varphi = 270^\circ$ are appearing. They are oriented along the elliptical cross section of the probe laser. If the value of $\vartheta_1(\varphi)$ at the maxima reaches the corresponding upper bound $\vartheta_u(\varphi)$, then two separate angular regions are formed. However, this effect appears only at larger collision angles – starting from $\vartheta_{\text{col}} \simeq 120^\circ$ – and becomes more pronounced with larger angles ϑ_{col} .

The area of the discernible signal increase with μ_y for each ϑ_{col} . At larger collision angles ϑ_{col} the total area $A(\mathcal{A}_{d,\mu_y})$ is smaller than for smaller ϑ_{col} .

In Fig. 4.15 we highlight the dependence of the number of discernible signal photons $N(\mathcal{A}_{d,\mu_y})$ as function of μ_y for different collision angles while we fix $\mu_x = \mu_{\text{max}N}(\vartheta_{\text{col}})$ for each collision angle ϑ_{col} . Additionally, we give the number of discernible signal photons as a function of μ_x using $\mu_y = \mu_{\text{max}N}(\vartheta_{\text{col}})$, see dashed lines in Fig. 4.15. Thereby the beam waist is kept constantly orthogonal to the collision plane and varied in the collision plane. Obviously, the discernible signal $N_{\text{Sig}}(\mathcal{A}_{d,\mu_y})$ or $N_{\text{Sig}}(\mathcal{A}_{d,\mu_x})$ increases with increasing collision angle ϑ_{col} for each value of μ_y or μ_x , respectively.

First we consider the results with fixed μ_x and varying μ_y . It is interesting to note that two maxima can occur in the intervals studied. In case of variable μ_y , the value $N(\mathcal{A}_{d,\mu_{\text{max}N}})$ for $\mu_y = \mu_{\text{max}N}$ is a maximum; this is already evident from the discussion of the setup with a circular probe.

ϑ_{col}	μ_x	μ_y	$N(\mathcal{A}_{\text{d},\bar{\mu}})$	$\mathcal{N}(\mathcal{A}_{\text{d},\bar{\mu}})$
100°	1	7.1	0.294	0.009
110°	1	6.9	0.586	0.009
120°	1	6.5	1.044	0.016
130°	1	6.4	1.864	0.032
140°	1.113	6.1	3.205	0.061
150°	1.32	5.8	5.243	0.116
160°	5.5	1.	11.633	0.248

Table 4.3.: *Maximum numbers of discernible signal photons $N(\mathcal{A}_{\text{d},\mu_{y,\text{max}N}})$ and its corresponding relative probe waist sizes μ_x and μ_y for two-beam (elliptic probe) collision.* The maximum of the signal is determined for different collision angles ϑ_{col} at $\mu_x = \mu_{\text{max}N}(\vartheta_{\text{col}})$, cf. Tab. 4.1, or μ_y for the corresponding region of discernible signal $\mathcal{A}_{\text{d},\bar{\mu}}$. These parameters are selected according to the maximum signal, whereby at least one parameter fulfills $\mu_x = \mu_{\text{max}N}$ or $\mu_y = \mu_{\text{max}N}$. For comparison, the corresponding number of background photons $\mathcal{N}(\mathcal{A}_{\text{d},\bar{\mu}})$ is also given here. See Fig. 4.15 for the laser parameters employed here.

For all solid graphs with $\vartheta_{\text{col}} > 100^\circ$ there exists a local minimum in the interval $\mu_y \in [1, \mu_{\text{max}N}(\vartheta_{\text{col}})]$. Therefore, the function increases with μ_y smaller than μ_y at this local minimum. This leads to a maximum value (it does not have to be a local maximum) at the position $\mu_y = 1$. However, this value is only for the collision angles $\vartheta_{\text{col}} = 150^\circ$ and $\vartheta_{\text{col}} = 160^\circ$ larger than the signal-photon number at $\mu_y = \mu_{\text{max}N}$. This implies that elliptical cross sections do not result in an increased discernible signal for smaller collision angles $\vartheta_{\text{col}} < 150^\circ$ as long as the semi-axes $\mu_y < \mu_{\text{max}N}$ and $\mu_x = \mu_{\text{max}N}$ are fixed. On the other hand, for large collision angles ϑ_{col} elliptical probe cross sections can significantly increase the discernible signal. For $\vartheta_{\text{col}} = 150^\circ$ we determine $N(\mathcal{A}_{\text{d},1}) = 4.90$ signal photons per shot, for $\vartheta_{\text{col}} = 160^\circ$ it is even $N(\mathcal{A}_{\text{d},1}) = 11.63$.

If, on the other hand, we consider μ_x as a free parameter and fix $\mu_y = \mu_{\text{max}N}$ for the corresponding angle ϑ_{col} , we find that in every case the number of discernible signal photons increases with decreasing μ_x . Except for $\vartheta_{\text{col}} = 140^\circ$, $\vartheta_{\text{col}} = 150^\circ$ and $\vartheta_{\text{col}} = 160^\circ$, the maximum value is always found at $\mu_x = 1$ and $\mu_y = \mu_{\text{max}N}$, see Tab. 4.3. Moreover, except for the angle $\vartheta_{\text{col}} = 160^\circ$, the maxima are always larger than in the case of variable μ_y and fixed μ_x , because with decreasing collision angle ϑ_{col} the pronounced maxima of $\rho(\varphi, \vartheta_1(\varphi))$ of the signal are closer to $\varphi = 0$ or $\varphi = 180^\circ$, i.e. the collision plane. Only at the angle $\vartheta_{\text{col}} = 160^\circ$ with $\varphi = 114.5^\circ$ and $\varphi = 245.5^\circ$ the pronounced maxima are closer to the plane of w_y than w_x . At the same time, the maximum of $N(\mathcal{A}_{\text{d},\bar{\mu}})$ for $\vartheta_{\text{col}} = 160^\circ$ is significantly larger for $\mu_y = 1$, $\mu_x = \mu_{\text{max}N}$, which is why we focus here on the case of variable μ_y .

As is visible from the small kinks in the data line, Fig. 4.15 contains numerical artifacts; they become more pronounced as the collision angle ϑ_{col} increases. These artifacts occur when two regions merge, as shown in Fig. 4.12 and are likely to be caused by a reduced precision of the angular integration. Also, the artifacts appear at the value for μ_y where $\varphi_i = 0$ and $\varphi_f = 2\pi$ for the boundary functions $\vartheta_{\text{l/u}}(\varphi)$ of $\mathcal{A}_{\text{d},\mu_y}$ appears for the first time. As the artifacts are on the $\mathcal{O}(1\%)$ level, they are acceptable for the present purpose.

In Tab. 4.3 we list the maxima of the discernible signal in the considered interval of $\mu_x \in [1, \mu_{\max N}]$, $\mu_y = \mu_{\max N}$ or $\mu_x = \mu_{\max N}$, $\mu_y \in [1, \mu_{\max N}]$ together with its position μ_x , μ_y and the corresponding number of background photons. In comparison with Tab. 4.1 we notice that for all collision angles ϑ_{col} we find cases, where a probe with elliptic cross section leads to a higher amount of discernible signal photons. Accordingly, depending on the possibilities of the experimental realization, an elliptical focusing of the probe beam can lead to a higher degree of measurability.

4.1.4. Discernible Vacuum Birefringence

In this last section, we consider vacuum birefringence. To this end, we concentrate exclusively on the collision angle $\vartheta_{\text{col}} = 160^\circ$ and the two experimental constellations (circular and elliptical cross section) where polarization insensitive measurements result in a maximum measurable signal, i.e. we use the waist parameters $\mu = 5.5$ for a probe with circular cross section or $\mu_x = 5.5$, $\mu_y = 1$, respectively. In a special scenario probing vacuum birefringence, the signal is maximized at an angle of $\beta_2 = 45^\circ$, see [165]. Therefore, we now set the polarization angle β_2 of the pump beam to $\beta_2 = 45^\circ$. Further references discuss vacuum birefringence from a general point of view, cf. [106, 114, 118, 217].

Furthermore, we now consider only signal photons whose polarization is perpendicular to the original linear polarization of the probe beam. We ensure this by determining the signal with flipped polarization angle β_\perp . Here it follows from this condition $\mathbf{e}_{\beta_\perp} \cdot \mathbf{e}_{E_1} = 0$ that $\beta_\perp = \arctan(\cos \vartheta \cot \varphi)$ holds.

The same steps for the determination of the number of signal photons as already described in Sec. 4.1.3 follow, with the restriction that no sum over the polarizations is performed, instead we use $(p) \rightarrow \beta_\perp$ and derive a signal-photon density

$$\rho_\perp(\varphi, \vartheta) = \frac{1}{(2\pi)^7} \frac{2}{45^2} \left(\frac{e}{m_e} \right)^8 \left[g_{\beta_\perp;121}^2 \int_0^\infty dk k^3 \mathcal{I}_{121}^2 + g_{\beta_\perp;212}^2 \int_0^\infty dk k^3 \mathcal{I}_{212}^2 \right] \quad (4.35)$$

analogously to Eq. (4.26). Compared to the result for polarization insensitive measurements, see Eq. (4.26), only the value of the function $g_{\beta_\perp;iji}$ changes. Using $\beta_2 = \frac{\pi}{4}$ and $\beta_\perp = \arctan(\cos \vartheta \cot \varphi)$, we determine

$$g_{\beta_\perp;121}^2 = \frac{\sin^4 \varphi (\cos \vartheta_{\text{col}} - 1)^2}{4 (2 \cos^2 \varphi \cos^2 \vartheta + 2 \sin^2 \varphi)} \left(7 \frac{\cos \vartheta}{\sin^2 \varphi} - 7 \frac{\cos^2 \varphi \cos^2 \vartheta}{\sin^2 \varphi} + 4 \frac{\cos \varphi \sin^2 \vartheta}{\sin^2 \varphi} - 7 \right)^2 \quad (4.36)$$

and

$$\begin{aligned} g_{\beta_\perp;212}^2 = & \frac{\sin^4 \varphi (\cos \vartheta_{\text{col}} - 1)^2}{16 (\cos^2 \varphi \cos^2 \vartheta + \sin^2 \varphi)} \left(3 \cos \vartheta_{\text{col}} \left(\frac{\cos^2 \varphi \cos^2 \vartheta}{\sin^2 \varphi} + 1 \right) - 3 \frac{\cos \vartheta}{\sin^2 \varphi} \right. \\ & \left. - 11 \frac{\cos \varphi}{\sin \varphi} \sin^2 \vartheta + \frac{\sin \vartheta \sin \vartheta_{\text{col}}}{\sin^2 \varphi} \left(3 \frac{\cos \varphi \cos \vartheta}{\sin \varphi} + 11 \right) \right)^2. \end{aligned} \quad (4.37)$$

Furthermore, the Fourier integrals and the energy integration persists equally in comparison

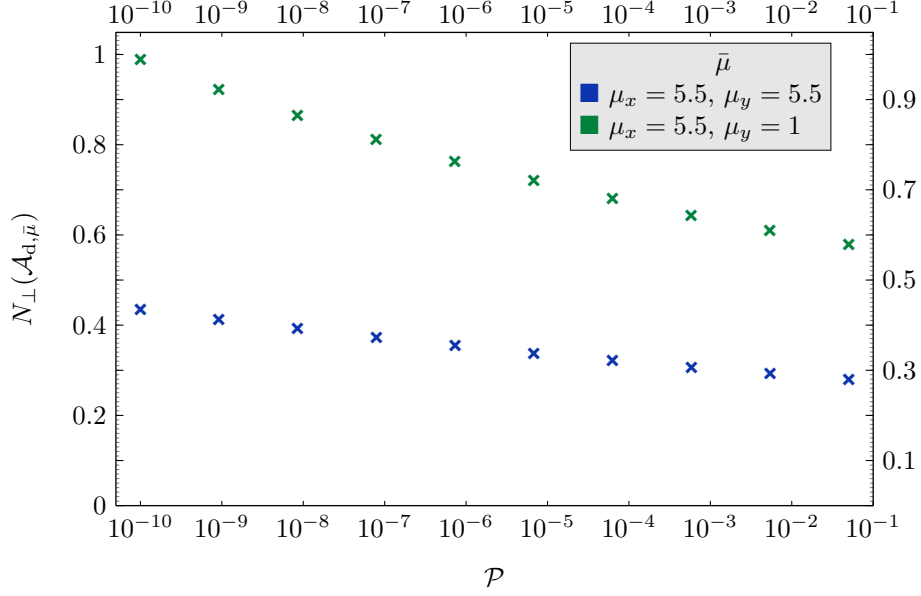


Figure 4.16.: Number of discernible polarization flipped signal photons in the solid angle regime $\mathcal{A}_{d, \bar{\mu}}$ as function of the purity \mathcal{P} of the polarization of the probe beam. Here only the collision scenarios for a collision angle $\vartheta_{\text{col}} = 160^\circ$ are analyzed. Both linear polarized driving lasers deliver photons of frequency $\omega_0 = 1.55$ eV at a pulse energy $W = 25$ J and duration $\tau = 25$ fs (FWHM). The pump is focused to $w_0 = 2\pi/\omega_0$. The probe waists are $w_x = \mu_x w_0$ and $w_y = \mu_y w_0$.

to Eq. (4.26). The full determination of the signal-photon density is completed by substituting $\sum_{(p)} g_{(p);iji}^2 \rightarrow g_{\beta_{\perp};iji}^2$ in Eq. (4.30). The number of polarization flipped signal photons $N_{\perp}(\mathcal{A})$ in the solid angle region \mathcal{A} yields analogous to the eq. 4.33.

To estimate the background, we introduce the polarization purity \mathcal{P} . We assume that all photons beyond this purity represent a background when measuring the polarization flipped signal. The purity depends on the optical instruments used in the experiments to adjust the driving laser pulses. For high-intensity x-ray pulses polarization purity of about 10^{-10} is achievable [146, 147]. However, we restrict ourselves to all-optical scenarios. Therefore, polarization purities are usually lower compared the x-ray purities. For generality, we investigate the effects of purities in the range $\mathcal{P} = 10^{-1}$ to $\mathcal{P} = 10^{-10}$ in logarithmic steps.

In order to estimate conservatively the solid angle region of the discernible signal photons we use a slightly different discernibility criterion

$$\mathcal{A}_{d, \bar{\mu}} = \left\{ (\varphi, \vartheta) \in [0, 2\pi] \times [0, \pi) \mid \rho_{\perp}(\varphi, \vartheta) \geq \mathcal{P} \varrho_1(\varphi, \vartheta) + \varrho_2(\varphi, \vartheta) \right\}, \quad (4.38)$$

where we do not apply any polarization constraints to the background of the pump beam, since this has no influence in the relevant region of the flipped signal and additionally gives us an upper bound $\vartheta_u(\varphi)$ for easier numerical evaluation of the solid angle integrals.

In Fig. 4.16, the number of discernible signal photons in the corresponding regions $N_{\perp}(\mathcal{A}_{d, \bar{\mu}})$ is plotted as function of the purity \mathcal{P} . Here we distinguish between a probe beam with elliptical and circular cross section. In both cases there is always a sufficient number of signal

photons that can be measured; as expected the number decreases linearly with the logarithm of the purity \mathcal{P} . The same observation was made for a collision with a high intensity x-ray probe pulse [119].

Finally, we briefly discuss the results using the purity $\mathcal{P} = 10^{-10}$. However, since all studied purities result in a relatively high number of discernible signal photons, cf. Fig. 4.16, this discussion can be adopted for different purities. Considering a probe beam with circular cross section we obtain $N_{\perp}(\mathcal{A}_{d,5.5}) = 0.44$ signal photons per shot against a background of $\mathcal{N}_{\perp}(\mathcal{A}_{d,5.5}) = 0.01$ on an area of $A(\mathcal{A}_{d,5.5}) = 0.85\pi$. In the case of the elliptically focused probe beam we get $N_{\perp}(\mathcal{A}_{d,1}) = 1.00$ discernible signal photons per shot and a background of $\mathcal{N}_{Bg,\perp}(\mathcal{A}_{d,1}) = 0.03$. The area of the region of the discernible signal is $A(\mathcal{A}_{d,1}) = 0.66\pi$.

To understand the quality of detection of these values, let us compare the result of discernible signal photons with the number of signal photons in the region $\mathcal{A}_{\frac{\pi}{4}} = \{(\varphi, \vartheta) \in [0, 2\pi] \times [0, \frac{\pi}{4}]\}$. This region corresponds to the forward cone of the probe laser with an aperture angle of 45° . Here we count $N_{\perp}(\mathcal{A}_{\frac{\pi}{4}}) = 0.86$ by using a probe beam with circular cross section or $N_{\perp}(\mathcal{A}_{\frac{\pi}{4}}) = 3.67$ with an elliptical probe, respectively. Due to the background, these numbers cannot be detected in an experiment. Accordingly, it is possible to measure a significant fraction 0.51% (0.27%) of the whole signal for a circular (elliptical) probe.

However, the number of driving laser photons beyond the output polarity occurring in $\mathcal{A}_{\frac{\pi}{4}}$ exceeds these numbers by far ($\mathcal{N}_{\perp}(\mathcal{A}_{\frac{\pi}{4}}) \approx 10^{20}$), which shows that our method for optimizing the measurement region of the signature of the quantum vacuum is also useful for the effect of birefringence.

4.2. Elastic and Inelastic Photon-Photon Scattering

In a second example the results of the channel analysis, cf. Sec. 3.2, are applied and discussed. Therefore, we consider an experimentally viable scenario involving the collision of several high-intensity laser pulses. Our main focus lies on the analysis and reconstruction of properties of the microscopic scattering processes giving rise to the dominant signal photon emission channels. Special attention is paid to signal-photon contributions which allow for a clear signal-to-background separation in experiment. In contrast to the previous study, no numerical method is used here to determine the regions of the discernible signals. Here, the focus is on other prominent criteria that enable such separation between signal and background. These are, for example, a distinct emission direction outside the forward cones of the main beams, or a frequency outside their spectra that allows unobstructed detection of the signal.

First, the setup of a potential experiment is explained in Sec. 4.2.1. This includes the conversion of an initial pulse to several pulses of different frequency. Following more general considerations about a prospective collision geometry involving beams of several colors, in Sec. 4.2.2 we analyze and outline the frequency and directional characteristics of the attainable signals and assess the possibility of their measurement against the background of the driving laser photons. In Sec. 4.2.3 we demonstrate in detail how the channel analysis can

be applied to understand the microscopic behavior of these results and further can be used to substantially enhance and simplify further studies. In particular, interpretations in terms of elastic and inelastic scattering processes turn out to be useful. These considerations highlight an aspect of the vacuum emission approach which was not yet fully exploited in previous all-optical quantum vacuum studies.

This section is strongly oriented along the results published in [160] and [164] and explicitly reproduces its contents.

4.2.1. Collision Geometry and Pulse Modeling

We suggest a special collision geometry of several driving laser pulses generating a tightly focused field configuration. Therefore, we introduce a superposition of three multi-color pulses labeled by $i \in \{1, 2, 3\}$ resulting in a narrow strongly peaked field region forming the apex of a regular pyramid. Our aim is to generate a narrow high-intensity scattering center. By superimposing laser fields with different frequency and focusing them on the same spot coherently we try to construct such a center. It has been demonstrated that by using the mechanism of coherent harmonic focusing quantum vacuum signatures can be boosted substantially. Studies of coherent harmonic focusing have so far considered only counter-propagating laser beams along one axis [159, 226, 227].

Moreover, we assume that each pair of the beams 1-3 encloses the same angle ϑ_{pyr} , such that the corresponding propagation directions $\hat{\mathbf{k}}_i$ satisfy

$$\hat{\mathbf{k}}_i \cdot \hat{\mathbf{k}}_j = (1 - \cos \vartheta_{\text{pyr}}) \delta_{ij} + \cos \vartheta_{\text{pyr}} \quad (4.39)$$

for $i, j \in \{1, 2, 3\}$ with Kronecker delta δ_{ij} . Accordingly we choose these unit wave vectors as

$$\hat{\mathbf{k}}_i = -a \left(\cos(2\pi \frac{i-1}{3}) \mathbf{e}_x + \sin(2\pi \frac{i-1}{3}) \mathbf{e}_y \right) + \sqrt{1-a^2} \mathbf{e}_z \quad (4.40)$$

with $a = \sqrt{2(1 - \cos \vartheta_{\text{pyr}})}/3$. This implies that the sum of all unit wave vectors is proportional to the vector \mathbf{e}_z ; this is the north pole of \mathbf{k} in spherical coordinates for the subsequent studies.

In addition, we add another pulse, denoted with index $i = 0$, almost counter-propagating to the other beams. It collides with the apex of the pyramid of the pyramid formed by beams 1-3 and its propagation direction is given by

$$\hat{\mathbf{k}}_0 = -\mathbf{e}_z. \quad (4.41)$$

Fig. 4.17 illustrates the geometry of this collision. The angle between beam 0 and any other beam is $\vartheta_{\text{apx}} = \pi - \arctan(a/\sqrt{1-a^2})$. In the remainder of this work, we set $\vartheta_{\text{pyr}} = \frac{\pi}{2} = 90^\circ$, such that $\vartheta_{\text{apx}} = \pi - \arctan \sqrt{2} \approx 125.26^\circ$.

The four multi-color driving laser fields are envisioned to be generated by a single high-intensity laser system of the 10 PW class, such as is available at the ELI-NP project [138, 197], cf. Sec. 2.2.2 and Tab. 2.1, by employing beam-splitting and frequency doubling techniques. More specifically, we assume the initial laser system to deliver pulses of energy $W = 250 \text{ J}$

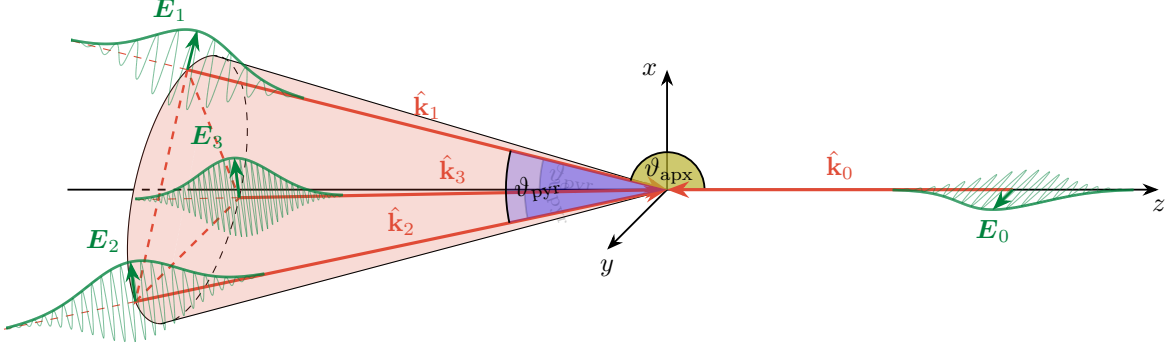


Figure 4.17.: *Illustration of a multi-color beam collision geometry.* The red arrows indicate the four unit vectors of the driving lasers. The corresponding directional electric fields are added in green. The temporal envelope is taken into account. To emphasize the regular pyramid spanned by beams 1, 2, 3, the corresponding base plane is shown with dashed lines. In addition, the cone spanned by these rays is indicated in red shading. Corresponding collision angles ϑ_{pyr} and ϑ_{apx} are added.

and duration $\tau = 25$ fs at a wavelength of $\lambda = 800$ nm. While each of the four laser fields generated in this way features exactly this pulse duration, we assume them to have different frequencies: beams 0 and 1 are fundamental frequency beams with $\omega_0 = \omega_1 = \frac{2\pi}{\lambda} \simeq 1.55$ eV, beam 2 is frequency-doubled $\omega_2 = 2\omega_0 = 3.1$ eV, and beam 3 is frequency-quadrupled $\omega_3 = 4\omega_0 = 6.2$ eV. Throughout this work, all pulses have a circular cross section and are focused to a waist spot size of $w_i = w_0 = \lambda$ at $\mathbf{r} = 0$, where all temporal pulse envelopes reach their maximum at $t = 0$. Furthermore, using the conventions introduced in Sec. 2.2.1, we measure their peak field amplitudes in units of the peak field \mathcal{E}_\star which could be achieved by focusing the initial laser pulse of energy $W = 250$ J to its diffraction limit. According to Eq. (3.25), it results in $\mathcal{E}_\star \approx 9 \times 10^{15}$ V/m.

We assume the driving laser fields to be well-described as paraxial Gaussian beams. The application of IRRA is justified here, because $\frac{w_i}{\zeta_{R,j}} = \frac{1}{\pi} \approx 0.318$ is valid for all beam combinations due to the same focusing. This value is clearly smaller than corresponding comparison values of the angles $|\sin \vartheta_{\text{pyr}}| = 1$ and $|\sin \vartheta_{\text{apx}}| = \sqrt{\frac{2}{3}}$, see Eq. (2.51).

Based on Sec. 2.2 and Sec. 3.2.1, in particular Eq. (2.49), the field amplitude of the i th beam is

$$\mathcal{E}_i(x) = A_i \mathcal{E}_\star e^{-4 \frac{(\zeta_i - t)^2}{\tau^2}} e^{-\frac{\mathbf{r}^2 - \zeta_i^2}{w_0^2}} \cos(\nu_i \omega_0 (\zeta_i - t)) , \quad (4.42)$$

where $\zeta_i = \mathbf{r} \cdot \hat{\mathbf{k}}_i$ and A_i gives the dimensionless relative amplitude, see Eq. (3.26). Analogously, we measure the oscillation frequencies of the beams in units of ω_0 , such that $\omega_i = \nu_i \omega_0$, with dimensionless relative frequencies ν_i . In the present case, here we have $\nu_0 = \nu_1 = 1$, $\nu_2 = 2$ and $\nu_3 = 4$.

Besides, we fix the linear polarizations of the laser fields, by choosing $\mathbf{e}_{E_0} = \mathbf{e}_y$ and $\mathbf{e}_y \cdot \mathbf{e}_{E_i} = 0$ for $i \in \{1, 2, 3\}$. This choice is motivated by the observation that the total number of signal photons attainable in a polarization insensitive measurement is maximized for counter-propagating beams with a relative polarization difference of $\pi/2$ [228]. This is also the case for

our setup, where beam 0 can be considered as effectively counter-propagating the combined field of beams 1-3. Together with the transversality condition $\hat{\mathbf{k}}_i \cdot \mathbf{e}_{E_i} = 0$ the above choice determines the polarization vectors of all laser fields up to a sign. Ensuring a positive sign for the x component, the polarization vectors of beams $i \in \{1, 2, 3\}$ read

$$\mathbf{e}_{E_i} = \frac{1}{\sqrt{1 - a^2 \sin^2(2\pi \frac{i-1}{3})}} \left(\sqrt{1 - a^2} \mathbf{e}_x + a \cos(2\pi \frac{i-1}{3}) \mathbf{e}_z \right). \quad (4.43)$$

The unit vectors for the associated magnetic fields are $\mathbf{e}_{B_i} = \hat{\mathbf{k}}_i \times \mathbf{e}_{E_i}$. In addition, Fig. 4.17 also shows the electric fields with its pulse envelope for a time shortly before the pulses collide.

Each frequency doubling process comes with a loss: we conservatively estimate the energy loss for the conversion process preserving the pulse duration as 50% [229]. Correspondingly, the energies $W_i = A_i^2 W$ of all beams do not add up to W but to $W^{\text{eff}} = \sum_{i=0}^3 W_i < W$. Only, for vanishing losses we would have $W^{\text{eff}} = W$. Here, we assume the beam splitting and higher harmonic generation to proceed in several steps. First, the original laser pulse of energy W is split into two parts: the part with energy $W_0 = (1 - q_0)W$ constitutes beam 0, and the remainder of energy $q_0 W$ is to be subdivided further; the factor $0 < q_0 < 1$ controls the partitioning ratio. Second, the remaining energy $q_0 W$ is again partitioned into a fundamental frequency part of energy $W_1 = q_0(1 - q_1)W$ constituting beam 1, and another one of energy $q_0 q_1 W$ which undergoes frequency doubling; as above $0 < q_1 < 1$. Accounting for the loss of 50% associated with the frequency doubling process, the latter contribution results in a frequency-doubled pulse of energy $\frac{1}{2} q_0 q_1 W$. In the last step, the procedure is repeated for the frequency-doubled pulse with a partitioning factor of $0 < q_2 < 1$. This results in an energy of $W_2 = \frac{1}{2} q_0 q_1 (1 - q_2) W$ for the frequency-doubled beam 2 and an energy of $W_3 = \frac{1}{4} q_0 q_1 q_2 W$ for the frequency-quadrupled beam 3. Hence, in the present scenario we have $A_0 = \sqrt{1 - q_0}$, $A_1 = \sqrt{q_0(1 - q_1)}$, $A_2 = \sqrt{q_0 q_1 (1 - q_2)/2}$ and $A_3 = \sqrt{q_0 q_1 q_2}/2$.

4.2.2. Analysis of the Signature of Quantum Vacuum Nonlinearities

The analysis of the signature of quantum vacuum nonlinearity in the experiment presented here is divided into three subsections. First, we discuss the effect of different distributions of the energy of the driving lasers on the signal in different frequency ranges. Subsequently, we proceed with a fixed splitting, knowing that it is arbitrary and the results can be adjusted. We investigate the different frequency and directional characteristics of the signal. At the end of this section, we discuss the discernibility of the signal.

To estimate the signal photons we use the full polarization insensitive signal-photon density $\rho(\varphi, \vartheta | \mathbf{k}_{\min}, \mathbf{k}_{\max}) = \sum_{p=1}^2 \rho_{(p)}(\varphi, \vartheta | \mathbf{k}_{\min}, \mathbf{k}_{\max})$, see Sec. 3.2 and in particular Eq. (3.64). Here, we especially observe the signal separated in different frequency regimes $\mathbf{k} \in [\mathbf{k}_{\min}, \mathbf{k}_{\max}]$. Due to the high number of different possible channel combinations we determine the full density numerically. The corresponding signal-photon number measured in the solid angle region \mathcal{A} is $N(\mathcal{A} | \mathbf{k}_{\min}, \mathbf{k}_{\max}) = \sum_{p=1}^2 N_{(p)}(\mathcal{A} | \mathbf{k}_{\min}, \mathbf{k}_{\max})$, see Eq. (3.23).

Consequences of beam splitting and losses

So far, we did not specify a particular choice of the dimensionless relative field amplitudes A_i of the driving laser beams. As detailed above, in an experiment these amplitudes can be adjusted by choosing the partition factors q_0 , q_1 and q_2 accordingly. For definiteness, we choose $q_0 = \frac{5}{6}$ in the following. In this way, a substantial fraction of the total laser energy is put into the beam that collides with the apex of the pyramid formed by the other beams.

We limit our discussion to three example distributions of the pulse energies of beam 1-3 forming the pyramid: either the pulse energy of each higher frequency component is doubled (such that $W_1 : W_2 : W_3 = 1 : 2 : 4$), bisected ($W_1 : W_2 : W_3 = 4 : 2 : 1$), or quartered ($W_1 : W_2 : W_3 = 16 : 4 : 1$). The explicit values of the required partition factors q_1 and q_2 are listed in Tab. 4.4, together with the respective effective energy W^{eff} put into the interaction region by all four driving laser pulses. Correspondingly, the associated energy loss is given by $W^{\text{loss}} = W - W^{\text{eff}}$.

	(a)	(b)	(c)
$W_1 : W_2 : W_3$	1 : 2 : 4	4 : 2 : 1	16 : 4 : 1
q_1	20/21	2/3	3/7
q_2	4/5	1/2	1/3
$W^{\text{eff}}[\text{J}]$	111.11	163.19	197.92
$W^{\text{loss}}[\text{J}]$	138.89	86.81	52.08
$N(4\pi 1.04 \text{ eV}, 2.06 \text{ eV})$	828.1	418.2	1447.8
$N(4\pi 2.59 \text{ eV}, 3.61 \text{ eV})$	3018.9	1240.8	1337.6
$N(4\pi 5.69 \text{ eV}, 6.71 \text{ eV})$	5037.7	1546.2	833.9
$N(4\pi 7.24 \text{ eV}, 8.26 \text{ eV})$	1.07	2.81	1.64

Table 4.4.: *Exemplary pulse-energies distributions for the multi-color pulse collision.* For each choice of energy distribution of pulse 1-3, we provide the values of the partition factors q_1 and q_2 required to ensure a given distribution for fixed $q_0 = 5/6$. W^{eff} is the effective energy put into the interaction region by all four beams and the associated energy loss is $W^{\text{loss}} = W - W^{\text{eff}}$. In addition, the evaluated signal-photon numbers $N(4\pi|k_{\text{min}}, k_{\text{max}})$ in all directions $\mathcal{A} = 4\pi$ are listed for three different frequencies intervals.

In the present scenario, we find substantial signal-photon contributions in the three distinct frequency regimes $1.04 \text{ eV} \lesssim k \lesssim 2.06 \text{ eV}$, $2.59 \text{ eV} \lesssim k \lesssim 3.61 \text{ eV}$ and $5.69 \text{ eV} \lesssim k \lesssim 6.71 \text{ eV}$, centered at the frequencies of the driving laser beams ω_0 , $2\omega_0$ and $4\omega_0$, respectively. Apart from these signals, it is noteworthy that we find a clear but comparably small signal in the frequency regime $7.24 \text{ eV} \lesssim k \lesssim 8.26 \text{ eV}$ peaked at a frequency of $5\omega_0$. The width of each of these regimes is 1.02 eV and has been chosen such as to cover the full signal; cf. also the discussion in Sec. 4.2.2 below. Tab. 4.4 lists the resulting pulse energies and signal-photon numbers in the considered frequency regimes. In the first approach, (a), we double the pulse energy put into each higher harmonic. This leads to a relatively high number of signal photons with $k \simeq 4\omega_0$ as compared to the other regimes. Interestingly, even when bisecting the pulse energy put into each higher harmonic, (b), the number of signal photons with $k \simeq 4\omega_0$ slightly surpasses that for $k \simeq 2\omega_0$. However, most signal photons are induced at $k \simeq \omega_0$. When

quartering the energy put into each higher harmonic, (c), most signal photons are again found at $k \simeq \omega_0$, but this time the amount of signal photons with $k \simeq 4\omega_0$ is smaller than that for $k \simeq 2\omega_0$. In addition, for the signal with frequency located around $5\omega_0$, we count a substantially smaller amount of signal photons associated with this frequency regime. For the pulse-energy distribution (a) we count 1.07, for (b) 2.81, and for (c) 1.64 signal photons per shot in this frequency regime. On the other hand, the fact that this signal lies outside the frequencies of the driving laser fields implies the possibility of an essentially background-free detection. As it is obvious from Tab. 4.4, higher pulse energies of the frequency doubled and quartered beams imply larger losses.

The fact that the clearly discernible signal at $5\omega_0$ becomes maximal for the pulse-energy distribution (b) with $q_1 = 2/3$ and $q_2 = 1/2$ motivates us to focus on this choice in the remainder of this article. For completeness, we note that the relative amplitudes associated with this choice are $A_0 = \frac{1}{\sqrt{6}}$, $A_1 = \frac{1}{3}\sqrt{\frac{5}{2}}$, $A_2 = \frac{\sqrt{5}}{6}$ and $A_3 = \frac{1}{6}\sqrt{\frac{5}{2}}$.

Frequency and directional characteristics of the signal

First, we aim at resolving the frequency spectrum of the full signal in detail. Since the analytical spectrum $dN(4\pi|k)$ results in an extensive expression, we sample the signal-photon number $N(4\pi|k, k + \Delta k)$ with a bin range of $\Delta k = 0.02 \text{ eV}$. The results of this analysis are presented as histograms in Fig. 4.18. The signal spectrum exhibits four pronounced maxima; the positions of three maxima match the oscillation frequencies of the driving laser fields. The additional maximum is centered around $k \simeq 5\omega_0$. Adding the contributions of all bins we obtain a total number of $N(4\pi|0, \infty) \simeq 5600$ signal photons.

In the present scenario, the positions of all the peaks can be understood in terms of elastic [98, 99, 106, 108, 220, 230–233] and manifestly inelastic [93–97, 101, 124, 234–240] sum or difference frequency generation processes involving only the oscillation frequencies of the driving laser fields; cf. in particular also [102, 155]. The reason is that the pulse duration τ is much larger than the cycle durations $1/(\nu_i \omega_0)$. In Sec. 3.2.5 it was shown that in the formal limit $\tau \rightarrow \infty$ the possible frequencies of the signal reduce to $k = \omega_0 |\pm \nu_i \pm \nu_j \pm \nu_l|$, see Eq. (3.69). The finite width of the peaks in frequency space is a consequence of the finiteness of τ , and implies that the frequency selection rules associated with the limit of $\tau \rightarrow \infty$ are fulfilled only approximately. While this is obvious for the quasi-elastic signal photon channels at ω_i , the signal with frequency $k \simeq 5\omega_0$ outside the frequency spectra of the driving beams highlighted in the inlay of Fig. 4.18 can be attributed to a sum and difference frequency generation process.

Besides the number of signal photons per bin, Fig. 4.18 shows the differential number of signal photons $dN(4\pi|k)/dk$ extracted from these histograms: upon dividing the signal-photon numbers in a given bin by the bin range Δk , we assume their distribution in a given frequency range to be well described by a Gaussian function. In all cases, the fitted peak values of the Gaussians are close to the frequencies $\nu_i \omega_0$. We numerically find the peak values at $(1.556 \pm 4.8 \times 10^{-5})\text{eV}$, $(3.11 \pm 2.8 \times 10^{-5})\text{eV}$, $(6.20 \pm 4.9 \times 10^{-6})\text{eV}$, and $(7.74 \pm 4.0 \times 10^{-5})\text{eV}$. The Gaussian standard deviations σ_G are $(84.47 \pm 0.19) \times 10^{-3} \text{ eV}$

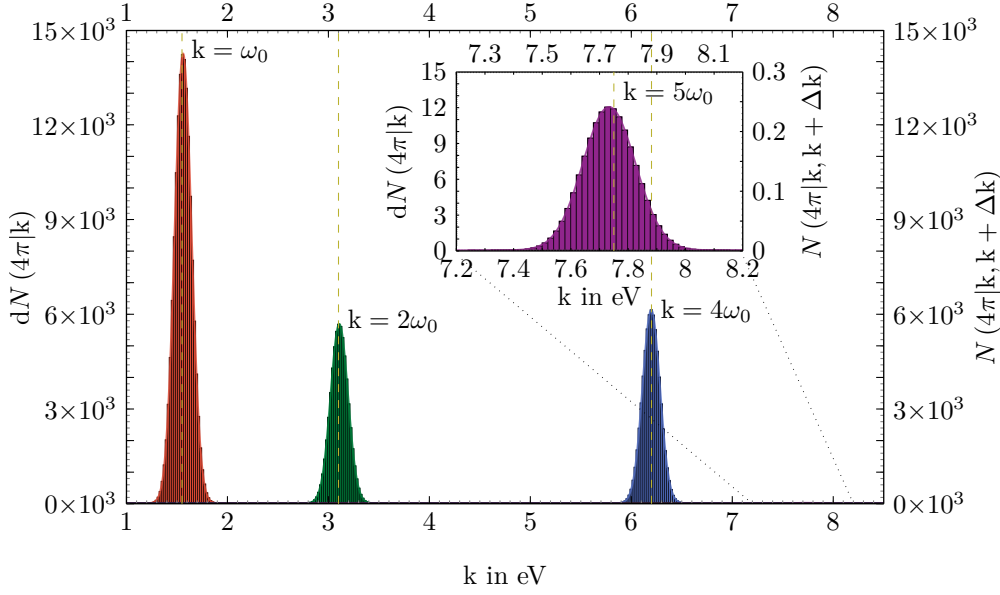


Figure 4.18.: *Spectral histogram and distribution of signal in a multi-color pulse collision.* Histogram of $N(4\pi|k, k + \Delta k)$ in the frequency regime $1 \text{ eV} \lesssim k \lesssim 8.5 \text{ eV}$; the bin range is $\Delta k = 0.02 \text{ eV}$ and the signal-photon number per bin is given on the right axis. The left axis gives the differential number of signal photons $dN(4\pi|k)$ determined by performing Gaussian fits to the histogram data (solid lines). The integrals of these curves reproduce the signal-photon numbers counted in the histograms reasonably well. In the spectral regime highlighted here, the signal photons are predominantly induced at frequencies $k \simeq n\omega_0$ with $n \in \{1, 2, 4\}$ (dashed vertical lines) matching those of the driving laser beams. In addition, we encounter a signal peaked around $5\omega_0$, see inlay.

for the ω_0 signal, $(87.01 \pm 0.11) \times 10^{-3} \text{ eV}$ for $2\omega_0$, $(86.97 \pm 0.02) \times 10^{-3} \text{ eV}$ for $4\omega_0$, and $(92.62 \pm 0.18) \times 10^{-3} \text{ eV}$ for $5\omega_0$. In the interval $\omega_i \pm 3\sigma_G$ 99% of the Gaussian distributed signal is located. The values for σ_G extracted here are about an order of magnitude smaller than the width of 1.02 eV employed to cover the full signal in the previous section. Correspondingly, the above choice should indeed reliably cover the full signal, while being still small enough to prevent an overlap of the signals associated with other frequencies. Besides, the bin size Δk should be sufficiently small to resolve potential deviations from Gaussian distributions in the spectral domain.

The directional distribution of the signal photons of energies $k_{\min} \leq k \leq k_{\max}$ attainable in a polarization insensitive measurement is encoded in the number density $\rho(\varphi, \vartheta|k_{\min}, k_{\max})$. Fig. 4.19 shows the Mollweide projection of the signal-photon density as a function of the azimuthal and polar angles φ and ϑ , accounting for four different frequency regimes.

In Fig. 4.19, the four different frequency regimes are highlighted in different colors. We adopt linear color scales which are normalized to the maximum value in a given frequency regime, see the caption of Fig. 4.19. The brightest areas of a given color mark the dominant emission directions of the signal photons. As expected, the signal photons of frequencies close to ω_0 , $3\omega_0$ and $4\omega_0$, respectively, are predominantly emitted in the forward cones of the driving laser pulses featuring the same frequencies: apart from a frequency- ω_0 (red) peak at

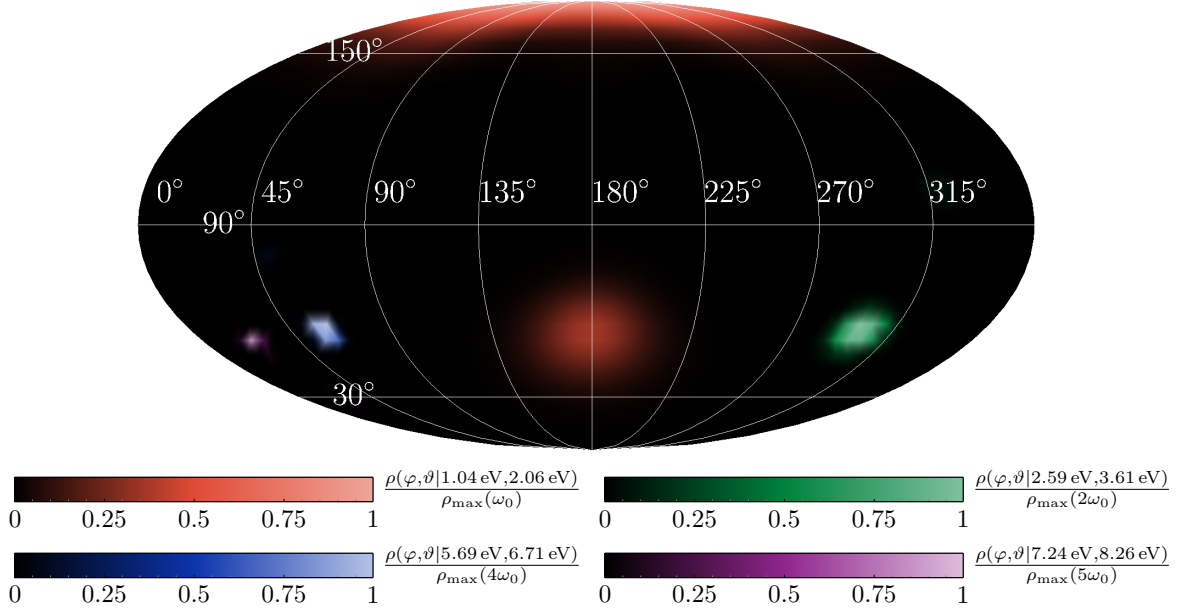


Figure 4.19.: *Mollweide plot of signal-photon density of multi-color pulse collision.* The Mollweide plot (longitude φ , latitude ϑ) of the signal-photon density $\rho(\varphi, \vartheta | k_{\min}, k_{\max})$ highlights four distinct frequency regimes $k_{\min} \leq k \leq k_{\max}$ in different colors given in the legend. All four color scales are normalized to the maximum value in the respective frequency interval, the maxima are $\rho_{\max}(\omega_0) = 7674.8$, $\rho_{\max}(2\omega_0) = 12992.2$, $\rho_{\max}(4\omega_0) = 33780.4$, and $\rho_{\max}(5\omega_0) = 155.8$.

$\vartheta = 180^\circ$, we observe three distinct maxima at $\vartheta \approx 54.74^\circ$ which are separated by $\approx 120^\circ$. These agree with the forward directions of the additional – from left to right – $4\omega_0$ (blue), ω_0 (red) and $2\omega_0$ (green) beams. Additionally, we encounter a $5\omega_0$ (violet) signal at $\varphi \approx 23.26^\circ$ and $\vartheta \approx 50.85^\circ$.

So far we have mainly focused on the total numbers of signal photons induced in specific frequency intervals and did not address the question of their measurability. This is particularly unclear for the signals at ω_0 , $2\omega_0$ and $4\omega_0$ which have been shown to be predominantly emitted into the forward directions of the associated driving beams. In the next subsection we will address this question and assess carefully which signal-photon contributions could be isolated from the large background of the driving laser photons in experiment.

Discernible signal photons

To assess if a specific signal can be discerned from the background of the driving laser photons or not, we first have to determine the angular distribution of the background. For this we use the density in the far field $\varrho_i(\varphi, \vartheta)$ introduced in Sec. 4, in particular see Eq. (4.10), and parameterize the angles $\theta_0(\varphi, \vartheta) = \vartheta - \pi$ and $\theta_i(\varphi, \vartheta) = -\arccos\{\cos \vartheta [\cos \vartheta_{\text{apx}} + \cos(\varphi - 2\pi \frac{4-i}{3}) \sin \vartheta_{\text{apx}}]\}$ for beams $i \in \{1, 2, 3\}$. Moreover, it is not necessary to parameterize ϕ_i because, due to the rotationally symmetric cross sections of the pulses, the angle ϕ_i in the density of the background photons drops out. In the following, we use the notation $\varrho(\varphi, \vartheta) = \sum_{i=0}^3 \varrho_i(\varphi, \vartheta)$ for the differential number of photons $\mathcal{N} = \sum_{i=0}^3 \mathcal{N}_i$ constituting all laser beams.

Since we have assumed that all laser beams are focused to the same waist $w_i = \lambda$, the far field angular divergences of the beams scale as $\sim 1/\nu_i$. This implies that the beam with the largest value of ν_i features the smallest far field divergence. At the same time, the effective extent of the interaction region, determining the far field divergences of the quasi-elastically scattered signal photons should be similar for all individual beams. The steeper decay of the laser photons constituting the $4\omega_0$ background suggests that the signal photons arising from the $4\omega_0$ beam should be more easily detectable than the analogous contributions for the other beams.

To illustrate the major challenge of signal-to-background separation we emphasize the huge background provided by the photons constituting the driving laser pulses. Their total number per shot is as large as $\mathcal{N} \simeq 5.3 \times 10^{20}$ to be contrasted with the number of $\mathcal{O}(10^3)$ signal photons achievable in this setup; cf. Tab. 4.4 above.

In contrast to the considerations in Sec. 4.1, not only a choice of the considered solid angle region shall lead to a discernible signal, but we want to take advantage of the different frequencies of the driving lasers and their consequences for the signal. For this, we proceed to a frequency-resolved analysis. More specifically, we search for discernible signal photons in the four distinct frequency regimes around ω_0 , $2\omega_0$, $4\omega_0$ and $5\omega_0$ introduced above.

Isolating the ω_0 signal from the background seems particularly challenging: the signal-photon density $\rho(\varphi, \vartheta | 1.02 \text{ eV}, 1.06 \text{ eV})$ features just two peaks in this frequency regime, both of which are coinciding with the forward directions of the two driving laser beams of frequency ω_0 . At the same time, exactly these beams come with the largest far field divergences. Besides, particularly due to the large energy put into beam 0, the number of background photons is maximal in this frequency regime. Though it might be an option to discern at least parts of the signal from the background by advanced detection techniques, based on analyses of the decay behavior or polarization details of both the background and the signal photons, see Sec. 4.1, here we proceed to the other frequency regimes suggesting more easily accessible signals.

Next, we focus on the frequency regime centered around $2\omega_0 \simeq 3.1 \text{ eV}$ and constrained by $k_{\min} = 2.59 \text{ eV}$ and $k_{\max} = 3.61 \text{ eV}$. Using the numerical Newton method we identify a local maximum of the signal-photon density $\rho(\varphi, \vartheta | 2.59 \text{ eV}, 3.61 \text{ eV})$ at $(\varphi, \vartheta) \simeq (317.65^\circ, 101.77^\circ)$. By comparison with Fig. 4.19, this particular maximum is clearly separated from the forward beam axis of the driving $2\omega_0$ beam constituting the main background in this specific frequency regime. For an estimate of the quantitative number of signal photons, we limit ourselves to the angular region $\mathcal{A}_{(2\omega_0)} = \{(\varphi, \vartheta) | \varphi \in [314^\circ, 324^\circ], \vartheta \in [96^\circ, 106^\circ]\}$ marked by the blue frame in Fig. 4.20 (left). An integration over this angular region results in $N(\mathcal{A}_{(2\omega_0)} | 2.59 \text{ eV}, 3.61 \text{ eV}) \simeq 62$ signal photons per shot. For completeness, we note that this value essentially constitutes the full number $N(\mathcal{A}_{(2\omega_0)} | 0, \infty)$ of signal photons emitted into this angular regime.

Upon numerically integrating Eq. (4.1) for the $2\omega_0$ beam $i = 2$ over the same angular interval, we find $\mathcal{N}_2(\mathcal{A}_{(2\omega_0)}) \simeq 0.01$ background photons per shot. Of course, the other driving beams do not induce a background in this frequency regime. This analysis implies that essentially all $\simeq 62$ photons with the considered directional characteristics are signal photons, which can thus be clearly distinguished from the background.

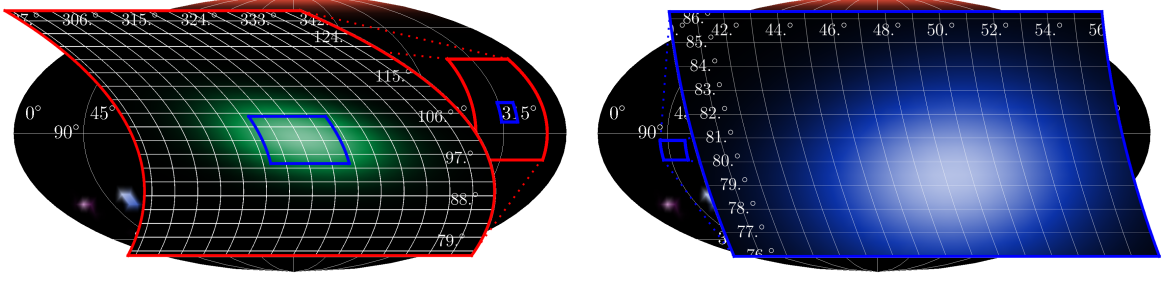


Figure 4.20.: Mollweide plot of signal-photon density of multi-color pulse collision with zoom for inelastic $2\omega_0$ and $4\omega_0$ signal. The zoom in the Mollweide plots (longitude φ , latitude ϑ) gives the signal-photon density $\rho(\varphi, \vartheta | k_{\min}, k_{\max})$ with $k_{\min} = 2.59$ eV, $k_{\max} = 3.61$ eV (left, green) and $k_{\min} = 5.69$ eV, $k_{\max} = 6.71$ eV (right, blue). We highlight the relevant angular region supporting a signal beyond the forward directions of the driving laser beam 2 and 3, respectively. The linear color scales are given in Fig. 4.19 with the maximum $\rho_{\max}(2\omega_0) = 2642.5$ and $\rho_{\max}(4\omega_0) = 7849.8$. The blue frames mark the angular region for which the number of discernible signal photons quoted in the main text is determined.

Further, we turn to the $4\omega_0$ frequency regime constrained by $k_{\min} = 5.69$ eV and $k_{\max} = 6.71$ eV. Also in this regime we search for a local maximum of the signal-photon density besides the dominant one in the forward cone of driving $4\omega_0$ laser beam $i = 3$. A numerical analysis of the signal-photon density $\rho(\varphi, \vartheta | 5.69 \text{ eV}, 6.71 \text{ eV})$ utilizing the Newton method allows us to identify a local maximum with the desired properties at $(\varphi, \vartheta) \simeq (49.43^\circ, 79.44^\circ)$. See Fig. 4.20 (right) for a graphical illustration of the signal-photon density in the relevant angular regime. An integration of the signal density over the area $\mathcal{A}_{(4\omega_0)} = \{(\varphi, \vartheta) | \varphi \in [40^\circ, 56^\circ], \vartheta \in [76^\circ, 86^\circ]\}$ highlighted in Fig. 4.20 (right) results in $N(\mathcal{A}_{(4\omega_0)} | 5.69 \text{ eV}, 6.71 \text{ eV}) \approx 129$ signal photons per shot. For comparison, in the same angular regime we find $\mathcal{N}_3(\mathcal{A}_{(4\omega_0)}) \simeq 0.006$ driving laser photons of frequency $4\omega_0$ per shot constituting the background.

As already noted, apart from the signals just discussed, we also identify a signal outside the frequencies of the driving laser beams in the energy regime of $7.24 \text{ eV} \leq k \leq 8.26 \text{ eV}$, featuring a peak in the spectrum at about $5\omega_0 \simeq 7.75 \text{ eV}$. A numerical analysis of the signal-photon density $\rho(\varphi, \vartheta | 7.24 \text{ eV}, 8.26 \text{ eV})$ unveils the existence of two pronounced maxima signaling two different main signal photon emission directions at (A): $(\varphi, \vartheta) \simeq (23.26^\circ, 50.85^\circ)$ and (B): $(\varphi, \vartheta) \simeq (31.32^\circ, 31.01^\circ)$, respectively. In Fig. 4.21 we illustrate the signal-photon density in the relevant angular areas. The two maxima are located in the two angular areas marked by blue frames. Maximum (A) is located in the upper blue frame delimiting the area $\mathcal{A}_{(5\omega_0,A)} = \{(\varphi, \vartheta) | \varphi \in [14^\circ, 35^\circ], \vartheta \in [42^\circ, 60^\circ]\}$, and maximum (B) in the lower frame the area $\mathcal{A}_{(5\omega_0,B)} = \{(\varphi, \vartheta) | \varphi \in [21^\circ, 42^\circ], \vartheta \in [25^\circ, 38^\circ]\}$.

Upon integration of the signal-photon density over the two angular regions $\mathcal{A}_{(5\omega_0,A)}$ and $\mathcal{A}_{(5\omega_0,B)}$, we obtain for (A) $N(\mathcal{A}_{(5\omega_0,A)} | 7.24 \text{ eV}, 8.26 \text{ eV}) \approx 2.3$ and for (B) $N(\mathcal{A}_{(5\omega_0,B)} | 7.24 \text{ eV}, 8.26 \text{ eV}) \approx 0.5$ signal photons per shot. We emphasize once again that there is no genuine laser photon background in the $5\omega_0$ frequency regime since the driving laser fields only contain frequencies in the vicinity of ω_0 , $2\omega_0$ and $4\omega_0$. By contrast, we do not find any significant signal at higher harmonic frequencies.

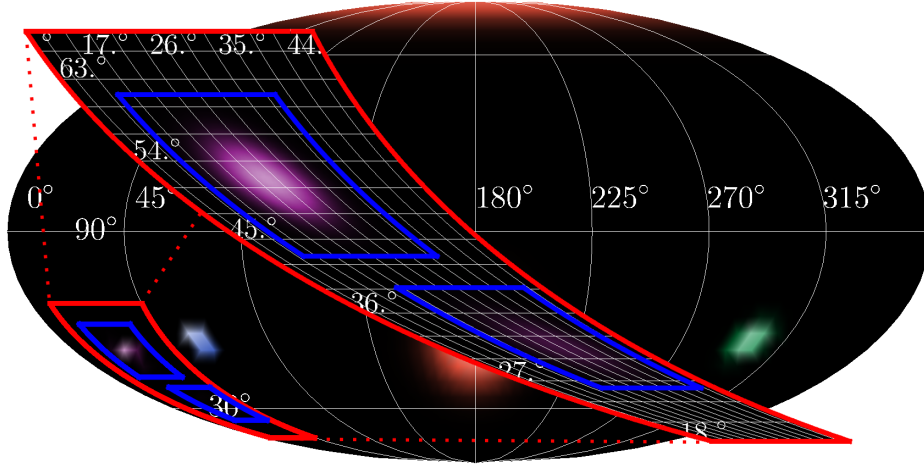


Figure 4.21.: *Mollweide plot of signal-photon density of a multi-color pulse collision zooming on the inelastic $5\omega_0$ signal.* The zoom in the Mollweide plot (longitude φ , latitude ϑ) gives the signal-photon density $\rho(\varphi, \vartheta|5.69 \text{ eV}, 6.71 \text{ eV})$. We highlight the relevant angular regions (A) (upper blue frame) and (B) (lower blue frame) containing the signal. The linear color scales is given in Fig. 4.19 with the maximum $\rho_{\max}(5\omega_0) = 162.1$. The blue frames mark the angular region for which the number of discernible signal photons quoted in the main text is determined.

We summarize the quantitative findings from the preceding sections in Tab. 4.5. This table features the prospective signal-photon numbers and numbers of driving laser photons constituting the background for various frequencies and emission directions.

	$2.59 \text{ eV} \leq k \leq 3.61 \text{ eV}$ $i = 2$, cf. Fig. 4.20	$5.69 \text{ eV} \leq k \leq 6.71 \text{ eV}$ $i = 3$, cf. Fig. 4.20	$7.24 \text{ eV} \leq k \leq 8.26 \text{ eV}$ cf. Fig. 4.21
$N(4\pi)$	1240.80	1337.67	2.81
$\mathcal{N}_i(4\pi)$	6.98×10^{19}	1.75×10^{19}	0.00
$N(\mathcal{A}_{(2\omega_0)})$	62.02	0.00	0.00
$\mathcal{N}_i(\mathcal{A}_{(2\omega_0)})$	10.13×10^{-3}	0.00	0.00
$N(\mathcal{A}_{(4\omega_0)})$	0.00	129.40	0.00
$\mathcal{N}_i(\mathcal{A}_{(4\omega_0)})$	0.00	5.91×10^{-3}	0.00
$N(\mathcal{A}_{(5\omega_0,A)})$	0.00	8.19×10^{-5}	2.31
$N(\mathcal{A}_{(5\omega_0,B)})$	0.00	0.00	0.46

Table 4.5.: *Number of discernible signal photons and corresponding background photons for the multi-color pulse collision.* The prospective numbers of signal photons $N(\mathcal{A}|k_{\min}, k_{\max})$ and driving laser photons $\mathcal{N}_i(\mathcal{A})$ in different energy regimes and angular emission regions \mathcal{A} are listed. See the main text for the definitions of the areas as well as further details.

4.2.3. Applying of the Channel Analysis

In Sec. 4.2.2 we have identified several promising signals and demonstrated that they are, in principle, discernible against the background of the photons of the driving laser beams. To obtain these results we have relied on a rather time consuming numerical evaluation of

the full signal-photon density $\rho(\varphi, \vartheta | k_{\min}, k_{\max})$. This quantity encodes information about all possible single photon emission processes mediated by quantum vacuum fluctuations in the macroscopic field driving the effect. In order to resolve different frequency regimes within this approach, we have evaluated $\rho(\varphi, \vartheta | k_{\min}, k_{\max})$ for various values of k_{\min} and k_{\max} .

Subsequently, we demonstrate how these results can be obtained with considerably less computational efforts, using the channel analysis introduced in Sec. 3.2 as benchmarks for the detailed discussion carried out here. Something similar to the channel analysis for various three-pulse setups has been performed in [101, 102].

So far, in Eq. (3.66) of Sec. 3.2.5, we worked out the nonphysical density $\rho_{ijl'i'j'l'}(\varphi, \vartheta | k_{\min}, k_{\max})$ of the channel combination (ijl) and $(i'j'l')$. Moreover, our analysis showed that a combination of individual channels is combined to form so-called *proto-physical* channels $\{ijl\}$, cf. Eq. (3.72). Recalling the selection rules Eq. (3.71), we can indicate the proto-physical channels. This selection rule is valid if the pulses contain enough cycles. In the scenario considered here we have $\omega_0\tau \simeq 59 \gg 1$, or equivalently $1/\tau \simeq \omega_0/59 \ll \omega_0$, which clearly hints at the fact that the spectral width of these Gaussian peaks is much smaller than the spectral separation of any two oscillation frequencies ω_i of the driving laser fields. This is in line with the findings of Sec. 4.2.2: here Gaussian fits to the various peaks encountered in the differential number of signal photons $dN(4\pi|k)/dk$ resulted in Gaussian standard deviations of the same magnitude. For the largest extracted frequency width $\sigma_G = 0.0926$ eV, the associated full peak-width measured at 1% of the peak-maximum is given by $\Delta\omega = 4\sqrt{\log 100} \sigma_G \simeq 0.513 \omega_0$. The numerical result fits the analytical estimation from Sec. 3.2.5, whereby the standard deviation is $\sigma = 2\sqrt{3}/\tau \approx 0.0912$ eV.

Furthermore, the channel analysis showed that with four laser pulses of different propagation directions, a total of 16 different proto-physical channels remain. We call all channels, which lead to an emission in the vicinity of the direction of the driving laser, *semi-elastic*. The direction of emission of a physical channel \mathbf{k} can be determined approximately by the sum of the contributing wave vectors in the plane-wave limit, see Eq. (3.70). Accordingly, all channels leading to photon-photon scattering in regions beyond the propagation directions are called *inelastic*. Here we are talking about 12 semi-elastic channels fulfilling $\{iji\}$ with $i \neq j$ and 4 inelastic channels $\{ijl\}$ with $i \neq j \neq l \neq i$.

To demonstrate this we first focus on the semi-elastic case where two indices agree. If, e.g., $i = l$ and $i \neq j$, Eq. (3.69) predicts signals either at $k \simeq \omega_j$ or at $k \simeq \omega_j \pm 2\omega_i$. However, at the same time, Eq. (3.70) implies $\mathbf{k} \simeq \pm\omega_j\hat{\mathbf{k}}_j$ or $\mathbf{k} \simeq \pm\omega_j\hat{\mathbf{k}}_j \pm 2\omega_i\hat{\mathbf{k}}_i$. From these findings it is obvious that only the conditions $k = |\mathbf{k}| = \omega_j$ are compatible with each other for generic values of ω_i and ω_j as well as non-collinear $\hat{\mathbf{k}}_i$ and $\hat{\mathbf{k}}_j$ as considered here. On the other hand, signal photons fulfilling $k = |\mathbf{k}| = \omega_j$ are expected to be predominantly emitted in the forward direction $\hat{\mathbf{k}}_j$ of the driving laser beam of frequency ω_j , rendering their experimental detection very challenging. For completeness, note the in-principle possibility of a quantum reflection signal in the opposite direction, which is completely negligible for the present scenario where focusing effects are found to be subleading [122].

As an illustrative example we determine the signal-photon number associated with the proto-physical channel $\{030\}$, yielding $N_{\{030\}}(4\pi|5.69 \text{ eV}, 6.71 \text{ eV}) \simeq 463.46$ photons per shot

in the frequency regime around $4\omega_0$. Here $N_{\{ijl\}}(\mathcal{A}|\mathbf{k}_{\min}, \mathbf{k}_{\max})$ results consistently from the integral of the proto-physical density $\rho_{\{ijl\}}(\varphi, \vartheta|\mathbf{k}_{\min}, \mathbf{k}_{\max})$ over the solid angle region \mathcal{A} . The signal of channel $\{030\}$ is peaked at $\hat{\mathbf{k}}_3$. On the other hand, we find $N_{\{030\}}(4\pi|0, \infty) \simeq 463.46$, such that – as expected, and in line with the arguments given above – obviously no signal photons at other frequencies contribute to this channel.

In the remainder of this section our focus is on the manifestly inelastic signal-photon contributions associated with the 4 proto-physical channels $\{012\}$, $\{013\}$, $\{123\}$, and $\{023\}$. In particular, we aim at verifying the signals arising in the angular regions $\mathcal{A}_{(2\omega_0)}$, $\mathcal{A}_{(4\omega_0)}$ and $\mathcal{A}_{(5\omega_0, A/B)}$ introduced in Sec. 4.2.2. This allows us to explicitly restrict our analysis to channels giving rise to signal photons of the desired energy and wave vectors pointing in the respective directions.

Tracking the $2\omega_0$ signal in $\mathcal{A}_{(2\omega_0)}$, we analyze all permutations of the indices 0, 1 and 2. Microscopically, we expect this signal to arise from a process involving the merging of two laser photons from beams 0 and 2, respectively, and the absorption of a laser photon of frequency ω_1 from beam 1. Resorting to the plane-wave approximation, this results in a signal photon wave vector of modulus $|\mathbf{k}_{\text{PW}}| \approx 2.201\omega_0$ pointing at $(\varphi, \vartheta) = (319.107^\circ, 101.07^\circ)$. Obviously this value is compatible with the condition $|\mathbf{k} - |\mathbf{k}_{\text{PW}}|| < \Delta\omega$ and $k \simeq 2\omega_0$. It thus allows for a nonvanishing signal in this parameter regime. A comparison with the emission direction of the discernible signal determined numerically in Fig. 4.20 (left) unveils an excellent agreement; the relative differences in the longitude φ and latitude ϑ are below 1%. The signal associated with this channel is found to be peaked around $k \simeq 2.015\omega_0$. Restricting on the proto-physical channel $\{020\}$ we obtain $N_{\{020\}}(4\pi|0, \infty) \simeq 78$ signal photons per shot, while an explicit restriction to the angular region $\mathcal{A}_{(2\omega_0)}$ results in $N_{\{020\}}(\mathcal{A}_{(2\omega_0)}|0, \infty) \simeq 62$. This fits accurately to the number of signal photons based on the full physical density with the energy constrain $2.59 \text{ eV} \leq k \leq 3.61 \text{ eV}$, see Tab. 4.5.

To study the importance of the individual contributions of each nonphysical channel to the proto-physical channel, in Tab. 4.6 (a) we explicitly list the contributions of all nine terms constituting the signal-photon number $N_{\{020\}}(4\pi|0, \infty)$. This also allows us to assess the relative importance of off-diagonal terms with $(ijl) \neq (i'j'l')$. Exactly the same number is obtained when the frequency regime is in addition restricted to $2.59 \text{ eV} \leq k \leq 3.61 \text{ eV}$. A comparison with the analogous number extracted in Tab. 4.5 establishes that all signal photons scattered into this parameter regime are indeed emerging from the microscopic process $\omega_0 - \omega_1 + \omega_2 \rightarrow k$.

The other signals can be analyzed along the same lines. For identifying the microscopic process giving rise to the inelastic signal of frequency $4\omega_0$, the proto-physical channel $\{013\}$ needs to be analyzed. The process responsible for this signal is $\omega_0 - \omega_1 + \omega_3 \rightarrow k$. The corresponding signal photon wave vector fulfills $|\mathbf{k}_{\text{PW}}| \approx 3.813\omega_0$ and is pointing at $(\varphi, \vartheta) \simeq (49.11^\circ, 78.93^\circ)$. This channel gives rise to $N_{\{013\}}(\mathcal{A}_{(4\omega_0)}|0, \infty) \simeq 129$ signal photons per shot. For the individual contributions constituting this number, see Tab. 4.6 (b).

Finally, we turn to the two distinct signals with frequencies around $5\omega_0$. These are triggered by the microscopic processes $-\omega_1 + \omega_2 + \omega_3 \rightarrow k$ and $-\omega_0 + \omega_2 + \omega_3 \rightarrow k$, respectively. We summarize the detailed properties of these signals in Tab. 4.7; this table also includes the

$i'j'l'$ ijl	0 1 2	1 2 0	0 2 1
0 1 2	1.557	0.327	6.516
1 2 0	0.327	2.143	5.122
0 2 1	6.516	5.122	34.394

(a): $k \simeq 2\omega_0$

$i'j'l'$ ijl	0 1 3	1 3 0	0 3 1
0 1 3	0.437	0.754	4.917
1 3 0	0.754	12.814	18.851
0 3 1	4.917	18.851	67.105

(b): $k \simeq 4\omega_0$

$i'j'l'$ ijl	1 2 3	2 3 1	3 1 2
1 2 3	0.052	-0.018	-0.206
2 3 1	-0.018	2.218	-0.242
3 1 2	-0.206	-0.242	0.973

(c): $k \simeq 5\omega_0$

$i'j'l'$ ijl	0 2 3	2 3 0	3 0 2
0 2 3	0.228	-0.957	0.449
2 3 0	-0.957	5.464	-2.625
3 0 2	0.449	-2.625	3.034

(d): $k \simeq 5\omega_0$

Table 4.6.: *Signal photons contribution per channel in multi pulse collision.* The signal-photon number of different inelastic proto-physical channels are decomposed in their non-physical contributions $N_{ijl i'j'l'}(\mathcal{A}_{(n\omega_0)}|0, \infty)$. Here, we highlight several photon emission channels resulting in manifestly inelastically scattered signal photons of frequency $k \simeq n\omega_0$ with $n \in \{2, 4, 5\}$.

channel	{012}	{013}	{023}	{123}
k	$2\omega_0$	$4\omega_0$	$5\omega_0, A$	$5\omega_0, B$
origin	$\omega_0 - \omega_1 + \omega_2$	$\omega_0 - \omega_1 + \omega_3$	$-\omega_1 + \omega_2 + \omega_3$	$-\omega_0 + \omega_2 + \omega_3$
φ	319.11°	49.11°	23.41°	30.90°
ϑ	101.07°	78.93°	50.95°	32.36°
$N_{\{ijl\}}(\mathcal{A}_{(n\omega_0)})$	62.02	129.40	2.31	0.46

Table 4.7.: *Discernible inelastic signal photons in multi-color pulse collision.* The properties of the manifestly inelastic proto-physical signal photon channels $\{ijl\}$ are listed. For each signal photon frequency $k \simeq n\omega_0$ with $n \in \{2, 4, 5\}$ we provide the longitude φ and latitude ϑ characterizing the main emission direction as well as the signal frequency k and the number of signal photons per shot in the respective channel emitted into the solid angle $\mathcal{A}^{(n\omega_0)}$ with the full frequency regime $k_{\min} = 0$, $k_{\max} = \infty$.

parameters characterizing the $2\omega_0$ and $4\omega_0$ signals just discussed. See Tab. 4.6 (c) and Tab. 4.6 (d) for the individual contributions constituting the signal-photon numbers in these channels.

In the preceding section, we have worked out a strategy allowing us to trace all-optical signatures of quantum vacuum nonlinearity back to the underlying four-wave mixing processes and thus infer information about their microscopic origin. To enable a clear measurement of a photonic signature of quantum vacuum nonlinearity it is desirable to maximize the signal at a given frequency and emission direction such as to achieve the best possible signal-to-background separation. A complete assessment of the question which signal channel amounts to the most prospective one for an experimental verification, of course, requires one to account for many more details of a concrete experimental set up, including, e.g., the sensitivity and efficiency of the few photon detectors [148].

As the simultaneous measurement in several well-separated directions and at several frequencies is, however, highly unlikely with state-of-the-art technology, the typical challenge is to maximize the signal at a certain frequency and emission direction. Here, we sketch how the insights obtained above can be used to enhance a given signal photon channel. Selecting a particularly promising signal, the channel analysis allows us to trace the microscopic origin of this signal and to modify the driving laser fields such as to enhance the signal in this channel, e.g., by redistributing the total available laser pulse energy into the individual beams.

This is especially obvious for the manifestly inelastic signals analyzed in detail: while originating from the effective interaction of different subsets of beams, each of these four signals (cf. Tab. 4.7) arises from the mixing of precisely three different driving laser fields. Hence, in order to increase the signal photon yield in any of these channels individually, the driving laser beam which acts as a pure spectator can be switched off and its energy instead be redistributed into the other beams participating in the interaction.

Here, we illustrate this point using the example of a manifestly inelastic $k \simeq 4\omega_0$ signal originating in the microscopic process $\omega_0 - \omega_1 + \omega_3 \rightarrow k$, where $\omega_1 = \omega_0$ and $\omega_3 = 4\omega_0$, respectively. Obviously, only beams 0, 1 and 3 are involved in this particular process. Let us now remove the spectator beam 2 and redistribute its energy into the other beams. Our choice for the new beam energies is $\tilde{W}_0 = \tilde{W}_1 = \tilde{W}_3 \approx 41.67 \text{ J}$, maximizing the Fourier integral $\tilde{I}_{013} \propto \sqrt{\tilde{W}_0 \tilde{W}_1 \tilde{W}_3}$; the other Fourier integrals do not support an inelastic channel or vanish for $\tilde{W}_2 = 0$. The partition factors associated with this choice are $\tilde{q}_0 = 5/6$, $\tilde{q}_1 = 4/5$ and $\tilde{q}_2 = 1$, resulting in $\tilde{W}^{\text{eff}} = \tilde{W}^{\text{loss}} = 1/2 W$; cf. Sec. 4.2.2. The new result for the number of signal photons in the manifestly inelastic $4\omega_0$ channel emitted into the angular area $\mathcal{A}_{(4\omega_0)}$ can straightforwardly be obtained from the corresponding signal-photon number $N_{\{013\}}(\mathcal{A}_{(4\omega_0)}|0, \infty) \simeq 129$. It follows upon rescaling this number with an overall factor of $\tilde{W}_0 \tilde{W}_1 \tilde{W}_3 / (W_0 W_1 W_3) = 36/25$, resulting in $\tilde{N}(\mathcal{A}_{(4\omega_0)}) = 36/25 N(\mathcal{A}_{(4\omega_0)}) \simeq 186$ signal photons per shot in this specific channel.

5.

Conclusion

“The most perfect philosophy of the natural kind only staves off our ignorance a little longer: as perhaps the most perfect philosophy of the moral or metaphysical kind serves only to discover larger portions of it.”

— David Hume, *An Enquiry Concerning Human Understanding* [241]

At the beginning of this work, a historical overview of the vacuum, in particular of the quantum vacuum, was given. Now, the content of this thesis will be related to it; we summarize the developed methodology and elaborate the main insights. Furthermore, we evaluate them in with reference to the state of the art of the current research.

In QED the quantum vacuum is a state of omnipresent fluctuations of particle-antiparticle pairs and their photonic interactions with the lightest charged experimentally evidenced particles being the electron and positron. In the presence of charges or fields, the fluctuations polarize the vacuum, which leads to a nonlinear extension of the laws of classical electrodynamics, as it was shown by Heisenberg and Euler [52]. To probe the nonlinearity of the quantum vacuum in an experiment strong electromagnetic fields are required, which can be provided by high-intensity lasers nowadays. A particular challenge is the separation of the signal from the enormous background of the driving lasers. Addressing this challenge is still one of the main tasks of current research.

And this is exactly where the research of this thesis starts: Based on the theory of Heisenberg and Euler, we have designed experimental scenarios that allow the measurement of the signature of the nonlinearities of the quantum vacuum. To this end, we have first showed conceptually, using the vacuum emission picture, how the number of signal photons encoding the nonlinearity of the quantum vacuum can be determined. We have then focused on scenarios consisting of the interaction of any number of high intensity Gaussian laser pulses. The formal analysis has led to a method that not only provides deep insights into the microscopic processes from the collision of strong laser fields but also allows an understanding of the effects of different laser pulses: the channel analysis.

With the help of channel analysis, the density of the signal photons can be decomposed into contributions of so-called channels, which are composed of the different products of three field profiles in the signal photon amplitude. The single individual contributions to the full density do not correspond to a pure physical density, but we succeeded in identifying proto-physical channels whose characteristics correspond to those of the signal under appropriate assumptions, such as the choice of relevant frequencies or the emission direction. A distinction is made between semi-elastic and inelastic channels; the former result from the combination

of two different field profiles, the latter involve contributions of three different lasers. A selection rule can be used to estimate which channels make contributions to the full density. Furthermore, the emission direction and frequency of the signal can be deduced from the proto-physical channels and we found a full analytical description of the (channel-dependent) signal-photon density in the infinite Rayleigh range approximation.

In order to apply and verify the insights from the channel analysis, we have studied two different experimental scenarios. Here, both investigations aim at identifying a discernible signal of the quantum vacuum nonlinearity. This signal is characterized by the fact that it surpasses the huge number of background photons of the driving lasers. We succeed here in tracking down this discernible signal by considering specific solid-angle regions or frequency ranges. To this end, we use different approaches in the two experiments to isolate corresponding signals.

In the first experimental scenario we have studied the discernible signatures of QED vacuum nonlinearities in the collision of two optical laser pulses under collisions angles $100^\circ \leq \vartheta_{\text{col}} \leq 160^\circ$. More precisely, we have determined the solid angles regions at which the signal of the QED vacuum nonlinearity is larger than the background of driving laser photons numerically. Thereby, we have paid special attention to the influence of the focusing of the lasers on the signal photons in so-called dominant regions, i.e. where the signal dominates the background. In particular, we have distinguished between circularly and elliptically focused probe beams and analyzed the different effects. The laser pulses used are so similar in their properties that in an experimental realization both can be generated from the same source. Therefore, we have used the properties of modern laser technologies to get as close as possible to the results of a future experiment.

As a first step, we investigate the quantitative dependence between the number of signal photons in the discernible region and the waist size of a circularly focused probe beam. One of our main key finding is that the maximum photon number does not occur for the tightest focusing as had been generically assumed in previous studies in the literature. We can explain this observation by an interplay of two effects: A narrow focus of the pulse increases the density of potentially interacting photons; on the other hand, a small beam waist is associated with a large propagation cone of the driving beam in the far field. This increases the angle measured from the propagation axis of the probe at which part the signal becomes dominant.

This result is surprising, since naively one would expect the largest signals at a maximally intense field in the interaction volume and disregarding the background of the driving lasers this is indeed true. These studies highlight the importance of controlling the background of the driving lasers in the far field in an experiment.

In another approach, we varied the focusing of the probe beam along the axis parallel to its magnetic field component while keeping the focusing orthogonal to it and to the propagation direction constant to the value for maximum signal with circular focusing. For the collision angle $\vartheta_{\text{col}} = 160^\circ$ we achieve an enhancement of the signal to about 11.6 signal photons per shot, whereas in the same solid-angle regions there are only 0.12 background photons. Depending on the orientation of the elliptical cross section of the probe laser, it is possible to increase the number of discernible signal photons at all collision angles investigated. We

explain this by the fact that the density of the interacting photons is boosted by the tight focusing; the regions of discernible signals are at the same time only partially covered by the background due to the elliptical shape, so that they are pronounced enough to provide a strong detectable signal.

Besides the discernible signal in polarization-insensitive measurements, we have also investigated the measurability of polarization-flipped signal photons. We find that even at low experimental purity of linearly polarized Gaussian pulses it is possible to find a significant signal beyond the background; this allows experimental detection of vacuum birefringence. In addition, the results emphasize the importance of the scattering of the signal in discernible regions, since within these regions, even using driving lasers with lower purity of polarization, a measurement of vacuum birefringence may be possible.

In a second scenario, we have studied all-optical signatures of QED vacuum nonlinearities in the collision of several high-intensity laser beams differing in frequency, polarization and propagation direction. More specifically, we have focused on an example scenario envisioning the collision of four laser pulses, each one originating from a single driving laser pulse by utilizing beam splitting and sum and difference frequency generation techniques.

One of the goals of our study has been to identify prospective proto-physical channels allowing for an efficient signal-to-background separation. To this end, we pay special attention to the question of how to efficiently infer information about the microscopic origin of prospective signatures of vacuum nonlinearity by means of the channel analysis. This allows us to answer relevant questions, such as which laser beams participate in the formation of a given signal, and what is the specific interaction process inducing the latter. Theoretical statements derived from the channel analysis about microscopic processes of photon-photon interaction mediated by the quantum vacuum have been confirmed. We have managed to not only identify inelastic signals beyond the background, we have also been able to identify laser pulses associated with a specific signal. In addition, we have explicitly demonstrated how this information can be used to enhance the discernible signal-photon number in a given signal photon channel.

The findings of the entire work are based on the 1-loop Heisenberg-Euler Lagrangian; furthermore, all calculations of signal photons have been performed in the weak-field limit $\mathcal{E}_\star \ll \mathcal{E}_{cr}$ and assuming single signal-photon processes. Nevertheless, we have indicated how to proceed beyond these limitations which is, in principle, straightforward [152, 155, 177]. Further, we use the IRRA as an approximation; it applies to weakly focused lasers or collision angles smaller than head-on collisions. This is always fulfilled in the considered cases, nevertheless the calculated numerical values are to be understood as estimations with an error on the few percent level. Surpassing the IRRA is, in principle, straightforward within the VEP, but typically requires to evaluate all amplitudes numerically. Furthermore, we use $\tau\omega \ll 1$ for the microscopic interpretation that a pulse comprises several cycles. Moreover, we have focused on purely optical scenarios; however, many results can be used for other alternative proposals [119, 120, 242] with corresponding detections beyond the optical regime. In all calculations, we have assumed ideal focusing of the interacting laser pulses with no shifts in time or in the collective focus point. For considerations of the effects of spatio-temporal

offsets, see, e.g., reference [165].

We are confident that the methods and ideas presented in this thesis will provide experimental access to the signature of the QED vacuum. Furthermore, these studies deliver prospects to optimize the measurability of photonic signatures of quantum vacuum nonlinearities. We hope that these results will encourage experimentalists in the near future to investigate the quantum vacuum and produce these discernible signal photons. Moreover, in view of our results and the experimental progress, for example by the detection of single photons or an increased control of the background of the driving laser pulses [148, 149], we are optimistic that an experimental confirmation is possible. This would be a breakthrough, as it would also consolidate our knowledge of the physics of elementary particles of the Standard Model and beyond at the high-intensity frontier – a regime that has remained largely untested so far.

A.

Notations and Conventions

In this work we use a fixed choice of notations and conventions. Here we briefly summarize the concepts.

The imaginary unit is i and we denote the base of the natural logarithms by e . The usual number sets are used, e.g. \mathbb{N} for integer, \mathbb{R} for reals, and \mathbb{C} for complex numbers. Further, the star is the symbol for complex conjugation, e.g. for a complex number $z = x + iy \in \mathbb{C}$ yields $z^* = x - iy$ with $x, y \in \mathbb{R}$, and for the Hermitian adjoint we use the dagger symbol, e.g. for a matrix $M \in \mathbb{C}_{2 \times 2}$ with components $(M)_{ij}$ it holds $(M^\dagger)_{ij} = (M^*)_{ji}$.

We use the metric convention

$$(\eta_{\mu\nu}) = \text{diag}(-, +, +, +) \quad (\text{A.1})$$

and the usual convention for relativistic four-vectors $(x^\mu) = (x^0, \mathbf{x})$, where the boldface type denotes the three-vectors. The three dimensional Euclidian space \mathbb{R}^3 is spanned by three orthonormal vectors; for Cartesian coordinates we use the unit vectors $\mathbf{e}_x, \mathbf{e}_y, \mathbf{e}_z$. Therefore, an arbitrary vector $\mathbf{r} \in \mathbb{R}^3$ decomposes in

$$\mathbf{r} = x\mathbf{e}_x + y\mathbf{e}_y + z\mathbf{e}_z. \quad (\text{A.2})$$

If we use (x) as the argument of a function, e.g. $\mathcal{E}(x)$ for a field profile, then x is representative for any four space-time coordinates. For functions which are defined exclusively in the three-dimensional Euclidean space, we use the argument (\mathbf{r}) , e.g. for a scalar function $U(\mathbf{r}) : \mathbb{R}^3 \rightarrow \mathbb{R}$.

For operators on Hilbert and Fock spaces, like A and B , we use the commutator

$$[A, B] = AB - BA \quad (\text{A.3})$$

and the anticommutator

$$\{A, B\} = AB + BA. \quad (\text{A.4})$$

Like the speed of light c and the reduced Planck constant \hbar , the Boltzmann constant k_B is one of the unit-defining constants. We use natural units $\hbar = c = k_B = 1$ and measure all of the following physical quantities – unless otherwise noted – based on the Heaviside Lorentz unit system. To construct a complete system of physical units, only one dimensionful unit is necessary: we use the energy unit electronvolts (eV). Tab. A.1 gives an overview over the

Appendix A. Notations and Conventions

Quantity	SI Magnitude	HL Magnitude
length	1 m	$5.07 \times 10^6 \text{ eV}^{-1}$
time	1 s	$1.52 \times 10^{15} \text{ eV}^{-1}$
mass	1 kg	$5.61 \times 10^{35} \text{ eV}$
current	1 A	1244 eV
energy	1 J	$6.24 \times 10^{18} \text{ eV}$
temperature	1 K	$8.62 \times 10^{-5} \text{ eV}$
power	1 W	$4.11 \times 10^3 \text{ eV}^2$
electric field strength	1 V/m	$6.5 \times 10^{-7} \text{ eV}^2$
magnetic field strength	1 T	195.5 eV^2
intensity of field strength	1 W/cm ²	$1.60 \times 10^{-6} \text{ eV}^4$

Table A.1.: *Relation between SI unit and Heaviside-Lorentz unit systems.* We use natural Heaviside-Lorentz units supplemented by electronvolts as energy unit. Here we list how basic physical quantities can be converted from the SI unit system to the Heaviside-Lorentz unit system.

relation between our chosen units and the equivalent in the SI unit system.

Consequently, the fine-structure constant is

$$\alpha = \frac{e^2}{4\pi} \approx \frac{1}{137}, \quad (\text{A.5})$$

and the elementary charge e is dimensionless. The current values of the constants of particle physics can be found in the review [243].

B.

Appendix

B.1. Vacuum Polarization in QED

Our aim is to get an impression of how vacuum polarization changes the understanding of classical electrodynamics to QED. To achieve this we will discuss the photon propagator.

A prominent perturbative representation of QED proceeds with the help of Feynman diagrams. With these QED scattering processes can be illustrated and calculated. Those scattering processes can be expressed by an S -matrix connecting the initial and final state.

At first we want to restrict ourselves to the internal free propagators. The free electron propagator S_0 with the physical mass m , carrying a four-momentum k , is

$$iS_0 = (k) \longrightarrow \longleftarrow = \frac{i}{\not{k} - m + i\varepsilon}, \quad (\text{B.1})$$

where the Dirac slash notation $\not{k} = \gamma_\mu k^\mu$ is used. To control the pole, we add $i\varepsilon$ in the denominator which corresponds to a causal prescription with infinitesimal $\varepsilon > 0$. In addition, we define the free photon propagator $\Delta_0(q)$ carrying four-momentum q as

$$-i\Delta_{0,\mu\nu}(q) = \mu \text{ ~~~~~ } \nu = -\frac{i\eta_{\mu\nu}}{q^2 + i\varepsilon}, \quad (\text{B.2})$$

where we have used Feynman gauge. Moreover, interactions between fermion and photon lines are described with a vertex. At each vertex the propagators couple with the contribution $-ie\gamma^\mu$. According to Feynman rules the prefactor is multiplied by $(-1)^n$ for n closed fermion loops. Further Feynman rules can be found in the references [71, 167, 169, 244].

To determine the exact photon two-point function, i.e. the full or *dressed* photon propagator $\Delta_{\mu\nu}(q)$, we have to consider the vacuum polarizations. With the help of the Feynman diagrams we can represent the full propagator as the sum of all possible processes with internal fermion loops according to the Feynman rules, thus

$$\begin{aligned} -i\Delta_{\mu\nu}(q) &= \mu \text{ ~~~~~ } \nu \\ &= \mu \text{ ~~~~~ } \nu + \mu \text{ ~~~~~ } \nu + \mu \text{ ~~~~~ } \nu \\ &\quad + \mu \text{ ~~~~~ } \nu + \dots \\ &= \mu \text{ ~~~~~ } \nu + \mu \text{ ~~~~~ } \nu + \mu \text{ ~~~~~ } \nu + \dots \end{aligned} \quad (\text{B.3})$$

Appendix B. Appendix

In the last step, we grouped the diagrams in terms of 1PI diagrams. These diagrams stand for the one-particle-irreducible diagrams, by which we mean diagrams that cannot be split into two separate diagrams by removing a single line. The 1PI diagrams can in turn be expanded in terms of a loop order corresponding to their power in α .

The contribution of the vacuum polarization $\Pi^{\mu\nu}(q)$ is defined by the one-particle-irreducible diagram as

$$i\Pi^{\mu\nu}(q) = \mu \text{ --- } \text{1PI} \text{ --- } \nu . \quad (\text{B.4})$$

Using the Ward identity $q_\mu \Pi^{\mu\nu}(q) = 0$ it follows that $\Pi^{\mu\nu}(q)$ must be proportional to the projector $\eta^{\mu\nu} - \frac{q^\mu q^\nu}{q^2}$. This suggests to introduce the scalar function $\Pi(q^2)$,

$$\Pi^{\mu\nu}(q) = \left(q^2 \eta^{\mu\nu} - q^\mu q^\nu \right) \Pi(q^2) , \quad (\text{B.5})$$

which satisfies Lorentz invariance.

With the Dyson equation [245]

$$\Delta(q) = \Delta_0 (1 - \Pi \Delta_0)^{-1} \quad (\text{B.6})$$

we can determine the full propagator from the vacuum polarization and the free propagator. For this we calculate the product

$$\Pi^{\mu\nu}(q) \Delta_{0,\mu\nu}(q) = \frac{q^2 \eta^{\mu\nu} - q^\mu q^\nu}{q^2 + i\varepsilon} \Pi(q^2) \eta_{\mu\nu} = \Pi(q^2) \quad (\text{B.7})$$

and yield the dressed propagator

$$-i\Delta(q) = \mu \text{ --- } \text{dressed} \text{ --- } \nu = -\frac{i\eta_{\mu\nu}}{q^2 (1 - \Pi(q^2)) + i\varepsilon} . \quad (\text{B.8})$$

In this representation, the dressed propagator is to be interpreted as an internal process with respect to vacuum fluctuations in scattering experiments.

To evaluate the propagator, we can use perturbation theory. In the 1-loop approximation we can determine the contribution $\Pi_2^{\mu\nu}(q)$ of $\Pi^{\mu\nu}(q)$ which is proportional to e^2 . Higher orders of loops are suppressed by higher potentials of e^2 . With the free propagators from Eq. (B.1) and Eq. (B.2) and the Feynman rules, it follows

$$i\Pi_2^{\mu\nu}(q) = \mu \text{ --- } \text{1-loop} \text{ --- } \nu = -(-ie)^2 \int \frac{d^4 k}{(2\pi)^4} \text{Tr} \left[\gamma^\mu \frac{i}{\not{k} - m + i\varepsilon} \gamma^\nu \frac{i}{\not{k} + \not{q} - m + i\varepsilon} \right] . \quad (\text{B.9})$$

If we look again at the full propagator in Eq. (B.8), we find that it has a pole at $q^2 = 0$, this reveals that photons have no mass. Obviously, this result is governed by the Ward identity. Using the residual $Z_e = 1/(1 - \Pi(0))$ of the pole $q^2 = 0$, we can distinguish between the bare charge e_0 and the measured physical charge $\sqrt{Z_e}e_0$ in scattering processes with low q^2 . We call this replacement $e_0 \rightarrow \sqrt{Z_e}e_0$ *charge renormalization*. At the lowest order, both charges are equal.

B.2. Approaches Beyond the Standard Model

There is a plethora of theories beyond the Standard Model (SM) of particle physics that attempt to extend or replace it. Generally they are summarized under Beyond the Standard Model (BSM), although they can be very different from the extension of further particles, via supersymmetry to the string theory. These approaches can also influence the phenomena of the quantum vacuum, therefore it is of interest to briefly mention here the most prominent examples of such models. Furthermore, the consequences of these models for the quantum vacuum serve as a motivation to investigate it in more detail, since they partly predict a different behavior compared to those of the nonlinear effects of the QED vacuum. Previous experiments like the Polarizzazione del vuoto con Laser (PVLAS) collaboration established the study of those effects [107, 116, 216]. Future experiments on the quantum vacuum could therefore revolutionize our fundamental understanding of physics.

First, in Sec. B.2.1, we will summarize the Born-Infeld model and its consequences for nonlinear effects in strong field electrodynamics. Subsequently in Sec. B.2.2 a short motivation of the axion-like particles, which couple as scalar field to the electromagnetic field and thus influence the nonlinear effects, follows. Finally, in Sec. B.2.3, the consequences of millicharged particles on our understanding of quantum vacuum physics considering BSM particles are briefly discussed.

B.2.1. Born-Infeld Model

In 1934 Max Born developed a theory of electrodynamics which allowed to calculate the self-energy of a point charge without renormalization. Born's theory, inspired by the special theory of relativity, is founded on the concept of an absolute maximum electric field strength b . He used the Lagrangian density [246]

$$\mathcal{L}_B = -b^2 \sqrt{1 + \frac{2\mathcal{F}}{b^2} + b^2}, \quad (\text{B.10})$$

where we use a modern kind of expression with the relativistic invariant $\mathcal{F} = \frac{1}{4}F^{\mu\nu}F_{\mu\nu}$ determined by the field strength tensor $F^{\mu\nu}$, see Eq. (2.16) in Sec. 2.1. The additional contribution b^2 in \mathcal{L}_B has no influence on the equations of motion, but it ensures that in the limit of small field strengths $F \ll b^2$ the Born Lagrangian approaches into the Maxwell Lagrangian $\mathcal{L}_M = -\mathcal{F}$ of classical electrodynamics. Higher order corrections revealed nonlinear electrodynamics. However, this was not the first nonlinear theory of electromagnetic radiation, already Gustav Mie published his ideas about such a theory in 1912 [247].

Together with Leopold Infeld, Max Born extended the Lagrangian by postulating two principles. First, the principle of finiteness, according to which physical quantities should not diverge. The idea behind this principle is already anticipated in the absolute field strength b or the finite self-energy. The second principle is also based on the special theory of relativity; the action associated with the Lagrangian is required to contain all Lorentz invariants of the field strength tensor. Since this is no longer fulfilled by \mathcal{L}_B , the Lagrangian has been extended

to [47]

$$\mathcal{L}_{\text{BI}} = -b^2 \sqrt{1 + \frac{2\mathcal{F}}{b^2} - \frac{\mathcal{G}^2}{b^4}} + b^2. \quad (\text{B.11})$$

Here, the second invariant of the field strength tensor $\mathcal{G} = \frac{1}{4}\tilde{F}^{\mu\nu}F_{\mu\nu}$ was added. For a review on electrodynamics according to the Born-Infeld model, see reference [248, 249] and for a historical overview with emphasis on photon-photon scattering, see reference [100].

As a consequence of this nonlinear Lagrangian, interactions between electromagnetic fields, or in the quantized form photons, occur. Among others Erwin Schrödinger showed that this nonlinearity had to allow the scattering of photons with photons [48–50, 54]. Later Guy Boillat succeeded in proving that, unlike the theory of nonlinear optics in polarized matter or based on QED, no vacuum birefringence is predicted by the Born-Infeld model to lowest order in the field expansion [104, 250, 251]. Thereby this approach is often considered to be in competition with QED.

Due to the enormous success of QED, research attention on the Born-Infeld model decreased over time, although it has not yet been falsified. It was string theory that brought the Born-Infeld model back into the focus of research [252–255]. In 1985 E. S. Fradkin and A. A. Tseytlin showed that the Lagrangian can be derived from quantized open strings.

To compare the Born-Infeld model with the Heisenberg-Euler Lagrangian of QED \mathcal{L}_{HE} , see Sec. 2.1, it is convenient to expand \mathcal{L}_{BI} as power series in \mathcal{F} and \mathcal{G} . For this we assume that the electromagnetic fields for \mathcal{F} and \mathcal{G} are small compared to the absolute field strength b . We obtain

$$\mathcal{L}_{\text{BI}} = -\mathcal{F} + \frac{1}{2b^2}\mathcal{F}^2 + \frac{1}{2b^2}\mathcal{G}^2 + \mathcal{O}(\mathcal{F}^3, \mathcal{F}\mathcal{G}^2) \quad (\text{B.12})$$

and compare it to the Heisenberg-Euler Lagrangian

$$\mathcal{L}_{\text{HE}} = -\mathcal{F} + \frac{2\alpha^2}{45m_e^4} (4\mathcal{F}^2 + 7\mathcal{G}^2) + \mathcal{O}(\mathcal{F}^3, \mathcal{F}\mathcal{G}^2), \quad (\text{B.13})$$

see Eq. (2.32). Therefore we formulate a general relativistically invariant nonlinear Lagrangian

$$\mathcal{L}_{\text{NL}} = -\mathcal{F} + \xi_L \mathcal{F}^2 + \frac{7}{4}\xi_T \mathcal{G}^2, \quad (\text{B.14})$$

where the prefactors ξ_L and ξ_T differ in the different theories. Furthermore, we restrict ourselves to the first order of nonlinearity. According to quantum electrodynamics the prefactors are identical and we use

$$\xi_L^{\text{QED}} = \xi_T^{\text{QED}} = \frac{8\alpha^2}{45m_e^4} \equiv \xi^{\text{QED}}. \quad (\text{B.15})$$

In the case of the Born-Infeld model

$$4\xi_L^{\text{BI}} = 7\xi_T^{\text{BI}} \quad (\text{B.16})$$

is valid and no statements about the absolute numerical values of these prefactors are possible, because they depend just on the limiting parameter b . A maximum field strength value $b \sim 10^{20}$ V/m was assumed by Born, but it is not an evidence of the theory itself and thus b can

be considered as a free parameter; upper bounds for b can be found in the references [256, 257].

For an experimental test of these two incompatible theories, further research in strong-field vacuum physics is necessary. The PVLAS experiment is a pioneer in this field. In the experiment, a linearly polarized optical laser beam propagates through a homogeneous magnetic field ($B \sim 5$ T) applied in a vacuum chamber. The polarization of the beam before and after propagation are measured and compared [107, 116, 216]. From the data of this experiment a lower limit for

$$\frac{|7\xi_T - 4\xi_L|}{3} < 3.2 \times 10^{-26} \frac{\text{m}^3}{\text{J}} > \xi^{\text{QED}} \approx 6.7 \times 10^{-30} \frac{\text{m}^3}{\text{J}} \quad (\text{B.17})$$

has been derived (in SI units) [98, 258, 259]. These results do not yet allow a final statement whether the Born-Infeld model is true. For QED we have strong evidence due to manifold verifications of various QED experiments. The limit Eq. (B.17) is larger than the value given by the QED. Furthermore, the Born-Infeld model is only falsifiable by an upper bound of $|7\xi_T - 4\xi_L|$; due to measurement inaccuracies, this difference can never vanish exactly in an experiment. However, an experimentally confirmed value with $|7\xi_T - 4\xi_L| < 3\xi^{\text{QED}}$ would complicate the justification of the sfQED values. Besides the test of the sfQED and the Born-Infeld model, the PVLAS experiment is also used to test other BSM theories which have influence on vacuum physics.

B.2.2. Axion-like Particles

The strong charge-conjugation parity symmetry (CP) problem is one of the unsolved problems, or rather naturalness issues, of the SM. One possible solution is given by the Peccei-Quinn mechanism, which includes the prediction of an uncharged pseudoscalar bosonic particle with a mass that could be smaller than that of the electron; the axion [260–265]. Further, axions could help to understand more about dark matter. Based on a model of axions as a candidate for dark matter, lattice quantum chromodynamics (QCD) calculations estimated the mass of the axion to be about 50×10^{-6} eV to 1500×10^{-6} eV [266].

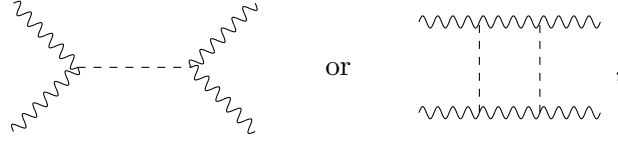
Axions or in general axion-like particles (ALPs) are not only important for the understanding of QCD, they can also be of importance for the phenomena of the quantum vacuum. By ALPs we mean uncharged spin-0 bosons whose mass is much smaller than the electron mass and which interact with the electromagnetic field. These particles can be described as a scalar field ϕ_S or a pseudoscalar field ϕ_P . The effective Lagrangian of a model including electromagnetic fields and ALPs is

$$\mathcal{L}_{\text{eff}}^{\text{ALP}} = \frac{1}{2} (\partial_\mu \phi_{S,P}) (\partial^\mu \phi_{S,P}) - \frac{1}{2} m_\phi \phi_{S,P}^2 - \mathcal{F} - g_{\phi_S \gamma} \phi_S \mathcal{F} - g_{\phi_G \gamma} \phi_P \mathcal{G} \quad (\text{B.18})$$

with \mathcal{F} and \mathcal{G} according to Eq. (2.16), the ALP-photon coupling $g_{\phi_{S/P} \gamma}$ (or just $g_{\phi \gamma}$ meaning both) and the ALP mass m_ϕ . For general insights about axions and ALPs with emphasis on the interaction with the electromagnetic field, see references [267–271].

The interaction between (pseudo) scalar field and electromagnetic field leads to a new kind of vertex connecting the scalar field with two photon lines. This gives rise to additional

diagrams in QFT, such as.


(B.19)

where the ALP lines are represented by the dashed lines. The latter diagram is an example for higher order contributions. These diagrams show that phenomena such as photon-photon scattering or four-wave mixing are affected by the presence of these particles [272–275]. Another consequence is the modification of the optical refraction of the vacuum pumped by a strong external electromagnetic field, which leads to vacuum birefringence. Considering a polarized photon with energy ω passing a homogeneous magnetic field $|\mathbf{B}| = B_{\text{ext}}$ with optical path length L , the refractive index difference between the two polarization components yields according to [107]

$$\Delta n = \frac{g_{\phi\gamma}^2 B_{\text{ext}}^2}{2m_\phi^2} \left(1 - \frac{2\omega}{Lm_\phi} \sin \frac{Lm_\phi^2}{2\omega} \right). \quad (\text{B.20})$$

Analogous to the Born-Infeld model and assuming that the energy of photons is in the range of radio frequencies, i.e. $\omega \ll m_\phi$, we can expand the ALP Lagrangian in a power series of \mathcal{F} and \mathcal{G} . In the first nonlinear order, we can extract the coefficients ξ_L and ξ_T of \mathcal{F}^2 and \mathcal{G}^2 , respectively, as we have already done with the Heisenberg-Euler Lagrangian in Sec. B.2.1, cf. Eq. (B.14) and Eq. (B.15). Since the ALP do not conflict with QED, the coefficients contain the values for pure QED $\xi_L^{\text{QED}} = \xi_T^{\text{QED}} = \xi^{\text{QED}}$ and we obtain

$$\xi_{L/T} = \xi_{L/T}^{\text{ALP}} + \xi^{\text{QED}}. \quad (\text{B.21})$$

The contributions of the ALP are [259]

$$\xi_L^{\text{ALP}} = \frac{g_{\phi S\gamma}^2}{2m_\phi^2} \quad \text{and} \quad \xi_T^{\text{ALP}} = 0 \quad (\text{B.22})$$

for scalar fields and

$$\xi_L^{\text{ALP}} = 0 \quad \text{and} \quad \xi_T^{\text{ALP}} = \frac{2g_{\phi P\gamma}^2}{7m_\phi^2} \quad (\text{B.23})$$

for pseudoscalar fields. Therefore, the difference from the QED value provides information about the kind of the ALP field. Further, studies on astronomical objects or with optical pulses in a laboratory restrict the potential ALP-photon coupling in dependence with the axion mass, cf. [276, 277].

B.2.3. Millicharged Particles

Similar to the axion or ALPs, in general the vacuum polarization can be affected by the existence of BSM particles. If we consider charged massive particles, then these amend the effective Lagrangian beyond the pure QED. In the SM we already find other charged particles contributing to the vacuum polarization and thus to the dressed photon propagator. However,

their contributions are much smaller than those of the electron at low energies, so that we can safely neglect them for the processes considered in this work. We show here by the example of the muon, why this approximation is justified and which consequences this argument has for the influence of BSM particles on the vacuum effects, respectively which properties a BSM particle must have that it influences these effects noticeably.

In deriving the Heisenberg-Euler Lagrangian we have assumed constant electromagnetic fields with fieldstrength $F = |F^{\mu\nu}|$, see section Sec. 2.1. This assumption is also justified if we consider spatially and temporally varying fields, as long as the characteristic scale L of the field, e.g. the wavelength of a laser pulse, is much larger than the Compton wavelength of the electron $\lambda_C = m_e^{-1}$. If we now consider the muon with a rest mass $m_\mu \approx 200m_e$, then the Compton wavelength of the muon is $\lambda_\mu \approx 0.005\lambda_C$ and thus much smaller, so the constant field approximation becomes even better.

Furthermore, in section Sec. 2.1 we have simplified the effective Lagrangian by an expansion in terms of weak fields $F \ll \mathcal{E}_{cr}$ to see the influence of nonlinearities, cf. Eq. (2.33). Here it becomes clear that the critical field strength $\mathcal{E}_{cr} = \frac{m_e^2}{e}$, also called Schwinger limit, is a measure for the strength of the fields. Higher contributions were suppressed by powers of order $\mathcal{O}\left((F/\mathcal{E}_{cr})^3\right)$. For the muon, which has an electric charge of e , the corresponding critical field strength is much higher, $\mathcal{E}_{cr,\mu} = \frac{m_\mu^2}{e} \approx 4 \times 10^4 \mathcal{E}_{cr}$, and thus requires much stronger fields, correspondingly increased by a factor of 4×10^4 , to observe the equivalent vacuum phenomena. Neglecting the influence of the muon, and also of other particles of the SM, is therefore justified for the scales considered here.

Let us assume that there is a BSM particle with mass m_{BSM} and charge ϵe , where ϵ is a dimensionless factor characterizing the charge relative to the electron. The Compton wavelength is then equal to $\lambda_{\text{BSM}} = m_{\text{BSM}}^{-1}$, and for the critical field strength $\mathcal{E}_{cr,\text{BSM}} = \frac{m_{\text{BSM}}^2}{\epsilon e}$ holds. We can now determine the parameter range of m_{BSM} and ϵ , see Fig. B.1, so that BSM particles could measurably influence the weak field expansion of an effective nonlinear Lagrangian and change predictions in future experiments beyond QED. In the laboratory constant field strengths with microscopically large L but relatively small $F \sim 100 \text{ eV}^2 \sim 10^8 \text{ V/m}$ are attainable. Furthermore, experiments on the decay of orthopositronium, an artificial atom consisting of electron and positron with total spin 1, show no evidence for BSM particles with $\epsilon > 10^{-4}$ [278]. Based on the observations from laboratories and the comparison to the critical field strength of the electron \mathcal{E}_{cr} , we can find hypothetical BSM particles in this region. Fig. B.1 illustrates the different limits. The reference [279] gives further limits with respect to previous findings from experiments on birefringence and dichroism and [280] deals with BSM particles with even spin. Due to the best optical laboratory bounds analyzed in reference [281], a magnetized vacuum constrain the charge to be less than $\epsilon < 10^7$ for masses smaller than $5 \times 10^{-2} \text{ eV}$. The boundaries from this references are derived by experiments with constant external magnetic field. Probing the BSM particles with inhomogeneous laser fields we have to restrict the estimation on Compton scales $\lambda \ll L$, where for L we can choose the wavelengths of different electromagnetic radiation. Theoretical proposals suggesting experiments with high-intensity optical or X-ray pulses exclude charge

particles with $\epsilon > 9 \times 10^{-7}$ and masses $0.1 \text{ eV} \leq m_{\text{BSM}} < 1.5 \text{ eV}$ [282]. Since this experiments haven not been preformed yet, this boarder remains theoretical until verification. Another theoretical boundary can be given by the tunneling of a photon through a barrier mediated by a minicharged particle–antiparticle loop [283].

Beyond model-independent laboratory bounds, astrophysical and cosmological considerations allow for model-dependent bounds relying on further assumptions on the astrophysical conditions. These may range down to $\epsilon \lesssim 10^{-7}$ for cosmological considerations and $\epsilon \lesssim 10^{-7}$ regarding astrophysical concepts [284, 285].

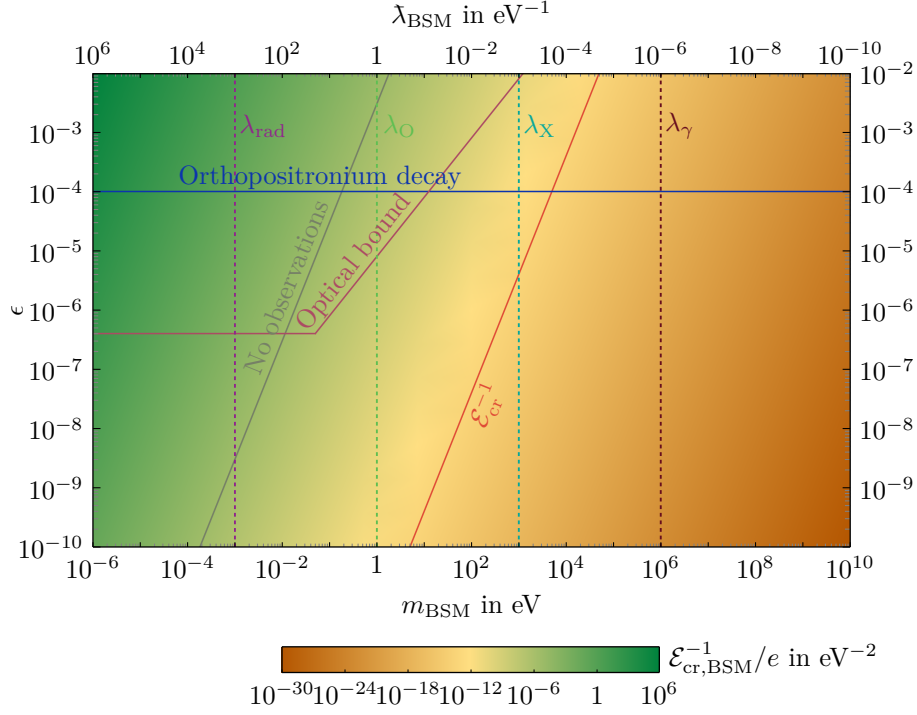


Figure B.1.: *Estimation of parameter regime of BSM particles.* Illustration of the inverse critical field strength $\mathcal{E}_{\text{cr,BSM}}^{-1}$ of a hypothetical BSM particle of mass m_{BSM} and charge ϵe . Above the upper limit for the charge marked by the blue orthopositronium line, and with a mass lower than in experiments with laboratory field strengths, marked by the gray line, there is no evidence of BSM particles affecting an effective nonlinear Lagrangian in the weak field limit. In addition, the purple line indicates the optical laboratory boundary according to reference [281]. Moreover, the red line marks $\mathcal{E}_{\text{cr,BSM}} = \mathcal{E}_{\text{cr}}$. The dashed lines denote the wavelengths equivalent to the Compton wavelength λ_{BSM} ; λ_γ for gamma rays, λ_X for X-ray, λ_O for optical light and λ_{rad} for radio radiation.

Finally, we can restrict the potential range of corresponding BSM particles to a charge range (much) smaller than $10^{-7}e$ to $10^{-4}e$ and accordingly refer to them as Millicharged Particles.

Bibliography

- [1] Bakhtin, M. *Rabelais and His World*. Indiana University Press (1984).
- [2] *The concise Oxford dictionary of current English*. Clarendon Pr., Oxford, 9th ed. (1995).
- [3] Aristotle (translated into english by R. P. Hardie and R. K. Gaye). *Physics, Book IV*. eBooks@Adelaide (2007). <https://web.archive.org/web/20120402105731/http://ebooks.adelaide.edu.au/a/aristotle/physics/book4.html>.
- [4] Berryman, S. “Democritus”. In “The Stanford Encyclopedia of Philosophy”, edited by E.N. Zalta. Metaphysics Research Lab, Stanford University, Winter 2016 ed. (2016).
- [5] Berryman, S. “Leucippus”. In “The Stanford Encyclopedia of Philosophy”, edited by E.N. Zalta. Metaphysics Research Lab, Stanford University, Winter 2016 ed. (2016).
- [6] Corbin, H., Corbin, P., Sherrard, L., Sherrard, P., et al. *History of Islamic Philosophy*. Kegan Paul International (1993). URL <https://books.google.de/books?id=DH8EAQAAIAAJ>.
- [7] Al-Jubouri, I. *History of Islamic Philosophy: With View of Greek Philosophy and Early History of Islam*. Bright Pen (2004). URL <https://books.google.de/books?id=3xJjNG5CNdwC>.
- [8] Druart, T.A. “al-Farabi”. In “The Stanford Encyclopedia of Philosophy”, edited by E.N. Zalta. Metaphysics Research Lab, Stanford University, Winter 2021 ed. (2021).
- [9] “Arabic and Islamic Natural Philosophy and Natural Science”. In “The Stanford Encyclopedia of Philosophy”, edited by E.N. Zalta. Metaphysics Research Lab, Stanford University, Winter 2018 ed. (2018).
- [10] El-Bizri, N. “In Defence of the Sovereignty of Philosophy: Al-Baghdādī’s Critique of Ibn Al-Haytham’s Geometrisation of Place”. *Arabic Sciences and Philosophy* **17** (1) (2007) 57–80. URL <http://dx.doi.org/10.1017/S0957423907000367>.
- [11] Sabra, A.I. *Dictionary of Scientific Biography*, vol. 6. Charles Scribner’s Sons, New York (1972).
- [12] Grant, E. *Much Ado about Nothing: Theories of Space and Vacuum from the Middle Ages to the Scientific Revolution*. Cambridge University Press, Cambridge (1981). URL <http://dx.doi.org/10.1017/CB09780511895326>.

- [13] Grabher, P. “Die Pariser Verurteilung von 1277 : Kontext und Bedeutung des Konflikts um den radikalen Aristotelismus” (2005). Universität Wien, Diplomarbeit, URL <http://dx.doi.org/10.25365/thesis.4725>.
- [14] Duhem, P.t. *The Aim and Structure of Physical Theory*. Atheneum paperbacks. Princeton University Press (1991). URL <https://books.google.de/books?id=5mVPK7QBdTkC>.
- [15] Kilian, U. and Weber, C., (editors) *Lexikon der Physik*, vol. 5. Spektrum Akademischer Verlag, Heidelberg (2000).
- [16] Thorp, J. “Aristotle’s Horror Vacui 1”. *Canadian Journal of Philosophy* **20** (2) (1990) 149–166. URL <http://dx.doi.org/10.1080/00455091.1990.10717213>.
- [17] Soegaard, M. “Horror Vacui: The Fear of Emptiness”. <https://www.interaction-design.org/literature/article/horror-vacui-the-fear-of-emptiness> (2021). [Online; accessed 01-February-2022].
- [18] von Guericke, O. *Neue (sogenannte) Magdeburger Versuche über den leeren Raum*. VDI-Verlag, Düsseldorf (1968).
- [19] Boyer, T.H. “The Classical Vacuum”. *Scientific American* **253** (2) (1985) 70–79. URL <http://www.jstor.org/stable/24967767>.
- [20] Greiner, W., Müller, B., and Rafelski, J. *Quantum Electrodynamics of Strong Fields*. Springer, Berlin (1985).
- [21] Schüller, V., (editor) *Der Leibniz-Clarke Briefwechsel*. Wiley-VCH Verlag, Berlin (1991).
- [22] Malzkorn, W. “Leibniz’s Theory of Space in the Correspondence with Clarke and the Existence of Vacuums”. In “Twentieth World Congress of Philosophy”, edited by S. Dawson (1998). URL <https://www.bu.edu/wcp/Papers/Mode/ModeMalz.htm>.
- [23] Newton, I. *The Mathematical Principles of Natural Philosophy*. No. Vol. 1 in The Mathematical Principles of Natural Philosophy. B. Motte (1729). URL <https://books.google.at/books?id=Tm0FAAAAQAAJ>.
- [24] Newton, I. *The Third Book of Opticks*. The Newton Project, London, vol. 2 ed. (1718). URL <https://www.newtonproject.ox.ac.uk/view/texts/normalized/NATP00051>.
- [25] Euler, L. *Anleitung zur Naturlehre*. 842. Euler Archive - All Works (1862). URL <https://scholarlycommons.pacific.edu/euler-works/842/>.
- [26] Malus, É.L. “Optique Dioptrique”. *Journ. École Polytechn* **7** (1808) 1–44. URL http://neo-classical-physics.info/uploads/3/0/6/5/3065888/malus_-_optics.pdf.

- [27] Schaffner, K. *Nineteenth-century Aether Theories*. Commonwealth and international library of science, technology, engineering and liberal studies. Elsevier Science & Technology (1972). URL <https://books.google.de/books?id=PuVWAAAAAYAAJ>.
- [28] Hertz, H. *Eine Vorlesung über die Grundlagen der Physik aus dem Jahre 1884*. Springer Verlag.
- [29] Michelson, A.A. “The relative motion of the Earth and of the luminiferous ether”. *American Journal of Science* **s3-22** (128) (1881) 120–129. <https://www.ajsonline.org/content/s3-22/128/120.full.pdf>, URL <http://dx.doi.org/10.2475/ajs.s3-22.128.120>.
- [30] Michelson, A.A. and Morley, E.W. “On the relative motion of the Earth and the luminiferous ether”. *American Journal of Science* **s3-34** (203) (1887) 333–345. <https://www.ajsonline.org/content/s3-34/203/333.full.pdf>, URL <http://dx.doi.org/10.2475/ajs.s3-34.203.333>.
- [31] Einstein, A. “Zur Elektrodynamik bewegter Körper”. *Annalen der Physik* **332** (1905) 891–921. URL <http://dx.doi.org/10.1002/andp.19053221004>.
- [32] Pringsheim, E. “Das Kirchhoff’sche Gesetz und die Strahlung der Gase”. *Annalen der Physik* **285** (6) (1893) 347–365. <https://onlinelibrary.wiley.com/doi/pdf/10.1002/andp.18932850609>, URL <http://dx.doi.org/https://doi.org/10.1002/andp.18932850609>.
- [33] Planck, M. “Über das Gesetz der Energieverteilung im Normalspectrum”. *Annalen der Physik* **309** (3) (1901) 553–563. <https://onlinelibrary.wiley.com/doi/pdf/10.1002/andp.19013090310>, URL <http://dx.doi.org/https://doi.org/10.1002/andp.19013090310>.
- [34] Planck, M. “Eine neue Strahlungshypothese”. *Verhandlungen der Deutschen Physikalischen Gesellschaft* p. 138–148. URL <https://books.google.de/books?id=8y7HPgAACAAJ>.
- [35] Planck, M. “Über die Begründung des Gesetzes der schwarzen Strahlung”. *Annalen der Physik* **342** (4) (1912) 642–656. <https://onlinelibrary.wiley.com/doi/pdf/10.1002/andp.19123420403>, URL <http://dx.doi.org/https://doi.org/10.1002/andp.19123420403>.
- [36] Heisenberg, W. “Über den anschaulichen Inhalt der quantentheoretischen Kinematik und Mechanik”. *Zeitschrift für Physik* **43** (3) (1927) 172–198. URL <http://dx.doi.org/10.1007/BF01397280>.
- [37] Dirac, P.A.M. “The Quantum Theory of the Electron”. *Proceedings of the Royal Society of London A: Mathematical, Physical and Engineering Sciences* **117** (1928) 610.

- [38] Dirac, P.A.M. “The Quantum Theory of the Electron. Part II”. *Proceedings of the Royal Society of London A: Mathematical, Physical and Engineering Sciences* **118** (1928) 351.
- [39] Dirac, P.A.M. “A theory of electrons and protons”. *Proceedings of the Royal Society of London A: Mathematical, Physical and Engineering Sciences* **126** (801) (1930) 360–365.
- [40] Pauli, W. “Über den Zusammenhang des Abschlusses der Elektronengruppen im Atom mit der Komplexstruktur der Spektren”. *Zeitschrift für Physik* **31** (1) (1925) 765–783. URL <http://dx.doi.org/10.1007/BF02980631>.
- [41] Einstein, A. “Über einen die Erzeugung und Verwandlung des Lichtes betreffenden heuristischen Gesichtspunkt”. *Annalen der Physik* **14** (132) (1905) 164–181. <https://onlinelibrary.wiley.com/doi/pdf/10.1002/andp.200590004>, URL <http://dx.doi.org/https://doi.org/10.1002/andp.200590004>.
- [42] Crețu, A.M. “Diagnosing Disagreements: The Authentication of the Positron 1931 - 1934”. *Studies in History and Philosophy of Science Part B: Studies in History and Philosophy of Modern Physics* **70**. URL <http://dx.doi.org/10.1016/j.shpsb.2019.10.001>.
- [43] Dirac, P.A.M. “Discussion of the infinite distribution of electrons in the theory of the positron”. *Mathematical Proceedings of the Cambridge Philosophical Society* **30** (2) (1934) 150–163. URL <http://dx.doi.org/10.1017/S030500410001656X>.
- [44] Heisenberg, W. “Bemerkungen zur Diracschen Theorie des Positrons”. *Zeitschrift für Physik* **90** (3) (1934) 209–231. URL <http://dx.doi.org/10.1007/BF01333516>.
- [45] Dirac, P.A.M. “Quantum Mechanics and the Aether”. *The Scientific Monthly* **78** (3) (1954) 142–146. URL <http://www.jstor.org/stable/20945>.
- [46] Sauter, F. “Über das Verhalten eines Elektrons im homogenen elektrischen Feld nach der relativistischen Theorie Diracs”. *Zeitschrift für Physik* **69** (11) (1931) 742–764.
- [47] Born, M., Infeld, L., and Fowler, R.H. “Foundations of the new field theory”. *Proceedings of the Royal Society of London. Series A, Containing Papers of a Mathematical and Physical Character* **144** (852) (1934) 425–451. <https://royalsocietypublishing.org/doi/pdf/10.1098/rspa.1934.0059>, URL <http://dx.doi.org/10.1098/rspa.1934.0059>.
- [48] Schrödinger, E. “Non-Linear Optics”. *Proceedings of the Royal Irish Academy. Section A: Mathematical and Physical Sciences* **47** (1941) 77–117. URL <http://www.jstor.org/stable/20488437>.
- [49] Schrödinger, E. “Dynamics and Scattering-Power of Born’s Electron”. *Proceedings of the Royal Irish Academy. Section A: Mathematical and Physical Sciences* **48** (1942) 91–122. URL <http://www.jstor.org/stable/20488443>.

- [50] Schrödinger, E. “A New Exact Solution in Non-Linear Optics (Two-Wave-System)”. *Proceedings of the Royal Irish Academy. Section A: Mathematical and Physical Sciences* **49** (1943) 59–66. URL <http://www.jstor.org/stable/20488451>.
- [51] Euler, H. and Kockel, B. “Über die Streuung von Licht an Licht nach der Diracschen Theorie”. *Naturwissenschaften* **23** (15) (1935) 246–247. URL <http://dx.doi.org/10.1007/BF01493898>.
- [52] Heisenberg, W. and Euler, H. “Folgerungen aus der Diracschen Theorie des Positrons”. *Zeitschrift für Physik* **98** (11) (1936) 714–732. URL <http://dx.doi.org/10.1007/BF01343663>.
- [53] Weisskopf, V.F. “Über die Elektrodynamik des Vakuums auf Grund der Quantentheorie des Elektrons”. *Kgl. Danske Videnskabernes Selskab. Matematisk-fysiske Meddelelser* **XIV** (1936) 3–39.
- [54] McConnell, J. “Non-Linear Quantum Electrodynamics of the Vacuum”. *Proceedings of the Royal Irish Academy. Section A: Mathematical and Physical Sciences* **49** (1943) 149–176. URL <http://www.jstor.org/stable/20488456>.
- [55] Yoshihiro, K., Kinoshita, J., Inagaki, K., Yamanouchi, C., et al. “Determination of the Fine Structure Constant Based on the Quantum Hall Effect”. *Progress of Theoretical Physics Supplement* **84** (1985) 215–223. <https://academic.oup.com/ptps/article-pdf/doi/10.1143/PTPS.84.215/5166739/84-215.pdf>, URL <http://dx.doi.org/10.1143/PTPS.84.215>.
- [56] Borie, E. “The Role of the Fine-Structure Constant in QED”. *Metrologia* **22** (3) (1986) 140–145. URL <http://dx.doi.org/10.1088/0026-1394/22/3/004>.
- [57] Cage, M., Dziuba, R., Elmquist, R., Field, B., et al. “NBS determination of the fine-structure constant, and of the quantized Hall resistance and Josephson frequency-to-voltage quotient in SI units”. *IEEE Transactions on Instrumentation and Measurement* **38** (2) (1989) 284–289. URL <http://dx.doi.org/10.1109/19.192289>.
- [58] Burkhardt, H. and Pietrzyk, B. “Update of the hadronic contribution to the QED vacuum polarization”. *Physics Letters B* **356** (2) (1995) 398–403. URL [http://dx.doi.org/https://doi.org/10.1016/0370-2693\(95\)00820-B](http://dx.doi.org/https://doi.org/10.1016/0370-2693(95)00820-B).
- [59] Bouchendira, R., Cladé, P., Guellati-Khélifa, S., Nez, F.m.c., et al. “New Determination of the Fine Structure Constant and Test of the Quantum Electrodynamics”. *Phys. Rev. Lett.* **106** (2011) 080801. URL <http://dx.doi.org/10.1103/PhysRevLett.106.080801>.
- [60] Mandaglio, G. “Measurement of the running of the fine structure constant and $\gamma\gamma$ physics at KLOE-2”. *Nuclear and Particle Physics Proceedings* **287-288** (2017) 95–98. The 14th International Workshop on Tau Lepton Physics, URL <http://dx.doi.org/https://doi.org/10.1016/j.nuclphysbps.2017.03.052>.

- [61] Larin, N.R., Dubov, V.V., and Roshchupkin, S.P. “Resonant photoproduction of high-energy electron-positron pairs in the field of a nucleus and a weak electromagnetic wave”. *Phys. Rev. A* **100** (2019) 052502. URL <http://dx.doi.org/10.1103/PhysRevA.100.052502>.
- [62] Yu, C., Zhong, W., Estey, B., Kwan, J., et al. “Atom-Interferometry Measurement of the Fine Structure Constant”. *Annalen der Physik* **531** (5) (2019) 1800346. <https://onlinelibrary.wiley.com/doi/pdf/10.1002/andp.201800346>, URL <http://dx.doi.org/https://doi.org/10.1002/andp.201800346>.
- [63] Morel, L., Yao, Z., Cladé, P., and Guellati-Khélifa, S. “Determination of the fine-structure constant with an accuracy of 81 parts per trillion”. *Nature* **588** (7836) (2020) 61–65. URL <http://dx.doi.org/10.1038/s41586-020-2964-7>.
- [64] Tomonaga, S. “On a Relativistically Invariant Formulation of the Quantum Theory of Wave Fields”. *Progress of Theoretical Physics* **1** (2) (1946) 27–42. <https://academic.oup.com/ptp/article-pdf/1/2/27/24027031/1-2-27.pdf>, URL <http://dx.doi.org/10.1143/PTP.1.27>.
- [65] Schwinger, J. “Quantum Electrodynamics. I. A Covariant Formulation”. *Phys. Rev.* **74** (1948) 1439–1461. URL <http://dx.doi.org/10.1103/PhysRev.74.1439>.
- [66] Feynman, R.P. “Space-Time Approach to Non-Relativistic Quantum Mechanics”. *Rev. Mod. Phys.* **20** (1948) 367–387. URL <http://dx.doi.org/10.1103/RevModPhys.20.367>.
- [67] Dyson, F.J. “The Radiation Theories of Tomonaga, Schwinger, and Feynman”. *Phys. Rev.* **75** (1949) 486–502. URL <http://dx.doi.org/10.1103/PhysRev.75.486>.
- [68] Hooft, G. *The Evolution of Quantum Field Theory: From QED to Grand Unification*, chap. Chapter 1, pp. 1–27 (2016). URL http://dx.doi.org/10.1142/9789814733519_0001.
- [69] Feynman, R.P. “Relativistic Cut-Off for Quantum Electrodynamics”. *Phys. Rev.* **74** (1948) 1430–1438. URL <http://dx.doi.org/10.1103/PhysRev.74.1430>.
- [70] Julian Seymour Schwinger, K., Mehra, U., Milton, K., Mehra, J., et al. *Climbing the Mountain: The Scientific Biography of Julian Schwinger*. Oxford University Press (2000). URL <https://books.google.de/books?id=9SmZSN8F164C>.
- [71] Peskin, M. and Schroeder, D. *An Introduction To Quantum Field Theory*. Frontiers in Physics. Avalon Publishing (1995). URL <https://books.google.de/books?id=EVeNNcs1vX0C>.
- [72] Schwinger, J. “On Gauge Invariance and Vacuum Polarization”. *Physical Review* **82** (5) (1951) 664–679.

- [73] Meitner, L. and Kösters, H. “Über die Streuung kurzweilliger γ -Strahlen”. *Zeitschrift für Physik* **84** (3) (1933) 137–144. URL <http://dx.doi.org/10.1007/BF01333827>.
- [74] Lamb, W.E. and Retherford, R.C. “Fine Structure of the Hydrogen Atom by a Microwave Method”. *Phys. Rev.* **72** (1947) 241–243. URL <http://dx.doi.org/10.1103/PhysRev.72.241>.
- [75] Wilson, R.R. “Scattering of 1.3^3 Mev Gamma-Rays by an Electric Field”. *Phys. Rev.* **90** (1953) 720–721. URL <http://dx.doi.org/10.1103/PhysRev.90.720>.
- [76] Jarlskog, G., Jönsson, L., Prünster, S., Schulz, H.D., et al. “Measurement of Delbrück Scattering and Observation of Photon Splitting at High Energies”. *Phys. Rev. D* **8** (1973) 3813–3823. URL <http://dx.doi.org/10.1103/PhysRevD.8.3813>.
- [77] Akhmadaliev, S.Z., Kezerashvili, G.Y., Klimenko, S.G., Malyshev, V.M., et al. “Delbrück scattering at energies of 140–450 MeV”. *Phys. Rev. C* **58** (1998) 2844–2850. URL <http://dx.doi.org/10.1103/PhysRevC.58.2844>.
- [78] Adler, S.L., Bahcall, J.N., Callan, C.G., and Rosenbluth, M.N. “Photon Splitting in a Strong Magnetic Field”. *Phys. Rev. Lett.* **25** (1970) 1061–1065. URL <http://dx.doi.org/10.1103/PhysRevLett.25.1061>.
- [79] Lee, R.N., Milstein, A.I., and Strakhovenko, V.M. “High-energy photon splitting on heavy atoms”. *Phys. Rev. A* **57** (1998) 2325–2338. URL <http://dx.doi.org/10.1103/PhysRevA.57.2325>.
- [80] Breit, G. and Wheeler, J.A. “Collision of Two Light Quanta”. *Phys. Rev.* **46** (1934) 1087–1091. URL <http://dx.doi.org/10.1103/PhysRev.46.1087>.
- [81] Reiss, H.R. “Absorption of Light by Light”. *Journal of Mathematical Physics* **3** (1) (1962) 59–67. <https://doi.org/10.1063/1.1703787>, URL <http://dx.doi.org/10.1063/1.1703787>.
- [82] Nikishov, A.I. and Ritus, V.I. “Pair Production by a Photon and Photon Emission by an Electron in the Field of an Intense Electromagnetic Wave and in a Constant Field”. *Soviet Physics JETP* **25** (6) (1967) 1135.
- [83] Jansen, M.J.A., Kamiński, J.Z., Krajewska, K., and Müller, C. “Strong-field Breit-Wheeler pair production in short laser pulses: Relevance of spin effects”. *Phys. Rev. D* **94** (2016) 013010. URL <http://dx.doi.org/10.1103/PhysRevD.94.013010>.
- [84] Di Piazza, A. “Nonlinear Breit-Wheeler Pair Production in a Tightly Focused Laser Beam”. *Physical Review Letters* **117** (21). URL <http://dx.doi.org/10.1103/physrevlett.117.213201>.
- [85] Titov, A.I. and Kämpfer, B. “Non-linear Breit–Wheeler process with linearly polarized beams”. *The European Physical Journal D* **74** (11). URL <http://dx.doi.org/10.1140/epjd/e2020-10327-9>.

- [86] Seipt, D. and King, B. “Spin- and polarization-dependent locally-constant-field-approximation rates for nonlinear Compton and Breit-Wheeler processes”. *Physical Review A* **102** (5). URL <http://dx.doi.org/10.1103/physreva.102.052805>.
- [87] Golub, A., Villalba-Chávez, S., and Müller, C. “Strong-field Breit-Wheeler pair production in QED₂₊₁”. *Physical Review D* **103** (9). URL <http://dx.doi.org/10.1103/physrevd.103.096002>.
- [88] Eckey, A., Voitkiv, A.B., and Müller, C. “Strong-field Breit-Wheeler pair production with bremsstrahlung γ -rays in the perturbative-to-nonperturbative-transition regime”. *Physical Review A* **105** (1). URL <http://dx.doi.org/10.1103/physreva.105.013105>.
- [89] Salgado, F.C., Grafenstein, K., Golub, A., Döpp, A., et al. “Towards pair production in the non-perturbative regime”. *New Journal of Physics* **23** (10) (2021) 105002. URL <http://dx.doi.org/10.1088/1367-2630/ac2921>.
- [90] Adamo, T., Ilderton, A., and MacLeod, A.J. “Particle-beam scattering from strong-field QED”. *Phys. Rev. D* **104** (2021) 116013. URL <http://dx.doi.org/10.1103/PhysRevD.104.116013>.
- [91] Golub, A., Villalba-Chávez, S., and Müller, C. “Non-linear Breit-Wheeler pair production in collisions of bremsstrahlung γ -quanta and a tightly focussed laser pulse” arXiv:2203.14776.
- [92] Karplus, R. and Neuman, M. “The Scattering of Light by Light”. *Phys. Rev.* **83** (1951) 776–784. URL <http://dx.doi.org/10.1103/PhysRev.83.776>.
- [93] Varfolomeev, A.A. “Induced Scattering of Light by Light”. *Soviet Physics JETP* **23** (4) (1966) 681.
- [94] Moulin, F. and Bernard, D. “Four-wave interaction in gas and vacuum: definition of a third-order nonlinear effective susceptibility in vacuum: $\chi_{\text{vacuum}}^{(3)}$ ”. *Optics Communications* **164** (1) (1999) 137 – 144. URL [http://dx.doi.org/https://doi.org/10.1016/S0030-4018\(99\)00169-8](http://dx.doi.org/https://doi.org/10.1016/S0030-4018(99)00169-8).
- [95] Bernard, D., Moulin, F., Amiranoff, F., Braun, A., et al. “Search for stimulated photon-photon scattering in vacuum”. *The European Physical Journal D - Atomic, Molecular, Optical and Plasma Physics* **10** (1) (2000) 141–145. URL <http://dx.doi.org/10.1007/s100530050535>.
- [96] Lundin, J., Marklund, M., Lundstrom, E., Brodin, G., et al. “Detection of elastic photon-photon scattering through four-wave mixing using high power lasers”. *Phys. Rev. A* **74** (2006) 043821. arXiv:hep-ph/0606136, URL <http://dx.doi.org/10.1103/PhysRevA.74.043821>.

- [97] Lundström, E., Brodin, G., Lundin, J., Marklund, M., et al. “Using High-Power Lasers for Detection of Elastic Photon-Photon Scattering”. *Phys. Rev. Lett.* **96** (2006) 083602. URL <http://dx.doi.org/10.1103/PhysRevLett.96.083602>.
- [98] Tommasini, D. and Michinel, H. “Light by light diffraction in vacuum”. *Phys. Rev. A* **82** (2010) 011803. URL <http://dx.doi.org/10.1103/PhysRevA.82.011803>.
- [99] Dinu, V., Heinzl, T., Ilderton, A., Marklund, M., et al. “Photon polarization in light-by-light scattering: Finite size effects”. *Phys. Rev. D* **90** (2014) 045025. URL <http://dx.doi.org/10.1103/PhysRevD.90.045025>.
- [100] Scharnhorst, K. “Photon-photon scattering and related phenomena. Experimental and theoretical approaches: The early period” arXiv:1711.05194.
- [101] Gies, H., Karbstein, F., Kohlfürst, C., and Seegert, N. “Photon-photon scattering at the high-intensity frontier”. *Phys. Rev.* **D97** (7) (2018) 076002. arXiv:1712.06450, URL <http://dx.doi.org/10.1103/PhysRevD.97.076002>.
- [102] King, B., Hu, H., and Shen, B. “Three-pulse photon-photon scattering”. *Phys. Rev. A* **98** (2018) 023817. URL <http://dx.doi.org/10.1103/PhysRevA.98.023817>.
- [103] Baier, R. and Breitenlohner, P. “VACUUM REFRACTION INDEX IN THE PRESENCE OF EXTERNAL FIELDS.” *Nuovo Cimento* (10), **47B**: 117-20(Jan. 11, 1967). URL <http://dx.doi.org/10.1007/BF02712312>.
- [104] Bialynicka-Birula, Z. and Bialynicki-Birula, I. “Nonlinear Effects in Quantum Electrodynamics. Photon Propagation and Photon Splitting in an External Field”. *Phys. Rev. D* **2** (1970) 2341–2345. URL <http://dx.doi.org/10.1103/PhysRevD.2.2341>.
- [105] Adler, S.L. “Photon splitting and photon dispersion in a strong magnetic field”. *Annals Phys.* **67** (1971) 599–647. URL [http://dx.doi.org/10.1016/0003-4916\(71\)90154-0](http://dx.doi.org/10.1016/0003-4916(71)90154-0).
- [106] Heinzl, T., Liesfeld, B., Amthor, K.U., Schwöerer, H., et al. “On the observation of vacuum birefringence”. *Opt. Commun.* **267** (2006) 318–321. arXiv:hep-ph/0601076, URL <http://dx.doi.org/10.1016/j.optcom.2006.06.053>.
- [107] Valle, F.D., Gastaldi, U., Messineo, G., Milotti, E., et al. “Measurements of vacuum magnetic birefringence using permanent dipole magnets: the PVLAS experiment”. *New Journal of Physics* **15** (5) (2013) 053026. URL <http://dx.doi.org/10.1088/1367-2630/15/5/053026>.
- [108] Karbstein, F., Gies, H., Reuter, M., and Zepf, M. “Vacuum birefringence in strong inhomogeneous electromagnetic fields”. *Phys. Rev.* **D92** (7) (2015) 071301. arXiv:1507.01084, URL <http://dx.doi.org/10.1103/PhysRevD.92.071301>.
- [109] Karbstein, F. “Vacuum Birefringence as a Vacuum Emission Process”. In “Photon 2015: International Conference on the Structure and Interactions of the Photon and

- 21th International Workshop on Photon-Photon Collisions and International Workshop on High Energy Photon Linear Colliders Novosibirsk, Russia, June 15-19”, (2015). arXiv:1510.03178.
- [110] King, B. and Elkina, N. “Vacuum birefringence in high-energy laser-electron collisions”. *Phys. Rev. A* **94** (2016) 062102. URL <http://dx.doi.org/10.1103/PhysRevA.94.062102>.
 - [111] Karbstein, F. “The quantum vacuum in electromagnetic fields: From the Heisenberg-Euler effective action to vacuum birefringence”. In “Proceedings, Quantum Field Theory at the Limits: from Strong Fields to Heavy Quarks (HQ 2016): Dubna, Russia, July 18-30, 2016”, pp. 44–57 (2017). arXiv:1611.09883, URL <http://dx.doi.org/10.3204/DESY-PROC-2016-04/Karbstein>.
 - [112] Bragin, S., Meuren, S., Keitel, C.H., and Di Piazza, A. “High-Energy Vacuum Birefringence and Dichroism in an Ultrastrong Laser Field”. *Phys. Rev. Lett.* **119** (2017) 250403. URL <http://dx.doi.org/10.1103/PhysRevLett.119.250403>.
 - [113] Karbstein, F. “Vacuum birefringence in the head-on collision of x-ray free-electron laser and optical high-intensity laser pulses”. *Phys. Rev. D* **98** (2018) 056010. URL <http://dx.doi.org/10.1103/PhysRevD.98.056010>.
 - [114] Ataman, S. “Vacuum birefringence detection in all-optical scenarios”. *Phys. Rev. A* **97** (2018) 063811. URL <http://dx.doi.org/10.1103/PhysRevA.97.063811>.
 - [115] Ahmadianiaz, N., Cowan, T.E., Sauerbrey, R., Schramm, U., et al. “Heisenberg limit for detecting vacuum birefringence”. *Phys. Rev. D* **101** (2020) 116019. URL <http://dx.doi.org/10.1103/PhysRevD.101.116019>.
 - [116] Ejlli, A., Della Valle, F., Gastaldi, U., Messineo, G., et al. “The PVLAS experiment: a 25 year effort to measure vacuum magnetic birefringence” arXiv:2005.12913.
 - [117] Hattori, K., Taya, H., and Yoshida, S. “Di-lepton production from a single photon in strong magnetic fields: vacuum dichroism”. *JHEP* **01** (2021) 093. arXiv:2010.13492, URL [http://dx.doi.org/10.1007/JHEP01\(2021\)093](http://dx.doi.org/10.1007/JHEP01(2021)093).
 - [118] Mosman, E.A. and Karbstein, F. “Vacuum birefringence and diffraction at an x-ray free-electron laser: From analytical estimates to optimal parameters”. *Physical Review D* **104** (1). URL <http://dx.doi.org/10.1103/physrevd.104.013006>.
 - [119] Karbstein, F., Sundqvist, C., Schulze, K.S., Uschmann, I., et al. “Vacuum birefringence at x-ray free-electron lasers”. *New J. Phys.* **23** (9) (2021) 095001. arXiv:2105.13869, URL <http://dx.doi.org/10.1088/1367-2630/ac1df4>.
 - [120] Ahmadianiaz, N., Bussmann, M., Cowan, T., Debus, A., et al. “Observability of Coulomb-assisted quantum vacuum birefringence”. *Physical Review D* **104** (1). URL <http://dx.doi.org/10.1103/physrevd.104.1011902>.

- [121] Agil, J., Battesti, R., and Rizzo, C. “Monte Carlo study of the BMV vacuum linear magnetic birefringence experiment” arXiv:2107.10527.
- [122] Gies, H., Karbstein, F., and Seegert, N. “Quantum Reflection as a New Signature of Quantum Vacuum Nonlinearity”. *New J. Phys.* **15** (2013) 083002. arXiv:1305.2320, URL <http://dx.doi.org/10.1088/1367-2630/15/8/083002>.
- [123] Gies, H., Karbstein, F., and Seegert, N. “Quantum reflection of photons off spatio-temporal electromagnetic field inhomogeneities”. *New J. Phys.* **17** (4) (2015) 043060. arXiv:1412.0951, URL <http://dx.doi.org/10.1088/1367-2630/17/4/043060>.
- [124] Gies, H., Karbstein, F., and Shaisultanov, R. “Laser photon merging in an electromagnetic field inhomogeneity”. *Phys. Rev. D* **90** (2014) 033007. URL <http://dx.doi.org/10.1103/PhysRevD.90.033007>.
- [125] Gies, H., Karbstein, F., and Seegert, N. “Photon merging and splitting in electromagnetic field inhomogeneities”. *Phys. Rev. D* **93** (2016) 085034. URL <http://dx.doi.org/10.1103/PhysRevD.93.085034>.
- [126] Reinhardt, J. and Greiner, W. “Quantum electrodynamics of strong fields”. *Reports on Progress in Physics* **40** (3) (1977) 219–295. URL <http://dx.doi.org/10.1088/0034-4885/40/3/001>.
- [127] Dittrich, W. and Gies, H. *Probing the quantum vacuum. Perturbative effective action approach in quantum electrodynamics and its application*, vol. 166. Springer Tracts Mod. Phys. (2000). URL <http://dx.doi.org/10.1007/3-540-45585-X>.
- [128] Dunne, G.V. *Heisenberg–Euler effective Lagrangians: basics and extensions*, pp. 445–522. Singapore: World Scientific (2014). URL http://dx.doi.org/10.1142/9789812775344_0014.
- [129] Marklund, M. and Lundin, J. “Quantum Vacuum Experiments Using High Intensity Lasers”. *Eur. Phys. J.* **D55** (2009) 319–326. arXiv:0812.3087, URL <http://dx.doi.org/10.1140/epjd/e2009-00169-6>.
- [130] Battesti, R. and Rizzo, C. “Magnetic and electric properties of a quantum vacuum”. *Reports on Progress in Physics* **76** (1) (2012) 016401. URL <http://dx.doi.org/10.1088/0034-4885/76/1/016401>.
- [131] Dunne, G.V. “The Heisenberg-Euler Effective Action: 75 Years On”. *International Journal of Modern Physics A* **27** (15) (2012) 1260004. <https://doi.org/10.1142/S0217751X12600044>, URL <http://dx.doi.org/10.1142/S0217751X12600044>.
- [132] Inada, T., Yamazaki, T., Yamaji, T., Seino, Y., et al. “Probing Physics in Vacuum Using an X-ray Free-Electron Laser, a High-Power Laser, and a High-Field Magnet”. *Science* **7** (2017) 671. arXiv:1707.00253, URL <http://dx.doi.org/10.3390/app7070671>.

- [133] Karbstein, F. “Probing Vacuum Polarization Effects with High-Intensity Lasers”. *Particles* **3** (1) (2020) 39–61. URL <http://dx.doi.org/10.3390/particles3010005>.
- [134] Schoeffel, L., Baldenegro, C., Hamdaoui, H., Hassani, S., et al. “Photon–photon physics at the LHC and laser beam experiments, present and future”. *Prog. Part. Nucl. Phys.* **120** (2021) 103889. arXiv:2010.07855, URL <http://dx.doi.org/10.1016/j.ppnp.2021.103889>.
- [135] Fedotov, A., Ilderton, A., Karbstein, F., King, B., et al. “Advances in QED with intense background fields” arXiv:2203.00019.
- [136] Heinzl, T. “QED and Lasers: A Tutorial” arXiv:2203.01245, URL <http://dx.doi.org/10.48550/arXiv.2203.01245>.
- [137] Laboratory for Laser Energetics - OMEGA EP Laser System. www.lle.rochester.edu/index.php/omega-laser-facility-2 (2022). [Online; accessed 21-February-2022].
- [138] Extreme Light Infrastructure - Nuclear Physics facility. www.eli-np.ro (2022). [Online; accessed 09-February-2022].
- [139] X-Ray Free Electron Laser. www.xfel.eu (2022). [Online; accessed 10-February-2022].
- [140] Schneidmiller, E.A. and Yurkov, M.V. “Photon beam properties at the European XFEL” (DESY-11-152; XFEL.EU TR-2011-006). URL <http://dx.doi.org/10.3204/DESY11-152>.
- [141] Heinzl, T. and Ilderton, A. “Exploring high-intensity QED at ELI”. *The European Physical Journal D* **55** (2) (2009) 359–364. URL <http://dx.doi.org/10.1140/epjd/e2009-00113-x>.
- [142] Di Piazza, A., Müller, C., Hatsagortsyan, K.Z., and Keitel, C.H. “Extremely high-intensity laser interactions with fundamental quantum systems”. *Rev. Mod. Phys.* **84** (2012) 1177–1228. URL <http://dx.doi.org/10.1103/RevModPhys.84.1177>.
- [143] King, B.J. and Heinzl, T. “Measuring vacuum polarization with high-power lasers”. *High Power Laser Science and Engineering* **4** (2016) e5. URL <http://dx.doi.org/10.1017/hpl.2016.1>.
- [144] Thaury, C., Quéré, F., Geindre, J.P., Levy, A., et al. “Plasma mirrors for ultrahigh-intensity optics”. *Nature Physics* **3** (6) (2007) 424–429. URL <http://dx.doi.org/10.1038/nphys595>.
- [145] Jeong, T.M., Bulanov, S.V., Valenta, P., Korn, G., et al. “Relativistic flying laser focus by a laser-produced parabolic plasma mirror”. *Phys. Rev. A* **104** (2021) 053533. URL <http://dx.doi.org/10.1103/PhysRevA.104.053533>.

- [146] Bernhardt, H., Marx-Glowna, B., Schulze, K.S., Grabiger, B., et al. “High purity x-ray polarimetry with single-crystal diamonds”. *Applied Physics Letters* **109** (12) (2016) 121106. <https://doi.org/10.1063/1.4962806>, URL <http://dx.doi.org/10.1063/1.4962806>.
- [147] Bernhardt, H., Schmitt, A.T., Grabiger, B., Marx-Glowna, B., et al. “Ultra-high precision x-ray polarimetry with artificial diamond channel cuts at the beam divergence limit”. *Phys. Rev. Research* **2** (2020) 023365. URL <http://dx.doi.org/10.1103/PhysRevResearch.2.023365>.
- [148] Salgado, F.C., Cavanagh, N., Tamburini, M., Storey, D.W., et al. “Single particle detection system for strong-field QED experiments”. *New Journal of Physics* **24** (1) (2021) 015002. URL <http://dx.doi.org/10.1088/1367-2630/ac4283>.
- [149] Doyle, L., Khademi, P., Hilz, P., Sävert, A., et al. “Experimental estimates of the photon background in a potential light-by-light scattering study”. *New Journal of Physics* **24** (2) (2022) 025003. URL <http://dx.doi.org/10.1088/1367-2630/ac4ad3>.
- [150] Marklund, M. and Shukla, P.K. “Nonlinear collective effects in photon-photon and photon-plasma interactions”. *Rev. Mod. Phys.* **78** (2006) 591–640. URL <http://dx.doi.org/10.1103/RevModPhys.78.591>.
- [151] King, B., Di Piazza, A., and Keitel, C.H. “A matterless double slit”. *Nature Photonics* **4** (2) (2010) 92–94. URL <http://dx.doi.org/10.1038/nphoton.2009.261>.
- [152] Karbstein, F. and Shaisultanov, R. “Photon propagation in slowly varying inhomogeneous electromagnetic fields”. *Phys. Rev.* **D91** (8) (2015) 085027. arXiv:1503.00532, URL <http://dx.doi.org/10.1103/PhysRevD.91.085027>.
- [153] Hill, W.T. and Roso, L. “Probing the quantum vacuum with petawatt lasers”. *Journal of Physics: Conference Series* **869** (2017) 012015. URL <http://dx.doi.org/10.1088/1742-6596/869/1/012015>.
- [154] C. Kohlfürst, R.A. “Ponderomotive effects in multiphoton pair production”. *Physical Review D* **97** (2018) 036026.
- [155] Gies, H., Karbstein, F., and Kohlfürst, C. “All-optical signatures of Strong-Field QED in the vacuum emission picture”. *Phys. Rev.* **D97** (3) (2018) 036022. arXiv:1712.03232, URL <http://dx.doi.org/10.1103/PhysRevD.97.036022>.
- [156] Blinne, A., Gies, H., Karbstein, F., Kohlfürst, C., et al. “All-optical signatures of quantum vacuum nonlinearities in generic laser fields”. *Phys. Rev.* **D99** (1) (2019) 016006. arXiv:1811.08895, URL <http://dx.doi.org/10.1103/PhysRevD.99.016006>.
- [157] Bulanov, S.V., Satorov, P.V., Pegoraro, F., Kadlecová, H., et al. “Electromagnetic solitons in quantum vacuum”. *Phys. Rev. D* **101** (2020) 016016. URL <http://dx.doi.org/10.1103/PhysRevD.101.016016>.

- [158] Karbstein, F. and Mosman, E.A. “Photon polarization tensor in pulsed Hermite- and Laguerre-Gaussian beams”. *Phys. Rev.* **D96** (11) (2017) 116004. arXiv:1711.06151, URL <http://dx.doi.org/10.1103/PhysRevD.96.116004>.
- [159] Karbstein, F., Blinne, A., Gies, H., and Zepf, M. “Boosting Quantum Vacuum Signatures by Coherent Harmonic Focusing”. *Physical Review Letters* **123** (9). URL <http://dx.doi.org/10.1103/physrevlett.123.091802>.
- [160] Klar, L. “Detectable Optical Signatures of QED Vacuum Nonlinearities Using High-Intensity Laser Fields”. *Particles* **3** (1) (2020) 223–233. URL <http://dx.doi.org/10.3390/particles3010018>.
- [161] Karbstein, F. and Mosman, E.A. “Enhancing quantum vacuum signatures with tailored laser beams”. *Physical Review D* **101** (11). URL <http://dx.doi.org/10.1103/physrevd.101.113002>.
- [162] Gies, H., Karbstein, F., and Klar, L. “All-optical Quantum Vacuum Signals in Two-Beam Collision” arXiv:2205.15684.
- [163] Karbstein, F. and Sundqvist, C. “Probing vacuum birefringence using x-ray free electron and optical high-intensity lasers”. *Phys. Rev. D* **94** (2016) 013004. URL <http://dx.doi.org/10.1103/PhysRevD.94.013004>.
- [164] Gies, H., Karbstein, F., and Klar, L. “Quantum vacuum signatures in multicolor laser pulse collisions”. *Phys. Rev. D* **103** (7) (2021) 076009. arXiv:2101.04461, URL <http://dx.doi.org/10.1103/PhysRevD.103.076009>.
- [165] Karbstein, F. and Oude Weernink, R.R.Q.P.T. “X-ray vacuum diffraction at finite spatiotemporal offset”. *Phys. Rev. D* **104** (2021) 076015. URL <http://dx.doi.org/10.1103/PhysRevD.104.076015>.
- [166] Ludwig, G. *Einführung in die Grundlagen der theoretischen Physik*, vol. 1–4. Bertelsmann, Düsseldorf (1974).
- [167] Weinberg, S. *The Quantum Theory of Fields*, vol. 1. Cambridge University Press (1995). URL <http://dx.doi.org/10.1017/CB09781139644167>.
- [168] Weinberg, S. *The Quantum Theory of Fields*, vol. 2. Cambridge University Press (1996). URL <http://dx.doi.org/10.1017/CB09781139644174>.
- [169] Ryder, L.H. *Quantum Field Theory*. Cambridge University Press, 2nd ed. (1996). URL <http://dx.doi.org/10.1017/CB09780511813900>.
- [170] Zinn-Justin, J. *Quantum Field Theory and Critical Phenomena*. Oxford University Press, 4th ed. (2002). URL <http://dx.doi.org/10.1093/acprof:oso/9780198509233.001.0001>.

- [171] Ritus, V.I. “The Lagrange Function of an Intensive Electromagnetic Field and Quantum Electrodynamics at Small Distances”. *Sov. Phys. JETP* **42** (1975) 774.
- [172] Dittrich, W. and Reuter, M. *Effective Lagrangians in Quantum Electrodynamics*, vol. 220. Springer (1985). URL <http://dx.doi.org/10.1007/3-540-15182-6>.
- [173] Landau, L., Lifschitz, E., and Berestetzki, V. *Quantenelektrodynamik*. Lehrbuch der theoretischen Physik. Verlag Harri Deutsch (2009). URL <https://books.google.de/books?id=oN5JxwEACAAJ>.
- [174] Kleinert, H. *Particles and Quantum Fields*. World Scientific Publishing, Berlin (2016). <https://www.worldscientific.com/doi/pdf/10.1142/9915>, URL <http://dx.doi.org/10.1142/9915>.
- [175] Das, A.K. and Farina, C. “Proper time method for fermions” arXiv:hep-th/9807152.
- [176] Huet, I., Rausch de Traubenberg, M., and Schubert, C. “Asymptotic Behaviour of the QED Perturbation Series”. *Advances in High Energy Physics* **2017** (2017) 6214341. URL <http://dx.doi.org/10.1155/2017/6214341>.
- [177] Gies, H. and Karbstein, F. “An Addendum to the Heisenberg-Euler effective action beyond one loop”. *J. High Energ. Phys.* [Addendum: JHEP 03, 108 (2017)], arXiv:1612.07251, URL [http://dx.doi.org/10.1007/JHEP03\(2017\)108](http://dx.doi.org/10.1007/JHEP03(2017)108).
- [178] Yariv, A. *Quantum electronics*. Wiley, New York [u.a.], 2nd ed. (1975).
- [179] Siegman, A.E. *Lasers*. Univ. Science Books, Mill Valley, Calif. (1986).
- [180] Saleh, B.E.A. and Teich, M.C. *Fundamentals of Photonics*. John Wiley & Sons, Ltd (1991). <https://onlinelibrary.wiley.com/doi/pdf/10.1002/0471213748>, URL <http://dx.doi.org/https://doi.org/10.1002/0471213748>.
- [181] Blackledge, J.M. *Optical Image Formation*, chap. 11, pp. 343–394. Woodhead Publishing Series in Electronic and Optical Materials. Woodhead Publishing (2005). URL <http://dx.doi.org/https://doi.org/10.1533/9780857099464.2.343>.
- [182] Robertson, J. *Introduction to Optics: Geometrical and Physical*. University physics series. Van Nostrand (1954). URL <https://books.google.je/books?id=UrIGAQAIAAJ>.
- [183] Svelto, O. *Ray and Wave Propagation Through Optical Media*, pp. 131–161. Springer US, Boston, MA (2010). URL http://dx.doi.org/10.1007/978-1-4419-1302-9_4.
- [184] Steinbach, A., Rauner, M., Cruz, F., and Bergquist, J. “CW second harmonic generation with elliptical Gaussian beams”. *Optics Communications* **123** (1) (1996) 207 – 214. URL [http://dx.doi.org/https://doi.org/10.1016/0030-4018\(95\)00626-5](http://dx.doi.org/https://doi.org/10.1016/0030-4018(95)00626-5).
- [185] Walker, B.C., Tóth, C., Fittinghoff, D.N., Guo, T., et al. “A 50-EW/cm² Ti:sapphire laser system for studying relativistic light-matter interactions”. *Opt. Express* **5** (10) (1999) 196–202. URL <http://dx.doi.org/10.1364/OE.5.000196>.

- [186] Withnall, R. “SPECTROSCOPY | Raman Spectroscopy”. In “Encyclopedia of Modern Optics”, edited by R.D. Guenther, pp. 119–134. Elsevier, Oxford (2005). URL <http://dx.doi.org/https://doi.org/10.1016/B0-12-369395-0/00960-X>.
- [187] Matras, G., Lureau, F., Laux, S., Casagrande, O., et al. “First sub-25fs PetaWatt laser system”. In “Advanced Solid-State Lasers Congress”, p. AF2A.3. Optical Society of America (2013). URL <http://dx.doi.org/10.1364/ASSL.2013.AF2A.3>.
- [188] Apollon Laser Facility. <https://apollonlaserfacility.cnrs.fr> (2022). [Online; accessed 01-March-2022].
- [189] Centre Interdisciplinaire Lumière Extrême. <http://cilexsaclay.fr> (2022). [Online; accessed 01-March-2022].
- [190] Garrec, B.L. and ”the Appolon team”. “Design update and recent results of the Apollon 10 PW facility”. In “Conference on Lasers and Electro-Optics”, p. SF1K.3. Optica Publishing Group (2017). URL http://dx.doi.org/10.1364/CLEO_SI.2017.SF1K.3.
- [191] Center for Relativistic Laser Science. <https://corels.ibs.re.kr> (2022). [Online; accessed 01-March-2022].
- [192] Yoon, J.W., Kim, Y.G., Choi, I.W., Sung, J.H., et al. “Realization of laser intensity over 10^{23} W/cm²”. *Optica* **8** (5) (2021) 630–635. URL <http://dx.doi.org/10.1364/OPTICA.420520>.
- [193] Extreme Light Infrastructure. <https://eli-laser.eu/> (2022). [Online; accessed 01-March-2022].
- [194] Aléonard, M., Altarelli, M., Antici, P., Apolonskiy, A., et al. *WHITEBOOK ELI – Extreme Light Infrastructure; Science and Technology with Ultra-Intense Lasers* (2011). URL <http://dx.doi.org/10.13140/2.1.1227.0889>.
- [195] Cernaianu, M.O., Boisdeffre, B.D., Ursescu, D., Negoita, F., et al. “Monitoring and control systems for experiments at ELI-NP”. *Romanian Reports in Physics* **68** (2016) S349–S443.
- [196] Rus, B., Bakule, P., Kramer, D., Naylor, J., et al. “ELI-beamlines: progress in development of next generation short-pulse laser systems”. In “Research Using Extreme Light: Entering New Frontiers with Petawatt-Class Lasers III”, vol. 10241, edited by G. Korn and L.O. Silva, pp. 14 – 21. International Society for Optics and Photonics, SPIE (2017). URL <http://dx.doi.org/10.1117/12.2269818>.
- [197] Lureau, F., Matras, G., Chalus, O., Derycke, C., et al. “High-energy hybrid femtosecond laser system demonstrating 2×10 PW capability”. *High Power Laser Science and Engineering* **8** (2020) e43. URL <http://dx.doi.org/10.1017/hpl.2020.41>.

- [198] Tanaka, K.A. “Status of high-power lasers and experiments at ELI-Nuclear Physics, Romania”. In “High Power Lasers and Applications”, vol. 11777, edited by J. Hein, T.J. Butcher, P. Bakule, C.L. Haefner, G. Korn, and L.O. Silva. International Society for Optics and Photonics, SPIE (2021). URL <http://dx.doi.org/10.1117/12.2596872>.
- [199] Negoita, F., Jaroszynski, D., Mckenna, P., Balascuta, S., et al. “High field physics and QED experiments at ELI-NP”. *Rom. Rep. Phys.* **68** (Supplement) (2016) S145.
- [200] Centre for Advanced Laser Applications. www.cala-laser.de (2022). [Online; accessed 31-January-2022].
- [201] Hartmann, J., Rösch, T.F., Balling, F., Berndt, M., et al. “Commissioning of the laser-driven ion acceleration beamline at the Centre for Advanced Laser Applications”. In “Laser Acceleration of Electrons, Protons, and Ions VI”, vol. 11779, edited by S.S. Bulanov, J. Schreiber, and C.B. Schroeder, pp. 44 – 49. International Society for Optics and Photonics, SPIE (2021). URL <http://dx.doi.org/10.1117/12.2592407>.
- [202] Helmholtz-Institut Jena. https://www.hi-jena.de/de/helmholtz_institute_jena/ueber-das-helmholtz-institut-jena/experimental_facilities/local/jeti200-laser/ (2022). [Online; accessed 31-January-2022].
- [203] Helmholtz-Institut Jena. https://www.hi-jena.de/en/helmholtz_institute_jena/about-the-helmholtz-institute-jena/experimental_facilities/local/polaris (2022). [Online; accessed 31-January-2022].
- [204] Meyerhofer, D.D., Bromage, J., Dorrer, C., Kelly, J.H., et al. “Performance of and initial results from the OMEGA EP Laser System”. *Journal of Physics: Conference Series* **244** (3) (2010) 032010. URL <http://dx.doi.org/10.1088/1742-6596/244/3/032010>.
- [205] Zhu, J., Xie, X., Yang, Q., Kang, J., et al. “Introduction to SG-II 5 PW Laser Facility”. In “Conference on Lasers and Electro-Optics”, p. SM1M.7. Optica Publishing Group (2016). URL http://dx.doi.org/10.1364/CLEO_SI.2016.SM1M.7.
- [206] Zhu, J., Xie, X., Sun, M., Kang, J., et al. “Analysis and construction status of SG-II 5PW laser facility”. *High Power Laser Science and Engineering* **6** (2018) e29. URL <http://dx.doi.org/10.1017/hpl.2018.23>.
- [207] Tucholsky (alias Kaspar Hauser), K. “Zur soziologischen Psychologie der Löcher”. *Die Weltbühne* **11** (1931) 389.
- [208] Kaspi, V.M. and Beloborodov, A.M. “Magnetars”. *Annual Review of Astronomy and Astrophysics* **55** (1) (2017) 261–301. <https://doi.org/10.1146/annurev-astro-081915-023329>, URL <http://dx.doi.org/10.1146/annurev-astro-081915-023329>.
- [209] Kouveliotou, C., Dieters, S., Strohmayer, T., van Paradijs, J., et al. “An X-ray pulsar with a superstrong magnetic field in the soft γ -ray repeater SGR1806 - 20”. *Nature* **393** (6682) (1998) 235–237. URL <http://dx.doi.org/10.1038/30410>.

- [210] Cioffi, R. “Modelling the Magnetic Field Configuration of Neutron Stars”. *Astron. Nachr.* **335** (2014) 624. arXiv:1406.7230, URL <http://dx.doi.org/10.1002/asna.201412083>.
- [211] Romero Jorge, A.W., Rodriguez Querts, E., Perez Rojas, H., Perez Martínez, A., et al. “The photon time delay in magnetized vacuum magnetosphere”. *Astronomische Nachrichten* **340** (9-10) (2019) 852–856. <https://onlinelibrary.wiley.com/doi/pdf/10.1002/asna.201913736>, URL <http://dx.doi.org/https://doi.org/10.1002/asna.201913736>.
- [212] Fan, X., Kamioka, S., Inada, T., Yamazaki, T., et al. “The OVAL experiment: a new experiment to measure vacuum magnetic birefringence using high repetition pulsed magnets”. *The European Physical Journal D* **71** (11) (2017) 308. URL <http://dx.doi.org/10.1140/epjd/e2017-80290-7>.
- [213] Mignani, R.P., Testa, V., González Caniulef, D., Taverna, R., et al. “Evidence for vacuum birefringence from the first optical-polarimetry measurement of the isolated neutron star RX J1856.5-3754”. *Monthly Notices of the Royal Astronomical Society* **465** (1) (2016) 492–500. <https://academic.oup.com/mnras/article-pdf/465/1/492/8593962/stw2798.pdf>, URL <http://dx.doi.org/10.1093/mnras/stw2798>.
- [214] Zherlitsyn, S., Wustmann, B., Herrmannsdörfer, T., and Wosnitza, J. “Magnet-Technology Development at the Dresden High Magnetic Field Laboratory”. *Journal of Low Temperature Physics* **170**. URL <http://dx.doi.org/10.1007/s10909-012-0764-7>.
- [215] Battesti, R., Beard, J., Böser, S., Bruyant, N., et al. “High magnetic fields for fundamental physics”. *Physics Reports* **765-766** (2018) 1–39. High magnetic fields for fundamental physics, URL <http://dx.doi.org/https://doi.org/10.1016/j.physrep.2018.07.005>.
- [216] Zavattini, E., Zavattini, G., Ruoso, G., Polacco, E., et al. (PVLAS Collaboration). “Experimental Observation of Optical Rotation Generated in Vacuum by a Magnetic Field”. *Phys. Rev. Lett.* **96** (2006) 110406. URL <http://dx.doi.org/10.1103/PhysRevLett.96.110406>.
- [217] Karbstein, F. and Shaisultanov, R. “Stimulated photon emission from the vacuum”. *Phys. Rev. D* **91** (2015) 113002. URL <http://dx.doi.org/10.1103/PhysRevD.91.113002>.
- [218] Galtsov, D. and Skobelev, V. “Photons creation by an external field”. *Physics Letters B* **36** (3) (1971) 238–240. URL [http://dx.doi.org/https://doi.org/10.1016/0370-2693\(71\)90077-3](http://dx.doi.org/https://doi.org/10.1016/0370-2693(71)90077-3).
- [219] Furry, W.H. “A Symmetry Theorem in the Positron Theory”. *Phys. Rev.* **51** (1937) 125–129. URL <http://dx.doi.org/10.1103/PhysRev.51.125>.

- [220] King, B. and Keitel, C.H. “Photon–photon scattering in collisions of intense laser pulses”. *New Journal of Physics* **14** (10) (2012) 103002. URL <http://dx.doi.org/10.1088/1367-2630/14/10/103002>.
- [221] Roso, L., Lera, R., Ravichandran, S., Longman, A., et al. “Towards a direct measurement of the quantum-vacuum Lagrangian coupling coefficients using two counterpropagating super-intense laser pulses”. *New Journal of Physics* **24** (2) (2022) 025010. URL <http://dx.doi.org/10.1088/1367-2630/ac51a7>.
- [222] Goethe, J.W.v. *Faust*. Reclam, Stuttgart, Jubiläums-Edition ed. (1992).
- [223] Abramowitz, M. and Stegun, I.A. *Handbook of Mathematical Functions with Formulas, Graphs, and Mathematical Tables*. Dover Publications, New York, 9th ed. (1964).
- [224] Gradshteyn, I. and Ryzhik, I. *Table of Integrals, Series, and Products*. Academic Press, New York, 4th ed. (1965).
- [225] Chen, S.y., Maksimchuk, A., and Umstadter, D. “Experimental observation of relativistic nonlinear Thomson scattering”. *Nature* **396** (6712) (1998) 653–655. URL <http://dx.doi.org/10.1038/25303>.
- [226] Gordienko, S., Pukhov, A., Shorokhov, O., and Baeva, T. “Relativistic Doppler Effect: Universal Spectra and Zeptosecond Pulses”. *Phys. Rev. Lett.* **93** (2004) 115002. URL <http://dx.doi.org/10.1103/PhysRevLett.93.115002>.
- [227] Gordienko, S., Pukhov, A., Shorokhov, O., and Baeva, T. “Coherent Focusing of High Harmonics: A New Way Towards the Extreme Intensities”. *Phys. Rev. Lett.* **94** (2005) 103903. URL <http://dx.doi.org/10.1103/PhysRevLett.94.103903>.
- [228] Karbstein, F. and Mosman, E.A. “X-ray photon scattering at a focused high-intensity laser pulse”. *Physical Review D* **100** (3). URL <http://dx.doi.org/10.1103/physrevd.100.033002>.
- [229] Marcinkevičius, A., Tommasini, R., Tsakiris, G., Witte, K., et al. “Frequency doubling of multi-terawatt femtosecond pulses”. *Applied Physics B* **79** (5) (2004) 547–554. URL <http://dx.doi.org/10.1007/s00340-004-1612-5>.
- [230] Di Piazza, A., Hatsagortsyan, K.Z., and Keitel, C.H. “Light Diffraction by a Strong Standing Electromagnetic Wave”. *Phys. Rev. Lett.* **97** (2006) 083603. URL <http://dx.doi.org/10.1103/PhysRevLett.97.083603>.
- [231] Monden, Y. and Kodama, R. “Enhancement of Laser Interaction with Vacuum for a Large Angular Aperture”. *Phys. Rev. Lett.* **107** (2011) 073602. URL <http://dx.doi.org/10.1103/PhysRevLett.107.073602>.
- [232] Kadlecová, H., Bulanov, S.V., and Korn, G. “Properties of finite amplitude electromagnetic waves propagating in the quantum vacuum”. *Plasma Physics and Controlled Fusion* **61** (8) (2019) 084002. URL <http://dx.doi.org/10.1088/1361-6587/ab21fb>.

- [233] Jeong, T.M., Bulanov, S.V., Sasorov, P.V., Korn, G., et al. “Photon scattering by a 4π -spherically-focused ultrastrong electromagnetic wave”. *Phys. Rev. A* **102** (2020) 023504. URL <http://dx.doi.org/10.1103/PhysRevA.102.023504>.
- [234] McKenna, J. and Platzman, P.M. “Nonlinear Interaction of Light in a Vacuum”. *Phys. Rev.* **129** (1963) 2354–2360. URL <http://dx.doi.org/10.1103/PhysRev.129.2354>.
- [235] Rozanov, N.N. “Four-wave interactions of intense radiation in vacuum”. *Soviet Physics JETP* **76** (6) (1993) 991.
- [236] Di Piazza, A., Hatsagortsyan, K.Z., and Keitel, C.H. “Harmonic generation from laser-driven vacuum”. *Phys. Rev. D* **72** (2005) 085005. URL <http://dx.doi.org/10.1103/PhysRevD.72.085005>.
- [237] Fedotov, A.M. and Narozhny, N.B. “Generation of harmonics by a focused laser beam in the vacuum”. *Physics Letters. A* **362**. URL <http://dx.doi.org/10.1016/j.physleta.2006.09.085>.
- [238] Fillion-Gourdeau, F.m.c., Lefebvre, C., and MacLean, S. “Scheme for the detection of mixing processes in vacuum”. *Phys. Rev. A* **91** (2015) 031801. URL <http://dx.doi.org/10.1103/PhysRevA.91.031801>.
- [239] Böhl, P., King, B., and Ruhl, H. “Vacuum high-harmonic generation in the shock regime”. *Phys. Rev. A* **92** (2015) 032115. URL <http://dx.doi.org/10.1103/PhysRevA.92.032115>.
- [240] Aboushelbaya, R., Glize, K., Savin, A.F., Mayr, M., et al. “Orbital Angular Momentum Coupling in Elastic Photon-Photon Scattering”. *Phys. Rev. Lett.* **123** (2019) 113604. URL <http://dx.doi.org/10.1103/PhysRevLett.123.113604>.
- [241] Hume, D. *An Enquiry Concerning Human Understanding*, vol. 1809, chap. 4, p. 90. Reclam Universal-Bibliothek (1748).
- [242] Sangal, M., Keitel, C.H., and Tamburini, M. “Observing light-by-light scattering in vacuum with an asymmetric photon collider”. *Phys. Rev. D* **104** (2021) L111101. URL <http://dx.doi.org/10.1103/PhysRevD.104.L111101>.
- [243] Tanabashi, M., Hagiwara, K., Hikasa, K., Nakamura, K., et al. (Particle Data Group). “Review of Particle Physics”. *Phys. Rev. D* **98** (2018) 030001. URL <http://dx.doi.org/10.1103/PhysRevD.98.030001>.
- [244] Grozin, A. “Lectures on QED and QCD”. In “3rd Dubna International Advanced School of Theoretical Physics”, (2005). arXiv:hep-ph/0508242.
- [245] Dyson, F.J. “The S Matrix in Quantum Electrodynamics”. *Phys. Rev.* **75** (1949) 1736–1755. URL <http://dx.doi.org/10.1103/PhysRev.75.1736>.

- [246] Born, M. and Fowler, R.H. “On the quantum theory of the electromagnetic field”. *Proceedings of the Royal Society of London. Series A, Containing Papers of a Mathematical and Physical Character* **143** (849) (1934) 410–437. <https://royalsocietypublishing.org/doi/pdf/10.1098/rspa.1934.0010>, URL <http://dx.doi.org/10.1098/rspa.1934.0010>.
- [247] Mie, G. “Grundlagen einer Theorie der Materie”. *Annalen der Physik* **342** (3) (1912) 511–534. <https://onlinelibrary.wiley.com/doi/pdf/10.1002/andp.19123420306>, URL <http://dx.doi.org/https://doi.org/10.1002/andp.19123420306>.
- [248] Kruglov, S.I. “Notes on Born–Infeld-type electrodynamics”. *Modern Physics Letters A* **32** (36) (2017) 1750201. <https://doi.org/10.1142/S0217732317502017>, URL <http://dx.doi.org/10.1142/S0217732317502017>.
- [249] Rebhan, A. and Turk, G. “Polarization effects in light-by-light scattering: Euler–Heisenberg versus Born–Infeld”. *International Journal of Modern Physics A* **32** (10) (2017) 1750053. <https://doi.org/10.1142/S0217751X17500531>, URL <http://dx.doi.org/10.1142/S0217751X17500531>.
- [250] Boillat, G. “Nonlinear Electrodynamics: Lagrangians and Equations of Motion”. *Journal of Mathematical Physics* **11** (3) (1970) 941–951. <https://doi.org/10.1063/1.1665231>, URL <http://dx.doi.org/10.1063/1.1665231>.
- [251] Kadlecová, H. “On the absence of shock waves and vacuum birefringence in Born-Infeld electrodynamics” arXiv:2107.12249.
- [252] Fradkin, E. and Tseytlin, A. “Non-linear electrodynamics from quantized strings”. *Physics Letters B* **163** (1) (1985) 123–130. URL [http://dx.doi.org/https://doi.org/10.1016/0370-2693\(85\)90205-9](http://dx.doi.org/https://doi.org/10.1016/0370-2693(85)90205-9).
- [253] Tseytlin, A.A. *Born-Infeld Action, Supersymmetry and Sting Theory*, pp. 417–452 (2000). https://www.worldscientific.com/doi/pdf/10.1142/9789812793850_0025, URL http://dx.doi.org/10.1142/9789812793850_0025.
- [254] Ambjørn, J., Makeenko, Y.M., Semenoff, G.W., and Szabo, R.J. “String theory in electromagnetic fields”. *Journal of High Energy Physics* **2003** (02) (2003) 026–026. URL <http://dx.doi.org/10.1088/1126-6708/2003/02/026>.
- [255] Muñoz, G. and Tennant, D. “Testing string theory via Born–Infeld electrodynamics?” *Physics Letters B* **682** (3) (2009) 297–299. URL <http://dx.doi.org/https://doi.org/10.1016/j.physletb.2009.11.021>.
- [256] Dávila, J.M., Schubert, C., and Trejo, M.A. “Photonic processes in Born–Infeld theory”. *International Journal of Modern Physics A* **29** (30) (2014) 1450174. <https://doi.org/10.1142/S0217751X14501747>, URL <http://dx.doi.org/10.1142/S0217751X14501747>.

- [257] Ellis, J.R., Mavromatos, N., and You, T. “Constraint on Born-Infeld Theory from Light-by-Light Scattering at the LHC”. *CERN Proc.* **1** (2018) 69. URL <http://dx.doi.org/10.23727/CERN-Proceedings-2018-001.69>.
- [258] Bregant, M., Cantatore, G., Carusotto, S., Cimino, R., et al. (PVLAS Collaboration). “Limits on low energy photon-photon scattering from an experiment on magnetic vacuum birefringence”. *Phys. Rev. D* **78** (2008) 032006. URL <http://dx.doi.org/10.1103/PhysRevD.78.032006>.
- [259] Tommasini, D., Ferrando, A., Michinel, H., and Seco, M. “Precision tests of QED and non-standard models by searching photon-photon scattering in vacuum with high power lasers”. *Journal of High Energy Physics* **2009** (11) (2009) 043–043. URL <http://dx.doi.org/10.1088/1126-6708/2009/11/043>.
- [260] ’t Hooft, G. “Symmetry Breaking through Bell-Jackiw Anomalies”. *Phys. Rev. Lett.* **37** (1976) 8–11. URL <http://dx.doi.org/10.1103/PhysRevLett.37.8>.
- [261] ’t Hooft, G. “Computation of the quantum effects due to a four-dimensional pseudoparticle”. *Phys. Rev. D* **14** (1976) 3432–3450. URL <http://dx.doi.org/10.1103/PhysRevD.14.3432>.
- [262] Peccei, R.D. and Quinn, H.R. “CP Conservation in the Presence of Pseudoparticles”. *Phys. Rev. Lett.* **38** (1977) 1440–1443. URL <http://dx.doi.org/10.1103/PhysRevLett.38.1440>.
- [263] Peccei, R.D. and Quinn, H.R. “Constraints imposed by CP conservation in the presence of pseudoparticles”. *Phys. Rev. D* **16** (1977) 1791–1797. URL <http://dx.doi.org/10.1103/PhysRevD.16.1791>.
- [264] Wilczek, F. “Problem of Strong P and T Invariance in the Presence of Instantons”. *Phys. Rev. Lett.* **40** (1978) 279–282. URL <http://dx.doi.org/10.1103/PhysRevLett.40.279>.
- [265] Weinberg, S. “A New Light Boson?” *Phys. Rev. Lett.* **40** (1978) 223–226. URL <http://dx.doi.org/10.1103/PhysRevLett.40.223>.
- [266] Borsanyi, S., Fodor, Z., Guenther, J., Kampert, K.H., et al. “Calculation of the axion mass based on high-temperature lattice quantum chromodynamics”. *Nature* **539** (7627) (2016) 69–71. URL <http://dx.doi.org/10.1038/nature20115>.
- [267] Sikivie, P. “Experimental Tests of the ”Invisible” Axion”. *Phys. Rev. Lett.* **51** (1983) 1415–1417. URL <http://dx.doi.org/10.1103/PhysRevLett.51.1415>.
- [268] Maiani, L., Petronzio, R., and Zavattini, E. “Effects of nearly massless, spin-zero particles on light propagation in a magnetic field”. *Physics Letters B* **175** (3) (1986) 359–363. URL [http://dx.doi.org/https://doi.org/10.1016/0370-2693\(86\)90869-5](http://dx.doi.org/https://doi.org/10.1016/0370-2693(86)90869-5).

- [269] Gasperini, M. “Axion production by electromagnetic fields”. *Phys. Rev. Lett.* **59** (1987) 396–398. URL <http://dx.doi.org/10.1103/PhysRevLett.59.396>.
- [270] Massó, E. and Toldrà, R. “Light spinless particle coupled to photons”. *Phys. Rev. D* **52** (1995) 1755–1763. URL <http://dx.doi.org/10.1103/PhysRevD.52.1755>.
- [271] Massó, E. “Axions and axion-like particles”. *Nuclear Physics B - Proceedings Supplements* **114** (2003) 67–73. Proceedings of the XXXth International Meeting of Fundamentals Physics, URL [http://dx.doi.org/https://doi.org/10.1016/S0920-5632\(02\)01893-5](http://dx.doi.org/https://doi.org/10.1016/S0920-5632(02)01893-5).
- [272] Beyer, K.A., Marocco, G., Bingham, R., and Gregori, G. “Axion detection through resonant photon-photon collisions”. *Phys. Rev. D* **101** (2020) 095018. URL <http://dx.doi.org/10.1103/PhysRevD.101.095018>.
- [273] Shakeri, S., Marsh, D.J.E., and Xue, S.S. “Light by Light Scattering as a New Probe for Axions” arXiv:2002.06123.
- [274] Nobuhiro, A., Hirahara, Y., Homma, K., Kirita, Y., et al. “Extended search for sub-eV axion-like resonances via four-wave mixing with a quasi-parallel laser collider in a high-quality vacuum system”. *Progress of Theoretical and Experimental Physics* **2020** (7). 073C01, <https://academic.oup.com/ptep/article-pdf/2020/7/073C01/33467477/ptaa075.pdf>, URL <http://dx.doi.org/10.1093/ptep/ptaa075>.
- [275] Domcke, V., Ema, Y., and Mukaida, K. “Chiral anomaly, Schwinger effect, Euler-Heisenberg Lagrangian and application to axion inflation”. *Journal of High Energy Physics* **2020** (2) (2020) 55. URL [http://dx.doi.org/10.1007/JHEP02\(2020\)055](http://dx.doi.org/10.1007/JHEP02(2020)055).
- [276] Villalba-Chávez, S., Podszus, T., and Müller, C. “Polarization-operator approach to optical signatures of axion-like particles in strong laser pulses”. *Physics Letters B* **769** (2017) 233–241. URL <http://dx.doi.org/https://doi.org/10.1016/j.physletb.2017.03.043>.
- [277] Dessert, C., Dunsky, D., and Safdi, B.R. “Upper limit on the axion-photon coupling from magnetic white dwarf polarization” arXiv:2203.04319.
- [278] Mitsui, T., Fujimoto, R., Ishisaki, Y., Ueda, Y., et al. “Search for invisible decay of orthopositronium”. *Phys. Rev. Lett.* **70** (1993) 2265–2268. URL <http://dx.doi.org/10.1103/PhysRevLett.70.2265>.
- [279] Gies, H., Jaeckel, J., and Ringwald, A. “Polarized Light Propagating in a Magnetic Field as a Probe for Millicharged Fermions”. *Phys. Rev. Lett.* **97** (2006) 140402. URL <http://dx.doi.org/10.1103/PhysRevLett.97.140402>.
- [280] Kruglov, S.I. “Pair production and vacuum polarization of vector particles with electric dipole moments and anomalous magnetic moments”. *The European Physical Journal C - Particles and Fields* **22** (1) (2001) 89–98. URL <http://dx.doi.org/10.1007/s100520100776>.

- [281] Ahlers, M., Gies, H., Jaeckel, J., Redondo, J., et al. “Laser experiments explore the hidden sector”. *Phys. Rev. D* **77** (2008) 095001. URL <http://dx.doi.org/10.1103/PhysRevD.77.095001>.
- [282] Villalba-Chávez, S., Meuren, S., and Müller, C. “Minicharged particles search by strong laser pulse-induced vacuum polarization effects”. *Physics Letters B* **763** (2016) 445–453. URL <http://dx.doi.org/https://doi.org/10.1016/j.physletb.2016.10.068>.
- [283] Döbrich, B., Gies, H., Neitz, N., and Karbstein, F. “Magnetically Amplified Tunneling of the Third Kind as a Probe of Minicharged Particles”. *Phys. Rev. Lett.* **109** (2012) 131802. URL <http://dx.doi.org/10.1103/PhysRevLett.109.131802>.
- [284] Davidson, S., Hannestad, S., and Raffelt, G. “Updated bounds on milli-charged particles”. *Journal of High Energy Physics* **2000** (05) (2000) 003–003. URL <http://dx.doi.org/10.1088/1126-6708/2000/05/003>.
- [285] Melchiorri, A., Polosa, A., and Strumia, A. “New bounds on millicharged particles from cosmology”. *Physics Letters B* **650** (5) (2007) 416–420. URL <http://dx.doi.org/https://doi.org/10.1016/j.physletb.2007.05.042>.

List of Figures

2.1. Paraxial Gaussian beam profile	21
2.2. Propagation of a Gaussian pulse	22
2.3. Profile of Gaussian beams	25
3.1. Vacuum emission direction and polarization	40
4.1. Collision of two high-intensity laser pulses	60
4.2. Pump-probe-collision with elliptical focused probe in IRRA	61
4.3. Scheme for numerical determination of the lower bound of ϑ_1 at constant φ for the region of discernible signal	63
4.4. Potential source of error of the numerical method for determining the solid angle region of the region of discernible signal	65
4.5. Area of the solid angle region $\mathcal{A}_{d,\mu}$ of discernible signal over μ for two-beam (circular probe) collision with $\vartheta_{\text{col}} = 160^\circ$	68
4.6. Mollweide plot of signal and background density for two-beam (circular probe) collision with $\vartheta_{\text{col}} = 160^\circ$ and $\mu = 5$	69
4.7. Number of discernible signal photons $N(\mathcal{A}_{d,\mu})$ over μ for two-beam (circular probe) collision with $\vartheta_{\text{col}} = 160^\circ$	70
4.8. Mollweide plot for equal signal and background density for two-beam (circular probe) collision with different angle ϑ_{col} and probe waists	71
4.9. Number of discernible signal photons $N(\mathcal{A}_{d,\mu})$ and corresponding background photons $\mathcal{N}(\mathcal{A}_{d,\mu})$ over μ for two-beam (circular probe) collisions	72
4.10. Area of the solid angle region $\mathcal{A}_{d,\mu}$ of discernible signal over μ for two-beam (circular probe) collision with different $\vartheta_{\text{col}} = 160^\circ$	73
4.11. Schematic of the possible increase in the yield of discernible signal photons by an elliptical probe beam	74
4.12. Area of the solid angle region \mathcal{A}_{d,μ_y} of discernible signal over μ_y for two-beam (elliptic probe, $\mu_x = \mu_{\text{max}N}$) collision with $\vartheta_{\text{col}} = 160^\circ$	75
4.13. Mollweide plot of signal and background density for a two-beam (elliptical probe) collision with $\vartheta_{\text{col}} = 160^\circ$ and $\mu_x = 5.5$, $\mu_y = 1$	76
4.14. Mollweide plot for equal signal and background density for two-beam (elliptical probe) collision with different angle ϑ_{col} and probe waists	77
4.15. Number of discernible signal photons $N(\mathcal{A}_{d,\mu_y})$ over μ_y and $N(\mathcal{A}_{d,\mu_x})$ over μ_x for two-beam (elliptical probe) collisions	78
4.16. Number of discernible polarization flipped signal photons in the solid angle regime $\mathcal{A}_{d,\bar{\mu}}$ as function of the purity \mathcal{P} of the polarization of the probe beam	81

List of Figures

4.17. Illustration of a multi-color beam collision geometry	84
4.18. Spectral histogram and distribution of signal in a multi-color pulse collision .	88
4.19. Mollweide plot of signal-photon density of multi-color pulse collision	89
4.20. Mollweide plot of signal-photon density of multi-color pulse collision with zoom for inelastic $2\omega_0$ and $4\omega_0$ signal	91
4.21. Mollweide plot of signal-photon density of a multi-color pulse collision zooming on the inelastic $5\omega_0$ signal	92
B.1. Estimation of parameter regime of BSM particles	110

List of Tables

2.1. High-intensity laser facilities	29
4.1. Maximum numbers of discernible signal photons $N(\mathcal{A}_{d,\mu_{\max N}})$ and its corresponding relative probe waist size $\mu_{\max N}$ for two-beam (circular probe) collision	72
4.2. Maximum numbers of background photons $N(\mathcal{A}_{d,\mu_{\max N}})$ and its corresponding relative probe waist size $\mu_{\max N}$ for two-beam (circular probe) collision	73
4.3. Maximum numbers of discernible signal photons $N(\mathcal{A}_{d,\mu_{y,\max N}})$ and its corresponding relative probe waist sizes μ_y and μ_y for two-beam (elliptic probe) collision	79
4.4. Exemplary pulse-energies distributions for the multi-color pulse collision . . .	86
4.5. Number of discernible signal photons and corresponding background photons for the multi-color pulse collision	92
4.6. Signal photons contribution per channel in multi pulse collision	95
4.7. Discernible inelastical signal photons in multi-color pulse collision	95
A.1. Relation between SI unit and Heaviside-Lorentz unit systems	102

Abbreviations

1PI	One-particle-irreducible
ALP	Axion like Particle
ATLAS(-3000)	Advanced Ti:Sapphire Laser 3000 Terawatt
BSM	Beyond standard model of particle physics
CALA	Center of Advanced Laser Applications
CILEX	Centre Interdisciplinaire Lumière Extrême
CoReLS	Center for Relativistic Laser Science
CP	Charge-conjugation parity symmetry
DESY	Deutsches Elektronen-Synchrotron
ELI	Extreme Light Infrastructure
ELI-ALPS	ELI Attosecond Light Pulse Source
ELI-NP	Extreme Light Infrastructure - Nuclear Physics
FWHM	Full width half maximum
HI Jena	Helmholtz Institute Jena
HL	Heaviside-Lorentz
IRRA	Infinite Rayleigh range approximation
JETI-200	Jenaer Titan:Saphir 200 Terawatt
LLE	Laboratory for Laser Energetics
LCFA	Locally constant field approximation
NLHPL	National Laboratory on High Power Lasers
OMEGA EP	OMEGA extended performance
POLARIS	Petawatt Optical Laser Amplifier for Radiation Intensive Experiments
PVLAS	Polarizzazione del vuoto con Laser
QCD	Quantum chromodynamics
QED	Quantum electrodynamics
QFT	Quantum field theory
SI	International System of Units
SG-II	Shen Guang-II
SM	Standard model of particle physics
TEM	Transverse electromagnetic
Ti:sapphire	Titanium-sapphire
UQBF	Ultrashort Quantum Beam Facility
VEP	Vacuum emission picture
XFEL	X-Ray Free Electron Laser

Danksagungen

Mein besonderer Dank gilt zunächst meinem Betreuer Prof. Dr. Holger Gies, der mich einerseits mit seiner umfassenden Expertise in der theoretischen Physik unterstützt hat, andererseits auch immer mit seiner angenehmen, verständlichen und offenen Art durchweg hervorragend betreut hat. Ich bin sehr dankbar für die vielen Gespräche, auch jenseits der Forschung, ebenso für die gemeinsame Arbeit, mit der ich mich wissenschaftlich weiterentwickelt habe und die mir sehr viel Freude bereitet hat.

Des Weiteren möchte ich mich bei Dr. Felix Karbstein bedanken. Sein fachliches Detailwissen sowie seine Heiterkeit waren immer eine Bereicherung für unsere enge Zusammenarbeit. Unsere wissenschaftlichen Diskussionen waren stets von einer konstruktiven und erquickenden Atmosphäre geprägt und mündeten in Erkenntnissen, die meine Forschung vorantrieben.

Außerdem danke ich allen, die ebenfalls am Quantenvakuum forschen, vor allem den Doktoranden Chantal Sundqvist und Ricardo Oude Weernink, sowie Kolleg:innen, Alumni und Freund:innen aus weiteren Instituten wie Dr. Elena Mosman, Dr. Christian Kohlfürst und Dr. Greger Torgrimsson.

Zudem bedanke ich mich beim Team der Forschungsgruppe 2783, dem Helmholtz-Institute Jena inklusive des Graduiertenkollegs RS-APS und bei der Deutschen Forschungsgemeinschaft für die finanzielle Förderung meiner Promotion.

Ich bin dankbar für die sehr schöne Zeit am Theoretisch-Physikalischen-Institut der Friedrich-Schiller-Universität Jena und ich bin froh um alle, die diese einmalige und tolle Atmosphäre des TPIs ausmachen. Großer Dank gilt Katrin Kanter, Lisann Schmidt, Cindy Büchner und Mathias Kirchner für die Organisation. Ohne euch wäre mein Reisekostenerstattungsantrag von meiner ersten Dienstreise immer noch in Arbeit. Darüber hinaus danke ich dem IT-Team des TPI, insbesondere Dr. Andre Sternbeck, Dr. Marc Steinhauser, Florian Attender, Ricardo Oude Weernink und Dr. Martin Weiß. Als Teil des Teams weiß ich um die Arbeit, die ihr täglich, meist im Hintergrund, leistet und ich bin froh, dass ihr mir in den letzten Monaten den Rücken frei gehalten habt, sodass ich mich auf meine Dissertation konzentrieren konnte.

Auch den anderen Kolleg:innen im TPI will ich danken: zunächst meinen beiden Bürokollegen Richard Schmieden und Jobst Ziebell, die mir jeden Tag mit ihrer guten Laune verschönern haben. Vor allem danke ich Richard Schmieden für die sprachliche Hinweise zu meiner Arbeit. Furthermore, I am very grateful to Matteo Breschi, Daniela Cors, Kemal Döner, Francesco Fabbri, Dimitri Gkiatas, Seán Gray, Julian Lenz, Dr. Camilo López, Michael Mandl, Linda van Manen, Dr. Riccardo Martini, Michel Pannier (besonders für die Bereitstellung der 87,36 Liter Kaffee, die mich durch die Promotion brachten), David Rumler, Sabor Salek, José Simão, Ivan Soler, Dr. Alessandro Ugolotti, Katharina Wölfl, and Francesco Zappa.

Ich danke allen meinen Freunden und allen weiteren Personen, die mich in der Zeit meiner Promotion begleitet haben, egal ob in Jena oder außerhalb. Vor allem Katharina Mesterom bin ich dankbar, die mich unerlässlich stärkt und mir insbesondere in der Endphase meiner Promotion zur Seite stand. Ganz besonders danke ich meiner Familie, die immer für mich da ist und mich stets unterstützt. So bedanke ich mich vor allem bei Gabriele Klar, Andreas Laupert, Maximilian Klar, Alina Klar und meinen Großeltern Ursula und Hans Rohde, denen ich diese Arbeit widme. Mit eurer Unterstützung von klein auf habt ihr mich zu dem gemacht, der ich bin und eure Liebe prägt mein ganzes Leben.

Ehrenwörtliche Erklärung

Ich erkläre hiermit ehrenwörtlich, dass ich die vorliegende Arbeit selbständig, ohne unzulässige Hilfe Dritter und ohne Benutzung anderer als der angegebenen Hilfsmittel und Literatur angefertigt habe. Die aus anderen Quellen direkt oder indirekt übernommenen Daten und Konzepte sind unter Angabe der Quelle gekennzeichnet.

Bei der Auswahl und Auswertung des Materials sowie beim Verfassen der Publikationen [160, 162, 164] haben mir die nachstehend aufgeführten Personen unentgeltlich geholfen:

- Prof. Dr. Holger Gies
- Dr. Felix Karbstein

Weitere Personen waren an der inhaltlich-materiellen Erstellung der vorliegenden Arbeit nicht beteiligt. Insbesondere habe ich hierfür nicht die entgeltliche Hilfe von Vermittlungs- bzw. Beratungsdiensten (Promotionsberater oder andere Personen) in Anspruch genommen. Niemand hat von mir unmittelbar oder mittelbar geldwerte Leistungen für Arbeiten erhalten, die im Zusammenhang mit dem Inhalt der vorgelegten Dissertation stehen.

Die Arbeit wurde bisher weder im In- noch im Ausland in gleicher oder ähnlicher Form einer anderen Prüfungsbehörde vorgelegt.

Die geltende Promotionsordnung der Physikalisch-Astronomischen Fakultät ist mir bekannt.

Ich versichere ehrenwörtlich, dass ich nach bestem Wissen die reine Wahrheit gesagt und nichts verschwiegen habe.

Ort, Datum:

Unterschrift